Electronic Thesis and Dissertation Repository

9-14-2018 3:00 PM

Electrocatalysts with high activity and stability for polymer electrolyte membrane fuel cells

Zhongxin Song
The University of Western Ontario

Supervisor
Sun, Xueliang
The University of Western Ontario

Follow this and additional works at: https://ir.lib.uwo.ca/etd

Part of the Catalysis and Reaction Engineering Commons, and the Nanoscience and Nanotechnology Commons

Recommended Citation

Song, Zhongxin, "Electrocatalysts with high activity and stability for polymer electrolyte membrane fuel cells" (2018). *Electronic Thesis and Dissertation Repository*. 5700.
https://ir.lib.uwo.ca/etd/5700

Abstract

In addressing the activity and durability challenges facing electrocatalysts in polymer electrolyte membrane fuel cells (PEMFCs), atomic layer deposition (ALD) is emerging as a powerful technique for deposition of noble metals and transition metal oxides due to its exclusive advantages over other methods. The primary advantages of ALD are derived from the sequential, self-saturating, gas-surface reactions, and angstrom level control that take place during the deposition process. Therefore, ALD possesses the advantage in precisely control the particle size and uniform distribution on the substrate. By forming chemical bonds between the initial layer of ALD precursor and support atoms during the first cycle of deposition, the strong interaction between the deposited material and support could be enabled, which is benefit for achieving the highly stable NPs.

In this thesis, an area-selective ALD of tantalum oxide (TaOx) on Pt/C catalyst to fabricate TaOx-anchored Pt NPs with triple-junction structure of Pt–TaOx–C was investigated in the first part of research work. By introducing a protective agent (oleylamine) to the Pt surface, TaOx NPs were selectively nucleated and grown around Pt NPs, thus forming the TaOx anchored-Pt NPs on the carbon surface. The electrochemical durability tests indicated that the 35ALD–TaOx–Pt/C catalyst exhibited superior durability compared to Pt/C. The enhanced stability of the 35ALD–TaOx–Pt/C catalyst is attributed to the anchoring effect of TaOx via the strong triple-junction of TaOx–Pt–C, which plays a significant role in stabilizing the Pt catalyst by preventing Pt NPs from migration/coalescence and detachment from the carbon support. Afterwards, to both improve the Pt/C catalyst activity and durability, a nitrogen-doped Ta_2O_5 was developed by ALD approach. It was found that the as-prepared $Pt/N\text{-}ALDTa_2O_5/C$ catalyst showed enhanced catalytic activity and significantly improved electrochemical durability toward oxygen reduction reaction (ORR). X-ray absorption spectroscopy provided direct evidence of change of the electronic structure of Pt NPs on $N\text{-}ALDTa_2O_5/C$ support compared to other supports, indicating the strong metal-support interactions formed between Pt NPs and the

modified N-ALDTa$_2$O$_5$/C support. It was revealed that by tuning the metal support interface, the highly active and stable Pt catalyst could be enabled.

To achieve the extremely low Pt loading while maintaining the high catalytic activity and long-life stability, ALD technique was applied to deposit Pt NPs into the PEMFCs anode layer. By controlling the ALD cycle number, the Pt NPs with different size and loading amount were directly deposited on the carbon coating layers to form the anode catalyst layers. The PEMFCs composed with ALD catalyst showed much better performance and durability than that prepared by the commercial catalyst with a conventional method. The electron microscopy reveals that the application of ALD for Pt deposition directly on the electrode carbon layers could effectively reduce the Pt loading while enhance the Pt dispersion, utilization, and Pt-support interaction, which achieve the high PEMFCs performance and excellent durability under the ultra-low Pt loading. Furthermore, downsizing Pt NPs size to subnano-clusters or even single atoms is highly desirable to maximize Pt atom utilization efficiency. Here we report on a practical synthesis method to produce isolated Pt single atoms and subnano-clusters using ALD technique. The Pt single atoms/subnano-clusters catalysts supported on metal-organic framework-derived nanocarbon support are investigated for the ORR, where they exhibit significantly enhanced catalytic activity and superior stability in comparison with the Pt NPs catalysts. The X-ray absorption indicates that the partially unsaturated coordination environment of Pt single atoms/subnano-clusters on nanocarbon support is responsible for the excellent performance.

The last experimental investigation of this thesis is development of an alternative non-noble-metal electrocatalyst of nitrogen and sulfur-co-doped nanocarbon (N,S-co-doped nanocarbon) for ORR. The N,S-co-doped nanocarbon is synthesized using metal organic frameworks as a solid precursor, followed by carbonizing and pore size design, then further co-doping sulfur to generate more active sites. The resulting N,S-co-doped nanocarbon demonstrates a high catalytic activity toward ORR, remarkable long-term stability and strong methanol tolerance in alkaline media. First-principles calculations reveal that N,S-co-doped nanocarbons possess enhanced ORR activity compared to N-doped carbon. More importantly, this work for the first time report that the N,S-coupled dopants can create active sites with higher activity than the isolated N and S dopants. The approach and analysis

adopted in this work offer a strategic consideration for designing the high performance nanocarbon electrocatalyst.

Keywords

Co-Authorship Statement

1.

Title: Metal organic frameworks for energy storage and conversion

Authors: Yang Zhao[1], Zhongxin Song[1], Xia Li, Qian Sun, Niancai Cheng, Stephen Lawes, Xueliang Sun

The final version of this manuscript was published as a review paper in **Energy Storage Materials** 2016, 2, 35-62. This review paper was organized and written by Yang Zhao, Zhongxin Song under the guidance of Dr. Xueliang Sun. Co-authors contributed to designing, writing, and modifying the manuscript.

2.

Title: Recent progress on MOF-derived nanomaterials as advanced electrocatalysts in fuel cells

Authors: Zhongxin Song, Niancai Cheng, Andrew Lushington and Xueliang Sun

The final version of this manuscript was published as a review paper in *Catalysts* 2016, *6* (8), 116. The manuscript was organized and written by Zhongxin Song under the guidance of Dr. Xueliang Sun. Coauthors contributed to reviewing, modifying and polishing the manuscript.

3.

Title: MOF-derived materials for extremely efficient electrocatalysis

Authors: Zhongxin Song, Lei Zhang, Matthew Zheng, Xueliang Sun

The final version of this manuscript was submitted <u>as a chapter to the book</u> of **Layered Materials for Energy Conversion and Storage**. The manuscript was organized and written by Zhongxin Song under the guidance of Dr. Xueliang Sun. Dr. Lei Zhang and Matthew Zheng contribute to reviewing and modifying the manuscript.

4.

Title: Atomic layer deposited tantalum oxide to anchor Pt/C for a highly stable catalyst in PEMFCs

Authors: Zhongxin Song, Biqiong Wang, Niancai Cheng, Lijun Yang, Dustin Banham, Ruying Li, Siyu Ye, and Xueliang Sun

The final version of this manuscript was published in **Journal of Materials Chemistry A**, 2017, 5, 9760-9767. The experimental and theoretical work was carried out by Zhongxin Song under the supervision of Dr. Xueliang Sun. The manuscript was organized and written by Zhongxin Song under the guidance of Dr. Xueliang Sun. Biqiong Wang conducted the ALD experiment. Niancai Cheng, Lijun Yang, Dustin Banham and Siyu Ye help analysis results, provide valuable suggestions and revise the manuscript. Ruying Li provided access to the equipment and samples shipping to Ballard company.

5.

Title: Origin of the high oxygen reduction reaction of nitrogen and sulfur co-doped MOF-derived nanocarbon electrocatalysts

Authors: Zhongxin Song, Weiwei Liu, Niancai Cheng, Mohammad Norouzi Banis, Xia Li, Qian Sun, Biwei Xiao, Yulong Liu, Andrew Lushington, Ruying Li, Limin Liu and Xueliang Sun

The final version of this manuscript was published in **Materials Horizons**, 2017, 4, 900-907. The experimental and theoretical work was carried out by Zhongxin Song under the supervision of Dr. Xueliang Sun. The manuscript was organized and written by Zhongxin Song under the guidance of Dr. Xueliang Sun. Dr. Weiwei Liu and Dr. Limin Liu conducted the first-principle calculations and analyzed the results. Dr. Niancai Cheng and Dr. Xia Li conducted the experimental training work. Dr. Biwei Xiao carried out the Raman characterization. Dr. Yulong measured the XRD patterns. Dr. Mohammad N. Banis and Dr. Andrew Lushington provided the suggestions, comments and discussion on this research work and contributed to the revision of the manuscript. Ruying Li provided access to the equipment.

6.

Title: Origin of achieving the enhanced activity and stability of Pt electrocatalysts with strong metal-support interactions via atomic layer deposition

Authors: Zhongxin Song[#], Mohammad Norouzi Banis[#], Lei Zhang, Biqiong Wang, Lijun Yang, Dustin Banham, Yang Zhao, Jianneng Liang, Matthew Zheng, Ruying Li, Siyu Ye*, Xueliang Sun*

The final version of this manuscript is published by **Nano Energy**, 2018. The experimental and theoretical work was carried out by Zhongxin Song under the supervision of Dr. Xueliang Sun. The manuscript was organized and written by Zhongxin Song under the guidance of Dr. Xueliang Sun. Dr. Mohammad N. Banis conducted the synchrotron radiation and data analysis. Dr. Biqiong Wang carried out the ALD experiment. Yang Zhao conducted the ICP analysis to determine the Pt content. Lei Zhang, Jianneng Liang, Lijun Yang, Dustin Banham, Siyu Ye, Matthew Zheng provided comments, suggestions and discussion for this project designing, and contributed to the manuscript revision. Ruying Li provided access to the equipment.

7.

Title: Ultra-low loading and high-performing Pt catalyst for PEMFC anode achieved by atomic layer deposition

Authors: Zhongxin Song, Mohammad Norouzi Banis, Hanshuo Liu, Lei Zhang, Yang Zhao, Junjie Li, Kieran Doyle Davis, Ruying Li, Siyu Ye, Shanna Knights, Gianluigi A. Botton, Ping He, and Xueliang Sun

The final version of this manuscript is ready to submit. The experimental and theoretical work was carried out by Zhongxin Song under the supervision of Dr. Xueliang Sun and Dr. Ping He. The manuscript was organized and written by Zhongxin Song under the guidance of Dr. Xueliang Sun and Dr. Ping He. Mohammad N. Banis conducted the ALD experiment. Yang Zhao conducted the ICP analysis to determine the Pt content. Ping He and Shanna Knights provide the industry internship for me to test the ALD samples in Ballard Power System. Dr. Hanshuo Liu carried out the high-resolution transmission electron microscopy

characterization under the supervision from Dr. Gianluigi A. Botton. Lei Zhang Junjie Li and Kieran D. Davis provided comments, suggestions and discussion for this project designing, and contributed to the manuscript revision. Ruying Li provided access to the equipment.

8.

Title: Platinum single-atom and subnano-cluster on MOF-carbon as superior oxygen reduction reaction catalysts

Authors: Zhongxin Song, Hanshuo Liu, Mohammad Norouzi Banis, Lei Zhang, Junjie Li, Ruying Li, Gianluigi A. Botton, Xueliang Sun

The final version of this manuscript is ready to submit. The experimental and theoretical work was carried out by Zhongxin Song under the supervision of Dr. Xueliang Sun. Mohammad N. Banis conducted the ALD experiment and synchrotron radiation analysis. Hanshuo Liu carried out the high-resolution transmission electron microscopy characterization under the supervision of Dr. Gianluigi A. Botton. Junjie Li carried out he ICP analysis to determine the Pt content. Lei Zhang provided the project discussion, manuscript designing and modifying. Ruying Li provided access to the equipment.

Acknowledgments

This Ph.D work was accomplished in Professor Andy Xueliang Sun's Advanced Materials for Clean Energy Group at the University of Western Ontario in London, Canada. Herein, it is my tremendous pleasure to express my acknowledgements to everyone who contributed to my research work throughout the past four years.

I would like to express my sincere gratitude to my supervisor Dr. Xueliang (Andy) Sun, an excellent professor at the Department of Mechanical & Materials Engineering of University of Western Ontario, Canada Research Chair, Fellow of the Canadian Academy of Engineering and the Royal Society of Canada, for giving me with this great opportunity and for his full support throughout my Ph.D project. He always provides guidance and encouragement during my thesis project and is an invaluable resource for anything related to nanomaterials and energy storage and conversion. Dr. Sun's dedication to the research work, his intelligence, diligence, brilliance, patience and kindness greatly inspired me and steered me towards highly successful research. He is the best advisor and one of the smartest people I know. I hope that someday I could be as lively, enthusiastic, and energetic as Dr. Sun.

I am also grateful forever to Mrs. Ruying (Kathy) Li, Prof. Sun's wife and lab manager in our group, for her kind help and strong support not only in my work, but also in my life. She has always been interested in the well-being of all our group members and her kindness is unending. Her hard work to keep the lab running smoothly has played a large role in the success of this group and she has always been willing to help whenever I needed it. Thanks Kathy for being a mother-figure for us all.

I would also like to express my greatest thanks to Dr. Lei Zhang, Dr. Mohammad Norouzi Banis and Dr. Niancai Cheng, my team members of fuel cell sub-group. Dr. Niancai supervised and guided me from my first day in the lab and has trained me on nearly everything I know about fuel cell. And Dr. Mohammad, for his tremendous expertise in so many analysis techniques, and frequent guidance in interpreting results. And Dr. Lei, he has always been available to spare his time for my questions. He is an excellent mentor. Lei is one of the most knowledgeable person that I know in this field and our many discussions

have taught me more than any textbook or course ever could. Many of my research would be impossible without suggestions and comments from Lei, Mohammad and Niancai.

I would like to extend my appreciation to Dr. Siyu Ye, Dr. Ping He, Dr. Dustin Banham and Dr. Lijun Yang from Ballard Power Systems Inc. Dr. Ye and Dr. He provided me with the opportunities to carry out internships in Ballard during the summer of 2016 and 2017. They mentored me directly and taught me the electrochemical and fuel cell testing techniques which were instrumental to my work at Western. The experience in Ballard help me gain knowledge of the connections between academic to industry. There is no doubt this industry experience will greatly benefit for my future career. Sincerely thanks to Prof. Gianluigi Botton and Dr. Hanshuo Liu from McMaster University for their help in TEM characterizations and discussions. I would also like to acknowledge Dr. Limin Liu and Dr. Weiwei Liu from Beijing Computational Science Research Center, for their kind help on the principle calculations and result analysis.

I am also grateful to my advisory committee members, Dr. Aaron David Price and Dr. Takashi Kuboki, professors in Engineering Department at UWO, for their advices, support, and concern in every step of my Ph. D project. I would also like to thank the examiners of my thesis defense, Dr. Zhifeng Ding, a professor in the Department of Chemistry at UWO, Dr. Jun Yang and Dr. Hamid Abdolvand, professors in the Department of Mechanical and Materials Engineering at UWO and Dr. Brad Easton, a Professor from the University of Ontario Institute of Technology, for their careful examination on my thesis and valuable consideration and suggestions.

I would like to sincerely thank to all current and former members in Prof. Sun's Advanced Materials for Clean Energy Group in Western. Thank you all created a free and friendly environment for work and study. I will never forget any single time we all spend together from every winter to summer, and forever be super proud as one member in this group. Especially, I would like to thank Dr. Qian Sun, Dr. Jian Liu, Dr. Xia Li, for their kind training, suggestions, discussion, and concern on my research; Dr. Biqiong Wang and Dr. Andrew Lushington for their help and discussion on ALD and careful concern on my paper work; Dr. Mohammad N. Banis, Dr. Biwei Xiao, Dr. Wei Xiao, Dr. Weihan Li, Miss Minsi Li for their hard work on synchrotron tests and data analysis; Dr. Yulong Liu and Mr.

Last but not least, I would like to express my gratitude to my parents and my sisters. Mr. Qingguo Song and Mrs. Fengzhi Han, they are the best parents in the world. Always all the time, they gave me their unconditional and unending love to support me and my research work. I should sincerely thank them for their good way of bringing me up and fully appreciate their love, commitment, and hard work. I would express my deep thanks to my sisters. They always share their experiences and feelings with me, which encourage me to be brave and strong when facing the challenges in my own life. Thanks all the understanding, encouragement, supports and everybody in my life!

Zhongxin Song

April 23, 2018

Table of Contents

List of Tables

List of Figures

List of Appendices

Chapter 1

1   Introduction

Due to the global warming issue and the ever-growing environmental concerns, the need for advanced clean energy technology has never been more urgent. To meet the coming energy challenges, a broad suite of alternative energy and renewable resources will be required, including biomass, solar, hydro, wind and nuclear. Among them, hydrogen has been identified as one of the most promising clean source for energy conversion and will certainly play a significant role in solving the energy challenges. [1]

Polymer electrolyte membrane fuel cell (PEMFCs) (also called proton exchange membrane fuel cells) as an innovative clean energy conversion device is considered as one of the technology for the future. PEMFC uses the chemical energy of hydrogen to cleanly and efficiently produce electricity, with water and heat as the only byproducts. [2, 3] PEMFCs have several advantages over the conventional combustion technologies currently used in many power plants and passenger vehicles. (i) PEMFCs can operate at higher efficiency than combustion engines and can convert the chemical energy to electricity with efficiency of up to 60%. [2, 3] (ii) PEMFCs have lower emissions than combustion engines. Hydrogen fuel cells emit only water, so there are no carbon dioxide emissions and no air pollutants that create smog and cause health problems at the point of operation. (iii) PEMFCs are quiet during operation as they have fewer moving parts. PEMFCs are unique in their variety of potential applications; they can provide power for systems as large as a utility power station and as small as a laptop computer. In fact, PEMFCs are already being used in a wide application, including transportation (bus, trail, automotive etc.), materials handling, stationary, portable power and emergency backup power system. [4]

1.1   Fundamentals of PEMFCs

PEMFCs are made from several layers of different materials (Figure 1.1). The heart of a PEMFC is the membrane electrode assembly (MEA), which involves the membrane electrolyte, the catalyst layers, and gas diffusion layers (GDLs). Hardware components used to incorporate a MEA into a fuel cell include gaskets, which provide a seal around the MEA

to prevent leakage of gases, and bipolar plates, which are used to assemble individual PEM fuel cells into a fuel cell stack and provide channels for the gaseous fuel and air. The catalysts layers, membrane and gas diffusion layers together form the MEA of a PEMFC. The catalyst coated membrane layers are the key part for the PEMFC technology. A layer of anode catalyst is coated on one side of the membrane and cathode catalyst layer on the other side. Conventional catalyst layers include nanoparticles (NPs) of platinum (Pt) dispersed on a high-surface-area carbon support. The supported Pt catalyst is mixed with an ion-conducting polymer (ionomer) and sandwiched between the membrane and the GDLs. In a hydrogen-oxygen PEMFC, the Pt catalyst at the anode separates hydrogen fuel into protons and electrons, which take different paths to the cathode. The electrons go through an external circuit, creating a flow of electricity. The protons migrate through the membrane to reach the cathode. On the cathode side, the Pt catalyst enables oxygen reduction reaction (ORR) by uniting with protons and electrons to produce water and heat. The ionomer mixed into the catalyst layers allows the protons to travel through these layers. The membrane electrolyte permits only the necessary protons to pass between the anode and cathode, other substances passing through the electrolyte would disrupt the chemical reaction. With the hydrogen oxidation reaction (HOR) and ORR occurring simultaneously during PEMFCs operation, the theoretical output cell voltage is given as 1.229 V.

Anode (HOR): $2H_2 \longrightarrow 4H^+ + 4e^-$ $E_0 = 0$ V

Cathode (ORR): $O_2 + 4e^- + 4H^+ \longrightarrow 2H_2O$ $E_0 = 1.229$ V
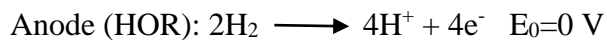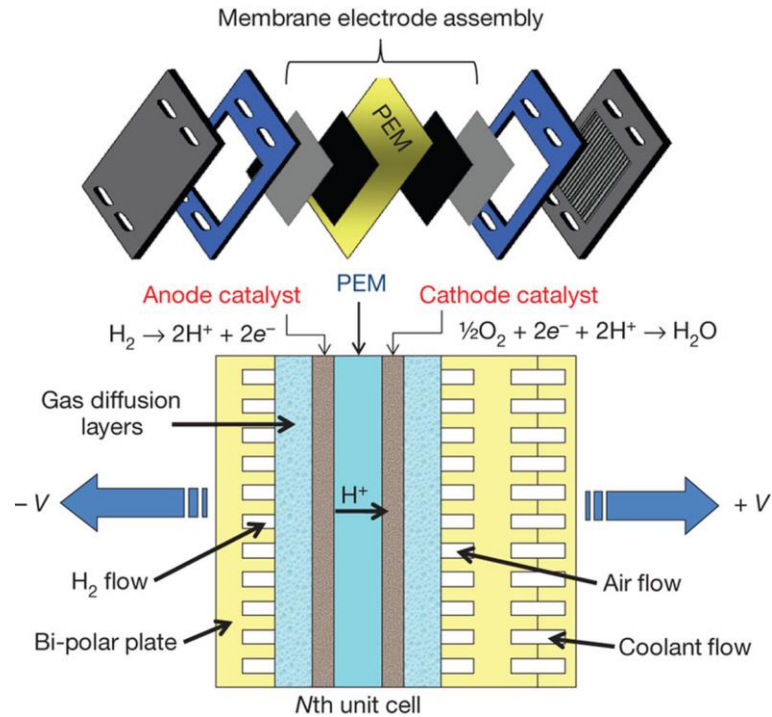
Figure 1.1. Schematic of the working principle of a typical PEMFC and the involved porous components: bipolar plate; gas diffusion layer (GDL); electrocatalyst layer and membrane.

For transportation applications, the membrane is very thin-in some cases under 25 microns. Another component of MEA is gas diffusion layers. The GDLs sit outside the catalyst layers and facilitate transport of reactants into the catalyst layer, as well as removal of product water. Each GDL is typically composed of a sheet of carbon paper in which the carbon fibers are partially coated with polytetrafluoroethylene (PTFE). Gases diffuse rapidly through the pores in the GDL. These pores are kept open by the hydrophobic PTFE, which prevents excessive water buildup. In many cases, the inner surface of the GDL is coated with a thin layer of high-surface-area carbon mixed with PTFE, called the microporous layer (MPL). The MPL can help adjust the balance between water retention (needed to maintain membrane conductivity) and water release (needed to keep the pores open so hydrogen and oxygen can diffuse into the electrodes).

1.2 Challenges of PEMFCs

With remarkable efficiency, high energy density and negligible emission of harmful gases, the polymer electrolyte membrane fuel cell (PEMFC) is considered to be a green technology that meets the energy requirement for future electrical vehicles and portable electronics. Unfortunately, a major limitation for the low-temperature PEMFCs is the kinetically-sluggish oxygen reduction reaction (ORR) at the cathode, which requires a large amount of catalyst to reach the adequate energy output. [5, 6] The state-of-the-art high-performance catalysts for ORR are the noble metal Pt-based catalysts. [7] To effectively utilize this expensive metal, Pt NPs are often supported on substrates such as high surface carbon support. However, Pt catalysts are seriously deactivated under severe PEMFCs operation conditions, resulting in the loss of Pt performance. Cost, performance, and durability are still key challenges in PEMFCs commercialization. [8]

Currently, carbon black is the most widely used support material to promote Pt activity in PEMFCs. However, carbon black suffers from severe corrosion during long-term PEMFCs operation (especially at potential above 0.9 V) which results in the Pt detaching from carbon surface and rapid degradation of the PEMFC performance. Moreover, the weak interactions between carbon support and metal catalysts trigger Pt NPs migration and aggregation to form big particles, consequent loss the surface area and decrease the activity. [9, 10] Besides the challenges in catalyst stability, it is highly desirable to improve Pt activity and decrease Pt loading in PEMFCs because of the high cost and limited availability of Pt. Therefore, it is extremely desirable to develop highly stable and active electrocatalysts with lower Pt loading.

For PEMFC stack cost, DOE has targeted total Pt group metal (PGM) content for both electrodes of 0.125 g/kW and total loading of 0.125 $mgPGM \cdot cm^{-2}$ (electrode area) by 2020. [11] DOE durability targets for stationary and transportation fuel cells are 40,000 hours and 5,000 hours, respectively, under realistic operating conditions. In the most demanding applications, realistic operating conditions include impurities in the fuel and air, starting and stopping, freezing and thawing, and humidity and load cycles that result in stresses on the chemical and mechanical stability of the fuel cell materials, components, and interfaces. Degradation-exacerbating conditions resulting from cyclic operation include hydrogen

starvation, differential pressure imbalance, oxidation-reduction cycling, and oxygen ingress to the anode, resulting in high cathode potentials. Significant progress has been made in determining the degradation mechanisms of fuel cell components and developing improved materials.

1.3 Solutions by designing highly stable and active electrocatalysts through ALD technique

1.3.1 Atomic layer deposition (ALD)

Atomic layer deposition (ALD) is a vapor phase technique used to deposit thin films and nanostructures. [12, 13] It is a technique that has pushed the advancement of semiconductor technology and hold promise for application in the field of energy storage and conversion. As materials become increasingly complex and move toward the nanoscale regime, coating techniques that can provide accurate control of growth and material composition becoming increasingly necessary. ALD can provide both these advantages due to its cyclic, self-saturating nature. This advantage results in ALD being the technique of choice for coating nanomaterials compared to other deposition techniques such as chemical vapor deposition and physical vapor deposition. In general, the ALD process consists of introducing gaseous chemical precursors that can react to the substrate. Additionally, a purge step separates precursor introduction ensuring that gas-surface reactions occur as half-reactions. This allows for each dose of the precursor to completely react with the substrate through a self-limiting process. As a result, ALD is a non-line-of-sight technique that can conformally coat complex, nanostructure substrates in a pin-hole free manner. Although ALD can be used to grow thin films, careful selection of substrate and chemical precursor can allow for the growth of nanoparticles. This imparts ALD with the ability to grow particles with atomic level control. Furthermore, particles can be grown in a non-line-of-sight fashion on nanomaterials, providing an optimal route in taking advantage of high surface area to volume materials.

In addressing the activity and durability challenges facing electrocatalysts in PEMFCs, ALD is emerging as a powerful technique for deposition of noble metals and transition metal oxides due to its exclusive advantages over other methods. The primary advantages of ALD are derived from the sequential, self-saturating, gas-surface reactions, and angstrom level

control that take place during the deposition process. Therefore, ALD possesses the advantage in controlling the target materials with precise particle size and uniform distribution on the substrate. The highly dispersed and uniform Pt particles designed by ALD method is supposed to possess the high active surface area. On the other hand, by forming chemical bonds between the initial layer of ALD precursor and support atoms during the first cycle of deposition, the strong interaction between the deposited Pt NPs and support could be enabled, which is benefit for achieving the highly stable catalyst.

1.3.2 Highly stable electrocatalysts: with strong metal-support interactions

The migration of supported metal NPs can be inhibited through steric stabilization by layers of porous inorganic oxide such as zirconia, [14] or tin oxide. [15] Metal oxides combined with carbon supports have been shown to promote Pt activity and improve stability as a result of synergistic effects between Pt-metal oxide interactions and electrical conductivity. The underlying metal oxides result in stronger interactions occurring with Pt NPs, generating active interfacial regions in the electrocatalysts resulting in enhanced activity and stability of the catalyst. To achieve superior controlled ultrathin and ultrafine deposition, area-selective ALD of porous metal oxide thin film or NPs can be done without blocking the active Pt surface. Recently, Cheng et al. [16] demonstrated a facile approach to stabilize Pt catalysts by encapsulation in zirconia nanocages which are synthesized by area-selective ALD. The Pt NPs were initially deposited on nitrogen-doped carbon nanotubes (NCNT) by ALD. Then, ALD zirconia was selectively grown around the Pt NPs but did not deposit on the Pt surface due to the presence of blocking agent. As a result, an open or holey nanocage architecture can be formed by precisely controlling the ALD metal oxide layers. The catalyst encapsulated in zirconia nanocages indicated high stability and activity towards ORR in acidic media. Pt NPs encapsulated in zirconia nanocages were 9 times more stable than ALD-Pt on NCNT without zirconia nanocages and 10 times more stable than commercial Pt on carbon black (Pt/C).

1.3.3   Highly active electrocatalysts: from nanoparticles to single atom

To overcome the challenges associated with the Pt catalysts activity and high-cost issue, it is very important to markedly decrease the Pt loading and increase the Pt utilization efficiency. Currently, supported Pt NPs are typically used to promote Pt activity towards the ORR and HOR. Unfortunately, the geometry of the NPs limits the majority of the Pt atoms to the particle core, deeming them ineffective, as only surface atoms are involved in the electrochemical reaction. Reducing the size of the Pt NPs to clusters or even single atoms could significantly decrease the noble metal utilization and increase their catalytic activity, which is highly desirable to enhance the Pt atomic efficiency and decrease the cost of the electrocatalysts.[17, 18] It has been shown that single Pt atoms dispersed on an FeOx surface have a higher catalytic activity for CO oxidation compared with the corresponding Pt NPs.[17] Moreover, the single-atom catalysts also exhibited a significantly improved catalytic activity towards methanol oxidation, up to 10 times higher than the state-of-the-art commercial Pt/C catalysts.[19]

Controlled and large-scale synthesis of stable single atoms and clusters remains a considerable challenge due to the high free energy of metal atoms that induce isolated atoms to diffuse and agglomerate, resulting in the formation of larger particles. [20, 21] In practical applications, it is required that the single atoms not only have a high activity but also exhibit a satisfactory stability. [22-24] Moreover, it is also desired to produce a high density of single atoms to meet the practical applications. Consequently, an ideal single-atom catalyst must have a high activity, a high stability and a high density. As it has been proven to be a powerful tool for large-scale synthesis of stable single atom and cluster catalysts, ALD is considered as an effective approach to synthesize ideal single-atom catalyst. [19, 25, 26] ALD is able to precisely control the size and distribution of particles on a substrate by using sequential and self-limiting surface reactions. In our previous work, [26] the Pt single atoms and clusters supported on nitrogen-doped graphene were prepared as hydrogen evolution reaction (HER) catalyst using ALD, resulting in the utilization of nearly all the Pt atoms. The size and density of the Pt catalysts on graphene support are precisely controlled by simple adjusting the number of ALD cycles. The Pt atoms and clusters show much higher activity for the HER in comparison with conventional Pt NP catalysts. The ALD provides a

promising approach for the design of highly active and stable next-generation catalysts based on Pt single atoms and clusters, which have a great potential to reduce the high cost of industrial commercial noble-metal catalysts.

1.4   Thesis objectives

PEMFCs have been applied as the clean energy conversion devices for electric vehicles and portable power supply. Unfortunately, the high-cost of noble metal catalysts and poor long-time stability are the main challenges that limit PEMFCs for widespread commercialization. To improve the performance and long-lifetime of PEMFCs for future application, development of advanced electrocatalysts with high activity and stability becomes necessary and urgent. Fabrication of strong metal-support interactions and downsizing the noble metal catalyst to clusters or even single atoms, are the key research directions to improve the PEMFCs performance and long-lifetime. In this thesis, the author focusses on two aspects to design the highly stable and active electrocatalysts.

Part I: To design highly stable Pt NPs electrocatalysts

(1)   To develop a highly stable Pt/C electrocatalysts by area-selective deposition of tantalum oxide (TaOx) anchors. The synthesis of TaOx was carried out via an ALD technique. By adjusting the TaOx anchors loading and coverage area on the Pt/C catalyst, we can purposely design high stable electrocatalyst for PEMFCs application.

(2)   To stabilize Pt NPs on carbon support by decorating a bridge layer of nitrogen-doped tantalum oxide (N-Ta_2O_5). The uniformly dispersed Ta_2O_5 NPs on carbon surface are developed by ALD. With NH_3-treatment to doping nitrogen into the tantalum oxide, the strong metal-support interactions between Pt catalyst and carbon support will be formed. This approach allows us to fabricate a highly stable electrocatalyst by enabling the strong metal-support interactions.

Part II: To design size controlled highly active electrocatalysts: from nanometer to single atoms.

(1)   To achieve the extremely low Pt loading in the anode catalyst layer while maintain the high PEMFC performance and long-life time, a series of high-performance PEMFCs with low Pt loading in anode layer are successfully prepared using an ALD technique. By controlling the ALD cycle number, the Pt NPs with different size and loading amount are directly deposited on the carbon coating layers to form the anode catalyst layers.

(2)   To investigate the impact of Pt atom utilization on the electrocatalysis for oxygen reduction reaction (ORR), Pt single atoms, subnano-clusters as well as NPs with different size and density on MOFs-derived carbon support are designed. Based on the advantages of high surface area, high porosity and rich of nitrogen doped species, MOFs-carbon is anticipated to be a promising support for single atoms catalysts. The supported Pt single atoms were prepared by ALD via chemical incorporation Pt atoms into the nitrogen or oxygen species from MOFs-carbon, which is considered to enable the sinter-resistant isolated Pt atoms with high dispersion on the support.

(3)   To minimize the use of precious metals, a metal-free catalyst of nitrogen and sulfur-co-doped nanocarbon would be designed as the electrocatalyst for ORR. First-principles calculations were investigated to reveal the catalytic mechanism and understand the active sites. This research will be of great significance for the rational design of a new-generation of nanocarbon electrocatalysts.

1.5   Thesis organization

This thesis is consisted of nine chapters (one introductory chapter, one literature review chapter, one experimental chapter, five articles, and one conclusive chapter) and is organized according to the requirements on "Integrated-Article" form as outlined in the Thesis Regulation Guide by the School of Graduate and Postdoctoral Studies (SGPS) of the University of Western Ontario. Specifically, it consists of the following parts:

Chapter 1 gives an introduction of polymer electrolyte membrane fuel cells. In this chapter, the components, work principle, challenges and opportunities of PEMFCs are introduced. Nanomaterials solutions on electrocatalysts, including development of highly stable and active electrocatalysts are highlighted. Furthermore, the research objective and thesis organization are stated in this chapter.

Chapter 2 is literature review, which summarize the development and progress of highly stable and active electrocatalysts for PEMFCs.

Chapter 3 outlines the experimental synthetic approaches of as-prepared nanomaterials. The characterizations techniques used to determine the materials physical and electrochemical properties are demonstrated in this chapter.

Chapter 4 presents a study on the atomic layer deposition of tantalum oxide to anchor Pt/C for a highly stable catalyst in PEMFCs. Controlled synthetic process with different tantalum oxide mass loading is investigated, detailed relationship between tantalum oxide loading and the electrocatalyst stability for ORR are also studied.

Chapter 5 investigates the nitrogen-doped tantalum oxide as a bridge layer to stabilize Pt catalyst on carbon surface. By testing the electrochemical activity and stability, the electrocatalyst decorated with nitrogen-doped tantalum oxide demonstrate a significantly enhanced performance compared with their counterparts.

Chapter 6 reports the Pt catalyst of particle size and loading effect on catalytic activity and stability for PEMFCs anode. The real fuel cell is designed in this study. Moreover, the hydrogen-oxygen fuel cell performance and startup/shutdown stability are evaluated here.

Chapter 7 presents the fabrication of single atoms and sub-nano clusters Pt catalyst on MOFs-derived nanocarbon. The ALD method used here shows great advantages in preparing single atoms catalysts. Electrochemical activity and stability are evaluated on all the as-prepared Pt/MOFs-C catalysts. It is find that the single atom and subnano-clusters make great contributions to achieve better catalytic activity for ORR.

Chapter 8 reports the development of a metal-free electrocatalysts derived from MOFs precursor. Effects of porous structure and heteroatoms doping on electrocatalysts performance for ORR are investigated. This research work also presents first-principles calculations to reveal the catalytic mechanism for metal-dree catalysts and understand the active sites for ORR.

Chapter 9 summarizes the results and contributions of the thesis work. Additionally, the author states the perspective and suggestions for future work on electrocatalysts.

References

[1]. Pivovar, B. H$_2$@SCALE: Deeply Decarbonizing our Energy System. http://www.energy.gov/sites/prod/files/2016/07/f33/fctowebinarslides_h$_2$_at_scale_072816.pdf.

[2]. Debe, M.K., Nature, 2012. **486**, p. 43-51.

[3]. Banham, D., T. Kishimoto, Y. Zhou, T. Sato, K. Bai, J.-i. Ozaki, Y. Imashiro, and S. Ye, Science Advances, 2018. **4** (3): p. 7180.

[4]. Fuel Cell Technical Team Rodamap. https://www.energy.gov/sites/prod/files/2017/11/f46/FCTT_Roadmap_Nov_2017_FINAL.pdf, .

[5]. Banham, D. and S. Ye, ACS Energy Letters, 2017. **2**(3): p. 629-638.

[6]. Su, L., W. Jia, C.M. Li, and Y. Lei, ChemSusChem, 2014. **7**(2): p. 361-378.

[7]. Sui, S., X. Wang, X. Zhou, Y. Su, S. Riffat, and C.-j. Liu, Journal of Materials Chemistry A, 2017. **5**(5): p. 1808-1825.

[8]. DOE Hydrogen and Fuel Cells Program: Program Record. 2017. https://www.hydrogen.energy.gov/program_records.html.

[9]. Dubau, L., L. Castanheira, F. Maillard, M. Chatenet, O. Lottin, G. Maranzana, J. Dillet, A. Lamibrac, J.C. Perrin, E. Moukheiber, A. ElKaddouri, G.D. Moor, C. Bas, L. Flandin, and N. Caqué, Wiley Interdisciplinary Reviews: Energy and Environment, 2014. **3**(6): p. 540-560.

[10]. Meier, J.C., C. Galeano, I. Katsounaros, J. Witte, H.J. Bongard, A.A. Topalov, C. Baldizzone, S. Mezzavilla, F. Schüth, and K.J.J. Mayrhofer, Beilstein Journal of Nanotechnology, 2014. **5**: p. 44-67.

[11]. DOE Technical Targets for Polymer Electrolyte Membrane Fuel Cell Components.https://www.energy.gov/sites/prod/files/2017/05/f34/fcto_myrdd_fuel_cells.pdf.

[12]. Cheng, N., Y. Shao, J. Liu, and X. Sun, Nano Energy, 2016. **29**: p. 220-242.

[13]. Grillo, F., H. Van Bui, J.A. Moulijn, M.T. Kreutzer, and J.R. van Ommen, The Journal of Physical Chemistry Letters, 2017. **8**(5): p. 975-983.

[14]. M., A.P., C. Massimiliano, and S. Ferdi, Angewandte Chemie International Edition, 2006. **45**(48): p. 8224-8227.

[15]. Lee, S.H., D.M. Hoffman, A.J. Jacobson, and T.R. Lee, Chemistry of Materials, 2013. **25**(23): p. 4697-4702.

[16]. Niancai, C., B.M. Norouzi, L. Jian, R. Adam, L. Xia, L. Ruying, Y. Siyu, K. Shanna, and S. Xueliang, Advanced Materials, 2015. **27**(2): p. 277-281.

[17]. Qiao, B., A. Wang, X. Yang, L.F. Allard, Z. Jiang, Y. Cui, J. Liu, J. Li, and T. Zhang, Nature Chemistry, 2011. **3**: p. 634.

[18]. Yang, S., J. Kim, Y.J. Tak, A. Soon, and H. Lee, Angewandte Chemie International Edition, 2016. **55**(6): p. 2058-2062.

[19]. Sun, S., G. Zhang, N. Gauquelin, N. Chen, J. Zhou, S. Yang, W. Chen, X. Meng, D. Geng, and M.N. Banis, Scientific reports, 2013. **3**: p. 1775.

[20]. Uzun, A., V. Ortalan, Y. Hao, N.D. Browning, and B.C. Gates, ACS Nano, 2009. **3**(11): p. 3691-3695.

[21]. Mackus, A.J.M., M.A. Verheijen, N. Leick, A.A. Bol, and W.M.M. Kessels, Chemistry of Materials, 2013. **25**(9): p. 1905-1911.

[22]. Yang, X.-F., A. Wang, B. Qiao, J. Li, J. Liu, and T. Zhang, Accounts of Chemical Research, 2013. **46**(8): p. 1740-1748.

[23]. Kim, J., H.-E. Kim, and H. Lee, ChemSusChem, 2018. **11**(1): p. 104-113.

[24]. Zhang, X., J. Guo, P. Guan, C. Liu, H. Huang, F. Xue, X. Dong, S.J. Pennycook, and M.F. Chisholm, Nature Communications, 2013. **4**: p. 1924.

[25]. Yan, H., Y. Lin, H. Wu, W. Zhang, Z. Sun, H. Cheng, W. Liu, C. Wang, J. Li, and X. Huang, Nature communications, 2017. **8**(1): p. 1070.

[26]. Cheng, N., S. Stambula, D. Wang, M.N. Banis, J. Liu, A. Riese, B. Xiao, R. Li, T.-K. Sham, and L.-M. Liu, Nature communications, 2016. **7**: p. 13638.

Chapter 2

2 Literature review

Polymer electrolyte membrane fuel cells (PEMFCs) are one of the promising energy-conversion devices due to their high efficiency and zero emission. However, the overall efficiency of PEMFCs is severely hindered by their high overpotential, which is mainly caused by the sluggish reaction kinetics of the oxygen reduction reaction (ORR) at the cathodic side. To mitigate the overpotential issue, in recent decades, Pt has been widely used as the active electrocatalyst, but its high-cost and low-durability are still problems in PEMFCs technology. Therefore, in electrochemical and materials science, the search for effective strategies to reduce the Pt loading while maintain the high activity and durability of the electrocatalyst has become critical. In this chapter, recent progress on the development of low-cost, highly stable and active electrocatalyst for PEMFCs is involved from the nanomaterial perspective. First, a functional link between the activity and durability on catalytic nanoparticles (NPs), as well as the degradation mechanisms, will be discussed. Then, we summarize the current strategies for developing the advanced Pt-based electrocatalysts with high stability and activity in reactions related to PEMFCs, and their structure impact on electrochemical performance will be discussed. Finally, an outlook on the future trends and developments of nanomaterial electrocatalysts in PEMFCs is presented.

2.1 Nanoparticle electrocatalysts issues and their degradation mechanisms

The state of the art electrocatalyst for both anode and cathode of PEMFCs are Pt or Pt-alloys dispersed in the form of NPs on a carbon support, in order to achieve a maximum of active sites. Concerning the use of NPs, the effects of NP size on the ORR activity have been studied for a long time. For finely size-controlled NPs, the ORR activity has been mainly investigated from two primary metrics: (1) specific activity ($\mu A \cdot cm^{-2}$) and (2) mass activity ($A \cdot mg^{-1}$). The specific activity is the activity per unit electrochemical surface area, which indicates the intrinsic reactivity of a unit area of the catalyst surface. The mass activity is the activity per unit catalyst mass, which indicates the effective utilization of a catalyst material. [1] For real electrocatalyst applications, cost is the primary consideration; thus, the mass

activity is ultimately what matters as this metric is directly transferable to cost. In this thesis, when discussing next-generation ORR catalysts, the primary activity metric will be mass activity. Electrochemical studies have shown the relationship between the ORR activity and the durability affected by particle size: in general, when the NP size is decreased, the activity increases, while the durability decreases (Figure 2.1). [2] Therefore, increasing nanoparticle durability while maintaining the high activity is critical for NP design.
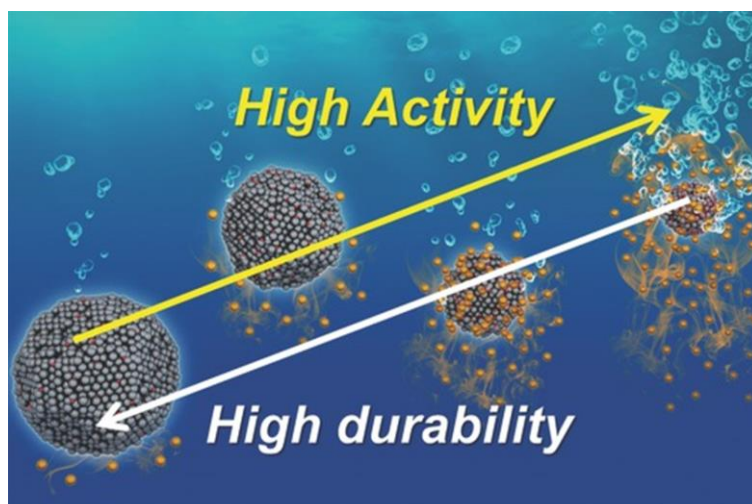
Figure 2.1. Schematic illustration of nanoparticle size effect for activity and durability. [2] Wiley-VCH Verlag GmbH & Co. KGaA. Copyright 2018.

To address this challenge, understanding the NP degradation mechanism is necessary for designing advanced electrocatalysts. Regarding Pt/C catalysts, major research efforts over the last decades have been made to explore the degradation mechanism and improve the durability of the Pt/C catalysts. Several mechanisms as shown in Figure 2.2 have been proposed for the degradation of Pt/C catalysts. [3-6] First is the corrosion of the carbon support, which directly initiates the detachment and aggregation of Pt NPs. Second is the dissolution of Pt from smaller particles. Third is the growth of Pt NPs via Ostwald ripening and aggregation. This includes the re-deposition of the soluble Pt species onto larger particles and the coalescence of Pt NPs via migration on the carbon support surface. There have been tremendous efforts to understand this behavior by particle size distribution analysis. [7-10] Recent in situ analysis has significantly helped the understanding of the degradation mechanism. Strasser et al. [11] investigated the durability of Pt NPs on various carbon supports by in situ small angle X-ray scattering (SAXS) analysis. The dominant degradation

mechanism of Pt NPs was suggested to be the coalescence of the Pt NPs on the support. Based on the control analysis, they also suggested that geometric barriers to prevent particle merging are effective for protecting nanoparticles.
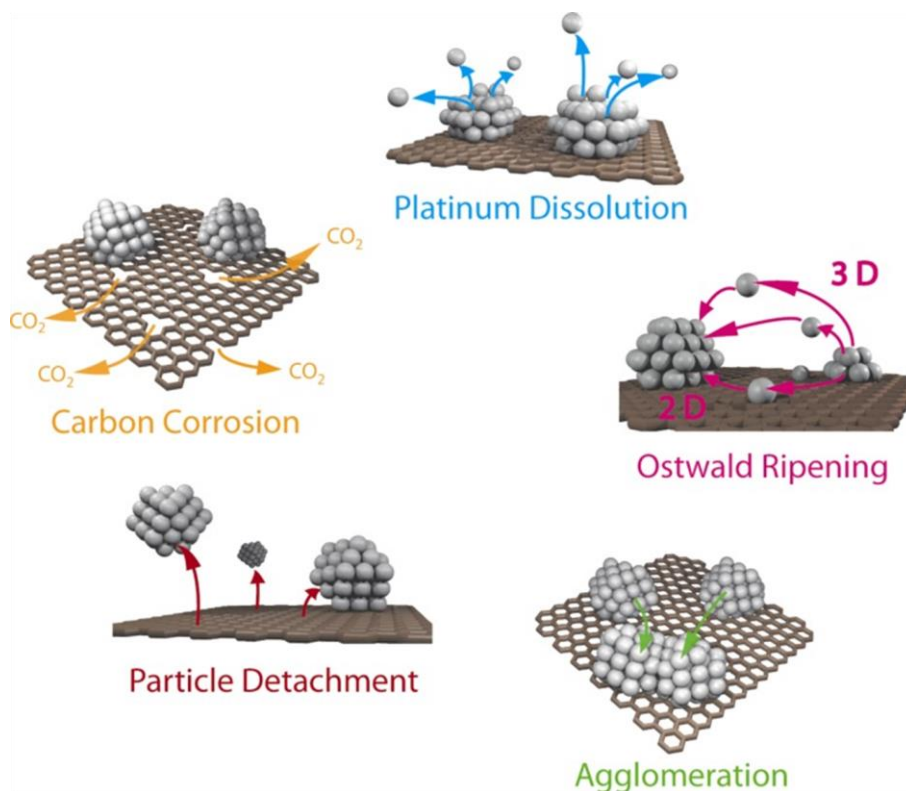
Figure 2.2 Schematic illustration of the suggested degradation mechanisms for Pt NPs on a carbon support in fuel cells. [3-6] Reproduced with permission from Nanotechnology. Copyright 2014.

Although a significant understanding of the fundamental mechanism of Pt NPs durability has been gained, there remain several unclear issues. The distinction of the dominant degradation mechanism is crucial because, depending on the mechanism, the solution for durable electrocatalyst design can be significantly different. If the catalyst support corrosion induced Pt NP detachment, is the major contributor to the performance degradation, the development of electrochemical stable catalyst support is a key factor. On the other hand, if Pt NPs coalescence is the primary cause, inhibiting particle migration and detachment would be a useful strategy, for example, enhancing the NP-support interaction or NP confinement effects. Therefore, a rational construction of catalysts from metals with optimized activity and

durability, and from supports with enhanced stability is a key point for improving PEMFCs performance.

2.2 Progress of highly stable electrocatalysts for PEMFCs

Improving electrocatalyst stability is pivotal for maintaining performance without activity loss. Many advances have been suggested to improve catalyst particle and catalyst support stability based on the suggested degradation mechanisms. The durability of catalysts is inherently determined by the properties of both the catalytic metals and the support materials and the specific interaction between them. It is reasonably expected that the higher the durability of catalytic metals and support materials, and the stronger the specific interaction between them, the higher the durability of the resultant catalysts. The strategies to improve the durability of catalysts can be in general categorized into two aspects: support materials and catalytic metals.

2.2.1 Novel stable catalyst support

The selection of catalyst support materials has a remarkable impact on the durability of the resultant supported catalysts. There are several basic requirements for an improved catalyst support: (i) high electrochemical stability under PEMFCs operating conditions (high potential, low PH); (ii) high surface area for the uniform dispersion of Pt NPs; (iii) excellent electronic conductivity. With the current state of technology, the state-of-the-art and the most practical electrocatalysts for PEMFCs are still carbon black supported Pt NPs catalysts. Although the carbon black with merits of large surface area, high electrical conductivity and pore structure, the phenomenon of carbon corrosion caused by electrochemical oxidation has been identified to be the major drawback for catalyst durability. Therefore, it is necessary to explore more stable catalyst supports to replace the traditional carbon black. In order to address the carbon corrosion issue, materials with high electrochemical stability have been studied as catalyst support, ranging from highly graphitic carbons (e.g. carbon nanotubes or graphene) to noncarbon supports (e.g. transition metal oxides, carbides). [12-14]

Novel carbon support

It is reported that the extent of graphitization of carbon plays an important role on carbon support stability, with more graphitic carbon being more thermally and electrochemically stable, which is due to the decreased defect sites on carbon surface. With the development of novel carbon nanostructure, carbon nanotubes (CNTs) have emerged as a promising support material for PEMFCs due to their large surface area, good electrical conductivity and excellent electrochemical durability. However, pristine CNTs contain relatively few binding sites for anchoring the Pt NPs due to the chemical inert surface of CNTs. To overcome these barriers, many studies have focused on the surface modification of CNTs. The surface modification involves (i) using special organic functional groups, functional polymers, and heteroatoms (e.g. N, P, S, F etc.) to decorate CNTs surface, [15, 16] and (ii) using homogeneous silica or metal oxides (e.g. TiO_2, ZrO_2, SnO_2 etc.) shell to link metal NPs and CNTs support. [17-19]

It was found that an ideal conducting polymer modified-CNTs used for stabilization of supported Pt NPs should not only provide an anchoring site for Pt NPs, but also maintain the original perfect structure of CNTs rather than destroying it. Fujigaya and co-workers [20] reported an "in situ surface growth method" to fabricate CNTs supported Pt NPs using polybenzimidazole (PBIs) as linker polymers, by means of which binding sites could be non-covalently introduced onto a CNT surface. PBI, recognized as a powerful candidate for use in PEMFCs due to its high proton conductivity, has a strong physical interaction with CNTs and serves as an effective binding site for anchoring of Pt NPs. A schematic of the structure of Pt/PBIs/CNTs is shown in Figure 3a. Due to the non-destructive functionalization of the CNTs, the Pt/PBIs/CNTs showed higher electrocatalytic activity and better stability for the ORR than Pt NPs supported on pure CNTs. In addition, the Pt/PBIs/CNTs have a highly dispersed Pt NPs, which promote the larger electrochemical active surface area than that of Pt/CNTs. The interface structure of Pt/PBIs/CNTs is most likely the "ideal" triple-phase boundary structure that enables excellent durability and activity of Pt catalyst.

Nitrogen-doped graphene (NGNs), as a unique 2D material with good conductivity, high surface area and mechanical strength, has attracted great attentions for electrocatalyst support application. To enhance the metal-support interaction and generate more interfacial regions in Pt/NGNs electrocatalyst, Sun et al. [21] developed a zirconia (ZrO_2) modified NGNs

hybrid as a support for further enhance the performance and durability of Pt/NGNs catalyst. The novel ZrO_2/NGNs hybrid support was prepared by growing ZrO_2 NPs on NGNs using atomic layer deposition (ALD) technique. Based on sequential and self-limiting surface reactions, ALD provides a powerful approach for the coating of ultra-fine metal oxides. The Pt NPs located and anchored at the interface of ZrO_2 and NGNs, which improves the interaction of Pt with support by metal-metal oxide-NGNs junction. High resolution transmission electron microscopy (HRTEM) image in Figure 2.3b shows that Pt NPs dispersion on ZrO_2/NGNs is uniform, with no indication of agglomeration. Moreover, it is revealed that major Pt NPs are exactly located between the grain boundaries of ZrO_2 NPs on NGNs, suggesting the formation of a unique triple-junction interaction in Pt/ZrO_2/NGNs nanostructure. For the electrochemical performance, Pt/ZrO_2/NGNs had a higher mass activity for ORR ($\sim$102 mA·mg^{-1} $_{Pt}$) than the Pt/NGNs ($\sim$78 mA·mg^{-1} $_{Pt}$). When 4000 continuous cycles of accelerated durability test (ADT) were performed, Pt/ZrO_2/NGNs retained 50.2% and 59% of its initial ECSA and mass activity, respectively, compared to only 23.5% and 28% for Pt/NGNs. The ADT test indicated that the Pt/ZrO_2/NGNs had 2.2 times higher durability than Pt/NGNs due to a stronger triple-interaction in ZrO_2-Pt-NGNs, as confirmed by X-ray absorption spectra. This unique metal oxide-metal-NGNs triple interaction is a promising stable catalyst structure for PEMFCs.
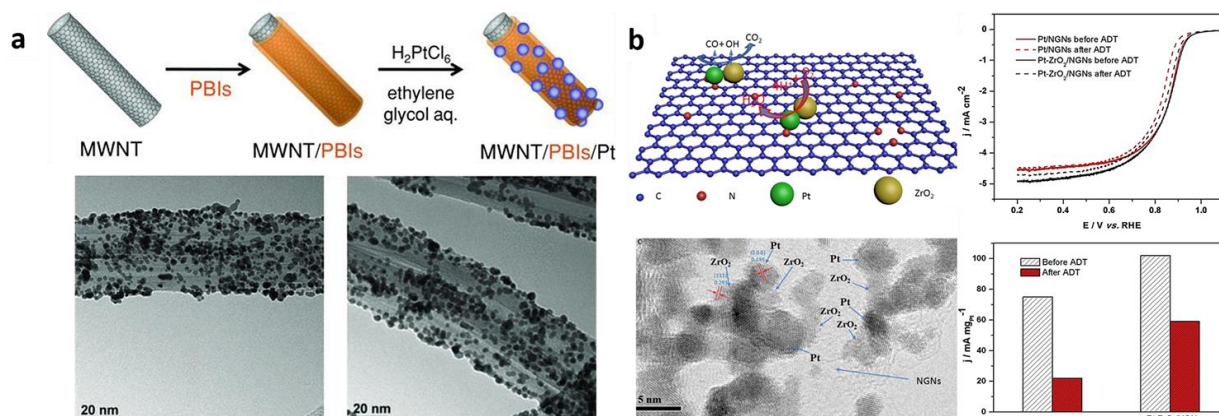
Figure 2.3. (a) Schematic illustration of the preparation of CNTs/PBIs/Pt, and TEM images of CNTs/PBIs/Pt. [20] (b) The schematic illustration of high stable catalyst of Pt/ZrO₂/NGNs, and the structure, electrochemical performance of Pt/ZrO₂/NGNs. [21] Wiley-VCH Verlag GmbH & Co. KGaA. Copyright 2013.

Novel noncarbon support

As discussed above, physical and chemical stability are highly demanding criteria for durable support materials. Among the several candidates, the transition metal oxides, metal carbides have been suggested as promising support materials because a specific metal oxide/carbide is corrosion-resistant in strong acidic media. Among the various metal oxides/carbides, the limited materials such as ZrO_2, TiO_2, CeO_2, Ta_2O_5, WO_3, MoO_3 and their carbides show chemical stability for strong acidic conditions for PEMFCs. For example, zirconium carbide (ZrC), a conductive ceramic material with high corrosion resistance, stability and high electron conductivity, has draw a great attention for the electrocatalysts support. It is reported that ZrC could promote the Pt activity and showed the superior electrochemical corrosion resistance. Sun et al. [22] for the first time used commercial ZrC as the catalyst support to develop the Pt/ZrC catalyst by an ALD method (Figure 2.4). TEM measurements revealed that the average size of Pt in ALD-Pt/ZrC was ~3.2 nm. Analysis of the X-ray absorption near edge structure (XANES) spectra at Pt L_3 and L_2 edges suggest that ALD-Pt/ZrC catalysts show noticeable change in the electronic structure of Pt due to strong interactions with ZrC support enabled by ALD. The analysis of intensity of the white line in both Pt L3 edges and Pt L2 edges indicates a stronger interaction between Pt and ZrC in the ALD-Pt/ZrC than in the Pt/C. Electrochemical measurement for ORR showed that ALD-Pt/ZrC catalyst exhibited a mass activity of 0.122 $A \cdot mg^{-1}_{Pt}$ at 0.9 V (vs. RHE), which was much higher than those for Pt/C (0.041 $A \cdot mg^{-1}_{Pt}$). After an ADT of 4000 continuous cycles, the ALD-Pt/ZrC had an ORR activity loss of ~26%, which was much lower than Pt/C (76% loss), while the ECSA loss of ALD-Pt/ZrC was only 17%, compared with 78% Pt/C. Based on the strong metal-support interactions, the ALD-Pt/ZrC catalyst exhibited promising electrocatalyst durability being almost five times more stable than Pt/C. The stabilization of Pt NPs on ZrC can be understood through the strong metal-support interaction, which is evidenced through XANES. Tightly bound Pt NPs are protected by the migration on the ZrC support, inhibiting Pt agglomeration.

Based on recent research results, finding stable support materials is still a challenging project although significant advances have been made in the field of metal oxides/carbides. Though

nitride and carbide materials can be considered as an alternative, delicate understanding and investigations are required for further advances.
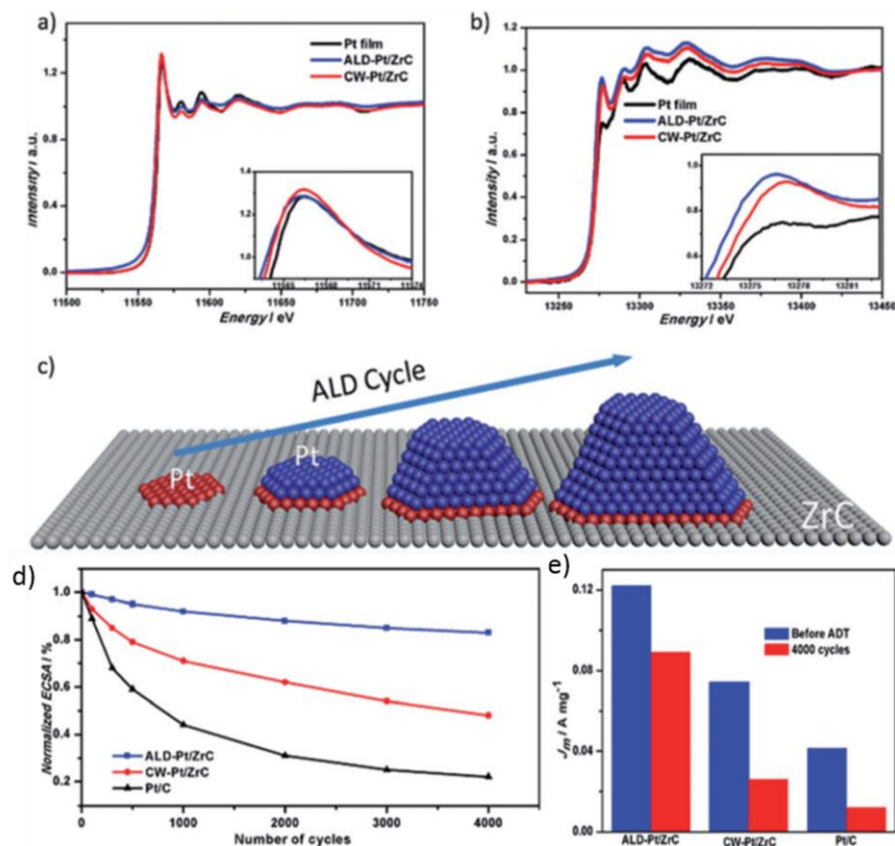
Figure 2.4. Normalized XANES spectra of Pt NPs on composite catalyst support at (a) the Pt L₃ edge and (b) the Pt L₂ edge. (c) Schematic illustration of ALD-Pt growth on ZrC support. Loss of electrochemical surface area (ECSA) (d) and mass activity (e) for ALD-Pt/Zr before and after ADT. Reproduced from [22] with permission from the Royal Society of Chemistry.

2.2.2   Novel structure of Pt nanoparticles

As discussed above, improving Pt NPs stability is pivotal for maintaining performance without activity loss. Various methods have been suggested to suppress the atomic dissolution of NPs and inhibit their agglomeration. For instance, crystal structure and shape control can help mitigate atomic dissolution and reduce particle coalescence. In this section, we summarize the recent development for enhancing Pt NPs durability with ultrafine particle shape and structure, such as Pt nanoframe, nanocage and nanowire.

Pt nanoframe

In 2014, Chen and co-workers presented highly crystalline bimetallic nanoframes with 3D structure as highly durable and active ORR electrocatalysts. [23] After synthesis of PtNi$_3$ polyhedral NPs, the interior corrosion of Ni in solution transforms the solid PtNi$_3$ nanocrystals into the Pt$_3$Ni nanoframes. Subsequently, a controlled thermal treatment of the resulting Pt$_3$Ni nanoframes forms the desired Pt-skin surface structure (Figure 2.5a). The combination of the 3D structure and the Pt-skin surface promoted ORR activity, achieving a remarkably high ORR activity. Moreover, the Pt-skin nanoframe also showed superior long-term durability without appreciable activity loss. After long-term durability tests, scanning TEM images indicated that the 3D frame structures were well preserved without noticeable changes. The origin of the long-term durability is ascribed to the lower coverage of oxygenated species arising from the weaker oxygen-binding energy and optimal Pt skin layer, which prevents the dissolution of the transition metals. Based on these superior electrochemical properties, various advances have been proposed by structure modification [24, 25] and expanded to various bimetallic or trimetallic nanoframe systems. [26-28]

In 2015, Zhang et al. reported the synthesis of catalytically active octahedral and cubic Pt NPs. The NPs are not solid but instead are hollow nanocages entirely enclosed by either (111) facets (octahedra) or (100) facets (cubic). [29] Unlike earlier studies on shape-selected Pt-Pd bimetallic core-shell NPs, the authors managed to carefully dissolve the metallic core without compromising the well-defined thickness and composition of a Pt shell that is a mere atomic layer thickness as shown in Figure 2.5b. The ORR performance of the octahedra nanocages showed a mass activity of 0.75 A·mg^{-1}$_{Pt}$ and a specific activity of 1.98 mA·cm^{-2} at 0.9 V, which are five and eight times higher than those of commercial Pt/C, respectively. Furthermore, the octahedral nanocages showed better long-term stability, with the ORR mass activity only reduced by 36% after 10,000 ADT cycles, showing 3.4-fold enhancement relative to the commercial Pt/C. The ECSAs of the octahedral nanocages only dropped by 6% after 5000 cycles and 23% after 10,000 cycles, respectively. During the durability test, the holes in the walls of the nanocages were slightly enlarged. These results demonstrated that the excellent durability associated with the core-shell catalysts was not affected by the

selective removal of Pd cores. Future investigations of the morphological and compositional stability of shaped catalysts under realistic PEMFCs conditions need be further investigated.
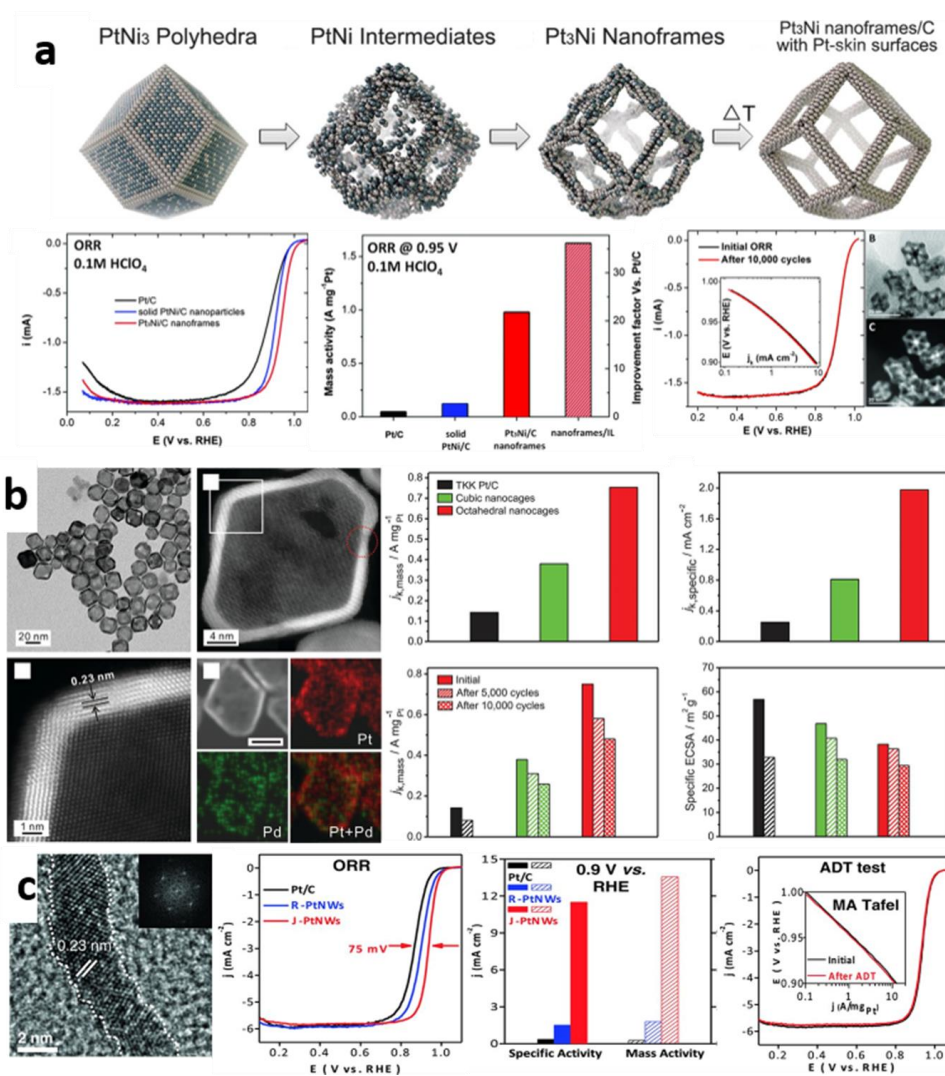
Figure 2.5. Shape control of nanoparticles for durable and active electrocatalysts. Durability results and TEM analysis: (a) Pt₃Ni nanoframe structure. [23] Reprinted by permission from Science. Copyright 2014 (b) Hollow structure of Pt nanocage. [29] Reprinted by permission from Science. Copyright 2015 (c) 1D Pt nanowire. [30] Reprinted by permission from Science. Copyright 2016

1D nanostructure of nanowires, have numerous advantages for use in electrocatalysis. nanowires have been proposed as an ideal structure, combining advantages from the increased electrocatalytic active sites of the nanoscale and the high stability of the bulk scale.

In 2016, Duan and co-workers verified the high activity and durability of a jagged Pt nanowire-based electrocatalyst for the ORR. [30] The ultrafine jagged Pt nanowire which are produced by the dealloying of a PtNi nanowire (Figure 2.5c). This structure was synthesized by the formation of Pt-core/NiO-shell nanowires, followed by their transformation into a PtNi alloy nanowire structure by high-temperature annealing at H_2/Ar atmosphere. Subsequently, electrochemical dealloying was used to leach away the Ni in the nanowire, generating a jagged Pt nanowire with a highly crystalline character. This jagged Pt nanowire showed high ECSA values of around 120 $m^2 \cdot g^{-1}$, which is even higher than those of Pt NPs (around 60-80 $m^2 \cdot g^{-1}$), and a high mass activity at 0.9 V (13.6 $A \cdot mg^{-1}_{Pt}$). Furthermore, the jagged Pt nanowires showed superior ORR durability. After 6000 cycles, the ECSA dropped by only 7% and together the mass activity dropped by only 12%. The superior ORR durability of jagged Pt nanowires is attributed to the unique 1D geometry of nanowires and the multipoint contacts with the carbon support. As discussed of the mechanism for catalyst degradation, dissolution followed by Ostwald ripening and NPs agglomeration, is the major cause of low durability, and these effects become even more serious as the NPs size decrease. Owing to their 1D structure, nanowires might prohibit the movement and aggregation of NPs and even mitigate Ostwald ripening, resulting in the maintenance of the initial morphology and contribution to the excellent durability. Because of their structural advantages, nanowires have been applied to bimetallic or trimetallic compounds and core-shell structures.[31, 32] Apart from the linear nanowire structure, Huang and co-workers recently reported a hierarchical PtCo nanowire structure that has a high-index, Pt-rich surface and an ordered intermetallic structure.[33] These structures showed significant enhancement in ORR activity compared to commercial Pt nanoparticles and long-term durability for up to 20,000 ADT-cycles, showing only 8% activity loss. The high activity and durability are attributed to the exposure of hollow sites on (110) and (310) high-index facets, suggesting that surface facet control while maintaining the 1D structure is promising for further activity and durability enhancement.

2.2.3　Pt NPs encapsulation or confinement

Recent studied have shown that a shell coating on catalyst NPs act as a physical barrier to inhibit the migration and coalescence of metal NPs. Such steric effects can greatly enhance

the durability of Pt catalyst while maintain the high activity. Various materials have been explored as effective coating and/or encapsulating agents, including the inorganic mesoporous materials (e.g. silica, carbon shells, metal oxide nanocage) and organic materials (e.g. polymers, macromolecules). To prevent Pt NPs from detaching, dissolving, migrating, and aggregating during electrochemical measurement and heat treatment, Hyeon et al. [34] designed a facile but effective strategy to embed PtFe nanocrystals into a very thin carbon shell and verified their unique stability. Solution-based polydopamine coatings on the active PtFe NPs can be converted into very thin N-doped carbon shell during thermal annealing. During the heat treatment, the NP crystal structure is converted into a durable intermetallic structure, without particle agglomeration, verifying their high thermal stability (Figure 2.6a). By controlling the thickness of the shell below 1 nm, the excellent protection of the PtFe NPs as well as high activity was achieved. The ordered PtFe/C nanocatalyst coated with a N-doped carbon shell shows 11.4 times higher mass activity and 10.5 times higher specific activity than Pt/C. Importantly, there was no significant activity loss up to 10,000 ADT potential cycles and high durability was also observed in MEA analysis, maintaining its maximum power density up to 100 h of consecutive operation. In addition to its high activity and durability, carbon-shell-thickness control results give an insight into the design principle for appropriate confinement or encapsulation of the particles. It was indicated that the proper design for NP encapsulation while exposing the active sites for reaction is critical for achieving both high activity and durability.

Besides carbon encapsulation systems, metal oxide and carbide systems have also been suggested as promising concept for stabilizing NPs and increasing the catalyst activity and durability. Sun et al. [35] suggested the Pt stabilization by depositing of zirconia (ZrO_2) nanocage at the interface between carbon and Pt NPs using the area-selective ALD method. To avoid the ZrO_2 depositing and covering on Pt active surface, an organic blocking agent was used to protect the Pt surface. Then ALD of ZrO_2 selectively grew around the Pt NPs but was not deposited on the Pt surface. A nanocage structure may be formed by precisely controlling the ALD ZrO_2 layers. Finally, removal of the organic agent to expose the active Pt surface for reaction (Figure 2.6b). In this system, exposing the Pt active surface while the NPs are confined in ZrO_2 nanocage is key for obtaining both high activity and durability. Because of the strong interaction between the Pt and carbon support and the Pt NPs

confinement effects, the ZrO$_2$ nanocage encapsulated Pt NPs showed remarkably high durability without significant changes in particle size, suggesting that the inhibition of particle agglomeration by physical confinement is critical for enhancing Pt NPs long-term stability.
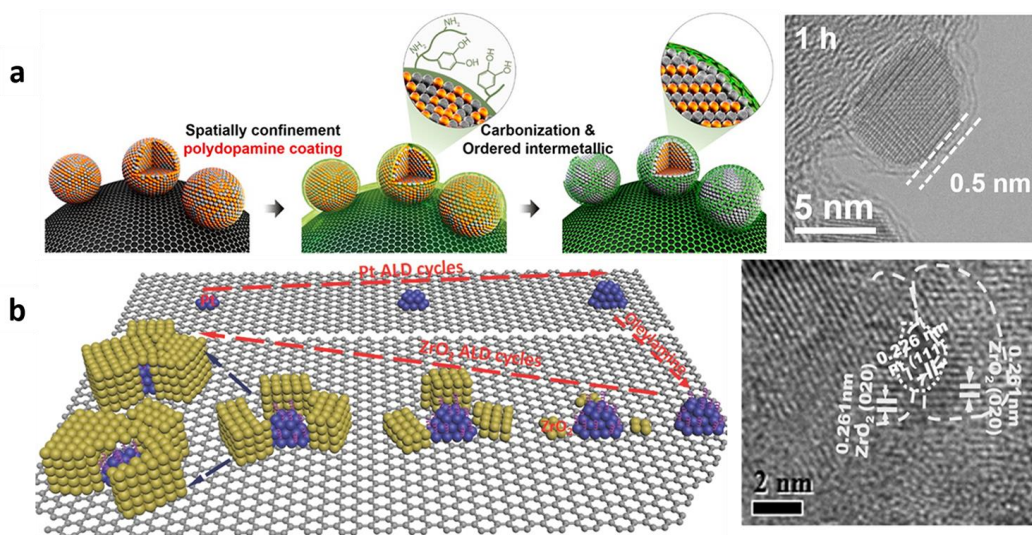
Figure 2.6. (a) A thin-layer-carbon shell-protected PtFe nanoparticle. [34] Copyright 2015 American Chemical Society (b) Area-selective ALD of Zirconia-stabilized Pt nanoparticles. [35] Wiley-VCH Verlag GmbH & Co. KGaA. Copyright 2016.

2.3 Progress of highly active single atom catalysts

Supported metal NPs are the most widely investigated heterogeneous catalysts in catalysis community. In heterogeneous catalysis by supported metal nanostructure, enormous efforts have been devoted to improving the performance of supported metal catalysts by downsizing the metal particles. In the conventional Pt/C electrocatalysts, Pt utilization is extremely low, as the active sites are only located on the surface of the catalyst particles. Downsizing catalyst NPs to single atom is highly desirable to decrease the cost and maximize the utilization efficiency. Single atom catalysts (SACs), as a new frontier in heterogeneous catalysis, have attracted considerable attention due to their unique catalytic properties. Different from the traditional particles, the catalytic performance of SACs is highly dependent on their low-coordination environment, quantum size effects and metal-support interaction. Recently, several methods have been developed for the preparation of SACs, including wet-impregnation method, [36] metal-organic frameworks-derived SACs (MOF-

SACs), [37, 38] high temperature atom trapping approach [39, 40] and atomic layer deposition method. [41, 42] In this section, we will briefly discuss the recent progress on preparation, characterization, catalytic activity of SACs. In addition, the main advantages of SACs as catalysts and the challenges faced for further improving catalytic performance are also highlighted.

2.3.1   Preparation and characterization of single atom catalysts

A prerequisite for studying the electrocatalytic performance of SACs is to construct the single atoms dispersed catalyst on the appropriate support surfaces. Fabrication of SACs, however, has been challenging as the tendency for aggregation of metal atoms either during the synthesis process or the subsequent treatments. During the past decade, several approaches to construct isolated single metal sites over the surface have been reported, including (i) wet-impregnation method; (ii) MOFs-derived SACs; (iii) high temperature atom trapping approach; (iv) atomic layer deposition technique. Another challenge is the approaches can be used for detecting SAs due to their unique physical and chemical properties. Atomic resolution aberration-corrected scanning tunneling microscopy (STEM) and X-ray absorption spectroscopy investigations are the most typical techniques for determining SACs. Based on these developments, we summarize the detailed approaches for the preparation of SACs. The local structural information of SACs at the atomic scale revealed by these techniques are discussed here.

Wet-impregnation

The metal nitrides, carbides, and oxides can be used as non-carbon supports to support Pt SAs. It was reported that Pt single atoms have been successfully immobilized on TiN,[43] TiC,[44] MoS_2[45] and FeOx[36, 46] supports. A simple incipient wetness impregnation method was reported for the synthesis of Pt SACs on FeOx substrate by Zhang and co-workers. [36, 47] Small amounts of Pt precursor (H_2PtCl_6) dissolved in aqueous solution mixed with the support precursors. The recovered solid was dried in a vacuum oven, then the powder was calcined and reduced at high temperature under a H_2 flow. The Pt SAs weight percent of the final products were 0.17-0.5 wt% determined by inductively coupled plasma spectroscopy.

The characterization of practical single-atom species is another important factor that hinders the development of SACs. Recent advances in atomic resolution characterization techniques, such as high-angle annular dark field scanning transmission electron microscopy (HAADF-STEM), can precisely locate the isolate metal atoms thus providing direct local structural information about the metal species on supports. In addition, with the combination of the state-of the art experimental techniques such as X-ray absorption spectroscopy and advanced modeling and simulation methods in computational chemistry, more in-depth characterizations about structures of SACs start to become accessible. Figure 2.7 shows the detailed surface structure of Pt SAs regarding the single-atom species on various supports obtained by the combination of X-ray absorption spectral characterizations. The HAADF-STEM images provide direct evidence for the existence of single atoms dispersed on the supports, but they cannot exclude the existence of nanoparticles. Extended X-ray absorption fine structure (EXAFS) spectra provide more decisive evidence for the presence of single atoms and the absence of NPs. Pt NPs typically show an EXAFS peak for the Pt-Pt bond at 2.6Å. Pt_1/FeOx, Pt_1/MoS_2, Pt_1/TiN, and Pt_1/C did not show these peaks, which means the Pt present as the single atoms dispersed on the substrate.
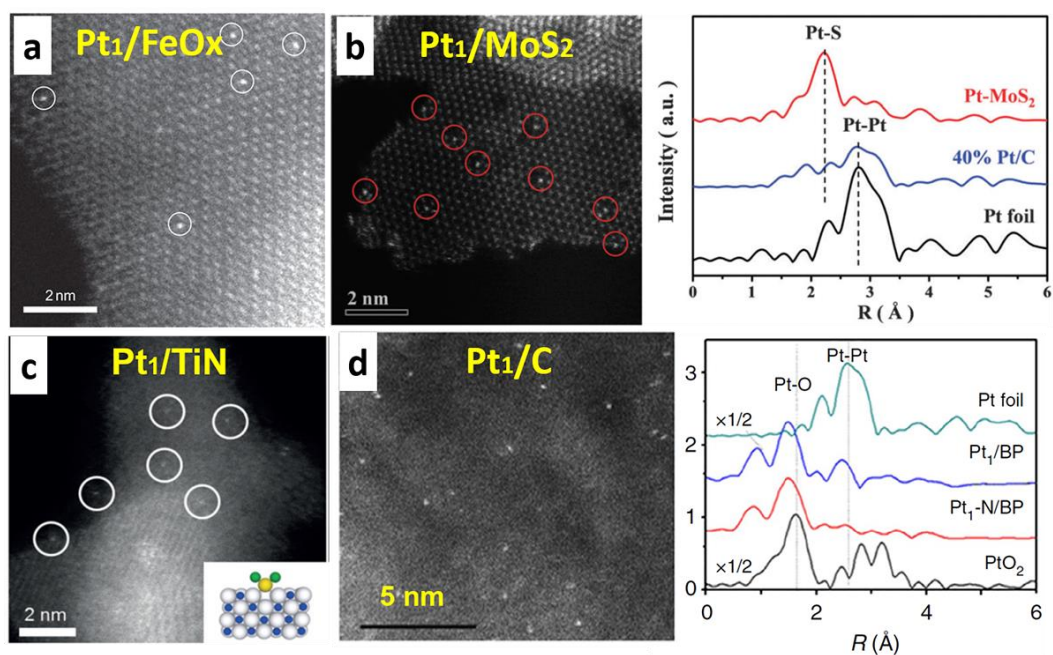
Figure 2.7. HAADF-STEM images and EXAFS spectra of Pt_1/FeOx (a), Pt_1/MoS_2 (b), Pt_1/TiN (c), Pt_1/C (d) to confirm the existence of isolated Pt atoms.

MOFs-derived SACs

MOF-derived single atoms, is based on the metal-ligand interaction in anchoring isolated atoms with designed configuration. This method is generally used for the introduction of isolated metal atoms into functional framework in which binding sites are orderly arranged. [49, 50] More specifically, the high porosity of MOFs and their composites is very helpful for the fabrication of atomically active sites and effectively improves the stability of SACs. In addition, the metal nodes of MOFs can act as anchoring sites to bind single atoms. Furthermore, some organic linkers of MOFs may offer additional coordination sites to connect single atoms. The loading content of isolated atoms is in direct proportion with the binding sites, and thus high density loading of isolated atoms can be reached by preliminary fixing of binding sites.

Ye and co-workers [51] realized the modular optimization of MOFs by incorporation of coordinatively unsaturated single cobalt (Co) atoms into porphyrin-based MOFs. Local coordination configuration of the Co atom upon insertion within the framework was confirmed by EXAFS. EXAFS curve fitting analysis reveals that the coordination number of the nearest-neighbor nitrogen atoms surrounding the isolated Co atom is 3.9 at the binding distance of 1.95 Å, confirming the square-planar configuration of Co in the newly developed porphyrin-MOFs and the presence of unsaturated active sites of Co SAs for catalytic reaction. Xu and co-workers [49] immobilized single Pt atoms into 2,2′-bipyridine-based microporous MOFs (MOF-253) using modular synthetic approach. The predesigned coordination sites are particularly well-suited for chelating of the single Pt atoms, the chelated atoms further coordinate with chloride ion in Pt-Cl bond length of 2.301 Å (resolved by EXAFS). This work clearly demonstrates that the concept of inserting metal salts in a porous framework can be employed successfully as a strategy for designing and constructing new types of photocatalysts for H_2 production. Further studies were reported by Jiang and co-workers using MOFs as a class of promising supports/hosts to stabilize single metal atoms for efficient catalysis. [37, 52] A highly stable aluminum-based porphyrin-MOFs (Al-TCPP), formulated as $(AlOH)_2H_2TCPP$ (H_2TCPP = (porphyrin-5,10,15,20-tetrayl) tetrabenzoate), in which infinite $Al(OH)O_4$ chains are interconnected by the porphyrin linkers into a 3D microporous framework, was employed for Pt(II) metalation into the porphyrin centers.

Following a simple reduction, the single Pt atoms based on the strong interaction with pyrrolic N atoms in the Al-TCPP was obtained (Figure 2.8). The spherical aberration-corrected electron microscope observation and XAFS results unambiguously evidenced the presence of single Pt atoms inside the MOFs. Remarkably, the resultant MOFs incorporating with single Pt atoms exhibits an extremely high photocatalytic H_2 production rate by water splitting, far superior to that of the reference Pt NPs catalyst stabilized by Al-TCPP.
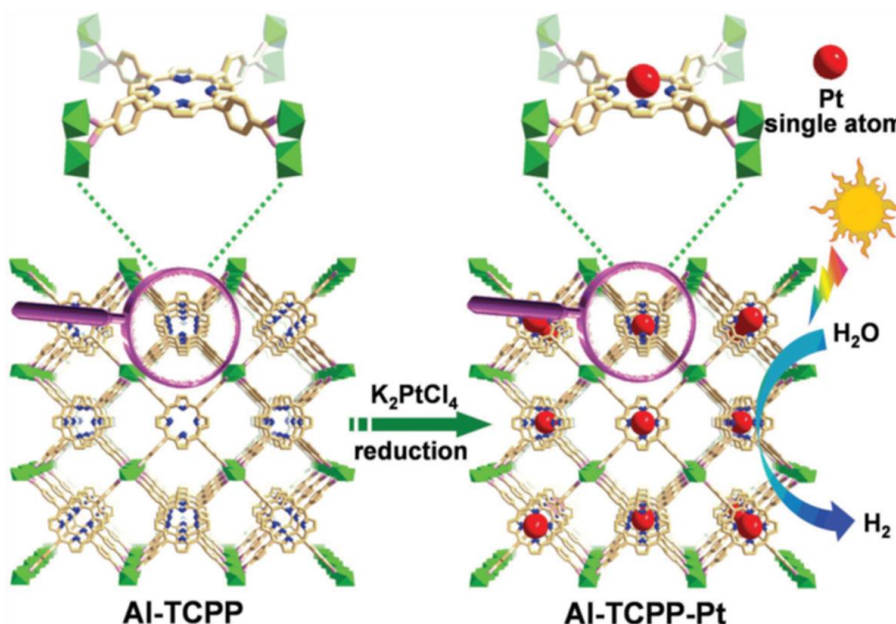
Figure 2.8. Schematic illustration showing the synthesis of Pt single atom on Al-TCPP for photocatalytic hydrogen production. [37] Wiley-VCH Verlag GmbH & Co. KGaA. Copyright 2018.

Not limited to pristine MOFs, MOFs-derived porous materials can also act as hosts for the synthesis of single atom catalysts. Using iron-acetate/phenanthroline/ZIF-8 (Fe/Phen/ZIF-8) as precursor, Zitolo et al. [53] obtained Fe–N–C catalysts and then investigated their structures of the active sites for ORR. XAFS demonstrated the formation of Fe-centered moieties in the Fe–N–C catalyst, which effectively catalyzed the four-electron reduction of oxygen to water based on the highly basic N-groups formed during the pyrolysis in NH_3 atmosphere. Wu, Shao and coworkers [54-56] developed a chemical doping approach to the synthesis of single-atom Fe catalyst by choosing Fe-doped ZIF-8 as a precursor. The catalyst

exhibited remarkable ORR performance in 0.5 M H_2SO_4 media. These findings would open an important approach to the synthesis of single-atom metal catalysts based on MOFs precursors.

High temperature atom trapping

Atom trapping should be broadly applicable as a method for preparing single-atom catalysts. The approach requires a supply of mobile atoms and a support that can bind the mobile species. In the atom trapping process, the thermal transport from bulk particles to the dispersed atoms is realized using a simple model system. The isolated metal was thermally transported from a bulk metal to support surface by heating together in air. [57] The catalyst supports have been shown to stabilized Pt in the form of isolated atoms. For example, penta-coordinated Al^{3+} sites on alumina [58], FeOx, [36] and the (111) surface of $MgAl_2O_4$. [59] However, when these catalysts are aged at 800°C in air, the formation of layer crystalline Pt NPs can be detected. Single atoms on catalyst supports can be mobile and aggregate into NPs when heated at elevated temperatures. High temperatures are detrimental to catalyst performance unless the mobile atoms can be trapped. Datye and coworkers [39] used ceria (CeO_2) powders having similar surface areas but different exposed surface facets as support to trap Pt single atoms under 800°C high temperature in air. When mixed with a Pt/aluminum oxide catalyst and aged in air at 800°C, the Pt transferred to the CeO_2 and was trapped. As shown in Figure 2.9, under oxidizing conditions and at high temperature, certain metal such as Pt can be emitted as volatile (PtO_2) molecules. If these molecules are captured by the surfaces of another CeO_2 support which stabilize the metal-containing molecule then metal single atoms can be uniformly dispersed onto the support surfaces to produce a SAC. Polyhedral CeO_2 and nanorods were more effective than CeO_2 cubes at anchoring the Pt. Performing synthesis at high temperatures ensures that only the most stable binding sites are occupied, yielding a sintering-resistant, atomically dispersed catalyst. Surface species such as hydroxyls and carbonates, which could prevent the trapping of mobile species, would have desorbed at high temperatures, providing a clean surface for the formation of covalent metal oxide bonds that are needed to stabilize single atoms. Trapping of atoms affords a plausible explanation for the role of ceria in slowing the rates of Ostwald ripening and may help to explain how other supports modify the rates of catalyst sintering.
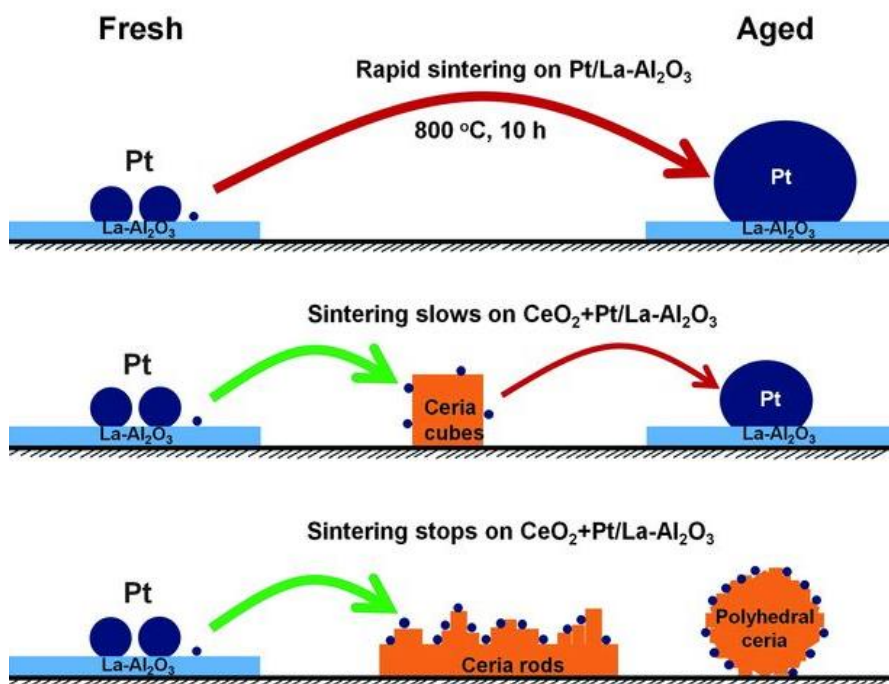
Figure 2.9. Illustration of Pt NPs sintering, showing how ceria can trap the mobile Pt to suppress sintering. Cubes appear to be less effective than rods or polyhedral ceria. [39] Reprinted by permission from Science. Copyright 2016

Atomic layer deposition (ALD)

ALD, relying on sequential self-terminating reactions between a solid surface and gas phase precursor molecules, is a cyclic process. [60, 61] The self-limiting nature of the chemical reactions makes it possible to precisely control over size of the deposited materials at the atomic level. Generally, one complete ALD cycle contains two half reactions (as shown in Figure 2.10a). In the first half reaction, the first precursor reacts with all available active sites (functional groups or defect) on the substrate, in which a fraction of ligands of the precursor are partially removed. Then residue of the first precursor and reaction by-products are purged away with an inert gas. In the second half reaction, the reactant precursor reacts with the adsorbed precursor on the substrate to get the target material by removing the remaining ligands of the first precursor. In this reaction, it is very important to regenerate active sites on the surface of deposited materials for the next cycle deposition. The residuals of the second

precursor and by-products are purged with an inert gas and complete the reaction cycle. The desired material size can be achieved by controlling the deposition cycles number. Based on sequential and self-limiting reactions, ALD is capable to produce a variety of materials from noble metals to metal oxides with precise control at the atomic level.

Sun et al. reported the preparation of single-atom Pt immobilized on graphene nanosheets or nitrogen-doped graphene nanosheets by using ALD. [41, 42] The graphene nanosheets were prepared by the oxidation of graphene, thermal exfoliation, and reduction. Nitrogen was added as a dopant by post-heating the graphene under ammonia at 900 °C. Then, Pt was deposited by ALD via using (methylcyclopentadienyl)trimethylplatinum ([MeCpPtMe$_3$]) and O$_2$ as the precursors. The deposition temperature was 250 °C. The size, morphology, and loading density of Pt over graphene can be well controlled by simply tuning the cycles of ALD. As shown in Figure 2.10b, single-atom Pt was clearly observed on the support of N-doped graphene nanosheets. The constructed SAC produces greatly enhanced catalytic performance and comparable with that of commercial Pt/C catalyst. As a method for synthesizing better-controlled SACs for fundamental study, it is anticipated that ALD can become a powerful tool for studying the structure–performance relationships of supported metal SACs.
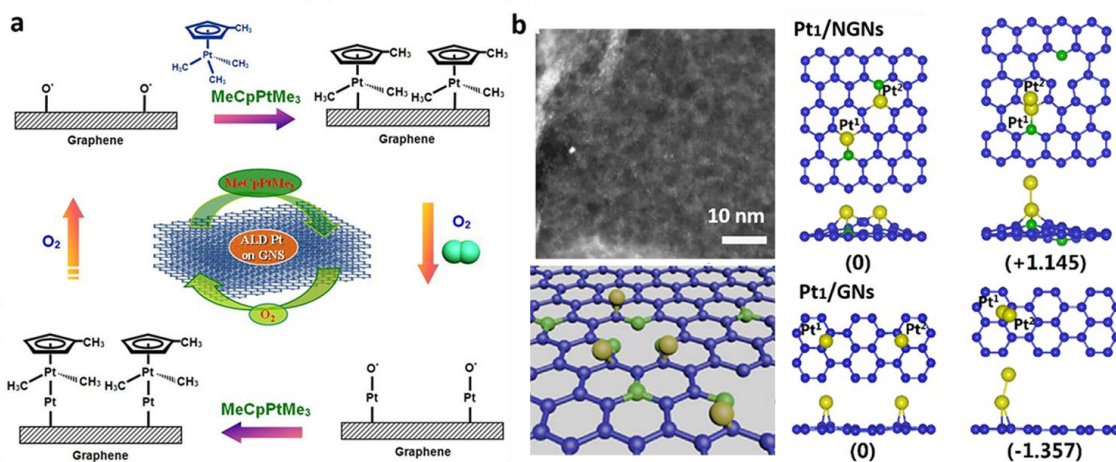
Figure 2.10. Schematic illustrations of Pt ALD mechanism on graphene nanosheets (a). HADF-STEM images Pt configurations on N-doped and pristine graphene (b). [42] Reprinted by permission from Macmillan Publishers Limited, Nature Communications. Copyright 2016.

2.3.2   Electrocatalytic performance of single-atom catalysts

Single-atom catalysts, in which metal atoms are dispersed on the support without forming NPs, have extremely high atom utilization efficiency, which makes them highly active catalysts for several catalytic reactions. The SACs have been proven to be highly efficient catalysts for several electrochemical reactions, including methanol oxidation reaction (MOR), hydrogen evolution reaction (HER) and oxygen reduction reaction (ORR). SACs have shown high activity, minimizing the use of precious metal, and unique selectivity distinct from nanoparticle catalysts owing to the absence of ensemble sites. Recent progress of SACs composed of precious and non-precious metals for use in electrochemical reactions are summarized and discussed.

Oxygen reduction reaction (ORR)

The big challenge for the widespread adoption of PEMFCs is their large use of scarce Pt catalyst, which is required especially at the cathode for the ORR owing to its sluggish kinetics. For the ORR process, two different pathways: two-electron pathway ($O_2 + 2H^+ + 2e^- \rightarrow H_2O_2$; E=0.70 V) and four-electron pathway ($O_2 + 4H^+ + 4e^- \rightarrow H_2O$; E=1.23 V), were demonstrated on single atom Pt catalysts. The support plays a significant role for the selective catalytic reaction route and final product. For instance, the single Pt atoms on sulfur-doped zeolite-templated carbon support could selectively transfer the O_2 to H_2O_2 through a two-electron pathway, [62] while single Pt atoms on nitrogen-doped carbon black exhibited great performance for highly efficient 4-electron ORR. [48]

Pt_1/TiN [43] was used as electrocatalyst to reduce O_2 and produce H_2O_2 with mass activity higher than Pt NPs. It was found that the single-atom Pt with content of 0.35 wt% on TiN substrate exhibited the high selectivity towards H_2O_2. The H_2O_2 oxidation currents were surprisingly high, and the H_2O_2 selectivity reached 65% (Figure 2.11a). Single-atom Pt immobilized on a sulfur-implanted carbon matrix, was used for the ORR with a two-electron pathway. [62] The newly constructed sulfur-doped carbon matrix enabled the stabilization of isolated Pt atoms in high loading content of 5.0 wt%. when turns to the oxygen reduction, the Pt SACs on sulfur-doped carbon could produce H_2O_2 with a very high selectivity of approximately 95% (Figure 2.11b). The density functional theory (DFT) calculations showed

that single-atom Pt would be ligated by two thiophenes and two thiolates. When the elementary steps for the ORR were calculated, it was found that the two-electron pathway was kinetically favored. It is notable that the support stabilized the single Pt atoms participates in the surface reaction, thus affecting the selectivity.
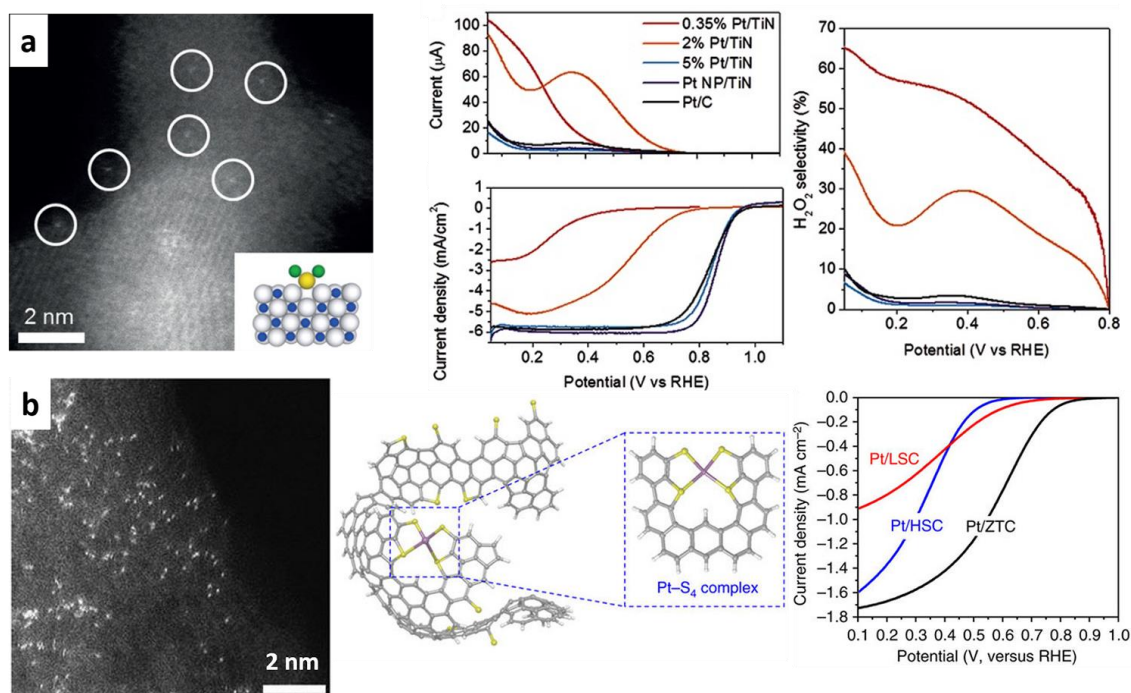
Figure 2.11. (a) HAADF-STEM image of Pt$_1$/TiN, electrochemical ORR polarization curves and H$_2$O$_2$ selectivity curves obtained for the Pt/TiN with various Pt loading. [43] Wiley-VCH Verlag GmbH & Co. KGaA. Copyright 2016. (b) HAADF-STEM image proposed atomistic structure and ORR activities of the Pt$_1$/sulfur-doped carbon catalyst. [62] Reprinted by permission from Macmillan Publishers Limited, Nature Communications. Copyright 2016.

The two-electron pathway produces H$_2$O$_2$ with less electricity generation; thus, this is an undesired reaction at the cathode. However, the O-O bonds are usually cleaved on Pt ensemble sites, making Pt SACs less than ideal for the ORR with four-electron pathway. There should be neighboring sites to the single-atom Pt to break the O-O bonds. Liu et al. reported that Pt$_1$/N-doped carbon black can be used as a high-performance and durable electrocatalyst towards efficient four-electron ORR. [48] Although they did not report the specific mass activity for the ORR, the high half-wave potential of 0.76 V vs. RHE indicates

the much higher catalytic activity of Pt_1/N-doped carbon for ORR compared with that of commercial Pt/C (Figure 2.12). This study implies that the catalytic activity of Pt single atoms for ORR could be triggered tremendously by the doped-N atoms to a high level due to the synergetic effect between nitrogen dopant and Pt single atoms, which contribute to a four-electron ORR pathway with a much lower H_2O_2 yield compared with the Pt_1/C. The density functional theory (DFT) calculations indicate that the single-pyridinic-nitrogen (P-N)-atom-anchored single Pt atom centers are the main active sites, which are not only highly active for ORR but also are tolerant to CO and methanol.
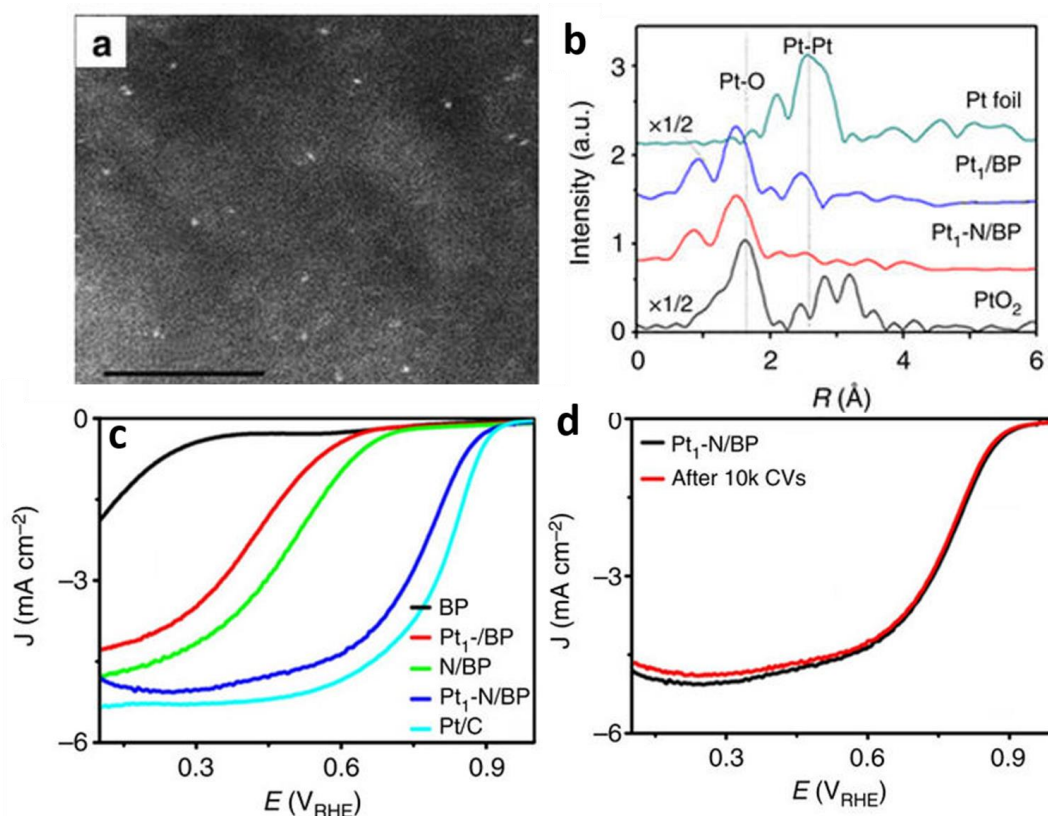
Figure 2.12. Physical characterization of HAADF-STEM images (a) and the k^2-weighted R-space FT spectra from EXAFS (b) for Pt_1/N-carbon. electrochemical ORR activity (c) and durability (d) of Pt_1/N-carbon. [48] Reprinted by permission from Macmillan Publishers Limited, Nature Communications. Copyright 2017.

Hydrogen evolution reaction (HER)

Hydrogen evolution through electrocatalytic reduction of water holds great promise for clean energy. The conductive substrate immobilized single-atom Pt catalyst is reported as an advanced HER catalyst.

Bao et al. first illustrated that the electrocatalytic HER activity of in-plane sulfur (S) atoms from MoS_2 can be enhanced by decorating isolated Pt single-atom. Sub-angstrom resolution HAADF-STEM images confirmed that isolated Pt atoms homogeneously distributed in the 2D MoS_2 plane, and the magnified domain verified that isolated Pt atoms exactly occupy the positions of the Mo atoms (Figure 2.13a). Compared with pure MoS_2, Pt_1/MoS_2 produces a greatly boosted hydrogen evolution activity in the HER process. The enhanced catalytic activity of the in-plane S atoms of MoS_2 was triggered by single-atom Pt doping, whereas the HER activity of MoS_2 sheets typically originate from edge sites. It was found that the density of states of an in-plane S atom in Pt-doped MoS_2 was similar to that of an edge S atom in pure MoS_2. Single-atom Pt itself was not an active site, and instead, the adsorption strength of hydrogen species on the in-plane S sites neighboring the Pt atoms were tuned to have a much higher HER activity and durability. Further DFT calculation confirmed that the activated in-plane S sites which neighboring the doped Pt atoms show modified free energy for hydrogen adsorption.

Sun and co-workers reported on the practical synthesis of isolated single Pt atoms on N-doped graphene using ALD, as shown in Figure 2.13b. [42] The single Pt atom catalysts have been investigated for the HER, where they exhibit significantly enhanced catalytic activity (up to 37 times) in comparison to the state-of-the-art commercial Pt/C catalysts. Thanks to the strong bonding energy between Pt and nitrogen doped graphene, the activity of the catalysts dropped only 4% after 1,000 cycles, indicating a high durability. Through the synchrotron radiation and DFT analysis, it was determined that the interaction between the metal atoms and the support played a vital role in the stabilization of single Pt atom. First-principles calculations showed that the interaction between single Pt atoms and N-dopants was about 5.3 eV, which is approximately 3.4 eV larger than the bonding strength between Pt atoms and the graphene substrate; thus, suggesting that Pt prefers to bind with N-doping sites. The strong bonding interaction of Pt_1-N dopants promotes the high stability of Pt single atoms during the potential cycling.
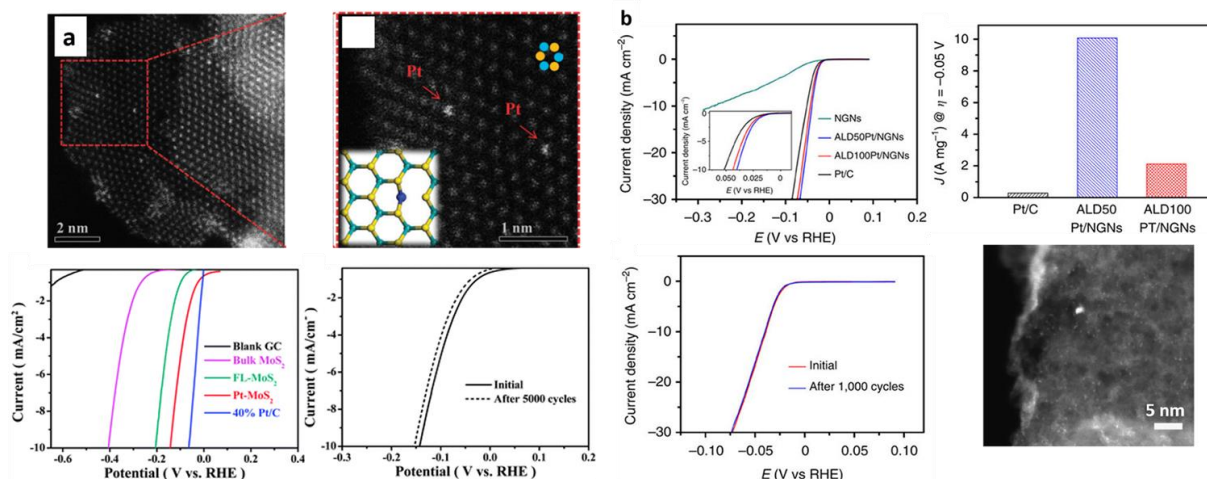
Figure 2.13. (a) HAADF-STEM images of Pt₁/MoS₂ showing the Pt atoms occupying the positions of Mo atoms. HER activity and durability measurement of Pt₁/MoS₂ and counterparts catalysts. (b) HER activity, durability curves and HAADF-STEM image of Pt₁/N-doped graphene prepared by ALD. [42] Reprinted by permission from Macmillan Publishers Limited, Nature Communications. Copyright 2016

2.3.3   Perspectives of Pt single atoms catalyst

Up till now, the initial active sites of single-atom catalysts for the enhanced mechanism is still unclear. More fundamental studies should focus on the influence of support on the performance of single atom catalysts, which might provide systematic understanding of the interactions between the SAC and supports. In addition to electrochemical catalytic reactions, the single atom Pt/CeO₂ catalyst exhibited a remarkable activity towards CO oxidation.[63] The single atom Pd/graphene catalysts obtained through ALD showed 100% butene selectivity in selective hydrogenation of 1,3-butadiene.[64] To further enhance the activity, the rational design of SACs with multiple compositions should be explored in the future, because bimetallic catalysts can exhibit improved performance compared to the pure metals.[65] By using the ALD method, the fabrication of bimetallic dimers is feasible through deposition of the secondary metal atom on the first single atomic metal. With the formation of dimer structures, the electronic structure of SAC could be tuned, which would further increase the activity of SACs to a new level.

The metal loading is usually very low due to the issues associated with agglomeration during the preparation process. Therefore, further improve the preparation techniques to achieve high loading of SACs is still challenge for their future commercial application. Furthermore, the selectivity of substrates is important for the dispersion of single atoms. Recently, Zeng et al. [66] found that the mass loading of singe Pt atom catalysts can reach up to 7.5% on MoS_2. In addition to the low loading issues, another key parameter for the SACs is the durability of the catalysts during the catalytic reactions. Single atom catalysts are highly mobile and tend to aggregate during the catalytic reactions due to high surface energy of SACs. The interaction between SAC and substrate plays an important role for their stability. Several studies have shown that nitrogen-doped carbon black, graphene and nitrogen-doped graphene can form a strong coordination site with metal atoms, thus observably improved their stability. However, the single atoms still tend to aggregate on traditional substrates. More studies should focus on the development of effective routes to stabilize the catalysts.

2.4 MOFs-derived nanomaterials for electrocatalysis

2.4.1 Introduction of MOFs

Nanostructured materials such as porous carbon, assembled metal/metal oxides nanoparticles (NPs), and their composites have been intensively studied in the field of electrocatalysis.[67-71] Metal-organic frameworks (MOFs), as precursor and/or template for designing these porous nanomaterials, have become a rapidly expanding research area in last two decades.[72, 73] As their name suggested, MOFs are constructed of coordination bonds by interconnecting metal ions and organic ligands to form the three-dimensional (3D) networks. The organic linkers are enormously diverse and have a variety of configurations. The vast number of metal ions and organic linkers available as well as their diverse assemblies have led to more than 20,000 MOFs being reported. [74] In addition to their adjustable compositions, another distinctive advantage of MOFs is their uniform pore size/shape and high specific surface area in contrast to traditional microporous and mesoporous materials. The pore size of MOFs can be adjusted from several angstroms to few nanometers, [75, 76] which allows the accessibility of reactants and products with specific size, endowing the selective catalysis of MOFs. Moreover, the high specific surface area (BET, usually>1000 $m^2 \cdot g^{-1}$, up to 7000 $m^2 \cdot g^{-1}$) favors the absorption and enrichment of reactant molecules around

the active sites, further benefiting the enhancement of catalytic activity. Therefore, MOFs-based nanomaterials being special solid catalysts are very promising, especially in fundamental electrocatalysis.

The remarkable advantages of MOFs-based materials in catalysis mainly arise from the inherent properties of MOFs precursor: MOFs possess high-density and uniform dispersion of active sites; high porosity that render all active sites readily accessible; open channels that greatly facilitate the transport and diffusion of reactants and products. Therefore, MOFs effectively integrate the advantages of heterogeneous catalysts with high reaction efficiency. However, the catalytic active centers involved in pristine MOFs are usually limited to the coordinatively unsaturated metal sites or the active group located on nonconductive organic ligands. These situations limit MOFs to a certain scope of electrocatalytic reactions. Fortunately, this challenge can be alleviated by two approaches: (i) functionalized modification-it is possible to converse the metal ions/cluster into metal/metal compound particles while carbonizing organic linker into conductive carbon support by the post-treatment modification. (ii) pore encapsulation-MOFs can incorporate a variety of catalytic active species into their pore space and behave as nanoreactor to host catalytic reactions. [77-79] The obtained nanocomposites derived from MOFs precursors with high surface area and dispersed active sites, were found to be important in electrocatalysis.

Generally, electrocatalysis is mainly challenged by either one or a few factors of poor catalytic activity, poor stability, and low conductivity. MOFs and their derivatives are suitable for highly efficient electrocatalysis due to their advantages of structural diversity and nearly infinite designability. In this section, detailed design and recent progress of MOFs-derived nanomaterials as electrocatalysts for ORR, hydrogen evolution reaction (HER), oxygen evolution reaction (OER) are described.

2.4.2   MOFs-derived electrocatalysts for ORR

The performance of electrocatalysts has become the limiting factor in most of the promising electrochemical energy conversion systems. ORR has been viewed as one of the most fundamentally and technologically important electrochemical reactions for fuel cells and lithium−air batteries. Although Pt-based catalysts are regarded as the most effective

electrocatalysts for promoting the ORR, their scale-up is still a big challenge due to the high cost, scarcity and poor stability of Pt catalysts. Bearing this in mind, extensive efforts have been devoted to developing alternative electrocatalysts for ORR. In recent years, considerable MOFs-derived nanomaterials such as monometal-MOFs, bimetal-MOFs, supported-MOFs composite, have been widely investigated and indicated advanced catalytic activity and durability for ORR.

Monometal-MOFs-derived electrocatalysts for ORR

Among the large variety of MOFs, transition metal-based MOFs, such as Co, Fe, or Zn, are the most investigated and widely used precursors for fabrication of non-precious metal catalysts. Their derived porous materials have been demonstrated to be effective electrocatalysts for ORR. Taking Co-MOF as an example, Liu and co-workers [80] used Co-ZIF as precursor for preparing non-precious metal electrocatalysts in 2011. Upon a facile pyrolysis under inert atmosphere at 750°C, the Co atoms and imidazole ligands from Co-MOFs can be converted into Co NPs and porous N-doped carbon respectively, resulting in a highly dispersed Co-Nx-C hybrid. Working as electrocatalyst, the Co-Nx-C displayed decent ORR activity, as noted by the positive onset potential of 0.83 V vs. RHE and the rapid increase of the cathodic current. Additionally, the electron numbers over this Co-Nx-C catalyst were found of 3.3-3.6, suggesting a dominative four-electron transfer process with certain peroxide formation.
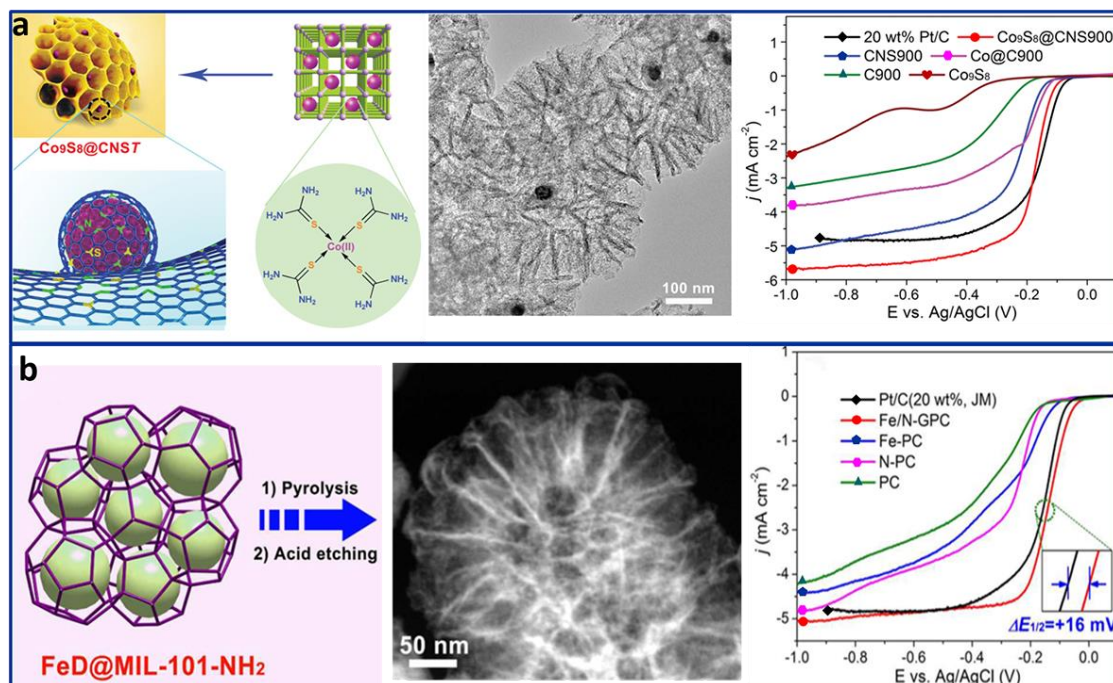
Figure 2.14. (a) Schematic illustration of preparation of Co₉S₈@NS-C; TEM images of as-prepared Co₉S₈@NS-C; ORR curves of Co₉S₈@NS-C and comparative catalysts. [81] Wiley-VCH Verlag GmbH & Co. KGaA. Copyright 2016. (b) Schematic representation for the preparation of the Fe/N-GPC catalyst; TEM images of Fe/N-GPC; ORR curves of Fe/N-GPC. [82] American Chemical Society. Copyright 2017.

To further enhance the catalytic activity of MOFs-derived nanostructures for ORR, the introduction of hierarchical pores and incorporation of active doping sites into the carbon frameworks by forming an enhanced synergetic effect are highly demand. Recently, Zhu and co-workers [81] reported the construction of a honeycomb-like porous carbon (NS-C) immobilized cobalt sulphide NPs (CoS) nanocomposite derived from MOFs precursor. An aluminium-based MOFs (MIL-101-NH$_2$) was selected as a host for the encapsulation of thiourea and cobalt chloride to form the catalyst precursor. Unexpectedly, the subsequent carbonization underwent an intriguing morphology-controlled process, which lead to the unique honeycomb-like N/S-co-doped porous carbon with Co₉S₈ NPs entrapment inside (as shown in Figure 2.14a). The resultant Co₉S₈@NS-C electrocatalyst exhibits the high catalytic activity toward ORR with an onset potential of 0.05 V and half-wave potential of 0.17 V (vs. Ag/AgCl), which are comparable to those of Pt/C (0.04 and 0.15 V vs. Ag/AgCl). The high

current density compared to Pt/C indicated the advantages of its unique open architecture. Highly dispersion of the guest precursors (thiourea, cobalt chloride) inside of MOFs pores contribute to the uniform distribution of the active species within the carbon matrix, which significantly promote the catalytic performance of Co_9S_8@NS-C during ORR. Moreover, the Co_9S_8@NS-C catalyst exhibited outstanding stability with only a slight activity loss (<10%) over 20000s, which ascribe to the graphitic layers coating form in Co_9S_8@NS-C nanocomposite that effectively prevent the catalyst corrosion and thus promise the long-term stability. Later, they constructed a new type of atomically dispersed Fe/N-doped hierarchical carbon architecture, achieving simultaneous optimization of catalysts material in both porosity and surface functionality. [82] The combination of hierarchical pores with the atomically dispersed Fe/N doping species would develop more accessible active sites and facilitate mass diffusion, and thus leading to the enhanced catalytic performance in the resultant materials. Consequently, the resultant catalyst of Fe/N-doped graphitic porous carbon (Fe/N-GPC) with 1.1 wt % Fe and 3.3 wt % N incorporation, achieved the more positive onset potential of -0.01 V, high half-wave potential of -0.13 V (vs. Ag/AgCl), and long-time durability (Figure 2.14b) in alkaline media, which exceed the performance of the Pt/C catalyst, suggesting a superior ORR catalytic activity of Fe/N-GPC. Furthermore, a high ORR catalytic activity of Fe/N-GPC in 0.5 M H_2SO_4 an acid electrolyte was also investigated in this work. The unique morphology and atomically dispersed active sites with a strong synergetic effect enable the MOFs-derived catalyst a highly efficient ORR activity.

Bimetal-MOFs-derived electrocatalysts for ORR

MOFs crystals precursor containing sole transition metal sites typically generate a large amount of metal agglomerations during the high temperature synthesis, which results in low active surface area and limited ORR activity. Designing a bimetal-MOFs simultaneously containing both an active metal (e.g., Co and Fe) and an inactive metal (e.g., Zn and Al) would be more desirable to achieve high surface area and uniform distributed active sites on the skeleton of MOFs matrix.

Bimetal Co/Zn MOFs crystals (ZIF-67/ZIF-8) can be prepared by mixing the Co^{2+} and Zn^{2+} salts together with 2-methylimidazole in the MOFs synthesis (Figure 2.15a). During high temperature pyrolysis, ZIF-8 component yield nitrogen-doped carbon with high surface area,

while ZIF-67 generate Co/N/C active sites which were encapsulated inside the porous carbon. This strategy well integrates the advantages of both ZIF-8 and ZIF-67, which was widely used for designing the conductive nanocarbon support bimetal catalyst NPs. You et al. [83] investigated Co^{2+} and Zn^{2+} in various ratio to synthesis Zn/Co-ZIF bimetal-MOFs, which was used as precursor for producing self-supported Co/N/C nano-polyhedrons as electrocatalyst for ORR. It was revealed that the presence of Zn species not only serve as spatial isolation for Co sites to suppress their sintering during pyrolysis, also promote the high surface area and porosity in the resultant catalysts due to the removal of Zn species. By altering the molar ratio of Zn vs. Co from MOFs precursor, the derived Co NPs size and overall surface area of Co/N/C after pyrolysis can be precisely controlled. An increase of Zn in the MOFs crystals resulted in an increased BET surface area from 270 $m^2 \cdot g^{-1}$ to 2148 $m^2 \cdot g^{-1}$, but decreased graphitization in corresponding catalysts. Due to the balance between surface area, nitrogen content, and dispersed Co/N active sites, the optimal ORR activity was achieved from $Zn_{0.8}Co_{0.2}(MeIM)_2$ framework (80 mol% Zn^{2+}, 20% mol Co^{2+}) yielding a half-wave potential of 0.871 V (30 mV more positive than that of Pt/C, 0.841 V vs. RHE), and a kinetic current density of 39.3 $mA.cm^{-2}$ at 0.80 V (3.1 times that of Pt/C, 12.4 $mA.cm^{-2}$) in 0.1 M KOH (Figure 2.15a). Moreover, this bimetal-MOFs derived Co/N/C also exhibited excellent ORR activity and stability in acidic and neutral electrolytes.
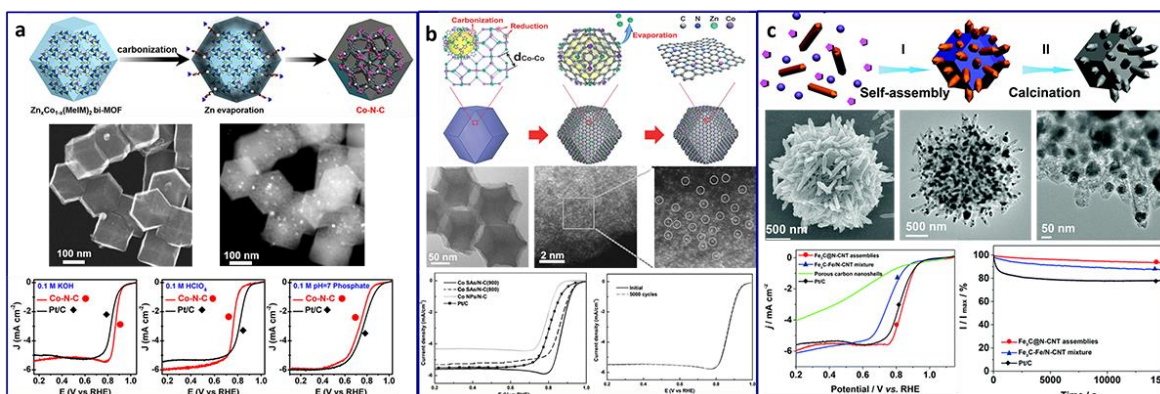
Figure 2.15. (a) Illustration of bi-metal-MOFs self-adjusted synthesis of Co/N/C; SEM and TEM images of Co/N/C derived from bi-metal-MOFs; electrocatalytic ORR performance of Co/N/C and Pt/C in different PH media. [83] American Chemical Society. Copyright 2015 (b) Illustration of the formation of Co SAs/NC; TEM and HAADF-STEM images of Co SAs/NC; ORR polarization curves of Co SAs/NC and

comparative catalysts in O₂-staurated 0.1 M KOH. [84] Wiley-VCH Verlag GmbH & Co. KGaA. Copyright 2016 (c) Schematic illustration of the formation of Fe₃C@NCNT assembly; SEM, TEM images of Fe₃C@NCNT; ORR activity and durability of Fe₃C@NCNT electrocatalyst. Reproduced from [85] Royal Society of Chemistry.

By accurate control the bimetal composition and post-treatment, the active metal size can be down to single atom level, thus enabling the maximum atomic utilization in electrocatalysis. Recently, a similar bi-metal CO/Zn strategy was developed for achieving stable Co single atoms on N-doped porous carbon with high metal atoms loading over 4 wt%. [84] The mechanism of synthesis process is proposed in Figure 2.15b. During the carbonization process, the organic ligands are pyrolyzed into N-doped porous carbon while the metal ions are reduced to Co by the generated carbon. The presence of Zn between the adjacent Co atoms, can effectively prevent the formation of Co-Co bonds under high temperature, which guarantee the highly dispersed Co single atoms. When the molar ratio of Zn/Co is higher than 1:1, Co single atoms/nitrogen-doped porous carbon (Co SAs/NC) can be obtained after the evaporation of Zn. The HRTEM images and EXAFS analysis for Co confirm that there are only highly dispersed atomic Co/N/C sites embedded into porous and graphitized carbon, instead of the formation in inactive metallic aggregates embedded in graphitized carbon. The atomic Co catalyst with remarkably enhanced activity and stability holds a great promise as high-performance next-generation catalyst for PEMFCs.

Besides Zn/Co bimetal MOFs precursor, the dual Zn/Fe-MOFs is another class of precursor for preparing the important Fe/N/C catalyst. Guan and co-workers [85] developed a bimetal-MOFs pyrolysis strategy to obtain iron carbide nanoparticle-embedded N-doped carbon nanotube assembly (Fe₃C@NCNT) as an efficient ORR electrocatalyst (Figure 2.15c). Unlike the conventional single MOFs precursor, the synthetic strategy relies on a composite precursor with two distinct MOFs: iron-based MOFs (MIL-88) nanorods embedded in the Zn-based ZIF-8 host. The introduction of the MIL-88 guests into the ZIF-8 host as co-precursors ensures the homogeneous formation of MIL-88 nanorods and favors the synthesis of small Fe₃C nanocrystals-embedded NCNTs. In addition, the carbonization confined within the carbon matrix derived from organic ligands can effectively alleviate the aggregation of Fe₃C nanocrystals. Combined the merits of uniform dispersed Fe₃C nanocrystals as well as

the porous N-doped carbon matrix, the as-synthesized Fe$_3$C@NCNTs assembly present superior catalytic activity for ORR with 4-electron process in alkaline media. In detail, the half-wave potential of Fe$_3$C@NCNTs assembly exhibit 20 mV positive shift compared to Pt/C, as well as remarkable long-term stability and methanol tolerance.

MOFs/composite-derived electrocatalysts for ORR

Coating the desired MOFs crystals onto functionalized/pre-treated substrate surfaces can provide an alternative avenue for further development of MOFs-derived electrocatalysts. Embedding MOFs nanocrystals onto various novel substrates (e.g. carbon cloth, cellulose aerogel, carbon nanotube, graphene) to construct remarkable active materials with large surface area and good conductivity have been extensively studied and further developed for electrocatalysis. For example, Xia and co-workers [86] developed a graphene aerogel assisted approach to convert bulk Co-based MOFs crystals into monodispersed metal oxide (Co$_3$O$_4$) hollow nanoparticles. In a typical synthesis process, N-doped graphene hydrogel was first prepared, then the Co-MOFs polyhedrons were in situ grown on N-doped graphene sheets by immersing the hydrogel in MOFs precursors, finally the MOFs loaded hydrogel was dried and thermally activated to obtain the Co$_3$O$_4$ hollow NPs-embedded N-doped graphene aerogels (Co$_3$O$_4$/NG-A) (Figure 2.16a). It is interesting to find that the as-obtained Co$_3$O$_4$ NPs with uniform size of 35 nm were successfully dispersed in N-doped graphene aerogels. Also, the Co$_3$O$_4$ NPs with hollow structures display highly defective surface with rich edges and corner sites, which potentially makes the Co$_3$O$_4$/NG-A a novel catalyst. Serve as a new electrocatalyst, the Co$_3$O$_4$/NG-A indicated a high onset potential of 1.019 V (vs. RHE) for ORR, which is much more positive than that of comparative materials. The halfwave potential is almost identical to that of Pt/C. The Co$_3$O$_4$/NG-A catalyst demonstrated the high kinetic current density of 32.5 mA·cm^{-2} at 0.750 V, which is 3.3 times larger than that of the Pt/C catalyst, revealing the higher intrinsic catalytic activity of the Co$_3$O$_4$/NG-A. In addition to the high catalytic activity, Co$_3$O$_4$/NG-A also exhibited remarkable stability for ORR catalysis. Recorded as a more than 82% current retention over 30,000 s of continuous operation at 0.76 V and no negative shift of halfwave potential after 3000 ADT potential cycles.
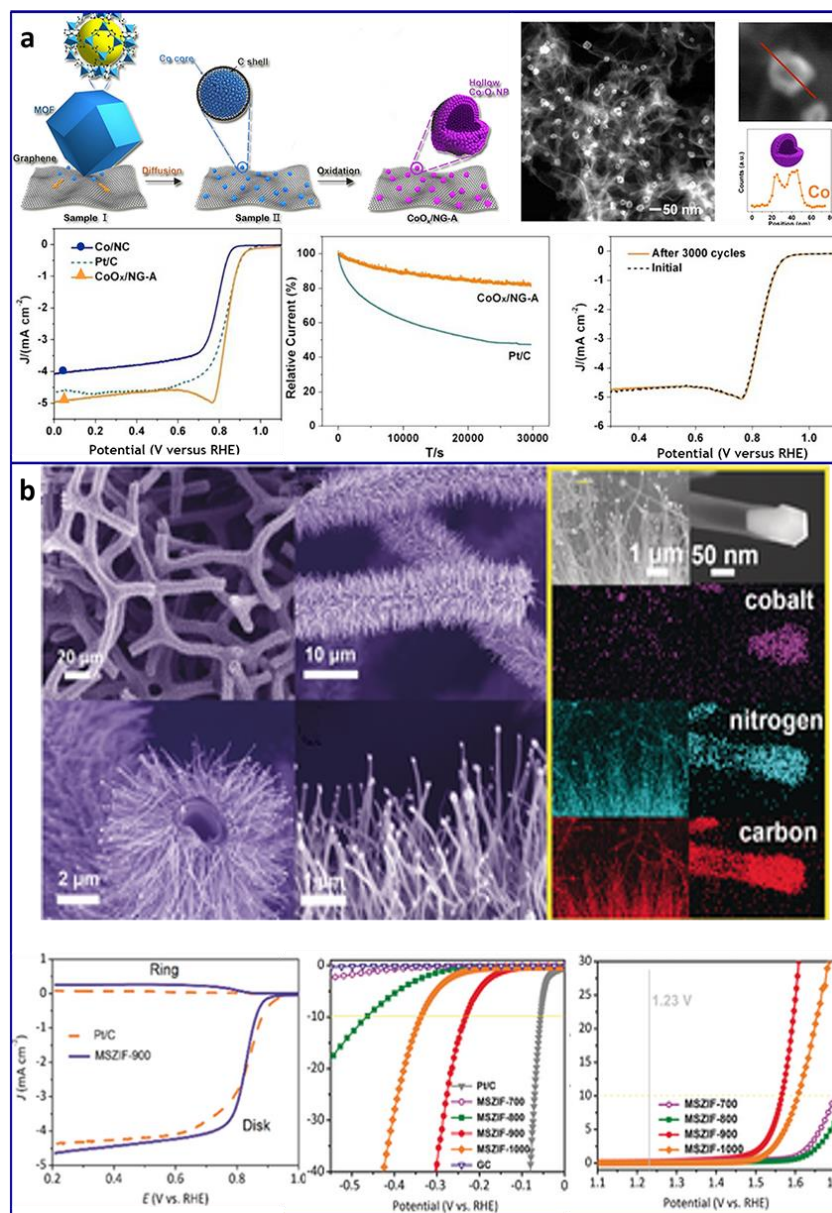
Figure 2.16. (a) Schematic of the formation process of CoOx/NG-A; STEM image of CoOx/NG-A and EDS profile of Co₃O₄ NP; ORR activity and durability of CoOx/NG-A in 0.1 M KOH. [86] American Chemical Society. Copyright 2017. (b) SEM, TEM images and elemental mapping of MSZIF-900; electrochemical performance of the MSZIF-900 catalyst for ORR, HER, OER. [87] Wiley-VCH Verlag GmbH & Co. KGaA. Copyright 2015.

Inspired by the rapid development of MOFs-derived materials in electrocatalysis, an efficient multifunctional catalyst with respectable electrochemical performances suitable for broad

application is undoubtedly needed. Most recently, Jia et al. [87] presented a method for the scalable fabrication of 3D hierarchical architectures by pyrolysis of a ZIF-67 thin film coated 3D macroporous polymeric substrate. HRTEM images indicated the as-prepared melamine sponge-ZIF-900 (MSZIF-900 derived under 900°C) characterized with finely distributed Co NPs located in the apex of ordered NCNTs (Figure 2.16b). X-ray photoelectron spectroscopy (XPS) indicate the well-graphitized carbon layers intimately interact with entrapped Co species, leading to the occurs of electron transfer between NCNTs and Co NPs. In terms of the electrocatalytic performance, MSZIF-900 displays a more positive onset potential (0.91V vs. RHE) and half-wave potential (0.84V vs. RHE) as well as a larger diffusion-limited current density (5.0 mA.cm^{-2}) than the other MOFs-based materials. Together with the remarkable performance in alkaline media, MSZIF-900 demonstrated decent ORR activity in acidic media. The satisfactory performance of the MSZIF-900 catalyst arises from its unique hierarchical structure. The NCNTs provide good conductivity and Co species are active to capture reactants ensuring the rapid mass transport for ORR. Besides the encouraging activity for ORR, MSZIF-900 exhibited an excellent HER activity, as noted by the rapid increase of the cathodic current density at low overpotential, reaching a geometric current density of 10 mA.cm^{-2} at an overpotential of only about 233 mV (Figure 2.16b). In addition to the ORR and HER electrocatalytic activities, the MSZIF-900 catalyst also displayed an impressive performance for OER. In 1.0 M KOH, the MSZIF-900 electrocatalyst exhibited an overpotential of 337 mV to reach a current density of 10 mA·cm^{-2} for OER, reflecting a higher activity than other contrast materials. The density functional theory calculations for the OER mechanism further highlight the synergetic coupling between the cobalt metal and nitrogen-doped carbon in generating a favorable surface electronic environment and consequently promoting the electrochemical performance.

2.4.3 MOFs-derived electrocatalysts for HER

Electrochemical splitting of water into hydrogen and oxygen has been considered as a highly desirable approach to produce hydrogen to store light or electric energy in the form of chemical bonds. The water-splitting reaction can be divided into two half-reactions: the hydrogen evolution reaction (HER; $2H^+ + 2e^- \rightarrow H_2$) and the oxygen evolution reaction (OER, $H_2O \rightarrow 1/2O_2 + 2H^+ + 2e^-$), both of which are crucial for the overall efficiency of

water splitting. Despite of the intense efforts devoted to this field, state-of-the-art HER electrocatalysts still rely on Pt-based materials. Therefore, the search for low-cost non-noble-metal electrocatalysts with high catalytic activity remains a big challenge. To address this issue, it has been found that some MOFs-derived metal/metal compound-carbon exhibit large potential in boosting HER.

Transition metal phosphides have got tremendous attention as attractive catalysts for HER due to appropriate hydrogen adsorption free energy (ΔG H *), high activity and durability. Among the existing myriad of transition metal phosphides, cobalt phosphide (CoP) has been identified as a promising candidate for HER as compared to iron, copper, nickel, and tungsten phosphides. A typical example of using MOFs as a new class of precursors for preparing CoP-based electrocatalysts was reported by Zou et al. [88] In their study, a novel bottom-up strategy for synthesis of CoP NPs encapsulated boron- and nitrogen-co-doped carbon nanotubes (CoP@B/N-CNTs) as HER electrocatalyst was reported. As shown in Figure 2.17a, two key steps were applied for the preparation of CoP@B/N-CNTs, which are based on the pyrolysis and phosphating. ZIF-67-derived Co NPs encapsulated in B/N-CNTs was fabricated first via the pyrolysis process. Then phosphorous acid was used as a second precursor to phosphating of Co@B/N-CNTs and as a result the CoP@B/N-CNTs composite was obtained accompany with Co converted into CoP NPs. The SEM and TEM images depicted that the CoP NPs of 25 nm in size were uniformly distributed inside of B/N-CNTs. As an electrocatalyst for HER, the CoP@B/N-CNTs exhibits large current density of 100 mA.cm^{-2} and low overpotential of 87, 215 and 122 mV in acidic, basic and PBS solution, respectively. Moreover, this novel CoP@B/N-CNTs catalyst shows outstanding stability for more than 8 h at different electrolyte with various PH. The excellent electrocatalytic performance of CoP@B/N-CNTs is attributed to the synergistic structure between the CoP NPs and heteroatom-doped carbon support. The dopants of B/N on the graphitic nanotubes already enlarges the catalytic surface area, when encapsulation of CoP NPs into B/N-CNTs cavity, the novel composite structure will not only produce the high density of active sites to enhance the HER performance, but also prevent the agglomeration of CoP with neighboring NPs which promise the high stability. Afterward, a similar MOFs-routed strategy was also proposed for the preparation of CoP NPs encapsulated in N-doped nanocarbon with ZIF-9 as metal precursor (Figure 2.17b). [89] The as-prepared nanohybrid not only exhibited superior

HER catalytic performance in acid solution but also could behave as an electrocatalyst for HER in alkaline solution with great efficiency and long-term durability. Interestingly, experiments and theoretical calculations reveal that the carbon atoms adjacent to N dopants on the shells of CoP@NC are active sites for hydrogen evolution. Moreover, CoP and N dopants synergistically optimize the binding free energy of H* on the active sites, which results in an outstanding electrocatalytic HER activity.
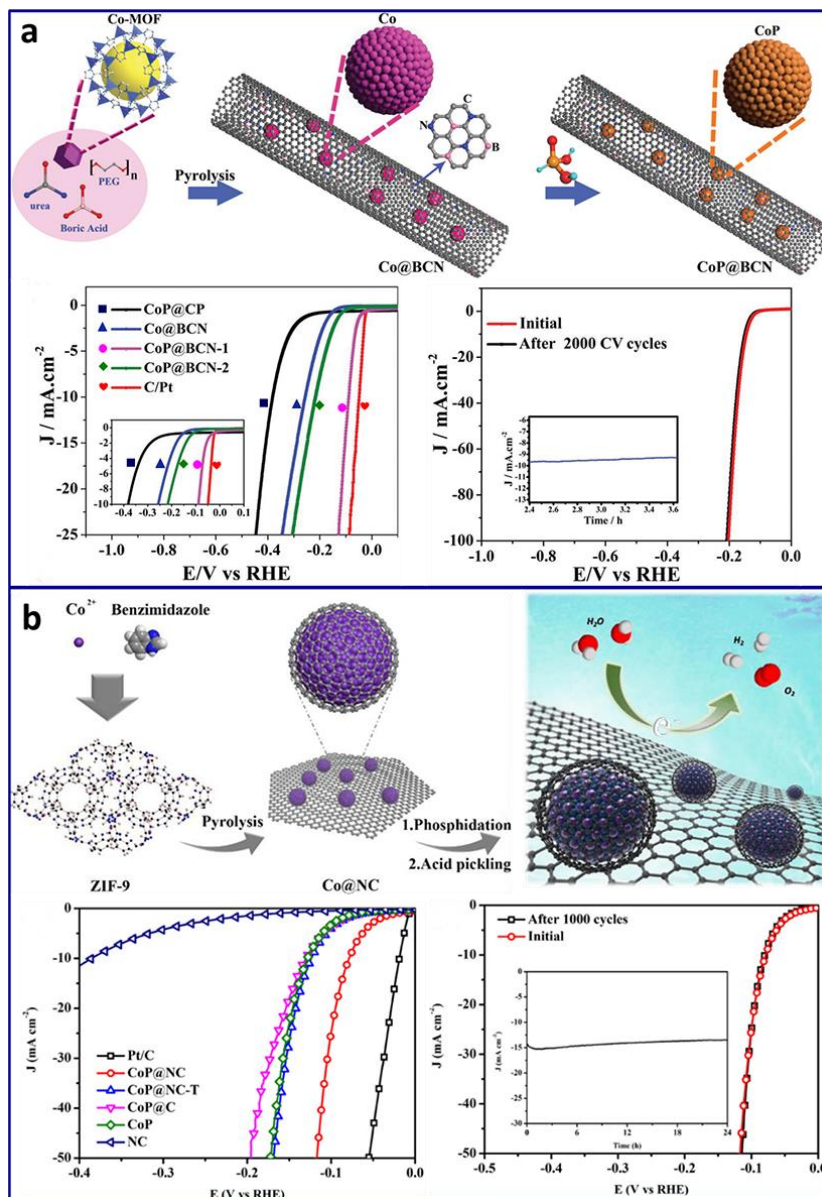
Figure 2.17. (a) Schematic illustration for the fabrication of CoP@BCN nanotubes; TEM image of CoP@BCN nanotubes; HER activity and stability of CoP@BCN

nanotubes in 0.5 M H₂SO₄ solution. [88] Wiley-VCH Verlag GmbH & Co. KGaA. Copyright 2017. (b) Schematic illustration of the synthesis of CoP@NC; HER activity and stability of CoP@NC in 0.5 M H₂SO₄ solution. [89] American Chemical Society. Copyright 2017.

In addition to Co-based electrocatalysts, MOFs-derived other transition metals and compound NPs encapsulated in a carbon matrix were also investigated for HER recently. For example, Wu et al. [90] developed a MOFs-assisted strategy for synthesis of nanostructured MoC_x nano-octahedrons as a highly active electrocatalyst for HER. Starting from a composite precursor consisting of Cu-based MOFs host and Mo-based polyoxometalates guest, mesoporous MoC_x nano-octahedrons are successfully prepared through a pyrolysis and Cu-etching process. Benefiting from the porous and ultrafine nanocrystal structure, the as-proposed MoC_x nano-octahedrons exhibit remarkable electrocatalytic activity performance. Figure 2.18a shows the electrocatalytic activity and durability performance of the MoC_x nano-octahedrons in both acid and basic conditions. In acid media, the MoC_x electrocatalyst shows a small onset potential of 25 mV beyond which the cathodic current increases rapidly. To achieve current densities of 1.0 and 10 mA.cm^{-2}, the MoC_x electrocatalyst requires very low overpotentials of 87 and 142 mV (vs. RHE), respectively. In basic condition, the MoC_x electrocatalyst outperforms the Pt/C catalyst with rapidly rising cathodic current. Small overpotentials of 92 and 151 mV (vs. RHE) are required for the MoC_x nano-octahedrons to drive 1.0 and 10 mA.cm^{-2}, respectively. Additionally, in order to further enhance the conductivity and electrocatalytic activity of MOFs-derived particles, Tang and co-workers [91] incorporated graphene oxide (GO) as an excellent conductive substrate to fabricate a GO supported POMOFs/GO composite. Due to the polyoxometalate (POM) is rich of phosphorous (P) which present opportunity to doping P atoms in the resultant product from POMOFs/GO. As expected, they got the target hybrid material consisting of Mo-oxide, P-doped porous carbon (PC), and reduced graphene oxide (rGO) substrates (MoO_2@PC-rGO) by carefully controlling the pyrolysis of POMOFs/GO precursor (as shown in Figure 2.18b). The MoO_2@PC-rGO nanocomposite displays a remarkable HER activity with small onset potential of about 0 mV, a low Tafel slope of 41 mV.dec^{-1}, a high exchange current density of 4.83 $\times 10^{-4}$ A.cm^{-2}, and long-term stability in acidic media. The superior activity is owing to the synergistic effects among highly

dispersive MoO$_2$ particles, P-doped porous carbon, and conductive rGO substrate. Also, the combination of MoO$_2$ and P-doped carbon both prevents the aggregation of MoO$_2$, and also increases the accessible number of active sites, which is the mainly reason for enabling the outstanding activity and stability performance.
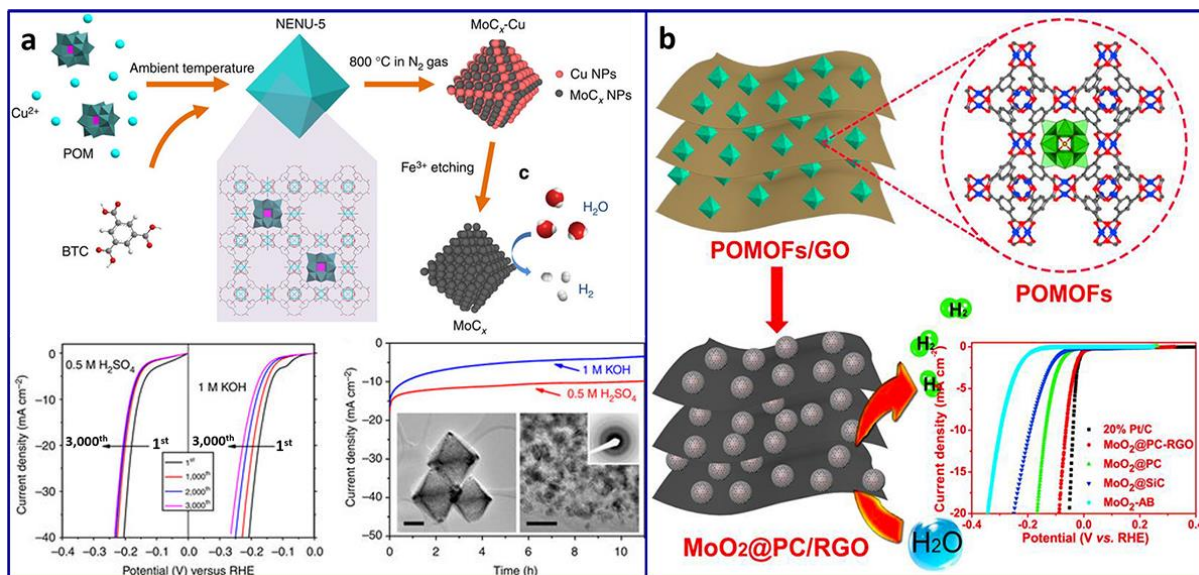
Figure 2.18. (a) Schematic for the synthesis for porous MoCx nano-octahedrons; Polarization HER curves before and after continuous potential sweeps in 0.5 M H$_2$SO$_4$ and 1.0M KOH. [90] Nature Communications. Copyright 2015 (b) Schematic illustration for the preparation of the MoO$_2$@PC-rGO nanocomposite; HER polarization curves of MoO$_2$@PC-RGO and comparative electrocatalysts. [91] Wiley-VCH Verlag GmbH & Co. KGaA. Copyright 2015.

2.4.4   MOFs-derived electrocatalysts for OER

OER is the counterpart of the HER, in which water is oxidized to produce dioxygen. State-of-the-art catalysts for OER are generally based on precious metal oxides such as RuO$_2$, IrO$_2$, which have limited commercial viability due to their low abundance and high cost. Rational tailoring of MOFs precursor has been identified as an efficient method to prepare non-precious metal catalysts for OER. MOFs-derived Co-based OER catalysts have been investigated extensively due to their working capability under varied pH, low cost, higher activity and stability. For example, Wang and co-workers [92] found the direct pyrolysis of ZIF-67 particles under Ar and then H$_2$ atmosphere could afford N-doped carbon nanotube

frameworks (NCNTFs). As observed from Figure 2.19a, the resultant NCNTFs retained the similar size and polyhedral morphology of the initial ZIF-67 particles and possessed hierarchical shells of interconnected crystalline NCNTs. It was demonstrated that the H_2 atmosphere played a critical role in the formation of hollow-structured NCNTs frameworks. Metallic Co NPs are quickly formed in the presence of H_2 atmosphere, followed by the catalytic growth of NCNTs and eventual formation of NCNTFs. With the advanced features of porous and conductive structure, and N-active doping sites, the NCNTFs exhibited higher electrocatalytic activity and stability for OER and ORR than the commercial Pt/C catalyst in alkaline solution. The NCNTFs catalyst obtained at 700 °C exhibit the best OER activity, as it gives a current density of 10 mA.cm^{-2} at a potential of 1.60 V vs. RHE, which compares favorably to Pt/C catalyst (10 mA·cm^{-1}; 1.78 V vs. RHE). Moreover, the durability test demonstrated that the NCNTFs is very stable for the OER, whereas Pt/C exhibits a continuous current loss during the accelerate durability test.
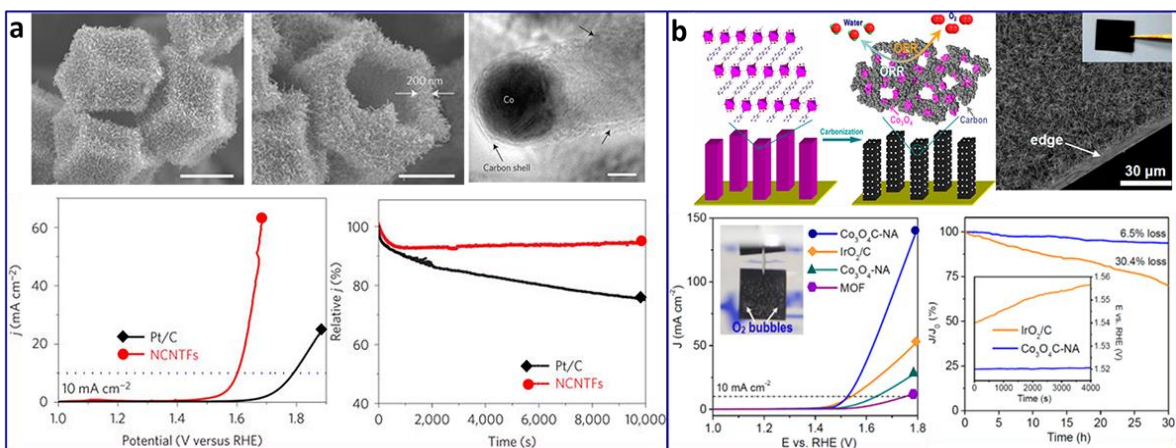
Figure 2.19. (a) SEM and TEM images for structural characterization of NCNTFs; Electrochemical activity and stability of NCNTFs and Pt/C catalysts for OER. [92] Nature Energy. Copyright 2016. (b) Schematic illustration for fabrication of hybrid Co$_3$O$_4$-carbon porous nanowire arrays; SEM image and electrochemical OER activity, stability of Co$_3$O$_4$-carbon. [93] American Chemical Society. Copyright 2014.

Generally, most of the reported OER catalysts were prepared in the forms of thin film or particle agglomerates, which could be coated onto glassy carbon, or other conductive substrates for performance testing. However, these time-consuming coating procedures often resulted in uncontrolled microstructure of the obtained electrodes, featuring limited active

surface area that are disapproving for electron conductivity and mass transport required for driving OER. Recently, Ma and co-workers [93] presented a novel strategy to fabricate an advanced 3D electrode with Co_3O_4 doped-carbon nanowire arrays loaded on Cu foil. As illustrated in Figure 2.19b, the Co-MOFs with a morphology of nanowire was directly grown on Cu foil through a hydrothermal process at 80 °C. Subsequently, the Co-MOFs was converted into Co_3O_4/C composite via carbonization under an N_2 atmosphere, which retained the original nanowire morphology of the parent MOFs with simultaneously generated pores inside. Due to the high surface area of the resulting Co_3O_4/C porous nanowire and the strong interactions between Co_3O_4/C and Cu foil, the obtained Cu foil-supported Co_3O_4/C-nanowire can be used directly as the working electrode for OER without employing extra substrate or binders. In the OER electrochemical test, this novel electrode showed an outstanding activity with a low onset potential of 1.47 V vs. RHE which is comparable to that of 1.45 V for the Cu foil supported-IrO_2/C catalyst, and a stable current density of 10 mA.cm^{-2} at 1.52 V in 0.1 M KOH solution for at least 30 h. The porous nanowire array electrode configuration and the in-situ carbon incorporation lead to enlarged active surface area, strong stability and rapid mass transport. All these features contribute to the excellent OER performance for Co_3O_4/C-nanowire.

It is generally agreed that changing in free energy for OER pathway should be 1.23 V for ideal catalysts. However, under real operating conditions, the binding energies of intermediates (OH*, OOH*) are much larger than the ideal 1.23 V. It was found that ΔG for reaction pathway of OER can be decreased significantly under the presence of coordinated bimetal active centers. [94, 95] By introducing of additional metal species on the Co-MOFs to form a bi-metallic electrocatalyst, the activity and stability of the MOFs-derived bi-metallic materials could be highly enhanced due to the nature of the coordinated bi-metallic center that provides a different type of environment to the species for electrocatalysis. Zhao and colleagues [96] reported the fabrication of ultrathin NiCo bimetal-MOFs sheets featuring with coordinatively unsaturated bi-metal sites. The ~3 nm thick bimetallic NiCo-MOFs nanosheets were prepared through combining the organic ligand (benzenedicarboxylic acid) with Ni^{2+} and Co^{2+} salts in solvent followed by ultrasonication under ambient conditions. After loading NiCo-MOFs onto copper foam electrodes, the Cu foam supported NiCo-MOFs electrocatalyst exhibits an OER overpotential of 189 mV to drive the current density of 10

mA.cm^{-2} in alkaline condition (Figure 2.20). By contrast, RuO$_2$ requires a much higher operating overpotential of 280 mV to achieve the same current density under the same conditions. Moreover, the current density, catalyst morphology, and crystallinity maintain high stability for 200 hours during electrocatalysis measurements. The characterization show evidence that high activity of the NiCo bi-metal catalyst is attributed to the enhanced interaction between water and the Ni^{2+} sites due to electron transfer from the Ni^{2+} sites to the Co^{2+} sites; the less filled orbitals of Co^{2+} compared to those of Ni^{2+} (Co^{2+} = d^7 vs. Ni^{2+} = d^8) can accept electron density from the Ni^{2+} sites. In turn, the oxidized Ni sites can more readily engage in electron transfer from water, thus offering a lower energy barrier for water oxidation. The ability of introducing different metal species into MOFs precursor to design multi-metal-based functional materials, which provides opportunities for incrementally adjusting the catalyst composition, so that the role of each component from MOFs can be well understood in the context of OER.
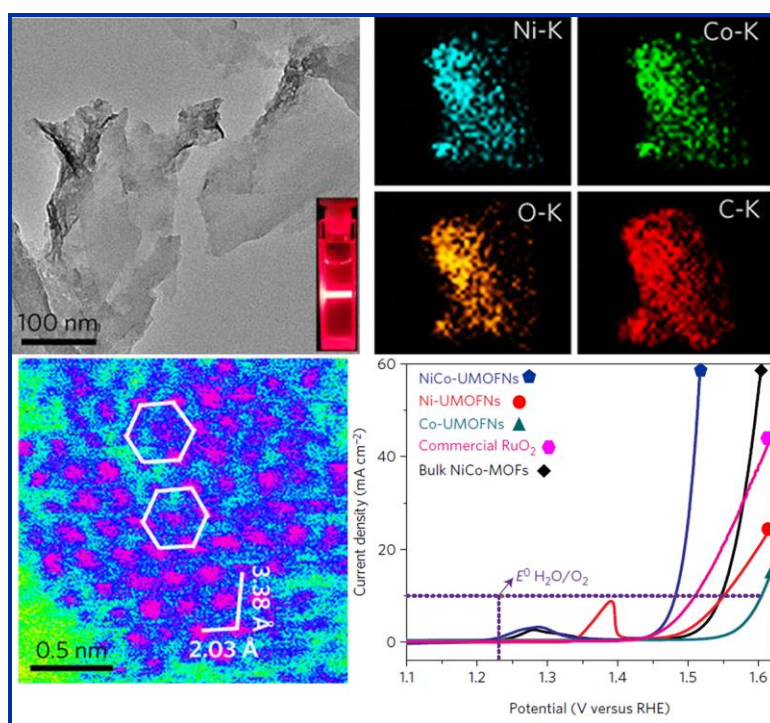
Figure 2.20. TEM and elemental mapping images of NiCo-MOFs; OER electrochemical activity of NiCo-MOFs electrocatalysts. [96] Reprinted by permission from Macmillan Publishers Limited. Nature Energy. Copyright 2016.

2.5   Summary and perspectives

In this chapter, we have summarized the challenges faced by the Pt-based nanoparticle electrocatalysts, focusing on their electrocatalytic activity and stability, and discussed recent promising proposals to design highly durable and active nanostructures effectively. As discussed above, the fabrication of novel stable catalyst support and novel structure/shape of Pt NPs are inevitable for enhancing the long-time stability of Pt catalysts. On the other hand, maximum the Pt atom utilization by develop the single Pt atom catalyst is in highly demand to decrease the cost while enhance the high catalytic activity. Recent candidates have been shown to be very promising; however, delicate analysis, mechanism understanding, and approaches are required for the application of novel catalysts to industrial electrochemical systems. Finally, we briefly suggest and summarize the future perspectives on the next-generation electrocatalyst issues regarding novel catalysts design and analysis.

Oxygen reduction reaction electrocatalysts research has been intensively explored with the strong motivation to obtain valuable solutions for economic and technological challenges faced by the fuel-cell industry. Nevertheless, while hundreds of Pt-based electrocatalysts have been reported to outperform commercial Pt/C under the liquid half-cell condition, only limited cases of the electrocatalysts have been shown to be active or durable in the membrane electrode assembly (MEA) of fuel-cell devices, which indicates a critical limitation in the current research field. Another big issue of a large discrepancy in electrocatalytic activity occurs when electrocatalysts are applied to the MEA scale, especially in the case of intrinsically active electrocatalysts. This discrepancy might originate from the difference in the operating environment; unlike in a liquid half-cell test, a large amount of electrocatalyst is deposited with an ionomer on the polymer electrolyte membrane in MEA. Due to the polymer electrolyte membrane and thick electrode configuration, electrocatalysts in MEA usually suffer from limited transport of protons and oxygen, as well as waterflooding within the cathodic electrode, which are usually neglected under the liquid half-cell condition. However, there have been only a few efforts to correlate these different operating conditions with activity discrepancy. Therefore, more systematic studies need to be organized to clarify the correlation between changes in operating conditions and electrocatalytic properties,

which will set a milestone for bridging a large gap between liquid half-cell studies and MEA-based full-cell device application.

References

[1].   Debe, M.K., Nature, 2012. **486**: p. 43-51.

[2].   Chung, D.Y., J.M. Yoo, and Y.E. Sung, Advanced Materials, 2018. p.1704123.

[3].   Li, L., L. Hu, J. Li, and Z. Wei, Nano Research, 2015. **8**(2): p. 418-440.

[4].   Meier, J.C., C. Galeano, I. Katsounaros, J. Witte, H.J. Bongard, A.A. Topalov, C. Baldizzone, S. Mezzavilla, F. Schüth, and K.J.J. Mayrhofer, Beilstein Journal of Nanotechnology, 2014. **5**: p. 44-67.

[5].   Su, L., W. Jia, C.M. Li, and Y. Lei, ChemSusChem, 2014. **7**(2): p. 361-378.

[6].   Shao, Y., G. Yin, and Y. Gao, Journal of Power Sources, 2007. **171**(2): p. 558-566.

[7].   Gilbert, J.A., N.N. Kariuki, R. Subbaraman, A.J. Kropf, M.C. Smith, E.F. Holby, D. Morgan, and D.J. Myers, Journal of the American Chemical Society, 2012. **134**(36): p. 14823-14833.

[8].   Holby, E.F., W. Sheng, Y. Shao-Horn, and D. Morgan, Energy & Environmental Science, 2009. **2**(8): p. 865-871.

[9].   Yu, C., E.F. Holby, R. Yang, M.F. Toney, D. Morgan, and P. Strasser, ChemCatChem, 2012. **4**(6): p. 766-770.

[10].   Yu, Y., H.L. Xin, R. Hovden, D. Wang, E.D. Rus, J.A. Mundy, D.A. Muller, and H.D. Abruña, Nano Letters, 2012. **12**(9): p. 4417-4423.

[11].   Tuaev, X., S. Rudi, and P. Strasser, Catalysis Science & Technology, 2016. **6**(23): p. 8276-8288.

[12].   Ioroi, T., H. Senoh, S.-i. Yamazaki, Z. Siroma, N. Fujiwara, and K. Yasuda, Journal of the Electrochemical Society, 2008. **155**(4): p. 321-326.

[13]. Parrondo, J., T. Han, E. Niangar, C. Wang, N. Dale, K. Adjemian, and V. Ramani, Proceedings of the National Academy of Sciences, 2014. **111**(1): p. 45-50.

[14]. Poh, C.K., S.H. Lim, J. Lin, and Y.P. Feng, The Journal of Physical Chemistry C, 2014. **118**(25): p. 13525-13538.

[15]. Higgins, D.C., D. Meza, and Z. Chen, The Journal of Physical Chemistry C, 2010. **114**(50): p. 21982-21988.

[16]. Chen, Y., J. Wang, H. Liu, M.N. Banis, R. Li, X. Sun, T.-K. Sham, S. Ye, and S. Knights, The Journal of Physical Chemistry C, 2011. **115**(9): p. 3769-3776.

[17]. Takenaka, S., H. Matsumori, K. Nakagawa, H. Matsune, E. Tanabe, and M. Kishida, The Journal of Physical Chemistry C, 2007. **111**(42): p. 15133-15136.

[18]. Masa, J., A. Bordoloi, M. Muhler, W. Schuhmann, and W. Xia, ChemSusChem, 2012. **5**(3): p. 523-525.

[19]. Banis, M.N., S. Sun, X. Meng, Y. Zhang, Z. Wang, R. Li, M. Cai, T.-K. Sham, and X. Sun, The Journal of Physical Chemistry C, 2013. **117**(30): p. 15457-15467.

[20]. Fujigaya, T. and N. Nakashima, Advanced Materials, 2013. **25**(12): p. 1666-1681.

[21]. Cheng, N., J. Liu, M.N. Banis, D. Geng, R. Li, S. Ye, S. Knights, and X. Sun, International Journal of Hydrogen Energy, 2014. **39**(28): p. 15967-15974.

[22]. Cheng, N., M. Norouzi Banis, J. Liu, A. Riese, S. Mu, R. Li, T.-K. Sham, and X. Sun, Energy & Environmental Science, 2015. **8**(5): p. 1450-1455.

[23]. Chen, C., Y. Kang, Z. Huo, Z. Zhu, W. Huang, H.L. Xin, J.D. Snyder, D. Li, J.A. Herron, M. Mavrikakis, M. Chi, K.L. More, Y. Li, N.M. Markovic, G.A. Somorjai, P. Yang, and V.R. Stamenkovic, Science, 2014. **343**(6177): p. 1339-1343.

[24]. Niu, Z., N. Becknell, Y. Yu, D. Kim, C. Chen, N. Kornienko, G.A. Somorjai, and P. Yang, Nature Materials, 2016. **15**: p. 1188.

[25]. Huang, X., Z. Zhao, L. Cao, Y. Chen, E. Zhu, Z. Lin, M. Li, A. Yan, A. Zettl, Y.M. Wang, X. Duan, T. Mueller, and Y. Huang, Science, 2015. **348**(6240): p. 1230-1234.

[26]. Wu, Y., D. Wang, G. Zhou, R. Yu, C. Chen, and Y. Li, Journal of the American Chemical Society, 2014. **136**(33): p. 11594-11597.

[27]. Park, J., Y.J. Sa, H. Baik, T. Kwon, S.H. Joo, and K. Lee, ACS Nano, 2017. **11**(6): p. 5500-5509.

[28]. Oh, A., H. Baik, D.S. Choi, J.Y. Cheon, B. Kim, H. Kim, S.J. Kwon, S.H. Joo, Y. Jung, and K. Lee, ACS Nano, 2015. **9**(3): p. 2856-2867.

[29]. Zhang, L., L.T. Roling, X. Wang, M. Vara, M. Chi, J. Liu, S.-I. Choi, J. Park, J.A. Herron, Z. Xie, M. Mavrikakis, and Y. Xia, Science, 2015. **349**(6246): p. 412-416.

[30]. Li, M., Z. Zhao, T. Cheng, A. Fortunelli, C.-Y. Chen, R. Yu, Q. Zhang, L. Gu, B.V. Merinov, Z. Lin, E. Zhu, T. Yu, Q. Jia, J. Guo, L. Zhang, W.A. Goddard, Y. Huang, and X. Duan, Science, 2016. **354**(6318): p. 1414-1419.

[31]. Mao, J., W. Chen, D. He, J. Wan, J. Pei, J. Dong, Y. Wang, P. An, Z. Jin, W. Xing, H. Tang, Z. Zhuang, X. Liang, Y. Huang, G. Zhou, L. Wang, D. Wang, and Y. Li, Science Advances, 2017. **3**(8): p.1603068.

[32]. Jiang, K., D. Zhao, S. Guo, X. Zhang, X. Zhu, J. Guo, G. Lu, and X. Huang, Science Advances, 2017. **3**(2): p.1601705.

[33]. Bu, L., S. Guo, X. Zhang, X. Shen, D. Su, G. Lu, X. Zhu, J. Yao, J. Guo, and X. Huang, Nature Communications, 2016. **7**: p. 11850.

[34]. Chung, D.Y., S.W. Jun, G. Yoon, S.G. Kwon, D.Y. Shin, P. Seo, J.M. Yoo, H. Shin, Y.-H. Chung, H. Kim, B.S. Mun, K.-S. Lee, N.-S. Lee, S.J. Yoo, D.-H. Lim, K. Kang, Y.-E. Sung, and T. Hyeon, Journal of the American Chemical Society, 2015. **137**(49): p. 15478-15485.

[35]. Cheng, N., M.N. Banis, J. Liu, A. Riese, X. Li, R. Li, S. Ye, S. Knights, and X. Sun, Advanced Materials, 2015. **27**(2): p. 277-281.

[36]. Qiao, B., A. Wang, X. Yang, L.F. Allard, Z. Jiang, Y. Cui, J. Liu, J. Li, and T. Zhang, Nature Chemistry, 2011. **3**: p. 634.

[37]. Fang, X., Q. Shang, Y. Wang, L. Jiao, T. Yao, Y. Li, Q. Zhang, Y. Luo, and H.-L. Jiang, Advanced Materials, 2018. **30**(7): p. 1705112.

[38]. Cheng, K., Z. Kou, J. Zhang, M. Jiang, H. Wu, L. Hu, X. Yang, M. Pan, and S. Mu, Journal of Materials Chemistry A, 2015. **3**(26): p. 14007-14014.

[39]. Jones, J., H. Xiong, A.T. DeLaRiva, E.J. Peterson, H. Pham, S.R. Challa, G. Qi, S. Oh, M.H. Wiebenga, X.I. Pereira Hernández, Y. Wang, and A.K. Datye, Science, 2016. **353**(6295): p. 150-154.

[40]. Liu, L., D.N. Zakharov, R. Arenal, P. Concepcion, E.A. Stach, and A. Corma, Nature Communications, 2018. **9**(1): p. 574.

[41]. Sun, S., G. Zhang, N. Gauquelin, N. Chen, J. Zhou, S. Yang, W. Chen, X. Meng, D. Geng, and M.N. Banis, Scientific reports, 2013. **3**: p. 1775.

[42]. Cheng, N., S. Stambula, D. Wang, M.N. Banis, J. Liu, A. Riese, B. Xiao, R. Li, T.-K. Sham, and L.-M. Liu, Nature communications, 2016. **7**: p. 13638.

[43]. Yang, S., J. Kim, Y.J. Tak, A. Soon, and H. Lee, Angewandte Chemie International Edition, 2016. **55**(6): p. 2058-2062.

[44]. Yang, S., Y.J. Tak, J. Kim, A. Soon, and H. Lee, ACS Catalysis, 2017. **7**(2): p. 1301-1307.

[45]. Deng, J., H. Li, J. Xiao, Y. Tu, D. Deng, H. Yang, H. Tian, J. Li, P. Ren, and X. Bao, Energy & Environmental Science, 2015. **8**(5): p. 1594-1601.

[46]. Lin, J., A. Wang, B. Qiao, X. Liu, X. Yang, X. Wang, J. Liang, J. Li, J. Liu, and T. Zhang, Journal of the American Chemical Society, 2013. **135**(41): p. 15314-15317.

[47]. Wei, H., X. Liu, A. Wang, L. Zhang, B. Qiao, X. Yang, Y. Huang, S. Miao, J. Liu, and T. Zhang, Nature Communications, 2014. **5**: p. 5634.

[48]. Liu, J., M. Jiao, L. Lu, H.M. Barkholtz, Y. Li, Y. Wang, L. Jiang, Z. Wu, D.-j. Liu, L. Zhuang, C. Ma, J. Zeng, B. Zhang, D. Su, P. Song, W. Xing, W. Xu, Y. Wang, Z. Jiang, and G. Sun, Nature Communications, 2017. **8**: p. 15938.

[49]. Zhou, T., Y. Du, A. Borgna, J. Hong, Y. Wang, J. Han, W. Zhang, and R. Xu, Energy & Environmental Science, 2013. **6**(11): p. 3229-3234.

[50]. Sawano, T., Z. Lin, D. Boures, B. An, C. Wang, and W. Lin, Journal of the American Chemical Society, 2016. **138**(31): p. 9783-9786.

[51]. Zhang, H., J. Wei, J. Dong, G. Liu, L. Shi, P. An, G. Zhao, J. Kong, X. Wang, X. Meng, J. Zhang, and J. Ye, Angewandte Chemie, 2016. **128**(46): p. 14522-14526.

[52]. Chen, Y.-Z., R. Zhang, L. Jiao, and H.-L. Jiang, Coordination Chemistry Reviews, 2018. **362**: p. 1-23.

[53]. Zitolo, A., V. Goellner, V. Armel, M.-T. Sougrati, T. Mineva, L. Stievano, E. Fonda, and F. Jaouen, Nature Materials, 2015. **14**: p. 937.

[54]. Zhang, H., S. Hwang, M. Wang, Z. Feng, S. Karakalos, L. Luo, Z. Qiao, X. Xie, C. Wang, D. Su, Y. Shao, and G. Wu, Journal of the American Chemical Society, 2017. **139**(40): p. 14143-14149.

[55]. Wang, X., H. Zhang, H. Lin, S. Gupta, C. Wang, Z. Tao, H. Fu, T. Wang, J. Zheng, G. Wu, and X. Li, Nano Energy, 2016. **25**: p. 110-119.

[56]. Yi, J.-D., R. Xu, Q. Wu, T. Zhang, K.-T. Zang, J. Luo, Y.-L. Liang, Y.-B. Huang, and R. Cao, ACS Energy Letters, 2018. **3**(4): p. 883-889.

[57]. McCarty, J.G., K.H. Lau, and D.L. Hildenbrand, *Vaporization-Assisted Degradation of High Temperature Combustion Catalysts*, in *Studies in Surface Science and Catalysis*, C.H. Bartholomew and G.A. Fuentes, Editors. 1997, Elsevier. p. 601-607.

[58]. Kwak, J.H., J. Hu, D. Mei, C.-W. Yi, D.H. Kim, C.H.F. Peden, L.F. Allard, and J. Szanyi, Science, 2009. **325**(5948): p. 1670-1673.

[59]. Li, W.-Z., L. Kovarik, D. Mei, J. Liu, Y. Wang, and C.H.F. Peden, Nature Communications, 2013. **4**: p. 2481.

[60]. Detavernier, C., J. Dendooven, S. Pulinthanathu Sree, K.F. Ludwig, and J.A. Martens, Chemical Society Reviews, 2011. **40**(11): p. 5242-5253.

[61]. O'Neill, B.J., D.H.K. Jackson, J. Lee, C. Canlas, P.C. Stair, C.L. Marshall, J.W. Elam, T.F. Kuech, J.A. Dumesic, and G.W. Huber, ACS Catalysis, 2015. **5**(3): p. 1804-1825.

[62]. Choi, C.H., M. Kim, H.C. Kwon, S.J. Cho, S. Yun, H.-T. Kim, K.J.J. Mayrhofer, H. Kim, and M. Choi, Nature Communications, 2016. **7**: p. 10922.

[63]. Wang, C., X.-K. Gu, H. Yan, Y. Lin, J. Li, D. Liu, W.-X. Li, and J. Lu, ACS Catalysis, 2017. **7**(1): p. 887-891.

[64]. Yan, H., H. Cheng, H. Yi, Y. Lin, T. Yao, C. Wang, J. Li, S. Wei, and J. Lu, Journal of the American Chemical Society, 2015. **137**(33): p. 10484-10487.

[65]. Lu, J., K.-B. Low, Y. Lei, J.A. Libera, A. Nicholls, P.C. Stair, and J.W. Elam, Nature Communications, 2014. **5**: p. 3264.

[66]. Li, H., L. Wang, Y. Dai, Z. Pu, Z. Lao, Y. Chen, M. Wang, X. Zheng, J. Zhu, W. Zhang, R. Si, C. Ma, and J. Zeng, Nature Nanotechnology, 2018. **13**: p.411-417.

[67]. Barkholtz, H.M. and D.-J. Liu, Materials Horizons, 2017. **4**(1): p. 20-37.

[68]. Cao, X., C. Tan, M. Sindoro, and H. Zhang, Chemical Society Reviews, 2017. **46**(10): p. 2660-2677.

[69]. Chaikittisilp, W., K. Ariga, and Y. Yamauchi, Journal of Materials Chemistry A, 2013. **1**(1): p. 14-19.

[70]. Liu, P., J. Chen, and N. Zheng, Chinese Journal of Catalysis, 2017. **38**(9): p. 1574-1580.

[71]. Chen, Y., Z. Huang, X. Gu, Z. Ma, J. Chen, and X. Tang, Chinese Journal of Catalysis, 2017. **38**(9): p. 1588-1596.

[72]. Guan, B.Y., X.Y. Yu, H.B. Wu, and X.W. Lou, Advanced Materials, 2017. **29**: p. 1703614.

[73]. Liang, Z., C. Qu, D. Xia, R. Zou, and Q. Xu, Angewandte Chemie, 2018. **57**: p. 9604-9633.

[74]. Bosch, M., S. Yuan, W. Rutledge, and H.-C. Zhou, Accounts of Chemical Research, 2017. **50**(4): p. 857-865.

[75]. Huang, Y.-B., J. Liang, X.-S. Wang, and R. Cao, Chemical Society Reviews, 2017. **46**(1): p. 126-157.

[76]. Kitao, T., Y. Zhang, S. Kitagawa, B. Wang, and T. Uemura, Chemical Society Reviews, 2017. **46**(11): p. 3108-3133.

[77]. Kaneti, Y.V., J. Tang, R.R. Salunkhe, X. Jiang, A. Yu, K.C.W. Wu, and Y. Yamauchi, Advanced Materials, 2017. **29**(12): p. 1604898.

[78]. Mahmood, A., W. Guo, H. Tabassum, and R. Zou, Advanced Energy Materials, 2016. **6**(17): p. 1600423.

[79]. Zhang, H., J. Nai, L. Yu, and X.W.D. Lou, Joule, 2017. **1**(1): p. 77-107.

[80]. Ma, S., G.A. Goenaga, A.V. Call, and D.J. Liu, Chemistry-A European Journal, 2011. **17**(7): p. 2063-2067.

[81]. Zhu, Q.-L., W. Xia, T. Akita, R. Zou, and Q. Xu, Advanced Materials, 2016. **28**(30): p. 6391-6398.

[82]. Zhu, Q.-L., W. Xia, L.-R. Zheng, R. Zou, Z. Liu, and Q. Xu, ACS Energy Letters, 2017. **2**(2): p. 504-511.

[83]. You, B., N. Jiang, M. Sheng, W.S. Drisdell, J. Yano, and Y. Sun, ACS Catalysis, 2015. **5**(12): p. 7068-7076.

[84]. Yin, P., T. Yao, Y. Wu, L. Zheng, Y. Lin, W. Liu, H. Ju, J. Zhu, X. Hong, and Z. Deng, Angewandte Chemie International Edition, 2016. **55**(36): p. 10800-10805.

[85]. Guan, B.Y., L. Yu, and X.W. Lou, Energy & Environmental Science, 2016. **9**(10): p. 3092-3096.

[86]. Xia, W., C. Qu, Z. Liang, B. Zhao, S. Dai, B. Qiu, Y. Jiao, Q. Zhang, X. Huang, and W. Guo, Nano Letters, 2017. **17**(5): p. 2788-2795.

[87]. Niancai, C., B.M. Norouzi, L. Jian, R. Adam, L. Xia, L. Ruying, Y. Siyu, K. Shanna, and S. Xueliang, Advanced Materials, 2015. **27**(2): p. 277-281.

[88]. Tabassum, H., W. Guo, W. Meng, A. Mahmood, R. Zhao, Q. Wang, and R. Zou, Advanced Energy Materials, 2017. **7**(9): p. 1601671.

[89]. Yang, F., Y. Chen, G. Cheng, S. Chen, and W. Luo, ACS Catalysis, 2017. **7**(6): p. 3824-3831.

[90]. Wu, H.B., B.Y. Xia, L. Yu, X.-Y. Yu, and X.W. Lou, Nature Communications, 2015. **6**: p. 6512.

[91]. Tang, Y.J., M.R. Gao, C.H. Liu, S.L. Li, H.L. Jiang, Y.Q. Lan, M. Han, and S.H. Yu, Angewandte Chemie International Edition, 2015. **54**(44): p. 12928-12932.

[92]. Xia, B.Y., Y. Yan, N. Li, H.B. Wu, X.W.D. Lou, and X. Wang, Nature Energy, 2016. **1**: p. 15006.

[93]. Ma, T.Y., S. Dai, M. Jaroniec, and S.Z. Qiao, Journal of the American Chemical Society, 2014. **136**(39): p. 13925-13931.

[94]. Guan, C., X. Liu, W. Ren, X. Li, C. Cheng, and J. Wang, Advanced Energy Materials, 2017. **7**(12): p. 1602391.

[95].   Duan, J., S. Chen, and C. Zhao, Nature Communications, 2017. **8**: p. 15341.

[96].   Khattak, A.M., N.A. Khan, Z. Wei, J. Zhang, S. Liu, H. Zhao, and Z. Tang, 2016. **1**: Nature Energy, p.16184.

Chapter 3

3 Experiment and Characterizations

In this chapter, the synthetic approaches of nanomaterials such as transition metal oxide, nitride, and noble metal catalysts are described. Moreover, the physical and electrochemical characterizations of these nanomaterials are involved here.

3.1 Experiment

3.1.1 Atomic layer deposition of tantalum oxide on carbon support

The atomic layer deposition (ALD) of tantalum oxide (Ta_2O_5) on Vulcan XC-72 carbon black was carried out in an ALD system (Savannah 100, Cambridge Nanotechnology Inc., USA) at 225 °C using tantalum(V) ethoxide ($Ta(OC_2H_5)_5$) and H_2O as precursors, and N_2 as the carrier gas, as shown in Figure 3.1. One ALD cycle consists of the following six steps: (1) 0.5 s pulse of $Ta(OC_2H_5)_5$ to ALD chamber for reaction with substrate materials; (2) a 3.0 s extended exposure to $Ta(OC_2H_5)_5$ in the reaction chamber; (3) a purging time of 16 s to pulse out the extra $Ta(OC_2H_5)_5$ precursor; (4) 1.0 s pulse of H_2O; (5) a 3.0 s extended exposure to H_2O in the reaction chamber; (6) 25 s purging time to pulse out the extra H_2O.[1, 2] Based on ALD mechanism, there is a linear relationship between the Ta_2O_5 particle size and the ALD cycle number. The growth rate of Ta_2O_5 nanoparticle is 0.5 Å per cycle, much close to that reported in another literature study. [3] This confirms that Ta_2O_5 was synthesized through an ALD process.

Figure 3.1. Savannah 100 ALD system (Cambridge Nanotech, USA)

3.1.2 Nitrogen-doping of tantalum oxide prepared by ALD

To further investigate N-doping effect of metal oxide on Pt catalyst activity and durability, the N-doped ALDTa$_2$O$_5$/C was prepared by post-treatment of ALDTa$_2$O$_5$/C with NH$_3$/Ar (1:10) under 700°C for 1h in a tube furnace. [4] After cooling down to room temperature, the N-doped Ta$_2$O$_5$ NPs were achieved with a highly dispersion on carbon support.

3.1.3 Atomic layer deposition of Pt on PEMFCs anode

The porous carbon coating layers with carbon black and Nafion binder coated on PTFE film, which supplied as the substrate for Pt deposition, were provided by Ballard power system company. Pt was deposited on the carbon layers by ALD method (Cambridge nanotechnology Inc., USA) using Trimethyl-(methylcyclopentadienyl)-platinum(IV) (MeCpPtMe$_3$) and O$_2$ as precursors as shown in Figure 3.2. High-purity N$_2$ was used as both purging gas and carrier gas. [5, 6] The carbon/PTFE coats with size around 10cm x 10cm was placed in ALD chamber. The deposition temperature is 250°C, while the bubbler of MeCpPtMe$_3$ was kept at 65°C to provide a steady-state flux of MeCpPtMe$_3$ vapor. Gas lines were hold at 100 °C to avoid precursor condensation. For each ALD cycle, 1.0 s of the MeCpPtMe$_3$ pulse and 5.0 s of the O$_2$ pulse were separated by a 20 s N$_2$ purge. By applying the ALD cycles

of 50, 30 and 20, the Pt NPs catalyst with controlled loading of 0.035, 0.02, 0.01 mg·cm^{-2} were prepared on carbon support, respectively.
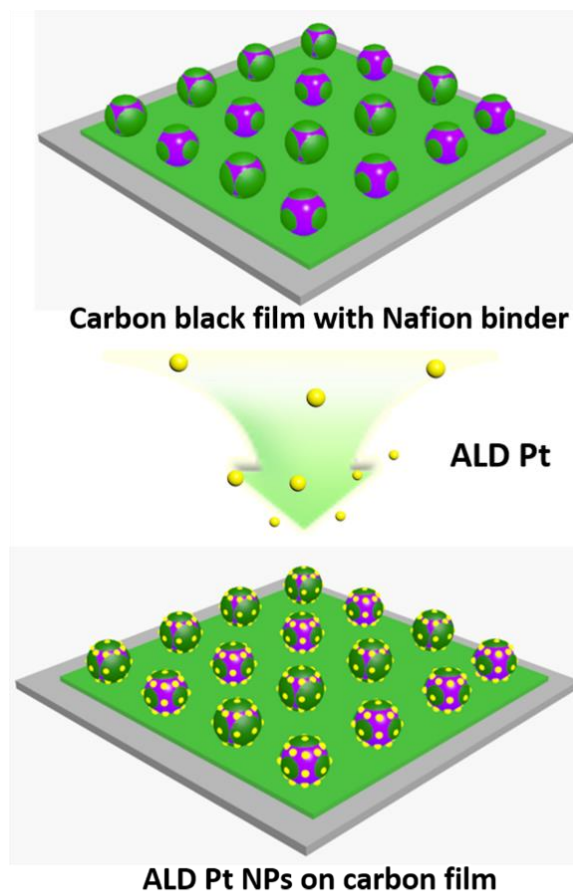
Figure 3.2. Schematic illustration of ALD Pt on carbon black film electrode.

3.1.4   Synthesis of MOFs-derived nanocarbon

Synthesis of ZIF-8 crystals was conducted following the procedure outlined by J. Cravillon. [7] In a typical experiment, two solutions were initially prepared by dissolving a known quantity of 2-methylimidazole (6.78 g, 82.0 mmol) in 250 ml of methanol and $Zn(NO_3)$ ·$6H_2O$ (6.15 g, 20.5 mmol) in 250 ml of methanol. The solution of $Zn(NO_3)$ ·$6H_2O$ was then added to 2-methylimidazole in a dropwise manner. The resulting mixture was stirred for 1h and aged for 24h at room temperature. Subsequently, white powder (ZIF-8 crystals) were collected by centrifugation and washed several times with methanol to remove the excess reactants. After dried in a vacuum at 60°C, the as-prepared ZIF-8 powder was carbonized at

1000°C for 8 h in Ar to produce N-doped nanocarbon (ZIF-C). Then, the as-prepared ZIF-C was treated with NH$_3$/Ar (10:100) for different time at 1000°C to control pore size and further N-doping, such as 3 min, 5 min, 7 min. The corresponding products were denoted as NH$_3$-C-3, NH$_3$-C-5, NH$_3$-C-7. To synthesis N, S co-doped nanocarbon, 20 mg of NH$_3$-C-7 was mixed with 300 mg of thiourea (w/w=1:15) in 5 ml of ethanol/water (v/v=4:1) to generate a suspension under sonication. The mixture was continuously stirred for 3h to facilitate a thiourea/NH$_3$-C-7 solid composite. Thiourea/NH$_3$-C-7 mixture was heated at 900°C for 1 h under Ar atmosphere to generate the N, S-co-doped nanocarbon denoted as N, S-NH$_3$-C-7 (Figure 3.3).
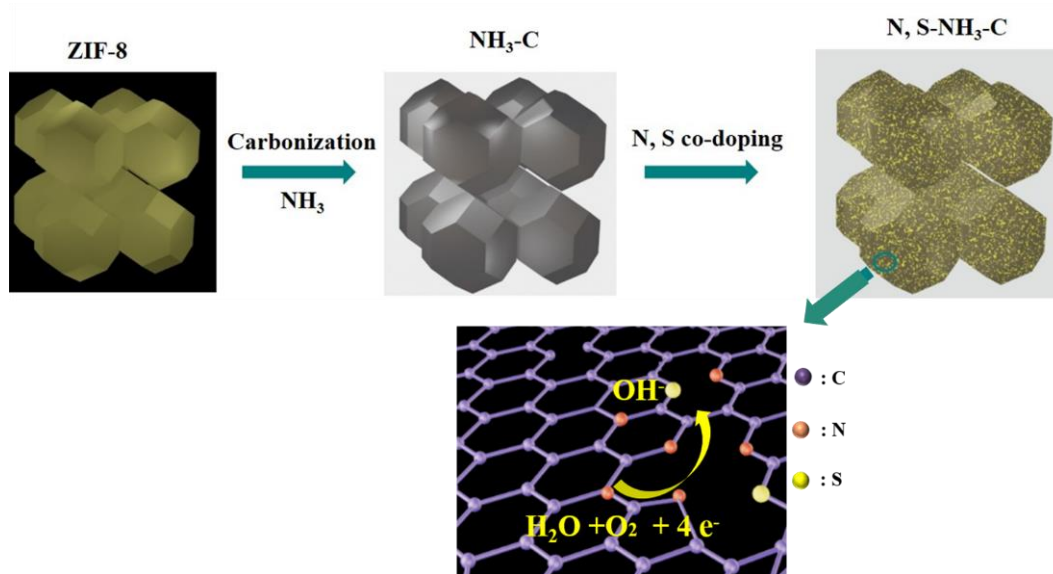
Figure 3.3. Schematic illustration of the fabrication of the MOFs-derived N, S-co-doped nanocarbon.

3.2 Characterizations

The morphology structure, chemical environment, functional groups information and crystalline property of the as-prepared materials are characterized using a variety of techniques including scanning electron microscopy (SEM), energy dispersive X-ray spectroscopy (EDS), high resolution transmission electron microscopy (HRTEM), electron energy loss spectroscopy (EELS), High-angle annular dark-field scanning transmission electron microscopy (HAADF-STEM), X-photoelectron spectroscopy (XPS), X-ray diffraction (XRD), Ramn spectroscopy, surface area analysis, X-ray

absorption spectroscopy (XAS). This section briefly reviews these physical and electrochemical techniques applied for materials characterization in this thesis.

3.2.1   Physical characterizations

The morphology of the materials is observed using Hitachi S-4800 field emission scanning electron microscopy (FE-SEM) operated at 5 kV as shown in Figure 3.4. The EDS/EDX equipped with FE-SEM is carried out to determine the element composition and distribution.

Figure 3.4. Field emission scanning electron microscope (Hitachi S-4800).

The morphology and microstructures of ALD metal or metal oxide nanoparticles are characterized by using high-resolution transmission electron microscopy (HRTEM, JEOL 2010FE) equipped with EDS and electron energy loss spectrometer (EELS). The HADDF-STEM images are conducted on an aberration-corrected FEI Titan Cubed 80-300 keV microscope (as shown in Figure 3.5) equipped with a monochromator, hexapole-based aberration corrector in both the probe and imaging lenses, which are used to study the atomic level structure of single atoms catalyst.
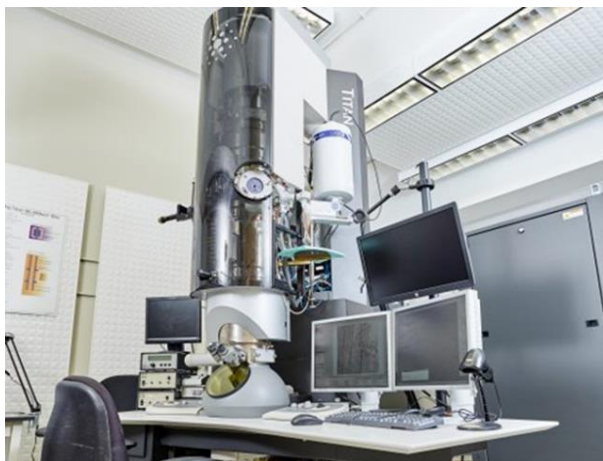
Figure 3.5. FEI Titan Cubed 80-300 kV high resolution transmission electron microscope.

To understand the chemical information of elements through detecting the number of unoccupied electrons from the surface of samples at certain binding energy, XPS measurement is conducted on a Kratos AXIS Ultra Spectrometer, the equipment is shown in Figure 3.6.

Figure 3.6. A Krato AXIS Ultra Spectrometer XPS.

XRD patterns are recorded using a Bruker D8-Advance diffractometer equipped with a Cu K_α radiation source, as shown in Figure 3.7 a. Raman spectra are performed on a HORIBA

Scientific LabRAM research Raman spectrometer using a laser excitation wavelength of 532.0 nm (Figure 3.7 b).
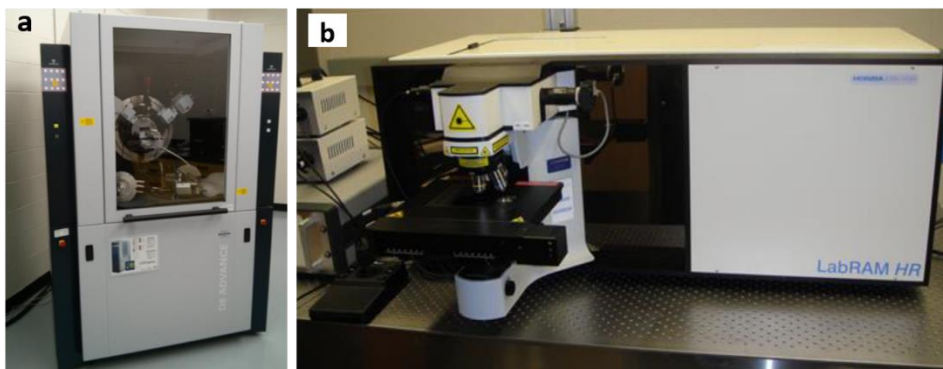
Figure 3.7. (a) Bruker D8 Advance Diffractometer XRD. (b) HORIBA Scientific LabRAM research Raman spectroscopy.

The nitrogen absorption-desorption isotherms are measured using the equipment of Micromeritics Tristar II, as shown in Figure 3.8. The total specific surface area is calculated from the Brunauer-Emmett-Teller (BET) equation. The mesopore size distribution is determined by the Barrett–Joyner–Halenda (BJH) method from the adsorption isotherms. The micropore area and volume are obtained from a t-plot method.

Figure 3.8. Micromeritics TriStar II 3020 Surface Area and Pore Size Analyzer

X-ray adsorption near edge structure (XANES) measurement at the Pt L_3-edge (11564 eV) and L_2-edge (13273 eV) are performed on the 061D superconducting wiggler sourced hard X-ray microanalysis (HXMA) beamline at the Canadian Light Source. The spectra are collected in fluorescence yield mode using a 32 Ge solid-state detector, and the spectra of high purity metal Pt foil are collected in transmission mode for comparison and mono energy calibration.

3.2.2   Electrochemical characterizations

The electrochemical characterizations of the catalysts are conducted in a standard three-electrode electrochemical cell using a glassy carbon (GC) rotating disk electrode (RDE) (Figure 3.10 a) setup on an Autolab potentiostat/galvanostat (Model, PGSTAT-30, Ecochemie, Brinkman Instruments) with rotation control (Pine Instruments) (Figure 3.10 b). A Pt wire is used as the counter electrode and a reversible hydrogen electrode (RHE) as a reference electrode. The thin film working electrode is prepared as follows: the catalyst ink is prepared by mixing 5 mg of catalyst powder in 5 mL ethanol and 50 μL of 5 wt % Nanfion solution, followed by ultrasonication to make the catalyst dispersion. Subsequently, the catalyst suspension is pipetted onto the GC substrate followed with dry in air to form a uniform thin film electrode.

The electrochemical measurements are carried out in 0.1 M $HClO_4$ electrolyte using a Pt wire as the counter electrode and a reversible hydrogen electrode (RHE) as a reference electrode. Each electrode is activated by cycling from 0.05 to 1.1 V at 50 mV·s^{-1} in N_2-saturated 0.1 M $HClO_4$ until no changes were observed in the cyclic voltammetry curves (CV curves). CV curves were recorded by scanning from 0.05 V to 1.1 V at 50 mV·s^{-1} in N_2. O_2 was then bubbled for 30 min to achieve an O_2-saturated electrolyte. Oxygen reduction reaction (ORR) linear sweep voltammetry (LSV, 10 50 mV·s^{-1}) was conducted in O_2-saturated 0.1M $HClO_4$ on the RDE system with a rotation speed of 1600 rpm. The CV curves obtained under N_2 were subtracted from the CV curves obtained under O_2 to remove the non-Faradaic current. The electrochemically active surface area (ECSA) was calculated by integrating the area of the CV curves in the hydrogen underpotential deposition (HUPD) region and using the charge value of 210 mC·cm^{-2} corresponding to a monolayer adsorption of hydrogen atoms on a polycrystalline Pt catalyst. To investigate the impact of potential cycling on catalyst

degradation, the aging protocols of accelerated durability tests (ADTs) are performed. PEMFC load-cycling protocol, where the electrode potential was modulated with a triangle wave from 0.6 to 1.0 V vs. RHE at a scan rate of 50 mV·s^{-1} in a N$_2$-saturated 0.1 M HClO$_4$ electrolyte. A total of 10 000 cycles were performed in the "degradation cell" and intermediate characterizations were recorded to monitor the ECSA and mass activity losses.
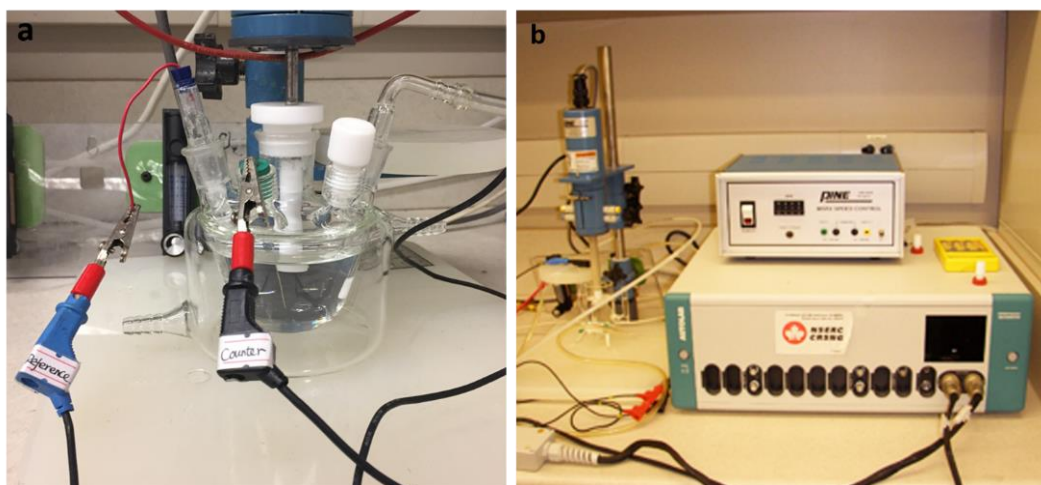
Figure 3.9. (a) three-electrode electrochemical cell. (b) Autolab potentiostat equipped with rotating controller.

3.2.3 Membrane electrode assembly fabrication and single fuel cell test

The MEA with an active area of 45 cm^2 is fabricated by a catalyst-coated membrane (CCM) method in Ballard Power System Inc. Prior to fabricating the CCM and MEA, a homogeneous catalyst ink is prepared by mixing the catalyst powder, Nafion (10 wt%) and ultrapure water. The as-prepared ink is coated on a Nafion® 211 membrane (25 mm thickness, DuPont Co.) and dried in air at room temperature. Then the anode catalyst layer is decal transferred onto the other side of the Nafion® 211 membrane by hot-pressing. Finally, the CCM is sandwiched between two gas diffusion layers using the Kapton frame with an active area of 45 cm^2. For MEA performance evaluation, the operating conditions are 75°C, 136 kPa, and 100% relative humidity (RH). Prior to testing, MEA conditioning is performed at the current density of 1.3 A·cm^{-2} for 16 h, at 75°C,136 kPa, and 100% RH. MEA durability testing is performed at 80°C, 136 kPa, loaded with a square wave and stepped

potential cycling of 0.6 V and 1.0 V holding 30 s at each potential. Then potential cycles are conducted on MEA and intermediate air polarization curves are recorded to monitor the cell voltage and performance loss.

References

[1]. Liu, J., M.N. Banis, X. Li, A. Lushington, M. Cai, R. Li, T.-K. Sham, and X. Sun, The Journal of Physical Chemistry C, 2013. **117**(39): p. 20260-20267.

[2]. Song, Z., B. Wang, N. Cheng, L. Yang, D. Banham, R. Li, S. Ye, and X. Sun, Journal of Materials Chemistry A, 2017. **5**(20): p. 9760-9767.

[3]. Kukli, K., M. Ritala, and M. Leskelä, Journal of the Electrochemical Society, 1995. **142**(5): p. 1670-1675.

[4]. Zhang, M., P. Hou, Z. Wang, and P. Kang, ChemElectroChem, 2018. **5**(5): p. 799-804.

[5]. Sun, S., G. Zhang, N. Gauquelin, N. Chen, J. Zhou, S. Yang, W. Chen, X. Meng, D. Geng, and M.N. Banis, Scientific reports, 2013. **3**: p. 1775.

[6]. Cheng, N., S. Stambula, D. Wang, M.N. Banis, J. Liu, A. Riese, B. Xiao, R. Li, T.-K. Sham, and L.-M. Liu, Nature communications, 2016. **7**: p. 13638.

[7]. Cravillon, J., R. Nayuk, S. Springer, A. Feldhoff, K. Huber, and M. Wiebcke, Chemistry of Materials, 2011. **23**(8): p. 2130-2141.

Chapter 4

4 Atomic layer deposited tantalum oxide to anchor Pt/C for a highly stable catalyst in PEMFCs

Tantalum oxide (TaOx) nanoparticles (NPs) are deposited on a commercial Pt/C catalyst by an area-selective atomic layer deposition (ALD) approach to enhance the stability of the catalyst in proton exchange membrane fuel cells (PEMFCs). Due to the application of a blocking agent for protecting the Pt surface, TaOx particles are selectively nucleated and grown around Pt NPs. The TaOx loading on the Pt/C surface could be controlled precisely by varying the number of ALD cycles. When deposited on the Pt/C surface with 35 ALD cycles, the TaOx-anchored Pt NPs formed an excellent triple-junction structure of TaOx–Pt–carbon. The electrochemical durability tests indicated that the TaOx-anchored Pt/C catalyst showed comparable catalytic activity and superior long-term stability to Pt/C. Moreover, the long-term stability test in membrane electrode assembly (MEA) indicated a very low power density loss (12%) after a 120h accelerated durability test. The significantly enhanced catalyst stability during PEMFCs operation is due to the anchoring effect of TaOx via strong metal oxide–support interactions. This strategy shows great potential for developing highly stable catalysts for PEMFCs.

4.1 Introduction

Fuel cells, especially proton exchange membrane fuel cells (PEMFCs), are considered as a new energy technology with potential applications in power demanding areas such as electronic vehicles, automobiles and distributed stationary power sources.[1–3] As a crucial component of PEMFCs, Pt-based catalysts are used to catalyze chemical reactions in PEMFCs (hydrogen oxidation at the anode and oxygen reduction at the cathode) for promoting electrochemical energy conversion.[4–9] However, the high cost and poor durability of Pt catalysts severely hamper the practical commercialization of such electrochemical devices.[10,11] This is because the catalysts must survive thousands of load

cycles over the lifetime of PEMFC operation under harsh conditions, such as high temperature and potential, low pH, and oxygen atmosphere.[12,13] In such an environment, Pt catalysts undergo significant degradation and performance loss due to Pt nanoparticles (NPs) dissolution, migration/coalescence, Ostwald ripening and detachment from the carbon support. Therefore, improving the durability of Pt catalysts has been one of the most important issues.

In order to overcome the durability problems, numerous research efforts have been made to enhance the stability of Pt catalysts by endowing Pt NPs with new morphologies (e.g. nanowires, nanotubes, and nanodendrites),[14–19] integrating Pt with other transition metals (Pt/M core–shell, alloy and nanoframe structures),[7,20–22] or developing durable catalyst supports with high corrosion-resistance and strong catalyst–support interactions (Pt–NGR, Pt–NCNTs, Pt–ZrC, Pt–CeO2).[9,23–26] Recently, anchoring Pt NPs on carbon supports by means of polymers,[27–29] ultrathin carbon layers,[30] or inorganic materials [31–33] to fabricate immobilized Pt catalysts has shown to be a promising method for stabilizing Pt NPs. There have also been several reports about loading metal oxides on Pt catalysts to improve their activity and durability.[31,34,35] Group IV and V compounds based on the elements Zr, Nb and Ta, mainly nitrides and oxides, have been used as ORR catalysts, owing to their high chemical stability in an acidic environment.[36,37] TaOx received considerable attention as alloying additives that enhance the activity and durability for various catalysts.[38] For instance, Bonakdarpour et al. found that Ta addition markedly enhances the durability and reduces the dissolution of Pt in the sputtered Pt/Ta alloy ORR catalyst by forming a thin Ta_2O_5 passivation layer.[39] Kazunari Domen et al.[40–43] reported that the ultrafine designed TaOx NPs, by electrodeposition as an electrocatalyst for ORR, showed excellent catalytic activity. Recently, Takeo Ohsaka et al. [44] demonstrated a unique structure of TaOx-capped Pt NPs on a Pt/TaOx/GC electrocatalyst. It was found that the amorphous TaOx of the Pt/TaOx/GC electrocatalyst caused enhancement of ORR activity and durability, which was due to the spillover effect and the strong interaction between Pt and TaOx. However, the methods used in these reports have several limitations, such as the loading amount of TaOx, local control and the synthesis yields of catalysts for practical PEMFC applications. Another challenge is to design and optimize the metal oxide–Pt structure without reducing the catalyst electrochemical surface area. In order to address the

stability issues of Pt catalysts in PEMFCs, atomic layer deposition (ALD) is gaining increasing attention as a technique for preparing noble metals or metal oxides, because of its advantages in developing ultrathin films and uniformly distributed particles in a sub-nanometer controllable growth process. [45–48] ALD processes are self-limiting surface reactions. Thus, the surface functional groups can be manipulated prior to ALD to carry out an area-selective ALD process. [49,50] For an area-selective ALD method, the desirable material can be deposited where needed without blocking the surface of the catalysts. For instance, N. Cheng et al. [51] demonstrated an area-selective ALD approach to stabilize Pt NPs using ALD zirconia nanocages. The Pt NPs catalyst encapsulated in zirconia nanocages exhibited much more stability than Pt–carbon nanotubes without zirconia nanocages.

In this study, we propose a facile area-selective ALD approach to stabilize the Pt/C catalyst through fabricating TaOx-anchored Pt NPs with the triple-junction structure of Pt–TaOx–C. By introducing a protective agent (oleylamine) to the Pt surface, TaOx NPs were selectively nucleated and grown around Pt NPs and formed TaOx anchored-Pt NPs on the carbon surface. The electrochemical durability tests indicated that the 35ALD–TaOx–Pt/C catalyst exhibited superior durability compared to Pt/C. The enhanced stability of the 35ALD–TaOx–Pt/C catalyst is attributed to the anchoring effect of TaOx via the strong triple-junction of TaOx–Pt–C, which plays a significant role in stabilizing the Pt catalyst by preventing Pt NPs from migration/coalescence and detachment from the carbon support.

4.2   Experimental

4.2.1   Area-selective ALD of TaOx on the Pt/C catalyst

100 mg of the commercial Pt/C catalyst (Tanaka Kikinzoku Kogyo TEC10E50E, with 50 wt% Pt on high surface area carbon black) was suspended in 50 ml ethanol solution and sonicated for 30 min. The dispersed Pt/C solution and 2 ml oleylamine were mixed and then stirred for 5 h. After filtration, washing, and drying under vacuum, oleylamine modified Pt/C (denoted as OA–Pt/C) was obtained. The area-selective deposition of TaOx on OA–Pt/C was carried out in an ALD reactor (Savannah 100, Cambridge Nanotechnology Inc., USA) at 225 °C using tantalum(V) ethoxide ($Ta(OC_2H_5)_5$) and H_2O as precursors, and N_2 as the carrier gas. [52] The prepared sample will be designated as TaOx–OA–Pt/C, hereafter. One ALD

cycle consists of the following six steps: (1) 0.5 s pulse of $Ta(OC_2H_5)_5$; (2) a 3.0 s extended exposure to $Ta(OC_2H_5)_5$ in the reaction chamber; (3) a purging time of 16 s; (4) 1.0 s pulse of H_2O; (5) a 3.0 s extended exposure to H_2O in the reaction chamber; (6) 25 s purging time. As reported in our previous work, [52] there is a linear relationship between the LiTaOx film thickness and TaOx subcycle number. The growth per cycle of TaOx deposition is 0.5 Å per cycle, much close to that (0.4 Å per cycle) reported in another literature study. [53] This confirms that TaOx was synthesized by an ALD process. The TaOx loading on Pt/C was accurately controlled by the number of ALD cycles. After ALD processes, the oleylamine in TaOx–OA–Pt/C samples was removed by heating at 700 °C in an Ar/H_2 atmosphere for 1 h, and the final catalyst is denoted as ALD–TaOx–Pt/C. In this work, samples of 15ALD–TaOx–Pt/C, 35ALD–TaOx–Pt/C, and 50ALD–TaOx–Pt/C loaded with 15, 35, and 50 ALD cycles of TaOx were prepared, and the TaOx loading was 7.8 wt%, 10.2 wt% and 13.5 wt%, tested by energy dispersive X-ray spectroscopy (EDS), respectively. To investigate the TaOx particle size, the 35ALD–TaOx–CB sample with 35 ALD cycles of TaOx on carbon black was also prepared.

4.2.2   Physical characterization

The morphology and microstructures of samples were characterized by using high-resolution TEM (HRTEM, JEOL 2010FEG) and scanning transmission electron microscopy (STEM) with energy dispersive X-ray spectroscopy (EDS). X-ray diffraction (XRD) patterns were collected on a Bruker D8 Advance diffractometer using Cu Ka radiation at 40 kV and 40 mA. The chemical compositions of TaOx were investigated by X-ray photoelectron spectroscopy (XPS, Kratos Axis Ultra-spectrometer).

4.2.3   Electrochemical characterization

The electrochemical characterizations were conducted in a three-compartment electrochemical cell using a rotating-disk electrode (RDE) setup with an Autolab electrochemistry station and rotation control (Pine Instruments). Catalyst inks were prepared by mixing 3 mg of the catalyst, 3 mL of an 80:20 (wt/wt) mixture of ethanol to ultra-pure H_2O, and 30 µL of Nafion (5 wt%). The mixture was then sonicated to ensure good dispersion and wetting of the catalyst. 20 µL of the catalyst ink was deposited onto a polished

glassy carbon electrode (Pine, AFE5T050AUHT, 5.0 mm dia.) and allowed to dry at room temperature. All electrochemical measurements were carried out in 0.1 M $HClO_4$ electrolyte using a Pt wire as the counter electrode and a reversible hydrogen electrode (RHE) as a reference electrode. All potentials reported henceforth are vs. RHE. Each electrode was activated by cycling from 0.05 to 1.1 V at 50 $mV \cdot s^{-1}$ in N_2-saturated 0.1 M $HClO_4$ until no changes were observed in the cyclic voltammetry curves (CV curves). CV curves were recorded by scanning from 0.05 V to 1.1 V at 50 $mV \cdot s^{-1}$ in N_2. O_2 was then bubbled for 30 min to achieve an O_2-saturated electrolyte. Oxygen reduction reaction (ORR) linear sweep voltammetry (LSV, 10 $mV \cdot s^{-1}$) was conducted in O_2-saturated 0.1M $HClO_4$ on the RDE system with a rotation speed of 1600 rpm. The CV curves obtained under N_2 were subtracted from the CV curves obtained under O_2 to remove the non-Faradaic current. The electrochemically active surface area (ECSA) was calculated by integrating the area of the CV curves in the hydrogen underpotential deposition (HUPD) region and using the charge value of 210 $mC \cdot cm^{-2}$ corresponding to a monolayer adsorption of hydrogen atoms on a polycrystalline Pt catalyst. [54] To investigate the impact of potential cycling on catalyst degradation, two aging protocols of accelerated durability tests (ADTs) were performed. (i) PEMFC load-cycling protocol, where the electrode potential was modulated with a triangle wave from 0.6 to 1.0 V vs. RHE at a scan rate of 50 $mV \cdot s^{-1}$ in a N_2-saturated 0.1 M $HClO_4$ electrolyte. A total of 10 000 cycles were performed in the "degradation cell" and intermediate characterizations were recorded to monitor the ECSA and mass activity losses. (ii) A start-up/shutdown ADT protocol, where the electrode potential was cycled with a triangle wave from 1.0 V to 1.6 V vs. RHE with a scan rate of 100 $mV \cdot s^{-1}$ in a N_2-saturated 0.1 M $HClO_4$ electrolyte. A total of 6000 cycles were performed and intermediate characterizations were recorded to monitor the ECSA and mass activity losses. [55]

4.2.4   Membrane electrode assembly (MEA) fabrication and single fuel cell testing

The fuel cell performance of the 35ALD–TaOx–Pt/C catalyst as a cathode was tested in a single cell system. The MEA with an active area of 45 cm^2 was fabricated by a catalyst-coated membrane (CCM) method. Prior to fabricating the CCM and MEA, a homogeneous catalyst ink was prepared by mixing the 35ALD–TaOx–Pt/C catalyst, Nafion (10 wt%) and ultrapure water. The as-prepared ink was coated on a Nafion® 211 membrane (25 mm

thickness, DuPont Co.) and dried in air at room temperature. Then the anode catalyst layer was decal transferred onto the other side of the Nafion® 211 membrane by hot-pressing. Finally, the CCM was sandwiched between two carbon paper of gas diffusion layers (GDLs) using the Kapton frame with an active area of 45 cm^2. Pt loadings at the anode/cathode side are 0.1/0.15 mg·cm^{-2}, respectively. For MEA performance evaluation, the operating conditions were 75°C, 136 kPa, and 100% relative humidity (RH). Prior to testing, MEA conditioning was performed at the current density of 1.3 A·cm^{-2} for 16 h, at 75°C,136 kPa, and 100% RH. MEA durability testing was performed at 80°C, 136 kPa, loaded with a square wave and stepped potential cycling of 0.6 V and 1.0 V holding 30 s at each potential. A total of 4700 cycles (around 120 h) were performed on MEA and intermediate air polarization curves were recorded to monitor the cell voltage and peak power density losses.

4.3   Results and discussion

Structural characterization

Figure 4.1 demonstrates a facile approach to construct anchored Pt NPs by area-selective deposition of TaOx on the commercial Pt/C catalyst. Due to the application of a blocking agent (oleylamine) for protecting the Pt surface, TaOx particles were selectively grown beside the Pt NPs and formed TaOx-anchored Pt NPs supported on the surface of carbon. The construction of TaOx anchors with triple junctions of TaOx–Pt–C was intended to enhance the catalyst durability while not reducing the activity. To investigate the potential trade-off between durability enhancement and activity loss, ALD cycles of 15, 35, and 50 were evaluated to generate protective TaOx anchors with a progressively increasing amount on the Pt/C matrix.
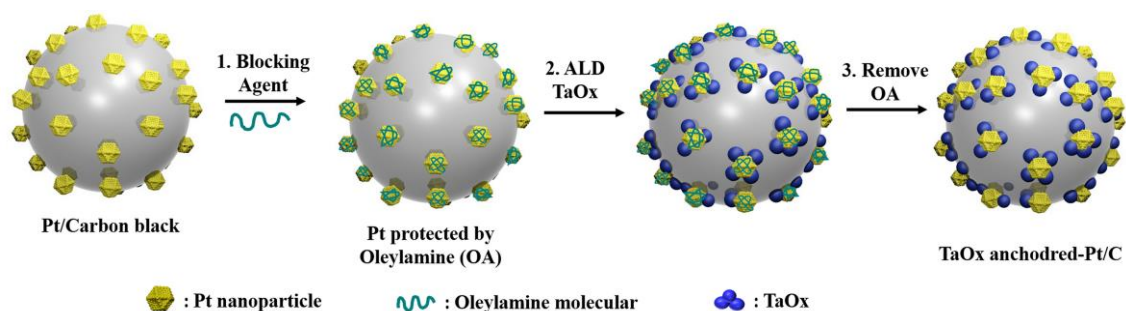
Figure 4.1. Schematic illustrations of TaOx-anchored Pt NPs via area-selective atomic layer deposition (ALD).

The morphology and structure of the as-prepared ALD–TaOx–Pt/C catalysts were characterized by using HRTEM. HRTEM images in Figure 4.2(a)–(c) indicate that the TaOx nanoparticles were successfully deposited on the surface of Pt/C. Increasing the number of ALD cycles leads to high TaOx coverage on the Pt/C matrix. After 15 ALD cycles (Figure 4.2(a) and SI4.1†), only 7.8 wt% TaOx could be deposited on the surface of Pt/C (based on EDS), and the resulting particles were too small to be viewed by HRTEM, while with 35 ALD cycles of TaOx deposition, the increased TaOx loading (10.2 wt%) led to a larger coverage area of TaOx on the Pt/C surface compared to 15ALD–TaOx–Pt/C. Fig. S4.2 shows that TaOx particles with an average particle size of 2.7±0.5 nm could be uniformly distributed on the carbon support. The STEM image and line scan spectra in Fig. 4.1(e) and (f) also indicate that the TaOx nanoparticles are finely dispersed on Pt/C and appear to be deposited adjacent to the Pt. With continuously increasing the ALD cycles to 50, the TaOx coating tended to form an over-coated thin layer on the Pt/ C catalyst (Fig. 4.2(c)). This densely packed TaOx layer would result in a large decrease of the active surface and thus negatively impact the activity. Therefore, it can be found that the ALD technology can be used to adjust the coverage and particle size of TaOx to optimize the hybrid structure.
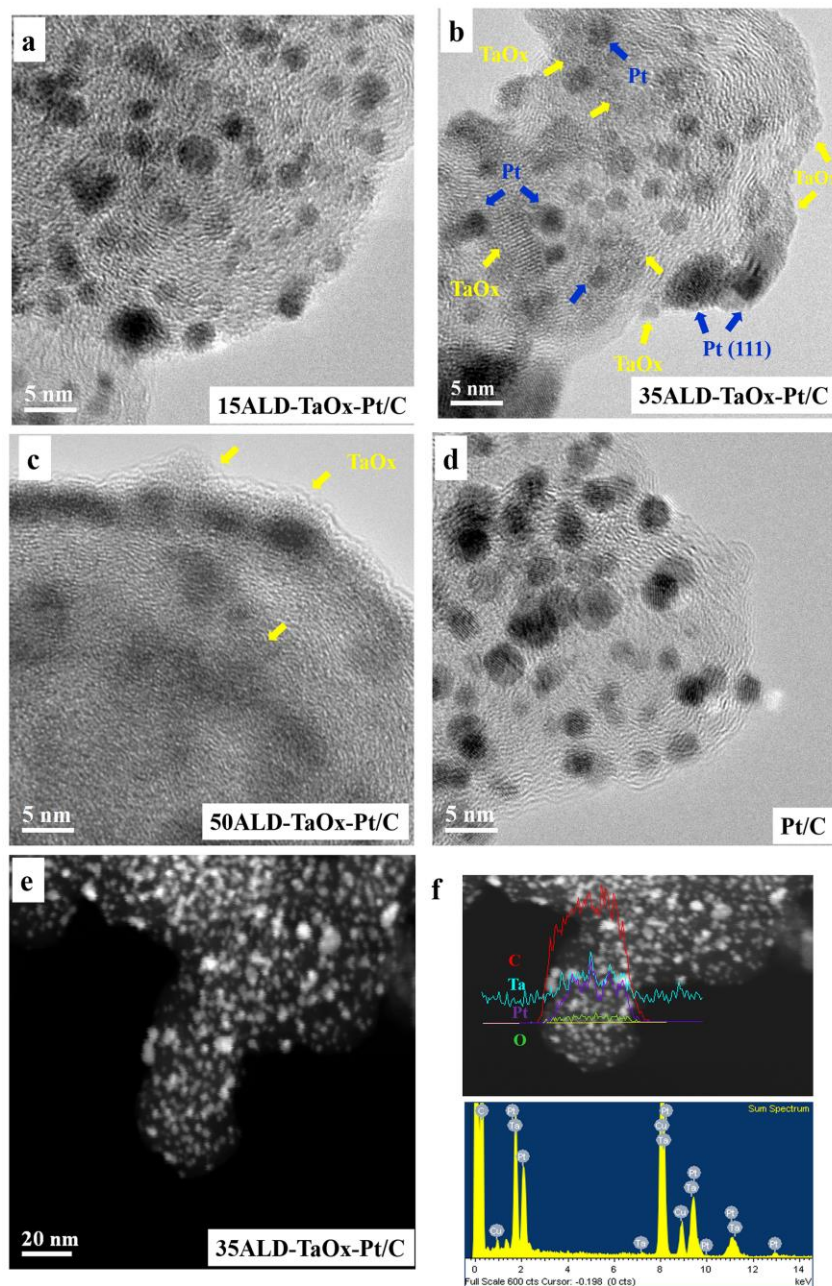
Figure 4.2. (a–d) HRTEM images of different catalysts: (a) 15ALD–TaOx–Pt/ C, (b) 35ALD–TaOx–Pt/C, (c) 50ALD–TaOx–Pt/C and (d) Pt/C (e and f) STEM image and STEM line scan spectra of the 35ALD–TaOx–Pt/C catalyst.

To examine the chemical species in the catalyst, XPS measurements were employed to study the composition of TaOx deposited by ALD, and the results for 35ALD–TaOx–Pt/C are displayed in Fig. 4.3. The XPS survey in Fig. 4.3(a) indicates the presence of Pt, Ta, O and C elements in the 35ALD–TaOx–Pt/C catalyst. Fig. 4.3(b) illustrates the chemical environment

of the Ta element by analyzing the Ta 4f spectrum. A couple of peaks located at binding energies of 28.5±0.1 and 26.7±0.1 eV is observed. These peaks are attributed to the responses of Ta 4f5/2 and Ta 4f7/2, respectively, belonging to the most stable Ta_2O_5 species. The other pair of Ta 4f5/2 and Ta 4f7/2 located at lower binding energies of 25.6±0.1 and 23.7±0.1 eV, respectively, is assigned as the TaO species. This result indicates that the Ta element in TaOx exists in two types of chemical environments, i.e., Ta_2O_5 and TaO, which consists of 96.3% and 3.7%, respectively. The dominant Ta_2O_5 species obviously resulted from the ALD of $Ta(OEt)_5$ and H_2O precursors. In the case of TaO, it could be expected that the oxygen can dissociate on the surface of Ta_2O_5 during high temperature annealing and thus result in the formation of a small amount of reduced TaOx species.
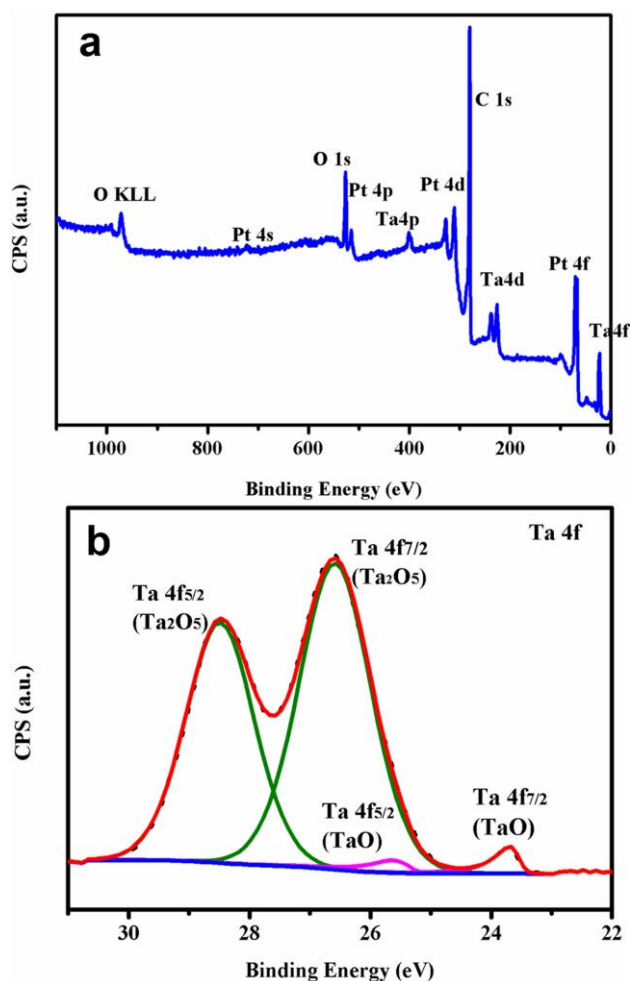
Figure 4.3. (a) XPS spectra of survey scan and (b) Ta 4f XPS spectra obtained for 35ALD–TaOx–Pt/C.

Electrocatalytic activity and durability

To determine the anchoring effect of TaOx on the Pt/C catalyst, the electrochemical durability of the ALD–TaOx–Pt/C catalysts was tested. The durability tests were performed by continuous triangle potential cycling between 0.6 V and 1.0 V (vs. RHE) in N_2-purged 0.10 M $HClO_4$ for 10 000 cycles to mimic the load-cycling experience during PEMFC operation. Fig. 4.4 illustrates the representative CV curves and ORR polarization curves recorded before and after ADT-10 000 for ALD–TaOx–Pt/C and Pt/C catalysts. With continuous potential cycling, the CV curves of the Pt/C catalyst exhibited a pronounced reduction of total charge in the hydrogen underpotential deposition (HUPD) region, indicative of a reduction in Pt active surface area. The peak currents drop significantly with potential cycling, indicating severe catalyst degradation and activity loss of Pt/C. The losses of ECSA for different catalysts with the cycling numbers are plotted in Fig. 4.4(c) (the initial ECSA of Pt/C is considered as the baseline to calculate the normalized ECSA%) and the corresponding ECSA values at typical cycling numbers are summarized in Table SI4.1. As can be seen, the Pt/C catalyst experienced a significant ECSA decrease following the ADT (from 68.8 to 48.4 $m^2 \cdot g^{-1}$ $_{Pt}$ shown in Table SI4.1†), losing 30% of its initial ECSA after ADT-10 000. The 15ALD–TaOx–Pt/C catalyst demonstrates a slower degradation trend, losing 24.6% of its initial ECSA after ADT-10 000. While a small benefit in durability was observed for the 15ALD–TaOx–Pt/C catalyst, the low coverage of the TaOx anchors resulted in only limited improvement over the baseline. Conversely, the 35ALD–TaOx–Pt/C catalyst shows an increased ECSA in the first 1000 cycles (from 60.6 up to 64.7 $m^2 \cdot g^{-1}$ $_{Pt}$), followed by a slight decrease to 62.7 $m^2 \cdot g^{-1}$ $_{Pt}$ after ADT-10 000 (with only 9.0% ECSA loss compared to the initial ECSA of Pt/C). These results reveal the superior durability of 35ALD–TaOx–Pt/C compared to Pt/C and 15ALD–TaOx–Pt/C catalysts. The increased ECSA in the initial ADT process suggests that a small percentage of the Pt surface may be covered by the TaOx for the 35ALD–TaOx–Pt/C catalyst, and the covered Pt surface can be activated by the potential cycling. It is hypothesized that the TaOx particles located on the Pt surface exhibit a weak Pt–TaOx interaction compared to the Pt–TaOx–C triple junctions, thus allowing them to redistribute during voltage cycling and expose additional Pt surface area. However, further increasing the TaOx loading to 50 ALD cycles results in an 80% decrease in beginning of life (BOL) ECSA vs. Pt/C. This is consistent with the HRTEM results and confirms an almost

overcoated Pt surface area by the TaOx layer. Notably, during the ADT, the ECSA of the 50ALD–TaOx–Pt/C catalyst gradually increased from 12.9 to 48.3 m^2·g^{-1} $_{Pt}$, which further indicates that the TaOx covered Pt surface can be activated by the potential cycling. However, even after 10 000 ADT cycles, the increased ECSA of 50ALD–TaOx–Pt/C is still much lower than that of 35ALD–TaOx–Pt/C. Overall, the 35ALD–TaOx–Pt/C catalyst with the triple junction of TaOx–Pt–C showed the most promise in terms of durability. Further catalytic activity toward ORR of this catalyst vs. Pt/C is provided below.
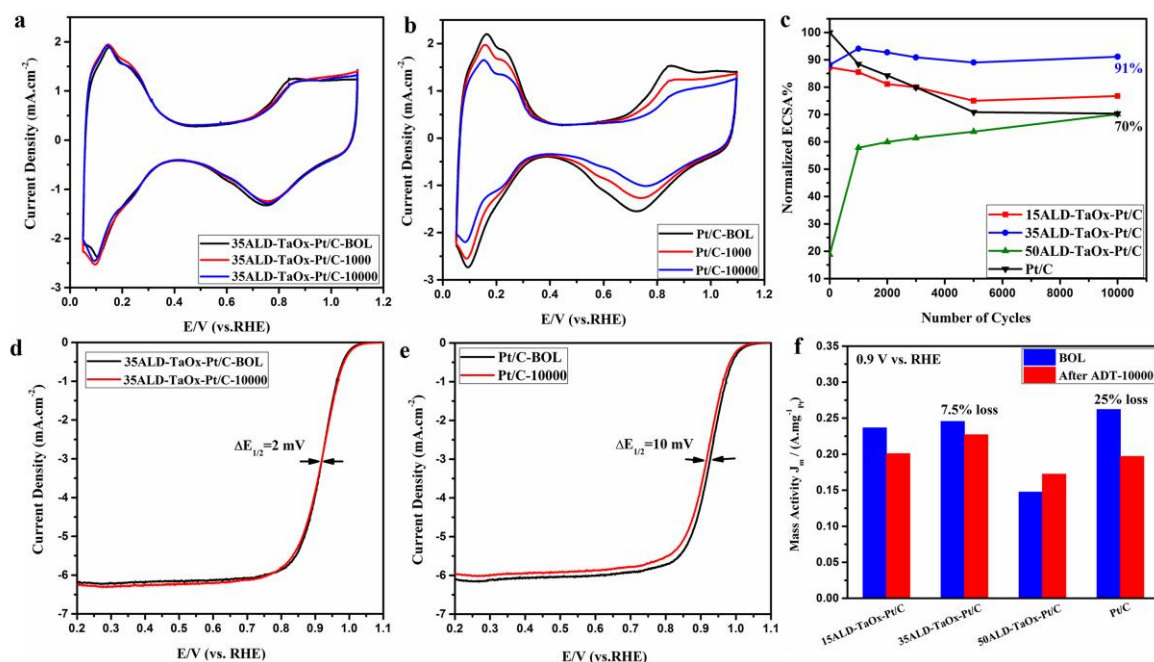
Figure 4.4. Intermediate characterization CV curves of (a) 35ALD–TaOx–Pt/C and (b) Pt/C catalysts during the load-cycling (0.6 V–1.0 V) durability tests in a N$_2$-saturated 0.1 MHClO$_4$ solution at a scan rate of 50 mV·s^{-1}. (c) ECSA variation with cycling number for different catalysts cycled from 0.6 to 1.0 V. ORR curves for (d) 35ALD-TaOx-Pt/C and (e) Pt/C before and after ADT-10000. (f) Mass activity of different catalysts at 0.9 V before and after ADT-10000.

The LSV curves obtained under O$_2$-saturated HClO$_4$ for different catalysts before and after ADT-10 000 are shown in Fig. 4.4(d) and (e). The results indicate that 35ALD–TaOx-Pt-C and Pt/C catalysts displayed an almost similar onset-potential of 1.075 V and 1.080 V, respectively, at BOL before ADT. The change in half-wave potential (E$_{1/2}$) after ADT-10 000

was used to evaluate the electrochemical durability. As shown in Fig. 4.4(d), the $E_{1/2}$ of 35ALD TaOx–Pt/C shifted from 0.920 V to 0.918 V with only a negligible degradation of 2 mV after ADT-10 000. However, for the Pt/C catalyst, a more severe degradation of 10 mV (from 0.920 V to 0.915 V) was observed after ADT-10 000. Based purely on the ECSA change, we would expect an $E_{1/2}$ loss of 7 mV calculated on the basis of Butler–Volmer kinetics. [56–58] The measured 10 mV loss is quite close to this, thus suggesting that the ECSA loss is primarily responsible for the activity loss. Furthermore, the ORR mass activities at 0.9 V before and after ADT-10 000 of the tested catalysts were calculated and are shown in Fig. 4.4(f) and Table S4.1. Initially, the 35ALD–TaOx–Pt/C catalyst exhibited comparable mass activity (0.246 A·mg^{-1} Pt) to that of Pt/C (0.262 A·mg^{-1} Pt). After ADT-10 000, the mass activity of 35ALD–TaOx–Pt/C at 0.9 V is 0.227 A·mg^{-1} Pt (only 7.5% loss), which is much higher than that of the Pt/C catalyst (0.197 A·mg^{-1} Pt). The high durability of the 35ALD–TaOx–Pt/C catalyst further confirms the anchoring effect of TaOx.
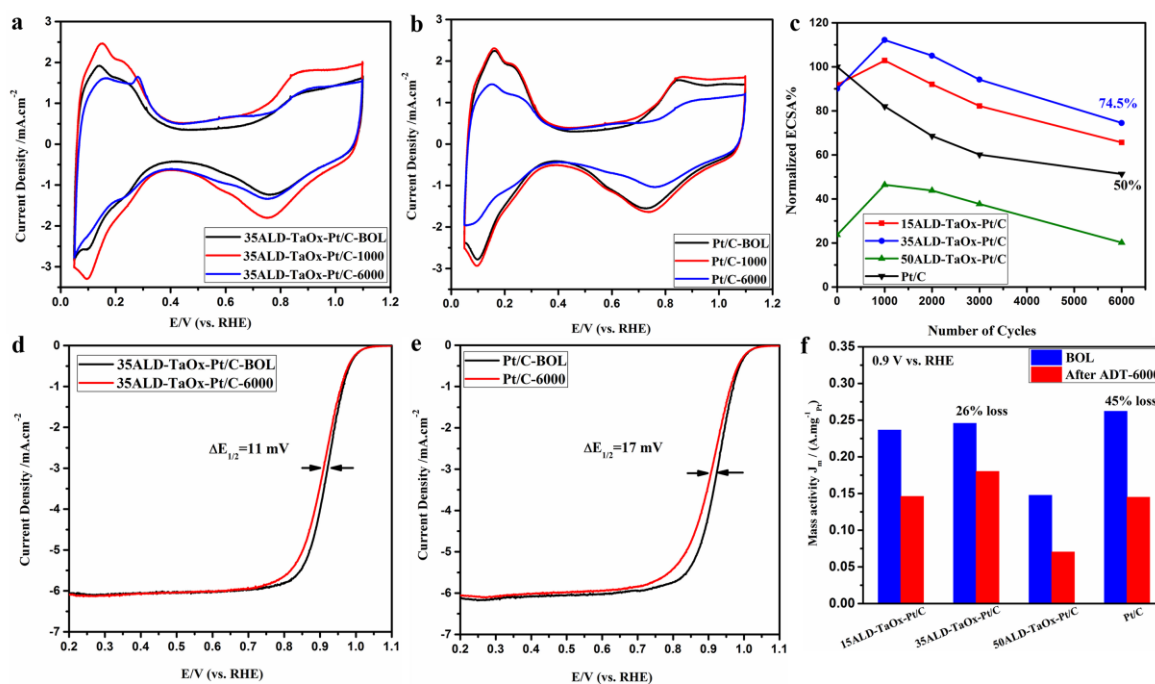
Figure 4.5. Intermediate characterization CV curves of (a) 35ALD–TaOx–Pt/C and (b) Pt/C catalyst during the start-up/shut-down (1.0 V–1.6 V) durability tests in a N$_2$-saturated 0.1 M HClO$_4$ solution at a scan rate of 100 mV·s^{-1}. (c) Variation of ECSA with cycling number for different catalysts cycled from 1.0 to 1.6 V. ORR curved for (d)

35ALD-TaOx-Pt/C and (e) Pt/C catalyst before and after cycling between 1.0 to 1.6V. (f) mass activity of catalysts at 0.9 V (vs. RHE) before and after ADT-6000.

The process of Pt crystal migration and coalescence directly impacts ECSA at a low potential (<1.0 V vs. RHE). [59–61] However, at high potentials (>1.1 V vs. RHE), the carbon support is prone to oxidation or corrosion. [62,63] Carbon corrosion can lead to physical detachment of Pt NPs, resulting in complete catalytic activity loss for the detached Pt NPs. [60] This is especially problematic during partial fuel starvation [64] or PEMFC start-up/ shutdown events when the cell voltage can reach up to 1.5 V or higher. [65,66] Thus, additional potential cycling experiments were carried out in a potential range of 1.0–1.6 V vs. RHE for 6000 cycles at a scan rate of 100 mV·s^{-1}, to mimic the experience of the cathode catalyst during PEMFC start-up/shutdown. Fig. 4.5(a) and (b) show the changes of CV curves for different catalysts during ADT-6000. The normalized ECSA variations with cycling numbers are shown in Fig. 4.5(c) and the corresponding ECSA values at typical cycling numbers are summarized in Table S4.2. For the Pt/C catalyst, the ECSA recorded after ADT-6000 is just 50% maintained (decreased from 66.4 to 34.0 m^2·g^{-1} $_{Pt}$), the E$_{1/2}$ experienced a 17.0 mV degradation and the mass activity at 0.9 V exhibited 45.0% loss (dropped from 0.262 to 0.145 A·mg^{-1} $_{Pt}$) after ADT-6000 (Fig. 4.5(d)–(f)). However, the catalytic activity of 35ALD–TaOx–Pt/C increased with potential cycling and revealed the highest ECSA after 1000 potential cycles. It retains 74.5% of the initial ECSA after ADT-6000 and is 24.5% higher than that of Pt/C. Additionally, the 35ALD–TaOx–Pt/C catalyst displayed a 24.0% higher mass activity at 0.9 V (0.180 A·mg^{-1} $_{Pt}$) than Pt/C (0.145 A·mg^{-1} $_{Pt}$) after ADT-6000. This confirmed that 35ALD–TaOx–Pt/C showed a much better stability than Pt/C even under the harsh cycling conditions. During potential cycling between 1.0 V and 1.6 V (vs. the RHE), the Pt/C and 35ALD–TaOx–Pt/C catalysts showed a notable increase in the capacitive double layer region (0.4 V–0.6 V). This is due to the carbon oxidation reaction which leads to the formation of pseudo-capacitive groups and/or micropores on the carbon surface. The carbon oxidation decreases the amount of carbon available to support Pt, resulting in detachment of the Pt NPs and decrease in the active surface area. [10] From 0 to 1000 cycles, the ECSA of Pt/C exhibited a drastic decrease (from 66.4 to 54.5 m^2·g^{-1} $_{Pt}$) with the increased double layer capacity, which indicated that detachment of Pt NPs occurs during the carbon corrosion process. However, the ECSA of 35ALD–TaOx– Pt/C exhibited no degradation

after 1000 potential cycles. This is because the TaOx anchors played a significant role in stabilizing Pt NPs and effectively prevented the detachment of the Pt NPs under the severe carbon oxidation and corrosion conditions.

PEMFC single cell performance
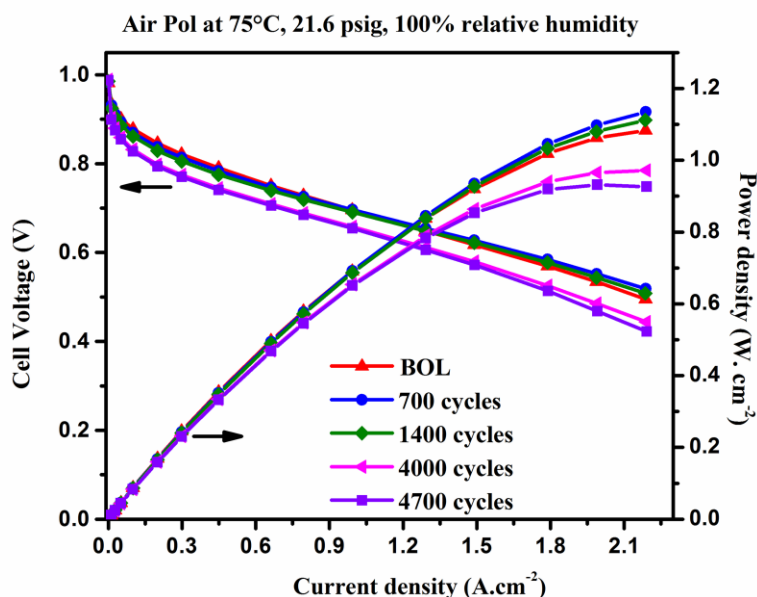
Figure 4.6. H$_2$–air fuel cell polarization curves for MEA using 35ALD–TaOx–Pt/C as the cathode after different aging cycles with the Pt loading on the anode and cathode of 0.1 and 0.15 mg·cm^{-2}, respectively.

Based on the electrochemical results, potential cycling between 0.6 V and 1.0 V vs. RHE was performed on MEA to further study the single cell durability performance. The current–voltage and corresponding current–power density curves for the MEA after different ADT cycles are shown in Fig. 4.6. Under conditions of high temperature and humidity (75°C, 100% RH), the MEA exhibited highly stable performance in the long-term durability test. As shown in Fig. 4.6, the cell voltage increased with the potential cycling and revealed the highest cell voltage of 653 mV at a high current density (1.3 A·cm^{-2}) after 700 potential cycles, with only 40 mV voltage loss after 4700 ADT cycles (~120 h), which indicated a highly stable catalyst performance. Furthermore, the beginning peak power density was 1.08 W·cm^{-2}, and it increased to 1.13 W·cm^{-2} and 1.11 W·cm^{-2} after 700 and 1400 ADT cycles,

respectively. Even after 4700 ADT cycles, the peak power density is maintained at 0.95 W·cm^{-2} with only 12% loss. This shows much better durability than the commercial Pt/C catalyst reported in the literature (with ~27% power loss after 100 h or less aggressive accelerated durability test). [67–70] The cathode catalyst was collected from the MEA after accelerate cycling, and the morphology of the 35ALD–TaOx–Pt/C catalyst before and after ADT was examined by TEM and XRD patterns. Fig. S4.4 shows that the Pt NPs were uniformly distributed on the carbon support after 4700 ADT cycles and the average particle size was 3.9±0.5 nm. The uniform distribution and small change in Pt particle size suggest that the TaOx was successful in stabilizing the Pt catalyst.
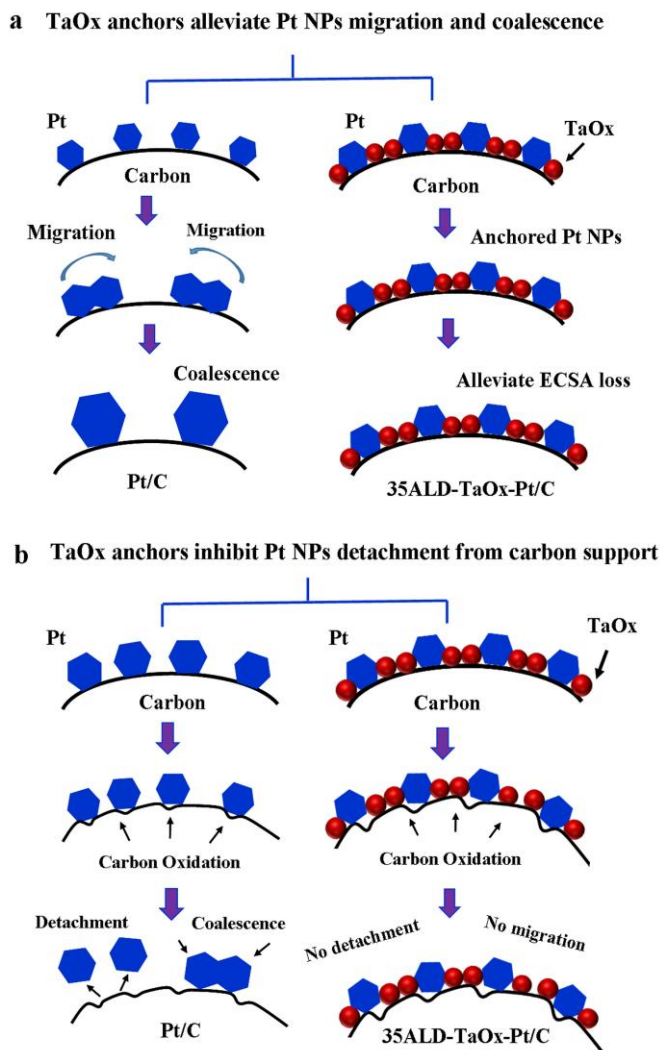
Figure 4.7. Schematic of the stability mechanism of the 35ALD–TaOx– Pt/C catalyst with triple junctions of TaOx–Pt–C. (a) TaOx alleviating Pt NPs migration and coalescence; (b) TaOx inhibiting the detachment and coalescence of Pt NPs.

The mechanism of the dramatically enhanced stability could be related to the triple-junction structure of the TaOx-anchored Pt NPs on the carbon support. First, Pt NPs in the commercial Pt/C catalyst are easy to migration and coalescence, due to the relatively weak interactions between Pt NPs and the carbon support, which is a major factor for catalyst degradation during PEMFC operation. For 35ALD–TaOx–Pt/C with TaOx-anchored Pt NPs, the migration and coalescence process might be alleviated due to the construction of triple junctions of TaOx–Pt–C. These strong interactions enhance the catalyst stability and minimize the ECSA loss, as illustrated in Fig. 4.7(a). Furthermore, as previously reported,

carbon corrosion often occurs in the presence of the Pt catalyst and at high potential (>1.5 V), especially under the conditions of PEMFC fuel starvation and start-up/shutdown. Thus, for the Pt/C catalyst, Pt NPs detach from the support when the carbon is oxidized, resulting in loss of catalytic activity. By contrast for 35ALD–TaOx–Pt/C catalyst, Pt NPs remain anchored on the carbon surface even when the carbon support is partly corroded. The strong triple-junction structure will efficiently prevent the detachment of Pt NPs and enhance the Pt catalyst stability. The detailed processes are illustrated in Fig.4.7(b).

4.4 Conclusions

In summary, metal oxide (TaOx) modified commercial Pt/C catalysts with TaOx-anchored Pt NPs were prepared by an area-selective atomic layer deposition method. After heat removal of the protective agent, the TaOx-anchored Pt NPs with a unique triple-junction structure were formed. The TaOx particles could tightly immobilize Pt NPs on the carbon support and played a significant role in stabilizing the Pt catalyst through the metal oxide anchoring effect. The electrochemical data revealed that the TaOx-anchored Pt catalyst with 35 ALD cycles of TaOx deposition displayed comparable catalytic activity to the commercial Pt/C catalyst. Significantly, the 35ALD–TaOx–Pt/C catalyst exhibited superior long-term stability of both electrochemical surface area and ORR mass activity in comparison to Pt/C. Furthermore, MEA durability tests show that the anchored 35ALD–TaOx–Pt/C catalyst exhibits good long-term stability with only 12% power density loss after 120 h aging. The excellent stability of 35ALD–TaOx–Pt/C should be ascribed to the strong anchoring effect of TaOx towards Pt NPs which hinders the migration, coalescence and detachment of Pt NPs from the support. Therefore, the construction of TaOx anchored Pt NPs can offer a persuasive approach towards increasing the lifetime of the catalysts applied in PEMFCs.

Acknowledgment

References

[1]. M. K. Debe, Nature, 2012, 486, 43–51.

[2]. M. Jacobson, W. Colella and D. Golden, Science, 2005, 308, 1901–1905.

[3]. R. F. Service, Science, 2002, 296, 1222–1224.

[4]. W. Yu, M. D. Porosoff and J. G. Chen, Chem. Rev., 2012, 112, 5780–5817.

[5]. C. Cui, L. Gan, M. Heggen, S. Rudi and P. Strasser, Nat. Mater., 2013, 12, 765–771.

[6]. L. Zhang, L. T. Roling, X. Wang, M. Vara, M. Chi, J. Liu, S.-I. Choi, J. Park, J. A. Herron, Z. Xie, M. Mavrikakis and Y. Xia, Science, 2015, 349, 412–416.

[7]. C. Chen, Y. Kang, Z. Huo, Z. Zhu, W. Huang, H. L. Xin, J. D. Snyder, D. Li, J. A. Herron, M. Mavrikakis, M. Chi, K. L. More, Y. Li, N. M. Markovic, G. A. Somorjai, P. Yang and V. R. Stamenkovic, Science, 2014, 343, 1339–1343.

[8]. M. Li, Z. Zhao, T. Cheng, A. Fortunelli, C. Y. Chen, R. Yu, Q. Zhang, L. Gu, B. V. Merinov and Z. Lin, Science, 2016, 354, 1414–1419.

[9]. N. Cheng, M. N. Banis, J. Liu, A. Riese, S. Mu, R. Li, T.-K. Sham and X. Sun, Energy Environ. Sci., 2015, 8, 1450–1455.

[10]. Y. Shao, G. Yin and Y. Gao, J. Power Sources, 2007, 171, 558–566.

[11]. A. Brouzgou, S. Song and P. Tsiakaras, Appl. Catal., B, 2012, 127, 371–388.

[12]. X. Yu and S. Ye, J. Power Sources, 2007, 172, 145–154.

[13]. Y. Shao-Horn, W. Sheng, S. Chen, P. Ferreira, E. Holby and D. Morgan, Top. Catal., 2007, 46, 285–305.

[14]. S. Sun, F. Jaouen and J. P. Dodelet, Adv. Mater., 2008, 20, 3900–3904.

[15]. Z. Chen, M. Waje, W. Li and Y. Yan, Angew. Chem., Int. Ed., 2007, 46, 4060–4063.

[16]. S. Sun, D. Yang, D. Villers, G. Zhang, E. Sacher and J.-P. Dodelet, Adv. Mater., 2008, 20, 571–574.

[17]. G. Zhang, S. Sun, M. Cai, Y. Zhang, R. Li and X. Sun, Sci. Rep., 2013, 3, 1–8.

[18]. S. Guo, S. Dong and E. Wang, ACS Nano, 2010, 4, 547–555.

[19]. Z. Peng, H. You and H. Yang, ACS Nano, 2010, 4, 1501–1510.

[20]. D. Wang, H. L. Xin, R. Hovden, H. Wang, Y. Yu, D. A. Muller, F. J. DiSalvo and H. D. Abru˜na, Nat. Mater., 2013, 12, 81–87.

[21]. V. R. Stamenkovic, B. Fowler, B. S. Mun, G. Wang, P. N. Ross, C. A. Lucas and N. M. Markovi´c, Science, 2007, 315, 493–497.

[22]. V. R. Stamenkovic, B. S. Mun, M. Arenz, K. J. Mayrhofer, C. A. Lucas, G. Wang, P. N. Ross and N. M. Markovic, Nat. Mater., 2007, 6, 241–247.

[23]. D. Geng, Y. Hu, Y. Li, R. Li and X. Sun, Electrochem. Commun., 2012, 22, 65–68.

[24]. S. Takenaka, H. Miyamoto, Y. Utsunomiya, H. Matsune and M. Kishida, J. Phys. Chem. C, 2014, 118, 774–783.

[25]. J. Jones, H. Xiong, A. T. DeLaRiva, E. J. Peterson, H. Pham, S. R. Challa, G. Qi, S. Oh, M. H. Wiebenga, X. I. Pereira Hern´andez, Y. Wang and A. K. Datye, Science, 2016, 353,150–154.

[26]. X. Tian, J. Luo, H. Nan, H. Zou, R. Chen, T. Shu, X. Li, Y. Li, H. Song and S. Liao, J. Am. Chem. Soc., 2016, 138, 1575–1583.

[27]. T. Fujigaya and N. Nakashima, Adv. Mater., 2013, 25, 1666–1681.

[28]. D. He, K. Cheng, H. Li, T. Peng, F. Xu, S. Mu and M. Pan, Langmuir, 2012, 28, 3979–3986.

[29]. D. He, S. Mu and M. Pan, Carbon, 2011, 49, 82–88.

[30]. K. Cheng, Z. Kou, J. Zhang, M. Jiang, H. Wu, L. Hu, X. Yang, M. Pan and S. Mu, J. Mater. Chem. A, 2015, 3, 14007–14014.

[31]. R. Kou, Y. Shao, D. Mei, Z. Nie, D. Wang, C. Wang, V. V. Viswanathan, S. Park, I. A. Aksay and Y. Lin, J. Am. Chem. Soc., 2011, 133, 2541–2547.

[32]. N. Cheng, J. Liu, M. N. Banis, D. Geng, R. Li, S. Ye, S. Knights and X. Sun, Int. J. Hydrogen Energy, 2014, 39, 15967–15974.

[33]. P. Lu, C. T. Campbell and Y. Xia, Nano Lett., 2013, 13, 4957–4962.

[34]. A. Kumar and V. Ramani, ACS Catal., 2014, 4, 1516–1525.

[35]. S. Shanmugam and A. Gedanken, Small, 2007, 3, 1189–1193.

[36]. J. Seo, D. Cha, K. Takanabe, J. Kubota and K. Domen, ACS Catal., 2013, 3, 2181–2189.

[37]. J. Y. Kim, T.-K. Oh, Y. Shin, J. Bonnett and K. S. Weil, Int. J. Hydrogen Energy, 2011, 36, 4557–4564.

[38]. T. Ushikubo, Catal. Today, 2000, 57, 331–338.

[39]. A. Bonakdarpour, R. L˙obel, S. Sheng, T. Monchesky and J. Dahn, J. Electrochem. Soc., 2006, 153, A2304–A2313.

[40]. J. Seo, D. Cha, K. Takanabe, J. Kubota and K. Domen, Chem. Commun., 2012, 48, 9074–9076.

[41]. J. Seo, D. Cha, K. Takanabe, J. Kubota and K. Domen, Phys. Chem. Chem. Phys., 2014, 16, 895–898.

[42]. J. Seo, D. H. Anjum, K. Takanabe, J. Kubota and K. Domen, Electrochim. Acta, 2014, 149, 76–85.

[43]. J. Seo, L. Zhao, D. Cha, K. Takanabe, M. Katayama, J. Kubota and K. Domen, J. Phys. Chem. C, 2013, 117, 11635–11646.

[44]. Z. Awaludin, J. G. S. Moo, T. Okajima and T. Ohsaka, J. Mater. Chem. A, 2013, 1, 14754–14765.

[45]. J. Lu, B. Fu, M. C. Kung, G. Xiao, J. W. Elam, H. H. Kung and P. C. Stair, Science, 2012, 335, 1205–1208.

[46]. C. Marichy, M. Bechelany and N. Pinna, Adv. Mater., 2012, 24, 1017–1032.

[47]. J. Lu, K.-B. Low, Y. Lei, J. A. Libera, A. Nicholls, P. C. Stair and J. W. Elam, Nat. Commun., 2014, 5, 3264.

[48]. J. Lu, J. W. Elam and P. C. Stair, Acc. Chem. Res., 2013, 46, 1806–1815.

[49]. R. H. A. Ras, E. Sahramo, J. Malm, J. Raula and M. Karppinen, J. Am. Chem. Soc., 2008, 130, 11252–11253.

[50]. R. Chen and S. F. Bent, Adv. Mater., 2006, 18, 1086–1090.

[51]. N. Cheng, M. N. Banis, J. Liu, A. Riese, X. Li, R. Li, S. Ye, S. Knights and X. Sun, Adv. Mater., 2015, 27, 277–281.

[52]. J. Liu, M. N. Banis, X. Li, A. Lushington, M. Cai, R. Li, T.-K. Sham and X. Sun, J. Phys. Chem. C, 2013, 117, 20260–20267.

[53]. K. Kukli, M. Ritala and M. Leskel, J. Electrochem. Soc., 1995, 142, 1670–1675.

[54]. S. Trasatti and O. Petrii, Pure Appl. Chem., 1991, 63, 711–734.

[55]. A. Riese, D. Banham, S. Ye and X. Sun, J. Electrochem. Soc., 2015, 162, F783–F788.

[56]. D. A. Noren and M. A. Hoffman, J. Power Sources, 2005, 152, 175–181.

[57]. W. Sheng, H. A. Gasteiger and Y. Shao-Horn, J. Electrochem. Soc., 2010, 157, B1529–B1536.

[58]. J. Wang, N. Markovic and R. Adzic, J. Phys. Chem. B, 2004, 108, 4127–4133.

[59]. M. S. Wilson, F. H. Garzon, K. E. Sickafus and S. Gottesfeld, J. Electrochem. Soc., 1993, 140, 2872–2877.

[60]. Y. Shao-Horn, P. Ferreira, D. Morgan, H. Gasteiger and R. Makharia, ECS Trans., 2006, 1, 185–195.

[61]. G. Gruver, R. Pascoe and H. Kunz, J. Electrochem. Soc., 1980, 127, 1219–1224.

[62]. R. Makharia, S. Kocha, P. Yu, M. A. Sweikart, W. Gu, F. Wagner and H. A. Gasteiger, ECS Trans., 2006, 1, 3–18.

[63]. L. Castanheira, W. O. Silva, F. H. Lima, A. Crisci, L. Dubau and F. d. r. Maillard, ACS Catal., 2015, 5, 2184–2194.

[64]. A. Taniguchi, T. Akita, K. Yasuda and Y. Miyazaki, J. Power Sources, 2004, 130, 42–49.

[65]. J. Durst, A. Lamibrac, F. Charlot, J. Dillet, L. F. Castanheira, G. Maranzana, L. Dubau, F. Maillard, M. Chatenet and O. Lottin, Appl. Catal., B, 2013, 138, 416–426.

[66]. J. Dillet, D. Spernjak, A. Lamibrac, G. Maranzana, R. Mukundan, J. Fairweather, S. Didierjean, R. Borup and O. Lottin, J. Power Sources, 2014, 250, 68–79.

[67]. D. Y. Chung, S. W. Jun, G. Yoon, S. G. Kwon, D. Y. Shin, P. Seo, J. M. Yoo, H. Shin, Y.-H. Chung and H. Kim, J. Am. Chem. Soc., 2015, 137, 15478–15485.

[68]. Y. Jeon, H. Na, H. Hwang, J. Park, H. Hwang and Y.-g. Shul, Int. J. Hydrogen Energy, 2015, 40, 3057–3067.

[69]. Z.-M. Zhou, Z.-G. Shao, X.-P. Qin, X.-G. Chen, Z.-D. Wei and B.-L. Yi, Int. J. Hydrogen Energy, 2010, 35, 1719–1726.

[70]. Z. Xia, S. Wang, L. Jiang, H. Sun, S. Liu, X. Fu, B. Zhang, D. Sheng Su, J. Wang and G. Sun, Sci. Rep., 2015, 5, 16100.

Supporting information
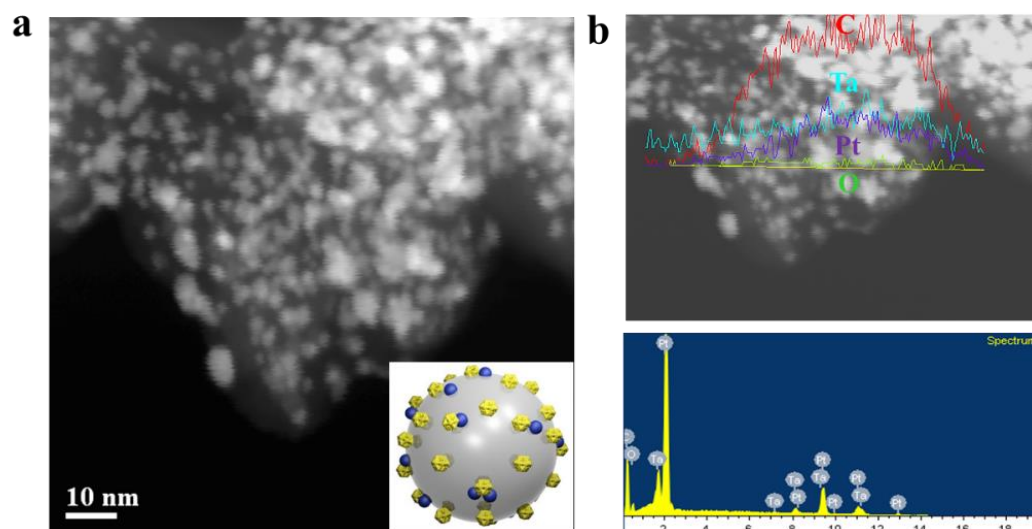
Figure S4.1. (a) STEM image and (b) STEM line scan spectra of 15ALD-TaOx-Pt/C catalyst.
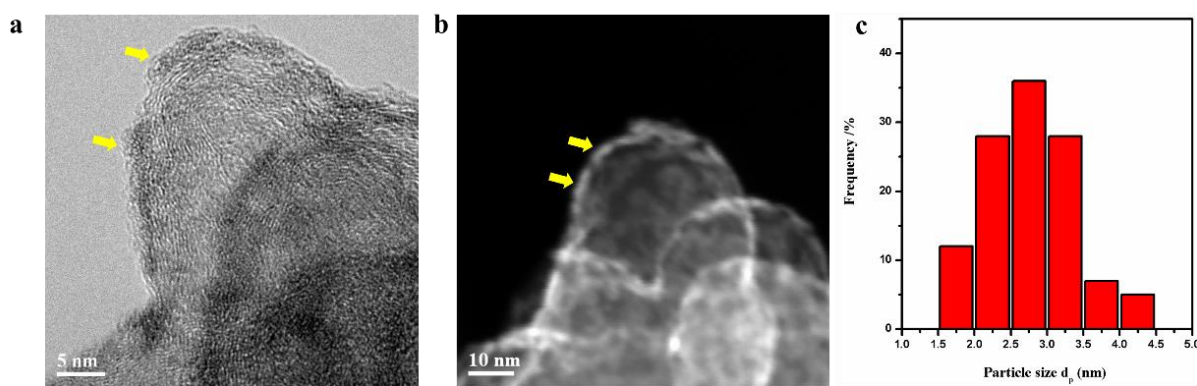
Figure S4.2. (a) HRTEM and (b) STEM images of 35ALD-TaOx on CB without Pt NPs. (c) The particle size distribution histogram of TaOx in 35 ALD-TaOx-CB sample.
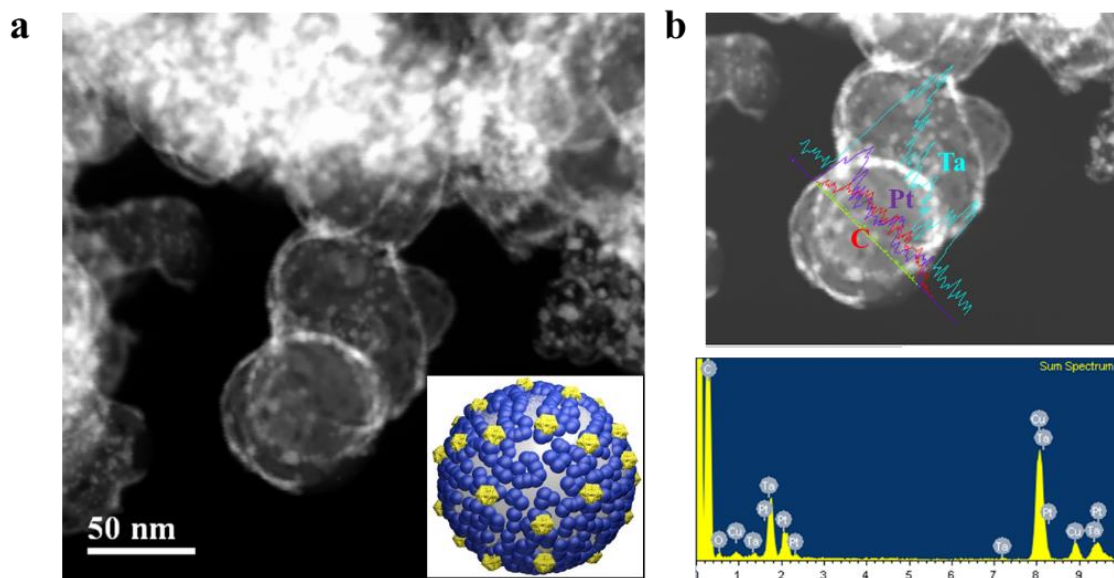
Figure S4.3. (a) STEM image and (b) STEM line scan spectra of 50ALD-TaOx-Pt/C catalyst.
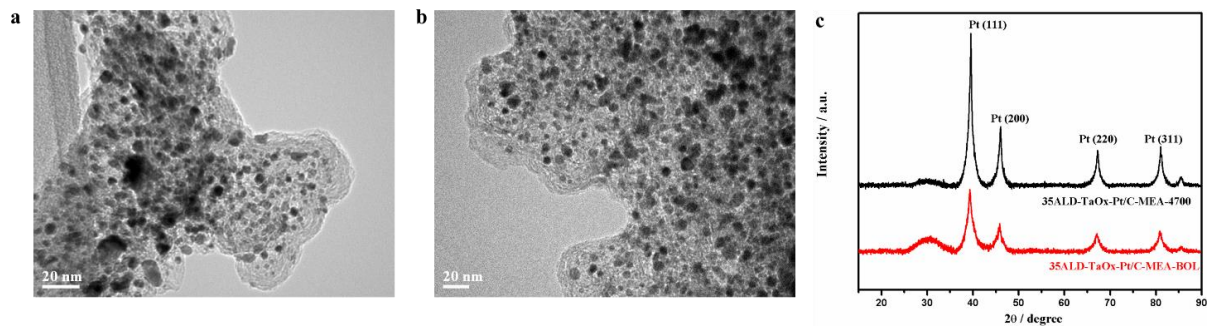
Figure S4.4. HRTEM images (a, b) and XRD patterns (c) of 35ALD-TaOx-Pt/C-MEA cathode before (a) and after (b) 4700 cycles aging test.

Table S4.1. The ECSA values and Mass activity of different catalyst during the ADT cycling between 0.6 V-1.0 V.

Catalyst	ECSA ($m^2 \cdot g^{-1}$ Pt)			Mass activity ($A \cdot mg^{-1}$ Pt) @0.9 V	
	BOL	ADT-1000	ADT-10,000	BOL	ADT-10000
15ALD-TaOx-Pt/C	60.0	58.8	52.8	0.237	0.200
35ALD-TaOx-Pt/C	60.6	64.7	62.7	0.246	0.227
50ALD-TaOx-Pt/C	12.9	39.8	48.3	0.148	0.173
Pt/C	68.8	60.8	48.4	0.262	0.197

Table S4.2. The ECSA values and Mass activity of different catalyst during the ADT cycling between 1.0 V-1.6 V.

Catalyst	ECSA ($m^2 \cdot g^{-1}$ Pt)			Mass activity ($A \cdot mg^{-1}$ Pt) @0.9 V	
	BOL	ADT-1000	ADT-6000	BOL	ADT-6000
15ALD-TaOx-Pt/C	61.0	68.3	43.6	0.237	0.146
35ALD-TaOx-Pt/C	59.8	74.5	49.5	0.246	0.180
50ALD-TaOx-Pt/C	15.7	30.8	13.4	0.148	0.070
Pt/C	66.4	54.5	34.1	0.262	0.145

Chapter 5

5 Origin of achieving the enhanced activity and stability of Pt electrocatalysts with strong metal-support interactions via atomic layer deposition

The enhancement of catalyst activity and stability by controlling the metal-support interaction is extremely important for the long-term operation of polymer electrolyte membrane fuel cells (PEMFCs). In this work, an extremely stable electrocatalyst of platinum nanoparticles (Pt NPs) is dispersed on a carbon support modified with an interphase of nitrogen-doped tantalum oxide (N-Ta_2O_5). The N-Ta_2O_5 interphase bridges the Pt NPs and carbon surface is synthesized by atomic layer deposition technique (ALD). It effectively prevents Pt nanocrystals from detachment, migration, and aggregation during the PEMFCs' operation. Electrochemical results indicate that the Pt/N-ALDTa_2O_5/C electrocatalyst exhibits an excellent durability and sufficient catalytic activity for the oxygen reduction reaction, compared to the Pt/C catalyst. X-ray absorption spectroscopy illustrates the strong interactions between the Pt NPs and the N-Ta_2O_5-modified carbon support. It is revealed that the bridge layer of N-Ta_2O_5 significantly affects the electronic structure of the Pt nanocrystals and contributes to the enhancement of the catalytic activity and durability for the Pt/N-ALDTa_2O_5/C catalyst. This strategy, by using ALD of N-doped metal oxide to tune the metal-support interface, results in strong interactions and will benefit the future design of a new electrocatalyst with an even better activity and long-term durability for PEMFCs application.

5.1 Introduction

Due to the highly efficiency in converting the chemical energy from hydrogen into electrical energy, polymer electrolyte membrane fuel cell (PEMFC) is considered as a promising technology in the renewable energy system. Currently, PEMFCs are being commercialized for a broad range of applications, involving portable power, backup

power and electric vehicles due to their high efficiency, room temperature operation, and zero emissions. [1-3] For the widespread commercial implementation of PEMFCs, developing a promising catalyst for enhanced oxygen reduction reaction (ORR) performance is of great significance. At present, carbon supported platinum nanoparticles (Pt NPs) is still considered as one of the most efficient catalysts for ORR. [4-7] Dispersing Pt NPs on carbon increases the electrocatalytic activity and utilization of Pt, thus effectively decreasing the overall cost of PEMFCs. Till now, carbon is the most widely used support material in PEMFCs, because of its large surface area, high electrical conductivity and well-developed pore structure. [8-11] However, the stability of Pt/C for ORR cannot satisfy the requirement for long-term operation of PEMFCs. Because the weak interaction between carbon support and metal particles leads to the Pt NPs migration, aggregation, and eventually a rapid degradation of electrocatalyst performance.[12-14] Significant number of studies have attempted to solve this issue, including enhancing the interaction between Pt NPs and supports by carbon surface modification with metal compound or polymer etc;[15-23] developing corrosion-resistant supports, such as TiO_2 and ZrC.[24-26] The resulting electrocatalysts exhibit improved stability and activity for ORR by forming strong metal-support interactions (SMSIs). Utilization of SMSIs is a promising approach to improve both activity and stability of electrocatalysts. The SMSIs between Pt NPs and metal oxide supports have been widely investigated and showed positive effect on maintaining the stability of catalyst NPs. [27, 28] However, the most stable metal oxides with maximum valency have poor electroconductivity, which means the metal oxides as catalysts supports would enhance the catalysts durability while sacrificing their high ORR activity. To enable the catalyst support with properties of both SMSIs and good electroconductivity, one of the solutions is to develop metal oxide decorated carbon composite by combing the merits of metal oxide and carbon. Therefore, carbon decorated with highly dispersed metal oxide NPs could be used as a nanocomposite support for Pt catalyst. [27, 29] By introducing metal oxide NPs to the position between Pt catalyst and carbon support, the stable and strong three-phase boundary of Pt, metal oxide and carbon could be achieved, which plays significant role in stabilizing Pt NPs on support. The group IV and V elements

such as Zr, Ti, Ta and Nb are known to be chemically stable under PEMFCs operation conditions. Several compounds based on these elements have been reported as ORR electrocatalysts or catalyst supports. [30-34] Despite many attempts, oxides based on Ta, Nb, and Zr have shown limited catalytic activity and durability for PEMFCs application due to the low conductivity. In addition, the nitrogen-doped support provides an opportunity to stabilize Pt NPs while indirectly improve the electrocatalytic activity due to the stronger electronic interactions between Pt and nitrogen-rich support. [34] Nevertheless, using nitrogen-doped metal oxide as additive to enable the noble metal catalyst with enhanced activity and long-term stability toward ORR have not been reported.

The conventional synthesis methods for the group IV-V metal compounds have considerable disadvantage because the as-prepared particles are easily aggregated and frequently form big particles, thus it is difficult to precisely control the metal-support interface. [35-37] In contrast, the atomic layer deposition (ALD) technique have gained considerable attention for the synthesis of transition metal oxide NPs on various substrate. Due to the sequential reactions and self-limiting nature, ALD possesses the advantage in controlling the target materials with precise particle size and density on the substrate. By forming chemical bonds between the initial layer of ALD precursor and support atoms during the first cycle of deposition, the strong interaction between the deposited material and support could be enabled, which is benefit for achieving the highly stable NPs. Moreover, various transition metal oxide or compound with controllable particle size and density have been developed on different substrate by ALD in our group. [38-41] These results enable the preparation of well-dispersed, nanoscale metal compounds for carbon surface modification, achieving controllable metal-support interface.

Herein, we explore the role of nitrogen-doped tantalum oxide (N-Ta_2O_5) bridge layer for the observed improvement in catalyst durability. Initially, the Ta_2O_5 NPs were developed by ALD technique to decorate the carbon black surface. As co-support, Ta_2O_5 NPs have much higher corrosion resistance in the electrochemical environment of PEMFCs compared to carbon. Subsequently, NH_3 treatment of ALDTa_2O_5/C

support was conducted to doping N species. It was found that Pt/N-ALDTa$_2$O$_5$/C showed enhanced catalytic activity and significantly improved electrochemical durability toward ORR. X-ray absorption spectroscopy provided direct evidence of change in the electronic structure of Pt NPs on N-ALDTa$_2$O$_5$/C support compared to other supports, illustrating the SMSIs formed between Pt NPs and the modified N-ALDTa$_2$O$_5$/C support. This is the first report for the application of N-doped tantalum oxide NPs as co-catalyst support to modify carbon surface. By tuning the metal support interface, the highly active and stable Pt catalyst was achieved in this study.

5.2 Experiment

5.2.1 Surface modification of carbon black with tantalum oxide via ALD

Vulcan-72 carbon black was used as the catalyst support to prepare the Pt/C catalyst. Prior to Pt deposition, surface modification of carbon black with Ta$_2$O$_5$ NPs was carried out by ALD technique. The Ta$_2$O$_5$ deposition was conducted in an ALD reactor (Savannah 100, Cambridge Nanotechnology Inc., USA) at 225 °C using tantalum (V) ethoxide (Ta(OC$_2$H$_5$)$_5$) and H$_2$O as precursors, and N$_2$ as carrier gas. One ALD cycle consisted of the following six steps: (1) 0.5 s pulse of Ta(OC$_2$H$_5$)$_5$; (2) 3.0 s extended exposure to Ta(OC$_2$H$_5$)$_5$ in the reaction chamber; (3) N$_2$ purging of 16 s; (4) 1.0 s pulse of H$_2$O; (5) 3.0 s extended exposure to H$_2$O in the reaction chamber; (6) N$_2$ purging of 25 s. 35 ALD cycles was carried out to achieve a uniform distribution of Ta$_2$O$_5$ NPs on carbon surface. The prepared sample was designated as ALDTa$_2$O$_5$/C. More detailed relationship between ALD cycles and Ta$_2$O$_5$ loading have been previously reported by elsewhere. [8, 39] To further investigate N-doping effect of metal oxide on Pt catalyst activity and durability, the N-doped ALDTa$_2$O$_5$/C (N-ALDTa$_2$O$_5$/C) was derived from post-treatment of ALDTa$_2$O$_5$/C with NH$_3$/Ar (10:100) under 700°C for 1h. The modified N-ALDTa$_2$O$_5$/C and ALDTa$_2$O$_5$/C composites were supplied as supports for Pt NPs deposition and finally the supported Pt/N-ALDTa$_2$O$_5$/C and Pt/ALDTa$_2$O$_5$/C catalysts were prepared, respectively.

5.2.2   Pt deposition on modified carbon support

For Pt deposition, the microwave assisted ethylene glycol (EG) reduction method was applied to deposit Pt NPs on different supports. Typically, the 20 mg of N-ALDTa$_2$O$_5$/C in 50 ml EG solution containing 0.6 mM H$_2$PtCl$_6$.6H$_2$O was sonicated for 30 min, and then saturated NaOH/EG solution was used to adjust the PH of the solution to ~10. The solution mixture was microwaved in an oven until the boiling point of EG. During microwaving process, Pt metallic NPs nucleation and growth proceeded by reducing H$_2$PtCl$_6$ precursor. The Pt NPs where then loaded on the available substrate surface of N-ALDTa$_2$O$_5$/C support. After cooling down, filtering and washing, the obtained Pt/N-ALDTa$_2$O$_5$/C catalyst was dried in a vacuum oven. For comparison, the Pt NPs were also deposited on ALDTa$_2$O$_5$/C and pure Vulcan-72 carbon supports using the same procedure to get the Pt/ALDTa$_2$O$_5$ and Pt/C catalysts.

5.2.3   Physical characterization

Structure characterizations of ALDTa$_2$O$_5$/C, N-ALDTa$_2$O$_5$/C and Pt/N-ALDTa$_2$O$_5$/C catalyst were performed by high resolution transmission electron microscope (HRTEM, JEOL 2010FEG, at 200 KV). The elemental distribution was determined by energy dispersive X-ray spectroscopy (EDS) and electron energy loss spectroscopy (EELS) mapping. The chemical state of ALDTa$_2$O$_5$/C and N-ALDTa$_2$O$_5$/C were investigated by X-ray photoelectron spectroscopy (XPS, Kratos Axis Ultra-spectrometer). The N content estimated by XPS was around 0.5 at% for the sample of N-ALDTa$_2$O$_5$/C, and Ta content was around 3.3 at% or 12.7 wt% determined by EDS. The Pt content for each of the electrocatalysts were determined by inductively coupled plasma-optical emission spectroscopy (ICP-OES). From ICP analysis, the Pt loading in Pt/N-ALDTa$_2$O$_5$/C, Pt/ALDTa$_2$O$_5$/C, and Pt/C catalysts were determined of 21.0 wt%, 22.6 wt%, 23.7 wt%, respectively.

5.2.4   X-ray absorption spectroscopy

X-ray absorption near edge structure (XANES) measurement at the Pt L$_3$-edge (11564 eV) and L$_2$-edge (13273 eV) were performed on the 061D superconducting wiggler

sourced hard X-ray microanalysis (HXMA) beamline at the Canadian Light Source. The spectra were collected in fluorescence yield mode using a 32 Ge solid-state detector, and the spectra of high purity metal Pt foil were collected in transmission mode for comparison and mono energy calibration. The acquired XANES data were processed according to the standard procedures using the Athena module. The XANES oscillation functions were obtained by subtracting the pre-edge, post-edge background from the overall absorption spectra and then normalized with respect to the edge-jump step to unity. For a better understanding of the impact of unoccupied densities of 5d states of Pt NPs on different supports, quantitative whiteline (WL) intensity analysis was conducted based on the method reported by Mansour et al., [42] Sham et al, [43, 44] and Sun et al. [17, 45, 46]

5.2.5 Electrochemical characterization

The electrochemical characterizations were performed in a three-electrode system using a rotating-disk electrode (RDE) setup with an Autolab electrochemistry station and rotation control (Pine Instruments). The ink was prepared by mixing 3.0 mg of catalyst in 3.0 ml of aqueous solution containing 0.6 mL of isopropyl alcohol and 30 µL of Nafion (5.0 wt%). Then 30 min sonication was conducted to ensure good dispersion and wetting of the catalyst. 20 µL of the catalyst ink was pipetted onto a polished glassy carbon electrode (Pine, 5.0 mm dia., 0.196 cm^2) and allowed to dry at room temperature. All electrochemical measurements were carried out in 0.1 M $HClO_4$ electrolyte using a Pt wire as a counter electrode and reversible hydrogen electrode (RHE) as a reference electrode. All potentials reported henceforth are vs. RHE. Each electrode was activated by scanning from 0.05 to 1.1 V at 50 mV·s^{-1} in N_2-saturated 0.1 M $HClO_4$ until no changes were observed in the cyclic voltammetry (CV) curves. O_2 was then bubbled into $HClO_4$ for 30 min to achieve an O_2-saturated electrolyte. Then ORR linear sweep voltammetry (LSV, 10 mV·s^{-1}) was conducted in O_2-saturated 0.1M $HClO_4$ on the RDE system with a rotation speed of 1600 rpm. The LSV curves obtained under N_2 were subtracted from the LSV curves obtained under O_2 to remove the non-Faradaic current. The electrochemically active surface area (ECSA) was calculated by integrating the area of the CV curves in the hydrogen underpotential deposition (HUPD) region and using the charge value of 210 µC·cm^{-2}

corresponding to a monolayer adsorption of hydrogen atoms on a polycrystalline Pt catalyst. [47] To evaluate the catalysts durability, an accelerate durability test of potential cycling from 0.6 to 1.0 V vs. RHE protocol was conducted on the as-prepared electrocatalysts. A total of 10,000 cycles in O_2-saturated 0.1 M $HClO_4$ at 50 $mV \cdot s^{-1}$ were performed to analysis the catalysts durability and intermediate characterizations were recorded to monitor the catalysts ECSA degradation and mass activity loss.

5.3   Results and discussion

5.3.1   Nanocomposite electrocatalysts preparation and characterization

The nanocomposite electrocatalyst with Pt NPs supported on N-ALDTa$_2$O$_5$/C were synthesized by a three-step procedure as illustrated in Scheme 1. Initially, ALD of Ta$_2$O$_5$ NPs was performed on the surface of carbon black to produce the Ta$_2$O$_5$-modified carbon. Based on our previous work, [8] 35 ALD cycles could ensure the appropriate loading and uniform distribution of Ta$_2$O$_5$ NPs on carbon surface. Thus, 35 ALD cycles were adopted here for the Ta$_2$O$_5$ NPs deposition. Then, the gas mixture of ammonia/argon (NH$_3$/Ar=10/90) was used for the post-treatment of the ALDTa$_2$O$_5$/C under 700°C for 1h to achieve the N-doped ALDTa$_2$O$_5$/C nanocomposite support. By doping the N atoms from NH$_3$ to Ta$_2$O$_5$ NPs, the composite of ALDTa$_2$O$_5$/C support could be transformed into N-Ta$_2$O$_5$/C. Finally, the Pt NPs were deposited on the surface of the modified N-Ta$_2$O$_5$/C support with a controlled Pt loading of ~20wt% to obtain the nanocomposite electrocatalyst of Pt/N-ALDTa$_2$O$_5$/C.
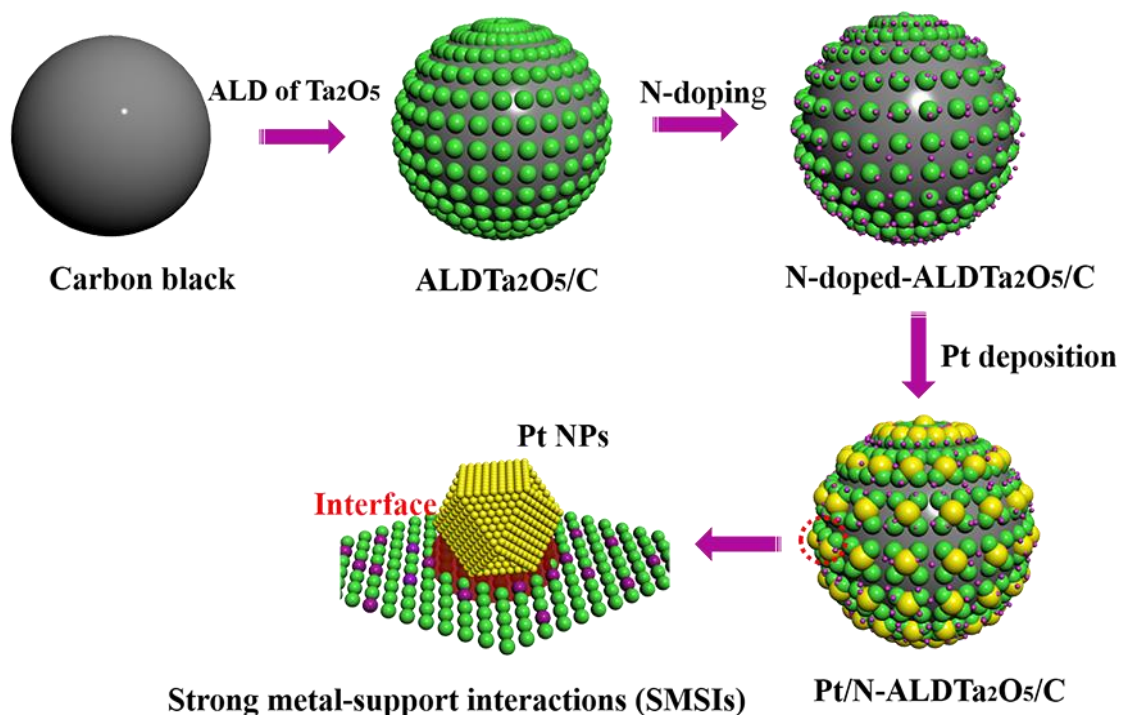
Figure 5.1. Schematic illustration for fabrication of nanocomposite electrocatalyst of Pt/N-ALDTa₂O₅/C with strong metal-support interactions.

The particle sizes and distribution of ALDTa$_2$O$_5$ NPs on carbon sphere achieved via ALD was characterized by HRTEM and aberration corrected scanning transmission electron microscopy (STEM). It can be observed in Figure 5.1 (a, b) that the Ta$_2$O$_5$ NPs under discontinuous morphology were deposited on the carbon surface with a uniform distribution. By further analysis HRTEM information, it was found that majority of Ta$_2$O$_5$ NPs prepared by ALD exist as amorphous structure, which is due to the small particles size (2.7±0.3 nm) and the relatively low deposition temperature (225 °C) for Ta$_2$O$_5$ synthesis. To understand the structure and morphology variations for ALDTa$_2$O$_5$/C after N-doping, a comparison of HRTEM/STEM images for N-ALDTa$_2$O$_5$/C was conducted. Figure 5.1 c and d indicate that the N-Ta$_2$O$_5$ from modified support of N-ALDTa$_2$O$_5$/C has similar particle size with that of Ta$_2$O$_5$, which exhibits uniform dispersion across the Vulcan carbon surface. Although undergone a high temperature NH$_3$ treatment, the N-Ta$_2$O$_5$ NPs still have a good dispersion and are closely anchored on the carbon surface, which suggests the tight integration of N-Ta$_2$O$_5$ NPs and carbon surface. Also, it is noteworthy that the N atoms have been successfully doped into the nanocomposite support, which is evidenced by the EELS

elemental maps (Figure 5.1 e). N-doping effect would further improve the electron conductivity of Ta_2O_5/C support, which would benefit for enhancing the metal catalysts activity and durability. Considering the modified N-ALDTa_2O_5/C as catalyst support, Pt NPs were deposited on this nanocomposite support, and finally the supported Pt/N-ALDTa_2O_5/C electrocatalyst was achieved. The HRTEM image in Figure 5.1 f shows that crystalline Pt NPs highly dispersed on the modified N-ALDTa_2O_5/C support surface, no NPs aggregation was detected. The pre-deposited N-Ta_2O_5 appears as amorphous island and surrounding the Pt NPs on carbon surface, effectively preventing the Pt NPs migration and aggregation with the neighboring NPs. This characterization evidenced the stabilization against mobility that the N-Ta_2O_5 bridge particle imparts on the Pt NPs. The HRTEM/EDS mapping (Figure S5.1) show Pt and Ta with a uniform distribution on carbon surface. STEM-EDS line scan image in Figure 5.1 h provides convincing evidence for the good incorporation of Pt with N-Ta_2O_5 NPs and carbon support. EDS spectra indicates the Ta and Pt loading is 12.7 wt% and 20.1 wt%, respectively, which is consistent to the Pt content of 21.0 wt% detected by ICP-OES. By tuning the interface between Pt NPs and carbon support via the bridge layer of conductive N-ALDTa_2O_5 NPs, the Pt/N-ALDTa_2O_5/C electrocatalyst is expected to have significantly enhanced electrocatalytic performance compared to pure Pt/C.
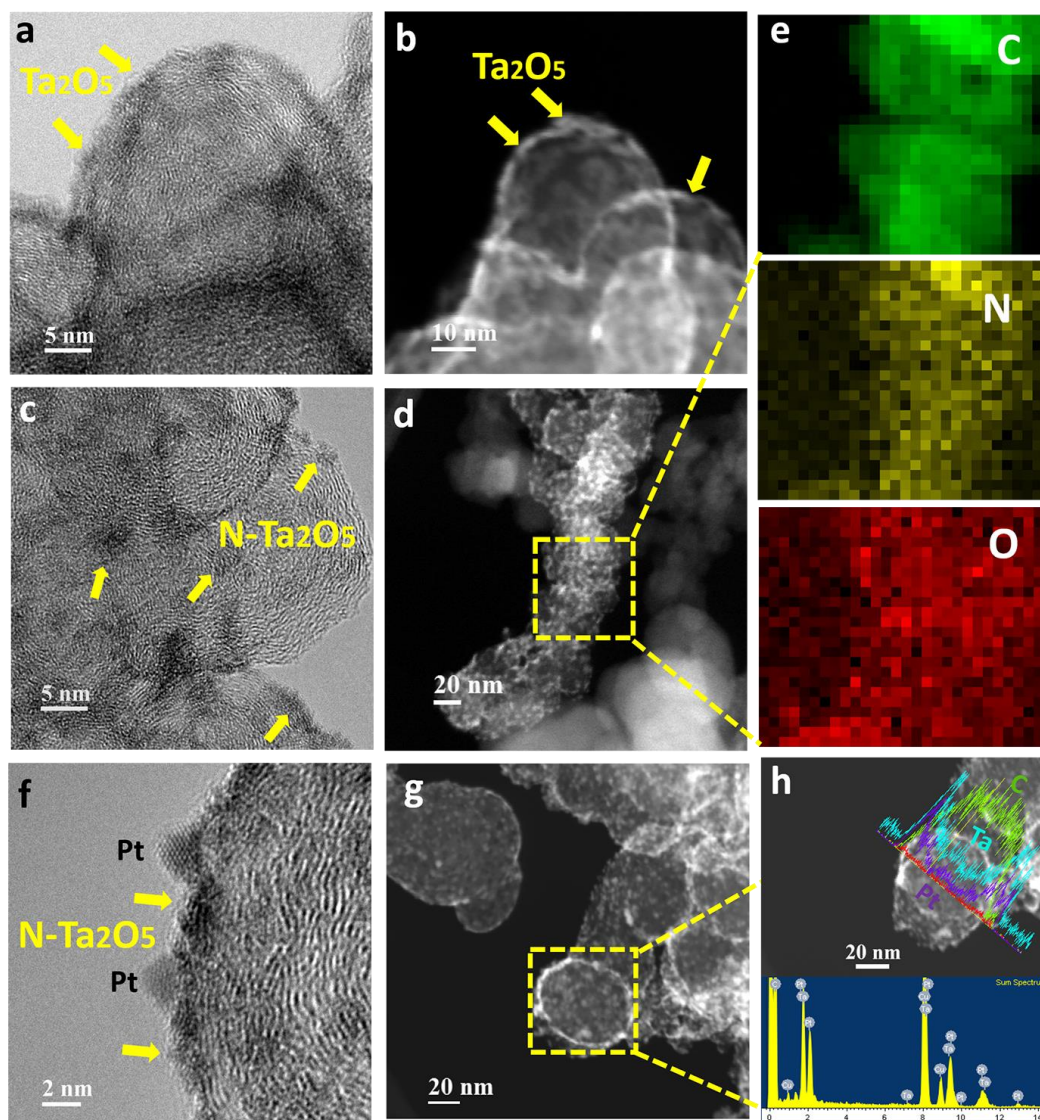
Figure 5.2. HRTEM and STEM images of ALDTa₂O₅/C (a-b), N-ALDTa₂O₅/C (c-d), and Pt/N-ALDTa₂O₅/C (f-g); EELS map of the C (green), N (yellow), O (red) elements for the N-ALDTa₂O₅/C (e); STEM-EDS line scan and spectra of Pt/N-ALDTa₂O₅/C (h).

A smaller particle size with a higher specific surface area in the current work is believed to provide a higher thermodynamically metastable surface area to facilitate the nitridation reaction, thereby yielding the N-doped Ta₂O₅ in addition to Ta₂O₅. Nitrogen doping of ALDTa₂O₅/C via the 700 °C NH₃ treatment was checked by X-ray photoelectron spectroscopy (XPS) to analysis the chemical composition of the modified N-ALDTa₂O₅/C. The XPS survey of N-ALDTa₂O₅/C in Figure 5.2a indicates the presence of Ta, O, N and C

elements with the atomic content of 3.3 %, 9.2 %, 0.5 % and 87.0 %, respectively. The Ta 4f doublets in Figure 5.2b, with the binding energy of 27.09 eV for Ta $f_{7/2}$ peak and 28.97 eV for the Ta $f_{5/2}$ peak, which are consistent with the Ta^{5+} signal from Ta_2O_5. The XPS spectra in Figure 5.2c showed N 1s peak at 397.7 eV accompanied with larger Ta $4p_{3/2}$ peak at 405.1 eV, which confirmed nitrogen atoms have been successfully doped into the Ta_2O_5 lattice. As reported by Kang et.al, [48] the nitrogen-doping content in Ta_2O_5 can be modulated by the temperature of NH_3 treatment. Under 700 °C, certain amounts of O atoms from Ta_2O_5/C are substituted by N atoms with larger radii than that of O atoms. Figure 5.2d indicated that major O 1s peak located at 531.6 eV is from the metal oxide of Ta_2O_5, and a small peak at 533.2 eV is attributed to the response of O-N, belonging to the N-doped-O species from N-ALDTa_2O_5/C. In this study, the O/Ta molar ratio is 2.78 and the N/Ta molar ratio was 0.15, which suggest that nitrogen atoms have been doped in a modest concentration via the 700°C NH_3 treatment for 1 h.
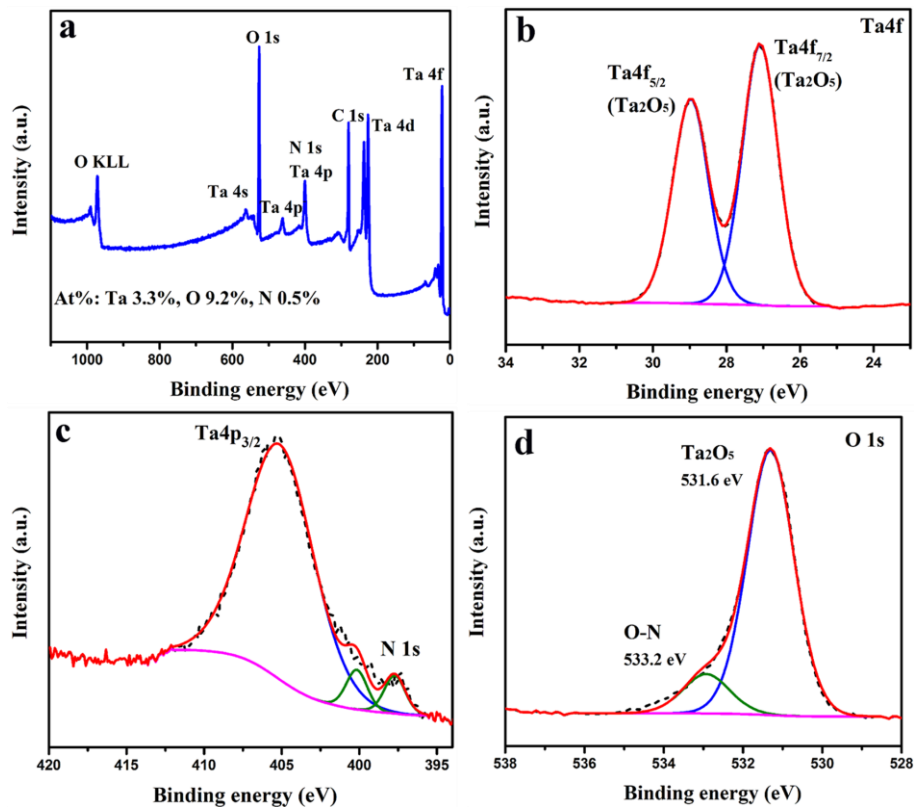
Figure 5.3. X-ray photoelectron spectra for N-ALDTa$_2$O$_5$/C. a) survey spectrum, b) Ta 4f$_{5/2}$ and Ta 4f$_{7/2}$, (c) Ta 4p$_{3/2}$ and N 1s, and (d) O 1s

5.3.2   Electrocatalytic activity and durability

To determine the impact of N-ALDTa$_2$O$_5$ and ALDTa$_2$O$_5$ on the Pt activity and durability, the ORR activity and potential cycling durability for catalysts of Pt/N-ALDTa$_2$O$_5$/C, Pt/ALDTa$_2$O$_5$/C and Pt/C were evaluated. The durability tests were performed by potential sweeping between 0.6 V and 1.0 V (vs. RHE) in O$_2$-purged 0.1 M HClO$_4$ for 10,000 cycles to mimic catalysts durability under the PEMFCs operation. During the accelerate durability test (ADT), Pt catalysts would undergo the NPs migration and aggregation, dissolution and re-deposition, thus loss of active surface area, leading to activity degradation. Figure S5.2 illustrate the representative CV curves (Fig. S2 a-c) and normalized electrochemical active surface area (ESCA) (Fig. S2 d) recorded before and after ADT-10,000 for these catalysts. With continuous potential cycling, the CV curves for Pt/C catalyst exhibited a pronounced decrease of total charge in the hydrogen underpotential deposition (HUPD) region, indicating the degradation in Pt active surface area. By analysis the ECSA of Pt/C catalyst before and after ADT-10,000, it indicated that the Pt/C catalyst experienced a significant surface degradation, with 47% initial ECSA loss after cycling. In contrast, the Pt/ALDTa$_2$O$_5$/C catalyst with the decoration of ALDTa$_2$O$_5$ NPs exhibited an enhanced stable CV peak current and showed 25.2% loss of ECSA after ADT-10,000. The more stable ECSA for Pt/ALDTa$_2$O$_5$/C than that of Pt/C implies the adhesive and/or anchoring effect of T$_2$O$_5$ bridge particles which benefit for immobilizing Pt NPs and inhibiting Pt NPs migration, aggregation, thus alleviating the rapid degradation of catalyst surface area. More importantly, with further doping N species into the ALDTa$_2$O$_5$, the modified N-ALDTa$_2$O$_5$ NPs display the optimum efficiency in stabilizing Pt NPs. Figure S5.2 (a) shows the CV curves for Pt/N-ALDTa$_2$O$_5$/C catalyst before and after ADT-10,000. By analysis of catalyst active surface area variation, it was found that Pt NPs show excellent stability in Pt/N-ALDTa$_2$O$_5$/C system, reflected as the much slower degradation trend with the proceeded potential cycling. After 10,000 ADT cycles, 85.1% initial ECSA was maintained and only 14.9% ECSA loss was revealed for Pt/N-ALDTa$_2$O$_5$/C catalyst. These results suggest the superior durability of Pt/N-ALDTa$_2$O$_5$/C compared than that of Pt/ALDTa$_2$O$_5$/C and Pt/C catalysts.

The ORR kinetics of these Pt electrocatalysts were evaluated by comparing their polarization curves that were acquired in O$_2$-saturated 0.1 M HClO$_4$ (Figure 5.3 a-c) and then calculated

their activities based on Koutecky-Levich plots.[49] The catalysts of Pt/N-ALDTa$_2$O$_5$/C, Pt/ALDTa$_2$O$_5$/C, Pt/C show the onset potential of 1.078 V, 1.076 V, and 1.079 V (vs. RHE), respectively, which implies the similar initial activity of these catalysts at the beginning of life (BOL). After performed ADT cycling, the Pt/C lost its ORR activity much faster than that of Pt/ALDTa$_2$O$_5$/C and Pt/N-ALDTa$_2$O$_5$/C catalysts, i.e., a pronounced 20 mV (shifted from 0.901 V to 0.881 V) of half-wave potential (E$_{1/2}$) degradation for Pt/C versus 10 mV (shifted from 0.982 to 0.882 V) E$_{1/2}$ degradation for Pt/ALDTa$_2$O$_5$/C. In contrast, the E$_{1/2}$ of Pt/N-ALDTa$_2$O$_5$/C electrocatalyst remained almost the same as their respective voltammograms nearly overlapped and only 4 mV of E$_{1/2}$ (shifted from 0.988 to 0.984 V) loss before and after the stability test. The kinetic currents at 0.9 V for all the studied electrocatalysts obtained from the Koutecký-Levich equation were used to get Pt mass activities (Figure 5.3 d). With the same Pt NPs size and loading, the electrocatalyst of Pt/N-ALDTa$_2$O$_5$/C shows the best mass activity and durability. The fresh Pt/ALDTa$_2$O$_5$/C electrocatalyst showed an initial mass activity of 0.222 A·mg^{-1}$_{Pt}$, and after ADT of 10,000 cycles the mass activity decreased to 0.168 A·mg^{-1}$_{Pt}$, which is 24.3% loss in activity. Notably, the fresh Pt/N-ALDTa$_2$O$_5$/C showed a higher initial activity of 0.280 A·mg^{-1}$_{Pt}$ and after ADT 10,000 cycles, the mass activity value decreased to 0.252 A·mg^{-1}$_{Pt}$ with only a 10.0% loss in Pt activity, which is around 2 times higher than that for Pt/C decreased from 0.213 to 0.129 A·mg^{-1}$_{Pt}$ and 39.4% activity loss. The potential cycling durability tests show that Pt/N-ALDTa$_2$O$_5$/C electrocatalyst is significantly more stable than the Pt/C catalyst. The observed decrease in the active surface area and the ORR catalytic activity for Pt/C and Pt/ALDTa$_2$O$_5$/C samples are predominantly caused by the coalescence of the Pt NPs. It was shown by Sheng et al. that small Pt NPs (~2 nm) easily coalesce to form large ones, which is consistent with particle migration and coalescence being a major catalyst degradation pathway. [50] The superior durability achieved for Pt/N-ALDTa$_2$O$_5$/C catalyst is assumed to arise from the strong interactions between Pt NPs and N-doped-Ta$_2$O$_5$ modified support. To confirm this assumption, the X-ray absorption spectroscopy was carried out to study the local electronic structures of Pt and evaluate the metal-support interactions in these electrocatalysts.
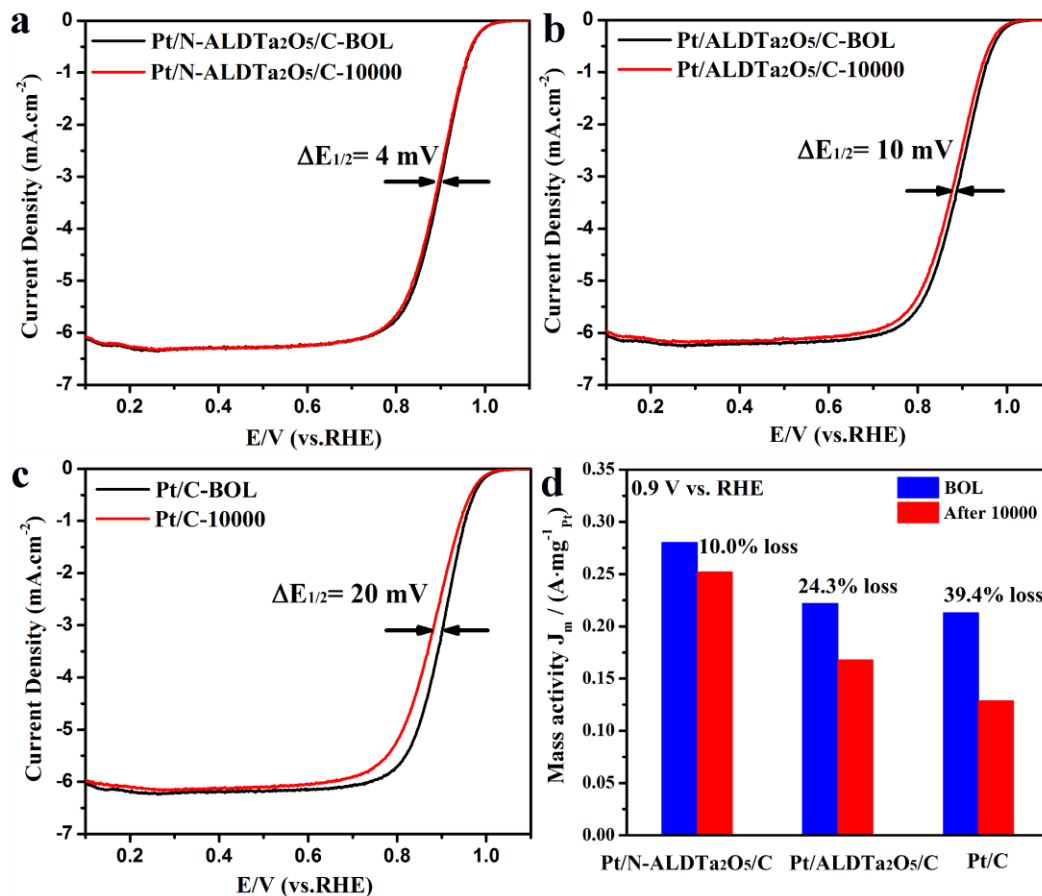
Figure 5.4. The polarization curves of (a) Pt/N-ALDTa₂O₅/C, (b) Pt/ALDTa₂O₅/C, and (c) Pt/C before and after 10,000 cycles of accelerate durability (ADT) test in O₂-saturated 0.1M HClO₄, 1600 rpm, scan rate of 10 mV·s⁻¹. (d) mass activity of different catalysts at 0.9 V (vs. RHE) before and after ADT-10000 (BOL stands for beginning of life).

5.3.3   X-ray absorption spectroscopy studies

To elucidate the chemical state and electronic structure of Pt and Pt-support interactions, the X-ray absorption spectra of Pt at L_3- and L_2-edge were studied. It is seen that the X-ray absorption near edge structure (XANES) of supported Pt NPs at both Pt L_3 and L_2 edge exhibit a considerable whiteline (WL) compared to the Pt foil (Figure 5.4). The WL at Pt L_2 and L_3 edges arise from the dominant $2p_{1/2}$ and $2p_{3/2}$ transition to $5d_{3/2}$ and $5d_{5/2,3/2}$, respectively, indicating the presence of unoccupied densities of states (DOS) of Pt $5d_{5/2}$ and $5d_{3/2}$ character in the catalysts. The catalytic activity and durability of Pt for ORR has a close

relationship with the DOS of the employed Pt NPs. The normalized XANES and derivative spectra for both the Pt L_3- and L_2-edges of the Pt/N-ALDTa$_2$O$_5$/C, Pt/ALDTa$_2$O$_5$/C, and Pt/C catalysts are shown in Figure 5.4 with comparison to a standard Pt foil. It can be observed in Figure 5.4a that the threshold energy (E_0) and the maximum energy (E_{peak}) of the Pt L_3-edge for these supported Pt catalysts are close to the reference of metallic Pt foil, confirming the metallic nature of the Pt NPs. However, the XANES profile and derivative spectra of Pt in Pt/N-ALDTa$_2$O$_5$/C catalyst demonstrate a dramatic difference from those of Pt/ALDTa$_2$O$_5$/C and Pt/C. It was noted that the slightly higher WL intensity (Figure 5.4a) and the positively shifted peak energy in derivative spectra (Figure 5.4b) for Pt/N-ALDTa$_2$O$_5$/C compared to other catalysts, implies that the depletion of d-band in Pt/N-ALDTa$_2$O$_5$/C is greater than that of Pt/ALDTa$_2$O$_5$/C and Pt/C catalysts. The appearance of higher unoccupied density of d states of Pt is likely due to the electron transfer from Pt to N-Ta$_2$O$_5$ NPs, which confirms the strong interactions between Pt NPs and N-Ta$_2$O$_5$/C support. Moreover, the corresponding Pt L_2-edge WL exhibits considerable variation among the catalysts. The results indicate that L_2-edge WL intensity increasing in the order of: Pt foil < Pt/C < Pt/ALDTa$_2$O$_5$/C < Pt/N-ALDTa$_2$O$_5$/C, which follows the same order with the long-term durability for different catalysts. Therefore, the increase of the WL intensity in Pt/N-ALDTa$_2$O$_5$/C compared to Pt/ALDTa$_2$O$_5$/C and Pt/C can reflect a stronger interaction between Pt and N-Ta$_2$O$_5$/C support. The quantitative analysis to determine the occupancy of 5d states through detailed examination of WL profile in each sample will be further discussed below.
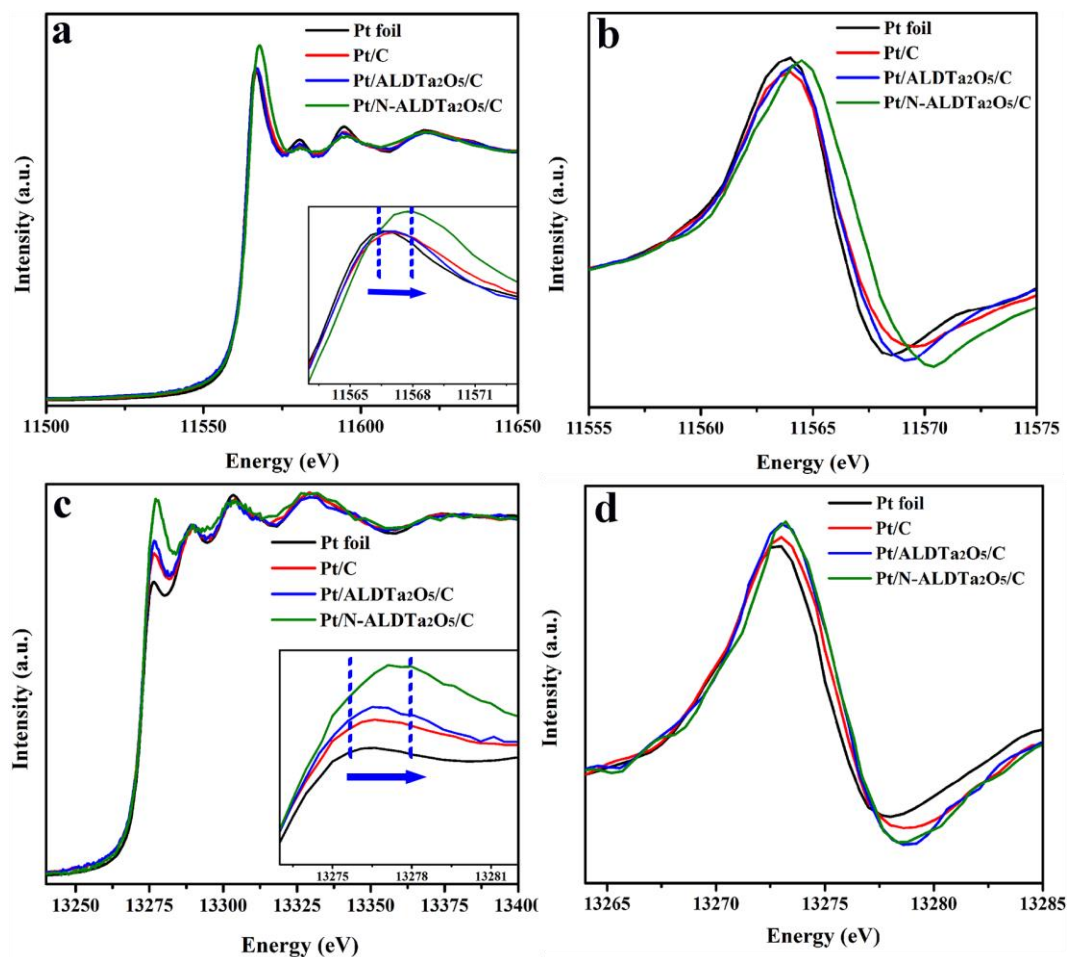
Figure 5.5. X-ray absorption studies. (a) The normalized and (b) derivative XANES spectra at the Pt L3-edge of the Pt/N-ALDTa₂O₅/C, Pt/ALDTa₂O₅/C, Pt/C and Pt foil. The inset shows the enlarged spectra at the Pt L3-edge white line (WL). (c) The normalized and (d) derivative XANES spectra at the Pt L2-edge of Pt/N-ALDTa₂O₅/C, Pt/ALDTa₂O₅/C, Pt/C and Pt foil. The inset shows the enlarged spectra at the Pt L2-edge white line (WL).

Table 5-1. Pt L3-edge and Pt L2-edge threshold and whiteline parameters of different catalysts.

Sample	Pt L_3 edge WL				Pt L_2 edge WL						
	E_0 (eV)[a]	$E_{(peak)}$(eV)[b]	Γ(eV)[c]	ΔA_3[d]	E_0(eV)[a]	$E_{(peak)}$(eV)[b]	Γ(eV)[c]	ΔA_2[d]	$h_{5/2}$	$h_{3/2}$	Total
Pt Foil	11564	11566.6	4.0	6.173	13273	13276.4	2.5	2.516	0.572	0.117	0.689
Pt/C	11564	11567.1	5.4	6.776	13273	13276.6	1.9	3.753	0.620	0.175	0.795

| Pt/ALDTa$_2$O$_5$/C | 11563.9 | 11566.9 | 4.5 | 7.018 | 13273 | 13276.8 | 1.3 | 3.956 | 0.642 | 0.184 | 0.826 |
| Pt/N-ALDTa$_2$O$_5$/C | 11564.5 | 11567.8 | 5.9 | 7.388 | 13273 | 13277.6 | 5.1 | 4.203 | 0.676 | 0.196 | 0.871 |

[a] Position of the point of inflection of the rising edge; [b] Peak position; [c] Line width at Half maximum of the WL; [d] Area under the difference curve for unity edge jump, the unity edge jump for the Pt L$_3$ and L$_2$ edge corresponds to a value of 2.5×10^3 cm^{-1} and 1.16×10^3 cm^{-1}, respectively.

For a better understanding of the effect of the unoccupied densities of 5d states of Pt NPs on different supports, the quantitative analysis of Pt L$_3$ and L$_2$ edge WL intensity has been conducted based on the method reported by Sham et al. [43] and Sun et al. [17, 45] For the set of experimental data recorded in this work, the Pt L$_3$ and L$_2$ edge threshold, WL parameters and the corresponding 5d hole counts of h$_{3/2}$ and h$_{5/2}$ are summarized in Table 1. These results quantitatively confirm the observations made on the Pt L$_3$ and L$_2$ edge XANES; i.e., the Pt/N-ALDTa$_2$O$_5$/C has the highest total unoccupied DOS of the 5d hole counts of 0.871 than that of 0.826 for Pt/ALDTa$_2$O$_5$/C and 0.795 for Pt/C. The character of Pt 5d unoccupied densities of states correlates well with its performance. The higher unoccupied DOS of Pt 5d hole number stands for the stronger interactions between Pt NPs and support, which leads to an advanced electrocatalytic activity and durability performance. It could be concluded that the modification of the N-Ta$_2$O$_5$/C support play significant role in affecting the electronic states of Pt NPs, thus forming the strong metal-support interaction and leading to the enhancement of long-term stability of Pt NPs.

5.4 Conclusion

In summary, we have successfully used the ALD method to prepare a novel Pt/N-ALDTa$_2$O$_5$/C electrocatalyst in which the carbon support is decorated by N-doped-Ta$_2$O$_5$ particles and yields Pt NPs that are well-anchored and stick tightly on the modified carbon surface. Experimental results demonstrate that Pt/N-ALDTa$_2$O$_5$/C catalyst shows improved activity for the ORR compared to the Pt/C catalyst. More interestingly, the Pt/N-ALDTa$_2$O$_5$/C catalyst exhibits superior long-term durability, reflected by a mass activity two times higher than that of Pt/C, after 10,000 cycles of accelerate durability tests. The improved activity and stability are attributed to the introduction of a N-Ta$_2$O$_5$ bridge layer between Pt NPs and carbon support, forming strong metal-support interactions and thus effectively prevent Pt nanocrystals from migration and aggregation. The X-ray absorption

spectra suggests that the Pt/N-ALDTa$_2$O$_5$/C catalyst shows noticeable electron delocalization of Pt d orbitals and with electron transfer from Pt to N-Ta$_2$O$_5$/C support, which give the most direct evidence for the strong interactions between Pt NPs and N-Ta$_2$O$_5$/C support. The result of this work provides insights for future design of electrocatalysts with high stability through increased interactions between catalytic metal particles and support.

Acknowledgment

Reference

[1]. Yoshida, T. and K. Kojima, The Electrochemical Society Interface, 2015. **24**(2): p. 45-49.

[2]. Debe, M.K., Nature, 2012. **486**: p. 43.

[3]. Eberle, U., B. Muller, and R. von Helmolt, Energy & Environmental Science, 2012. **5**(10): p. 8780-8798.

[4]. Chung, D.Y., J.M. Yoo, and Y.-E. Sung, Advanced Materials: p. 1704123.

[5]. Park, S., Y. Shao, J. Liu, and Y. Wang, Energy & Environmental Science, 2012. **5**(11): p. 9331-9344.

[6]. Su, L., W. Jia, C.-M. Li, and Y. Lei, ChemSusChem, 2014. **7**(2): p. 361-378.

[7]. Sui, S., X. Wang, X. Zhou, Y. Su, S. Riffat, and C.-j. Liu, Journal of Materials Chemistry A, 2017. **5**(5): p. 1808-1825.

[8].   Song, Z., B. Wang, N. Cheng, L. Yang, D. Banham, R. Li, S. Ye, and X. Sun, Journal of Materials Chemistry A, 2017. **5**(20): p. 9760-9767.

[9].   Guo, L., W.-J. Jiang, Y. Zhang, J.-S. Hu, Z.-D. Wei, and L.-J. Wan, ACS Catalysis, 2015. **5**(5): p. 2903-2909.

[10]. Cheng, N., M.N. Banis, J. Liu, A. Riese, X. Li, R. Li, S. Ye, S. Knights, and X. Sun, Advanced materials, 2015. **27**(2): p. 277-281.

[11]. Li, Y., Y. Li, E. Zhu, T. McLouth, C.-Y. Chiu, X. Huang, and Y. Huang, Journal of the American Chemical Society, 2012. **134**(30): p. 12326-12329.

[12]. Li, L., L. Hu, J. Li, and Z. Wei, Nano Research, 2015. **8**(2): p. 418-440.

[13]. Meier, J.C., C. Galeano, I. Katsounaros, A.A. Topalov, A. Kostka, F. Schüth, and K.J.J. Mayrhofer, ACS Catalysis, 2012. **2**(5): p. 832-843.

[14]. Speder, J., A. Zana, I. Spanos, J.J.K. Kirkensgaard, K. Mortensen, M. Hanzlik, and M. Arenz, Journal of Power Sources, 2014. **261**: p. 14-22.

[15]. Akalework, N.G., C.-J. Pan, W.-N. Su, J. Rick, M.-C. Tsai, J.-F. Lee, J.-M. Lin, L.-D. Tsai, and B.-J. Hwang, Journal of Materials Chemistry, 2012. **22**(39): p. 20977-20985.

[16]. Awaludin, Z., M. Suzuki, J. Masud, T. Okajima, and T. Ohsaka, The Journal of Physical Chemistry C, 2011. **115**(51): p. 25557-25567.

[17]. Banis, M.N., S. Sun, X. Meng, Y. Zhang, Z. Wang, R. Li, M. Cai, T.-K. Sham, and X. Sun, The Journal of Physical Chemistry C, 2013. **117**(30): p. 15457-15467.

[18]. Ho, V.T.T., C.-J. Pan, J. Rick, W.-N. Su, and B.-J. Hwang, Journal of the American Chemical Society, 2011. **133**(30): p. 11716-11724.

[19]. Huang, S.-Y., P. Ganesan, S. Park, and B.N. Popov, Journal of the American Chemical Society, 2009. **131**(39): p. 13898-13899.

[20].   Huang, S.-Y., P. Ganesan, and B.N. Popov, ACS Catalysis, 2012. **2**(5): p. 825-831.

[21].   Kumar, A. and V. Ramani, ACS Catalysis, 2014. **4**(5): p. 1516-1525.

[22].   He, D., C. Zeng, C. Xu, N. Cheng, H. Li, S. Mu, and M. Pan, Langmuir, 2011. **27**(9): p. 5582-5588.

[23].   Chen, S., Z. Wei, X. Qi, L. Dong, Y.-G. Guo, L. Wan, Z. Shao, and L. Li, Journal of the American Chemical Society, 2012. **134**(32): p. 13252-13255.

[24].   Cheng, N., M.N. Banis, J. Liu, A. Riese, S. Mu, R. Li, T.-K. Sham, and X. Sun, Energy & Environmental Science, 2015. **8**(5): p. 1450-1455.

[25].   da Silva, G.C., M.R. Fernandes, and E.A. Ticianelli, ACS Catalysis, 2018: p. 2081-2092.

[26].   Duma, A.D., Y.-C. Wu, W.-N. Su, C.-J. Pan, M.-C. Tsai, H.-M. Chen, J.-F. Lee, H.-S. Sheu, V.T.T. Ho, and B.-J. Hwang, ChemCatChem, 2018: p. 1-12.

[27].   Kou, R., Y. Shao, D. Mei, Z. Nie, D. Wang, C. Wang, V.V. Viswanathan, S. Park, I.A. Aksay, Y. Lin, Y. Wang, and J. Liu, Journal of the American Chemical Society, 2011. **133**(8): p. 2541-2547.

[28].   Binninger, T., E. Fabbri, R. Kötz, and T.J. Schmidt, Journal of The Electrochemical Society, 2014. **161**(3): p. H121-H128.

[29].   Lewera, A., L. Timperman, A. Roguska, and N. Alonso-Vante, The Journal of Physical Chemistry C, 2011. **115**(41): p. 20153-20159.

[30].   Epshteyn, A., Y. Garsany, K.L. More, H.M. Meyer, V. Jain, A.P. Purdy, and K.E. Swider-Lyons, ACS Catalysis, 2015. **5**(6): p. 3662-3674.

[31].   Garsany, Y., M.B. Sassin, B.D. Gould, and K. Swider-Lyons, ECS Transactions, 2015. **69**(17): p. 1243-1250.

[32]. Korovina, A., Y. Garsany, A. Epshteyn, A.P. Purdy, K. More, K.E. Swider-Lyons, and D.E. Ramaker, The Journal of Physical Chemistry C, 2012. **116**(34): p. 18175-18183.

[33]. Seo, J., D. Cha, K. Takanabe, J. Kubota, and K. Domen, ACS Catalysis, 2013. **3**(9): p. 2181-2189.

[34]. Seo, J., L. Zhao, D. Cha, K. Takanabe, M. Katayama, J. Kubota, and K. Domen, The Journal of Physical Chemistry C, 2013. **117**(22): p. 11635-11646.

[35]. Bezerra, C.W.B., L. Zhang, H. Liu, K. Lee, A.L.B. Marques, E.P. Marques, H. Wang, and J. Zhang, Journal of Power Sources, 2007. **173**(2): p. 891-908.

[36]. Ishihara, A., M. Tamura, K. Matsuzawa, S. Mitsushima, and K.-i. Ota, Electrochimica Acta, 2010. **55**(26): p. 7581-7589.

[37]. Oh, T., J.Y. Kim, Y. Shin, M. Engelhard, and K.S. Weil, Journal of Power Sources, 2011. **196**(15): p. 6099-6103.

[38]. Li, X., X. Meng, J. Liu, D. Geng, Y. Zhang, M.N. Banis, Y. Li, J. Yang, R. Li, and X. Sun, Advanced Functional Materials, 2012. **22**(8): p. 1647-1654.

[39]. Liu, J., M.N. Banis, X. Li, A. Lushington, M. Cai, R. Li, T.-K. Sham, and X. Sun, The Journal of Physical Chemistry C, 2013. **117**(39): p. 20260-20267.

[40]. Meng, X., J. Liu, X. Li, M.N. Banis, J. Yang, R. Li, and X. Sun, RSC Advances, 2013. **3**(20): p. 7285-7288.

[41]. Liu, J., X. Meng, Y. Hu, D. Geng, M.N. Banis, M. Cai, R. Li, and X. Sun, Carbon, 2013. **52**: p. 74-82.

[42]. Mansour, A., J. Cook Jr, and D. Sayers, The Journal of Physical Chemistry, 1984. **88**(11): p. 2330-2334.

[43]. Sham, T., S. Naftel, and I. Coulthard, Journal of applied physics, 1996. **79**(9): p. 7134-7138.

[44]. Kuhn, M. and T. Sham, Physical Review B, 1994. **49**(3): p. 1647.

[45]. Sun, S., G. Zhang, N. Gauquelin, N. Chen, J. Zhou, S. Yang, W. Chen, X. Meng, D. Geng, M.N. Banis, R. Li, S. Ye, S. Knights, G.A. Botton, T.-K. Sham, and X. Sun, Scientific Reports, 2013. **3**: p. 1775.

[46]. Cheng, N., S. Stambula, D. Wang, M.N. Banis, J. Liu, A. Riese, B. Xiao, R. Li, T.-K. Sham, and L.-M. Liu, Nature communications, 2016. **7**: p. 13638.

[47]. Trasatti, S. and O. Petrii, Pure and applied chemistry, 1991. **63**(5): p. 711-734.

[48]. Zhang, M., P. Hou, Z. Wang, and P. Kang, ChemElectroChem, 2018. **5**(5): p. 799-804.

[49]. Mayrhofer, K., D. Strmcnik, B. Blizanac, V. Stamenkovic, M. Arenz, and N. Markovic, Electrochimica Acta, 2008. **53**(7): p. 3181-3188.

[50]. Sheng, W., S. Chen, E. Vescovo, and Y. Shao-Horn, Journal of the Electrochemical Society, 2011. **159**(2): p. B96-B103.

Supporting information
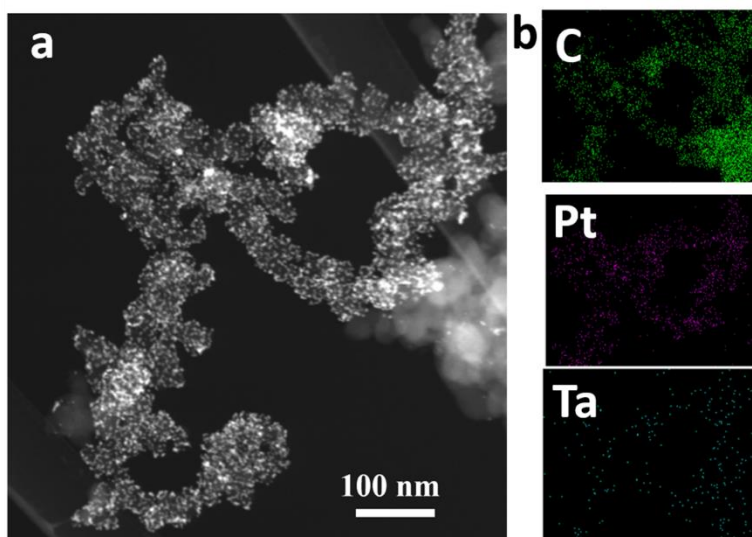
Figure S5.1. TEM image and corresponding element maps of C, Pt, Ta for sample of Pt/N-ALDTa$_2$O$_5$/C.
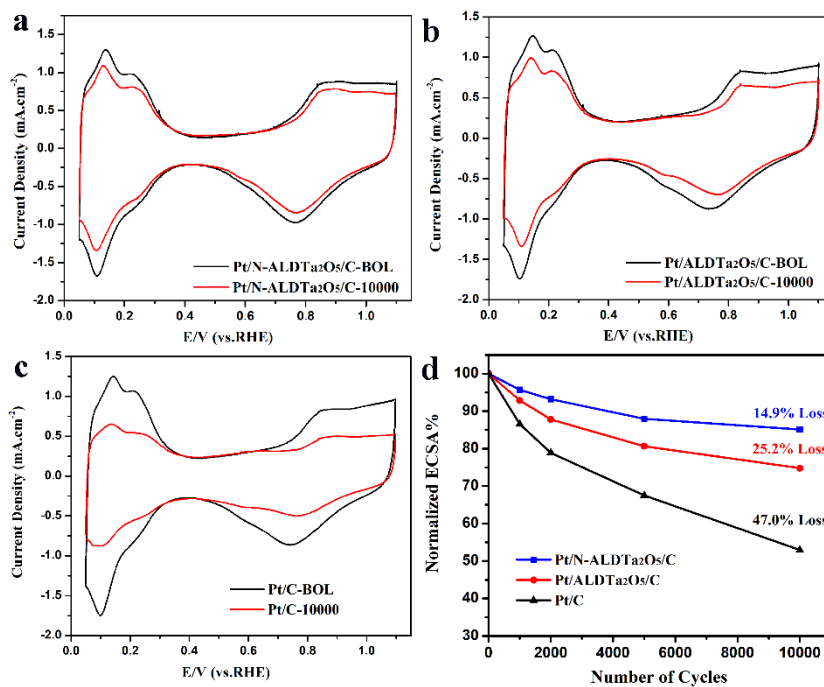
Figure S5.2. Intermediate characterization CV curves of (a) Pt/N-ALDTa$_2$O$_5$/C, (b) Pt/ALDTa$_2$O$_5$/C and (c) Pt/C catalysts during the potential-cycling (0.6 V–1.0 V vs. RHE) durability tests in an O$_2$-saturated 0.1 M HClO$_4$ solution at a scan rate of 50 mV·s^{-1}.

Chapter 6

6 Ultra-low loading and high-performing Pt catalyst for PEMFC anode achieved by atomic layer deposition

*This chapter is to be submitted for peer-reviewed publication.

Decreasing Pt loading in the anode layer below ~0.025 mg·cm^{-2} is found to reduce the hydrogen oxidation reaction (HOR) rate during polymer electrolyte membrane fuel cells (PEMFCs) normal operation, when using conventional Pt/C catalysts and electrode coating methods. To achieve extremely low Pt loading in the anode catalyst layer while maintaining high PEMFC performance and durability, a series of membrane electrode assemblies (MEAs) with low Pt loading in the anode layer are successfully prepared using an atomic layer deposition (ALD) technique. By controlling the ALD cycle number, the Pt nanoparticles (NPs) with different size and loading amount are directly deposited on the bonded carbon layer to form the anode catalyst layer. The ALDPt NPs with uniform particle size are highly dispersed on all the available carbon surface, which promote the ALDPt with high electrochemical active surface area and enable enhanced performance of ALDPt-MEAs. Particularly, the 50ALDPt-MEA with the anode Pt prepared by 50ALD cycles shows excellent H$_2$-air PEMFC activity and durability. Importantly, the 20ALDPt-MEA with ultra-low Pt loading of 0.01 mg·cm^{-2} displays much higher anode Pt surface area of 155 m^2·g^{-1}$_{Pt}$ which is around 3.0 times higher than that of 50.3 m^2·g^{-1}$_{Pt}$ for commercial Pt catalyst. The 20ALDPt anode also shows better durability performance with only 10.2% power density loss than that of commercial Pt/C anode (14.5 % loss) after anode potential cycling accelerated stress test. The ultra-low Pt loading, uniform Pt distribution, high MEA performance and durability achieved indicate that the ALD technique has a great potential for developing next-generation electrocatalysts

6.1 Introduction

Polymer electrolyte membrane fuel cells (PEMFCs) are one of the most efficient devices for converting the stored chemical energy from hydrogen into the useable electrical energy, making it a key technology as society transitions toward clean forms of energy.[1-5] Unfortunately, the electrode catalyst layers in PEMFCs require high loading amount of platinum-based (Pt) noble metal catalysts to drive the desired electrochemical reactions (hydrogen oxidation reaction (HOR) at the anode, and oxygen reduction reaction (ORR) at the cathode). Therefore, it is of great importance to reduce Pt-based noble metal catalysts loading to make PEMFCs cost-competitive with conventional technologies. [6, 7] The U.S. Department of Energy (DOE) targeting a total Pt loading of 0.125 mg·cm^{-2} by 2020 [8] for the cost requirement, allowing only 0.025 mg·cm^{-2} for the anode, which is the lowest loading achievable by the conventional method without losing performance towards HOR kinetics.[9-12] The fast HOR kinetics on supported platinum catalyst (Pt/C) requires a very small amount of anode catalyst, and it has been found that the anode is not likely to fail when operating in neat hydrogen with Pt/C catalysts.[13-16] However, when extremely reduce the Pt loading to less than 0.025 mg·cm^{-2}, the risk of the conventional coated anode could result in reduced HOR performance in MEA due to the very thin layer thickness. If using low Pt content (<50% Pt/C) catalyst to increase the layer thickness, the proton and the electric conductivities could be the issues. Besides, the cycling durability of the low Pt loading anodes in air/air startup/shutdown (SUSD) could become another critical failure modes. [17-20] For example, during PEMFC air/air startup/shutdown (SUSD) process, the anode potential may vary from ~ 0 V up to ~ 1.0 V (vs. RHE) when the anode channel gas alternates from hydrogen rich fuel gas to atmospheric air. This potential variation will generate the oxidation of Pt NPs to ions and oxides. Consequently, the oxidized Pt species can migrate and re-deposit in the anode layer and/or membrane components during the SUSD operation. [21, 22] This phenomenon will loss the Pt utilization and consume the effective Pt amount in anode layer, which decrease the PEMFC performance and durability significantly. Although significant advances have been achieved on lowering Pt loading in anode layer, very few of them are concerned for both the high performance, stability and durability during the SUSD cycling. [23-26] Therefore, pursuing a new technology to prepare

the electrode catalyst layer with not only low Pt loadings, but also excellent performance and durability is necessary to realize the commercialization of low-cost PEMFCs.

Direct deposition of Pt NPs on the surface of carbon-coated electrode layer is recognized as an efficient way for preparing the high efficient fuel cell catalysts, because it can promote the exposure of Pt active surface and enhances the Pt utilization in the membrane electrode assembly (MEA). [23, 24, 26-29] Among the synthesis method for Pt catalyst, atomic layer deposition (ALD) has emerged as an attractive technique for deposition of Pt NPs due to the advantages of good uniformity, high dispersion and precise size control. [30-32] Theoretically, the self-limiting reaction nature of ALD enables the achievement of monolayer dispersion of metal atoms on the substrate, which makes ALD an attractive technique for preparing Pt NPs in PEMFCs electrode with high dispersion and controllable loading. To date, a few studies have reported on the preparation of highly dispersed Pt catalyst or transition metal oxide NPs by ALD for PEMFCs application. Sun et al. prepared Pt NPs on different carbon support by the ALD method, and the synthesized ALDPt-CNTs or ALDPt-Graphene are used as electrocatalysts for ORR, methanol oxidation, and water splitting, which show significantly enhanced electrocatalytic activity. [32-34] However, direct deposition of the Pt NPs on the bonded carbon electrode layer by ALD has not been reported yet. Additionally, low Pt loading impact on the PEMFCs performance and durability prepared by ALD still indicates lack of investigations.

In this work, ALD technology is used for the first time to deposit ultra-low Pt loadings on the bonded carbon layer, by which the Pt NPs are directly deposited onto the surface of carbon black to form the anode catalyst layer. The novelty of post deposition of Pt on PEMFC anode layer is that it can effectively improve the Pt utilization and enhance the PEMFC performance while reducing the Pt loading. Through control the number of ALD cycles (50, 30 and 20), a series of anode layers with different Pt loadings and particle size are obtained. The MEA assembled with anode Pt catalyst prepared by ALD showed much better H_2-air PEMFCs performance and durability than the MEA prepared with the commercial catalyst (50%Pt/C) through a conventional method. The ultra-low Pt loading, uniform Pt distribution, excellent H_2-air PEMFCs performance and durability, indicate that the ALD technique has great potential for developing next-generation electrocatalysts in PEMFCs application.

6.2 Experiment

ALD of Pt NPs on carbon support layers

The porous carbon coating layers with carbon black and Nafion binder coated on PTFE film, which served as the substrate for Pt deposition, are provided by Ballard power system company. Pt NPs are deposited on the anode carbon layers by ALD method (Cambridge nanotechnology Inc., USA) using $MeCpPtMe_3$ and O_2 as precursors and a similar procedure with our previously reported work. High-purity N_2 is used as both purging gas and carrier gas. The carbon coating sheets with size around 10 cm x 10 cm is placed in ALD chamber. The deposition temperature is 250°C, while the bubbler of $MeCpPtMe_3$ is kept at 65°C to provide a steady-state flux of $MeCpPtMe_3$ vapor. Gas lines are hold at 100 °C to avoid precursor condensation. For each ALD cycle, 1.0 s of the $MeCpPtMe_3$ pulse and 5.0 s of the O_2 pulse were separated by a 20 s N_2 purge. [32] By applying the ALD cycles of 50, 30 and 20, the ALDPt/C anode catalyst with controlled Pt loading of 0.035, 0.02, 0.01 $mg \cdot cm^{-2}$ were prepared, respectively.

MEA preparation and single fuel cell performance testing

Prior to fabricating the MEA, a catalyst-coated membrane (Nafion membrane) was prepared by a decal transfer method. First, a half-CCM of cathode-coated Nafion membrane with Pt loading of 0.4 $mg \cdot cm^{-2}$ was prepared using the commercial 50wt%Pt/C catalyst (Tanaka Kikinzoku Kogyo TEC10E50E). Then the anode catalyst layer with Pt NPs deposited by ALD was decal transferred onto the other side of the Nafion membrane by hot-pressing. Finally, the CCM was sandwiched between two gas diffusion layers (GDL) and assembled by the Kapton frame with an active area of 45 cm^2. To understand the Pt loading impact on anodic HOR activity and investigate the lower limiting of anode Pt loading for PEMFC application, the MEAs composed with anode of ALDPt with loading of 0.035, 0.02, 0.01 $mg \cdot cm^{-2}$ and cathode with 0.4 $mg \cdot cm^{-2}$ commercial Pt/C were prepared, respectively. Additionally, the MEA made by commercial Pt/C with Pt loading of 0.4 $mg \cdot cm^{-2}$ for cathode and 0.035 $mg.cm^{-2}$ for anode was fabricated for comparison.

The MEA single cell performance was tested at Ballard Power System. PEMFC single cell performance testing was conducted under conditions of 75 °C, 5 psig, 100% relative

humidity (RH), with anode feeding of hydrogen and cathode of air at the flow rate of 2 and 4 slpm, respectively. Before testing, MEA conditioning was performed at the current density of 1.3 A·cm^{-2} for 16 h. The PEMFC H$_2$-air polarization curved were recorded using standard fuel cell test stations in a current control mode. Moreover, to understand the active surface area of anode catalyst, the CV and CO striping was carried out on the MEA anode side. The current-voltage curves of MEA anode catalyst for hydrogen oxidation was determined. To evaluate the durability and lifetime of anode catalyst, a startup/shutdown cycling protocol using a square wave potential control with 30 s intervals by holding at 0.1 V and 1.0 V (vs. RHE) was performed on anode catalyst. During the accelerated durability test (ADT), the anode feeding with N$_2$ serves as the working electrode, while cathode under the H$_2$ atmosphere works as the counter electrode. In this cycling protocol, cathode side conditioned at H$_2$ with negligible or even no cathode catalyst degradation occurs. While, the working electrode of anode went through the alternate low and high potential cycling, which would display varied catalyst degradation for the different anode catalysts. A total 2000 ADT cycles were performed on MEA and intermediate performance was recorded to monitor the air polarization curves, power density and anode electrochemical catalyst active surface area (ECSA) loss.

Physical characterization

The morphology and microstructure of Pt NPs were characterized by high-resolution transmission electronic microscopy (HRTEM, JEOL 2010FEG) and a Hitachi S-4800 field emission scanning electronic microscopy (FESEM). The Pt loading on anode layers prepared by ALD was determined by inductively coupled plasma-optical emission spectroscopy (ICP-OES). The cross-sections of MEA thin film after ADT cycling were prepared by a microtome (Leitz microtome type 1310) technique for a detailed structural analysis. To understand the MEA cross-section structures after ADT cycling, HRTEM coupled with electron energy loss spectroscopy (EELS) characterization were carried out on an aberration-corrected (probe and image-forming lenses) FEI Titan Cubed 80–300 kV microscope equipped with a Gatan Image Filter Quantum-965 spectrometer operated at 200 kV. EELS maps were recorded with a 0.25 eV/channel dispersion of the spectrometer.

6.3   Result and discussion

Structural characterization
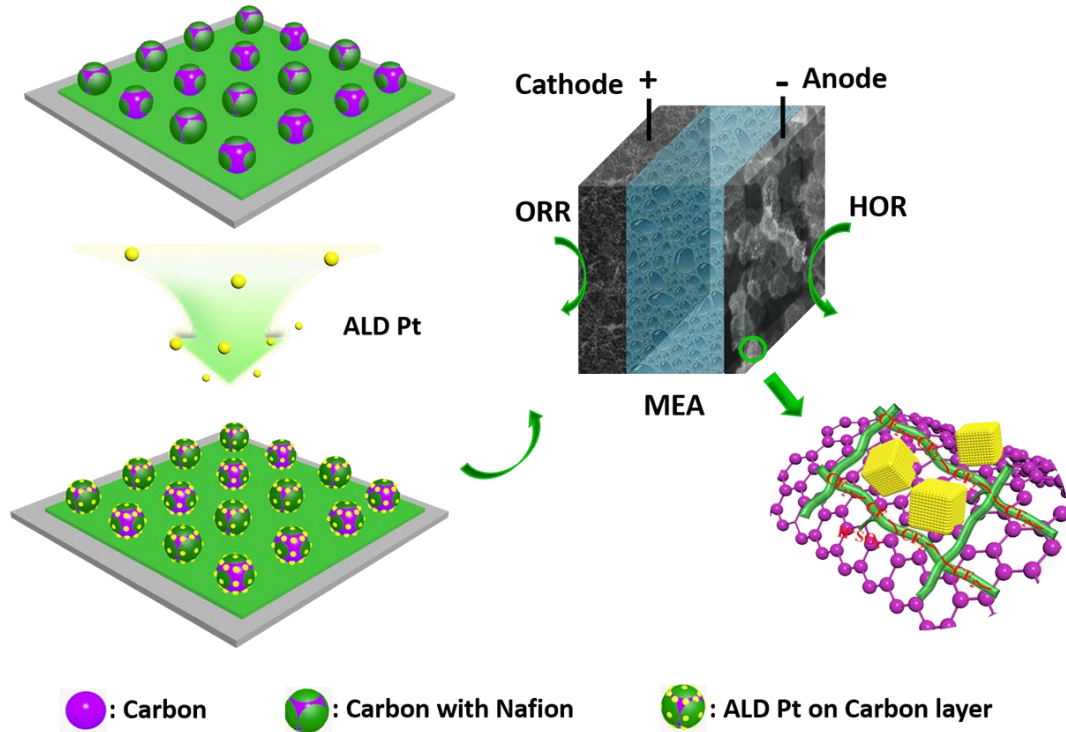
Figure 6.1. Schematic illustration of deposit Pt NPs on anode carbon layers by ALD for PEMFCs.

Figure 6.1 presents the deposition of Pt NPs on the carbon layers using ALD technique. By controlling the ALD cycle number, different Pt loadings can be designed on the carbon layers, forming the anode catalyst layers for PEMFC application. After ALD of Pt NPs, the anode catalyst layer was decal transferred to the Nafion membrane by a method of hot-pressing and obtained the CCM. Subsequently, by assembling CCM with GDL layers to fabricate the MEA single cell. From the TEM images of Figure 6.2 and SEM images of Figure S6.1, it can be found that, the Pt particle size and loading amount can be controlled by varying the ALD cycles. For 50 ALD cycles, the Pt loading of 0.035 mg·cm^{-2} can be achieved on the carbon layers, with the average Pt NPs size of 3.3±0.05 nm (Figure 6.2b). By contrast for the commercial Pt/C catalyst with the same Pt 0.035 mg·cm^{-2} loading, the Pt NPs in commercial Pt/C catalyst was tended to aggregate along the edges and defective sites with

low energy spots (Figure 6.2a). Therefore, it could be found that the ALD Pt exhibit significant advantage in uniform dispersion on all the available carbon surface, which is expected to benefit for achieving the high ECSA of Pt catalyst. By lowering the ALD cycles to 30, a decreased Pt loading of 0.02 mg·cm^{-2} and smaller Pt particle size of 2.3±0.05 nm was deposited on carbon layers (Figure 6.2c). To further enable the ultra-low Pt loading to 0.01 mg·cm^{-2}, 20 ALD cycles were applied to construct the Pt NPs on carbon layers. The HREM image in Figure 6.2d indicates that tiny Pt NPs with the average size of 1.4±0.025 nm are deposited on the carbon support with a homogeneous distribution on all the available surface.
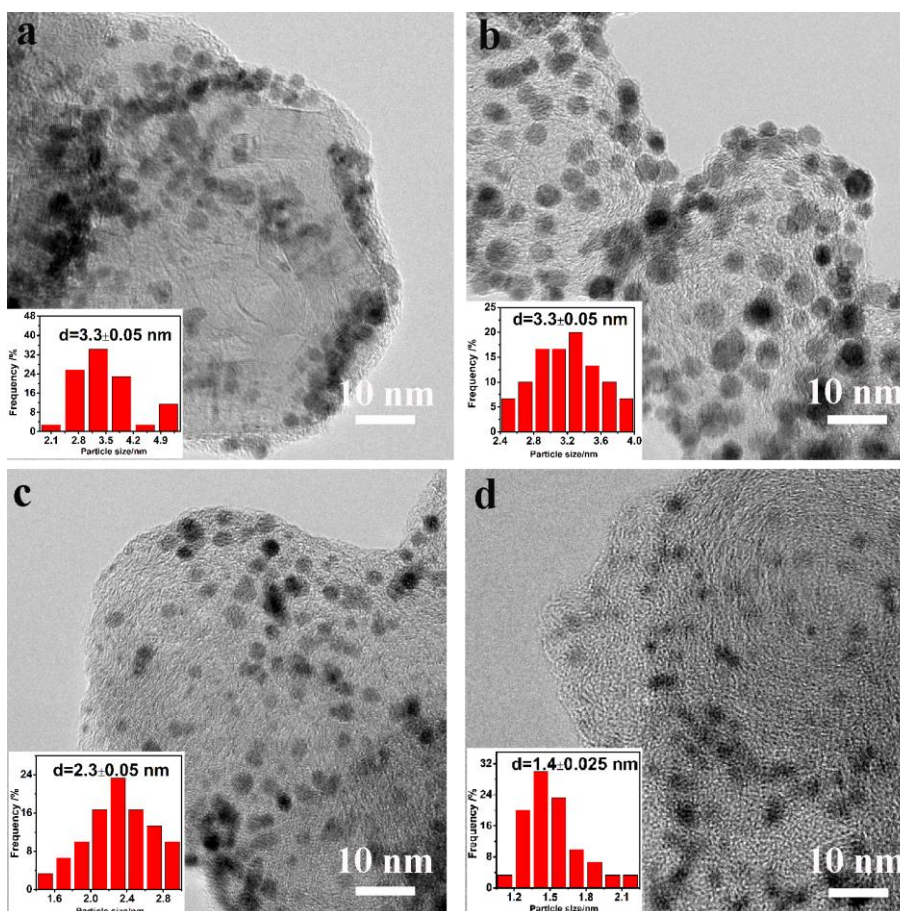
Figure 6.2. HRTEM images and corresponding size distribution histogram of anode catalyst layer with Pt NPs made by (a) commercial Pt/C, (b) 50ALD, (c)30ALD, (d)20ALD.

Fuel cell performance of ALDPt catalysts

To understand the anode Pt loading impact on the single cell performance. A series MEAs single cells with anode/cathode Pt loadings of: 0.035/0.4, 0.02/0.4 and 0.01/0.4 mg·cm^{-2}, in which anode Pt catalyst made by ALD and cathode of commercial Pt/C were prepared. In Figure 6.3a, the beginning-of-life (BOL) performance of H$_2$-air polarization curves for MEAs with different anode Pt loading are displayed. It is noticed that all the MEAs show the open circuit voltage (OCV) with a high value of ~0.954 V (vs. RHE). This indicates that no short circuit or gas leaking is occurring during PEMFC operation. In the low current density region (0-0.2 A·cm^{-2}), all the MEAs exhibit the similar high cell voltage. However, with increasing the current density to the ohmic and mass polarization region (0.2-2.0 A·cm^{-2}), an obvious cell voltage difference appears between the ALD Pt-MEAs and commercial Pt-MEA. The 50ALDPt-MEA with anode Pt loading of 0.035 mg·cm^{-2} demonstrates an impressive performance and achieves considerable high cell voltage of 540 mV at the current density of 1.5 mA·cm^{-2}. At this current, it is indicated that there is a trend of performance and cell voltage decrease with reducing the anode ALDPt loading. However, the big surprise is that ALDPt catalyst still can achieve much higher performance than that of the commercial Pt/C even though at a much lower Pt loading. When lower the anode ALDPt loading to 0.02 and 0.01 mg·cm^{-2}, the 30ALDPt-MEA and 20ALDPt-MEA show the cell voltage of 522 and 506 mV at 1.5 mA·cm^{-2}, respectively, which are still higher performance than that of 502 mV obtained by commercial Pt-MEA with high Pt loading of 0.035 mg·cm^{-2}. The U.S. Department of Energy (DOE) targeting a total Pt-group metal loading of 0.125 mg·cm^{-2} by 2020. Allowing only 0.025 mg·cm^{-2} for the anode, which likely the lowest loading achievable without losing HOR performance. Using the conventional technology, it is not able to achieve the anode with Pt loading lower than 0.025 mg·cm^{-2}. However, in our research, by using the ALD technique the ultra-low Pt loading (0.01 mg·cm^{-2}) with uniform Pt distribution and high PEMFC performance could be achieved in the anode catalyst

layer.
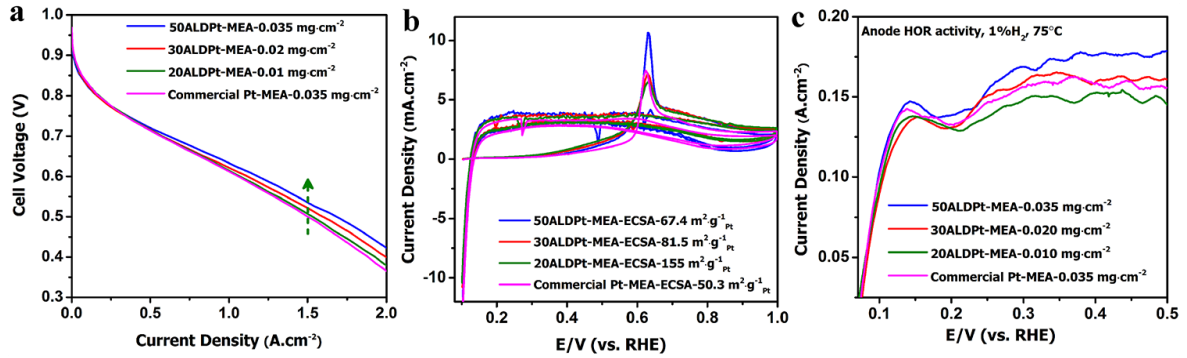
Figure 6.3. (a) the H₂-air polarization curves of ALDPt-MEAs and commercial Pt-MEA with varied anode Pt loading. (b) the CV and CO stripping I-V curves of ALDPt-MEAs and commercial Pt-MEA to investigate the anode catalyst active surface, scanning from 0.1-1.0 V at the rate of 20 mV·s⁻¹. (c) HOR cyclic voltammograms acquired with anode as working electrode feeding of 1%H₂/N₂ gas mixer and cathode as the counter electrode feeding of H₂, scanning from OCV to 0.6 V at the scan rate of 10 mV·s⁻¹.

The mass-transport profile of the ALDPt-MEAs is improved at the high current density region ($>1.5 \text{mA·cm}^{-2}$), suggesting the high electrochemical active surface area of ALDPt at anode, which shorten the proton pathway and promote diffusion and transportation of the reactants. To understand the real active Pt surface area in anode layer, the in-situ CO stripping voltammetry is conducted on the MEAs anode layer (Figure 6.3b). The CO adsorption to anode catalyst is carried out for 2min, followed by another 2min flowing away the extra CO using N_2. Subsequently, the voltammetry CO stripping measurement was conducted with anode as the working electrode feeding of N_2 and cathode as counter electrode feeding of H_2. As illustrated in Figure 6.3b, the 50ALDPt-MEA with ~3.3 nm Pt NPs dispersed on carbon support, which indicates the ECSA of 67.4 $m^2·g^{-1}_{Pt}$, higher than that of 50.3 $m^2·g^{-1}_{Pt}$ revealed by the commercial Pt-MEA under the same Pt loading of 0.035 mg·cm⁻². Interestingly, by reducing the ALD cycles to 30 and 20, much higher ECSA of 81.5 and 155 $m^2·g^{-1}_{Pt}$ could be achieved under the ultra-lower Pt loading of 0.02 and 0.01 mg·cm⁻², respectively. The enhanced ECSA of ALDPt catalyst implies the distinct advantage of ALD, which enables the highly dispersed and uniform Pt NPs on the carbon surface, promoting the high Pt active surface and enhancing the Pt utilization efficiency. The

significantly enhanced catalyst active surface of ALDPt contributes to the excellent ALDPt-MEA performance even the ultralow Pt loading applied at anode layers.

To test anode Pt catalytic activity toward HOR, the H_2 oxidation polarization curves are determined on the ALDPt-MEAs and commercial Pt-MEA with anode as the working electrode feed of 1%H_2/N_2 gas mixer and cathode as the counter electrode feed of H_2, then scanning the I-V curves from OCV to 0.6V (vs. RHE) at the scan rate of 10mV·s^{-1}. Figure 6.3c shows the HOR polarization curves on anode layers of ALDPt-MEAs and commercial Pt-MEA. There are three elementary reaction steps for HOR on Pt surface, based on the Tafel-Heyrovsky-Volmer mechanism. For all the MEAs anode surfaces, the HOR currents show a fast increase at small overpotentials, with the limiting current density of ~ 0.15 A·cm^{-2} being reached at overpotential of ~ 0.14 V. Moreover, it was found that the 50ALDPt-MEA shows higher limiting current density than that of commercial Pt-MEA, indicating the higher surface area of 50ALDPt than that of commercial Pt. Remarkably, the extremely low loading of 20ALDPt-MEA (0.01 mg·cm^{-2}) yielded no noticeable limiting current density loss compared with the high loading commercial Pt catalyst. Therefore, it could be concluded that 20ALDPt-MEA with extremely low Pt loading but contains more specific heterogenous hydrogen oxidation sites than commercial Pt catalyst, which signifying its significantly enhanced catalytic abilities toward the HOR.

PEMFCs anode catalyst stability during startup/shutdown cycling

Since the MEA anode catalyst degradation occurs by cell reversal current upon reducing the anode Pt loading, thus anode catalyst stability during the SUSD cycling should be investigated under the ultra-low Pt loading. For SUSD cycling, holding the anode potential at 0.1 V for 30s and then switching to 1.0 V for another 30s, totally 60s for each cycle and 2000 SUSD cycles were carried out on the anode to determine the catalyst stability. As shown in Figure 6.4 a-d, at low current density range (0-0.2 A·cm^{-2}), there presents a negligible cell voltage loss for both the ALDPt-MEAs and commercial Pt-MEA, which implies the constant ORR kinetics and no cathode catalyst degradation during SUSD cycling. When increased to the high current density of 0.2-2.0 A·cm^{-2} region, the cell voltage shows a linear relationship with the current density. In this region, the cell voltage loss is mainly arising from the ohmic loss, which is from the resistance to the flow of protons in electrolyte. When the SUSD

cycling is executed on the anode layer, the cell voltage loss in 0.2-2.0 $A \cdot cm^{-2}$ region is mainly resulted from the anode catalyst degradation. Due to the anode active surface loss, the HOR kinetics decrease with proceeding the SUSD cycling and showing as the high overpotential at anode for HOR, which results the lower cell voltage and high voltage loss after SUSD cycling. Therefore, by analysis and comparison the cell voltage loss of MEAs after the SUSD cycling, the anode catalyst degradation and stability could be revealed. By measuring the H_2-air polarization curves of PEMFC before and after 2000 SUSD cycling, it was found that both the ALDPt-MEAs and commercial Pt-MEA display the anode catalyst degradation and performance loss (Figure 6.4 a-d). Differently, the 50ALDPt-MEA and 30ALDPt-MEA show much high BOL peak power density of 0.87 $W \cdot cm^{-2}$ and 0.82 $W \cdot cm^{-2}$, which decreased to 0.81 $W \cdot cm^{-2}$ and 0.75 $W \cdot cm^{-2}$ with only 6.9% and 8.5 % power density loss after 2000 SUSD cycling, respectively, indicating the excellent PEMFC performance and durability for the ALD Pt catalyst. For 20ALDPt-MEA with 0.01 $mg \cdot cm^{-2}$ extremely low Pt loading at anode, the BOL peak power density is 0.78 $W \cdot cm^{-2}$ higher than that of 0.76 $W \cdot cm^{-2}$ for commercial Pt-MEA with higher Pt loading. The power density of 20ALDPt-MEA decreased to 0.70 $W \cdot cm^{-2}$ with 10.2% loss better than that of commercial Pt-MEA which degrades from 0.76 $W \cdot cm^{-2}$ to 0.65 $W \cdot cm^{-2}$ with 14.5% performance loss. The SUSD cycling test indicates the ALD Pt shows much higher stability than that of commercial Pt catalyst even under the extremely lower Pt loading. The Pt NPs prepared by ALD with strong covalent bonding between ALDPt NPs and carbon support, which supposed makes great contributions to the superior stability of ALD Pt during the SUSD cycling procedure. Figure 6.4 e shows the degradation of cell voltage as a function of current density after 2000 SUSD cycles. At the small current density, both ALDPt-MEA and commercial-MEA indicate lower cell voltage loss. It is worth noting that the 50ALDPt-MEA and 30ALDPt-MEA show a constant platform of ~20 mV voltage loss with the current density increasing after 2000 cycling. However, with further lower the ALDPt loading to 20ALDPt of 0.01 $mg \cdot cm^{-2}$, the voltage loss will increase with the current density and showed a maximum loss of ~50 mV at 2.0 $A \cdot cm^{-2}$ which is comparable to that of the commercial Pt-MEA with higher 0.035 $mg \cdot cm^{-2}$ Pt loading. The relatively poor stability of lower ALDPt catalyst is ascribed to the tiny Pt particles, which are very active and with high surface energy, thus the migration and

aggregation of small Pt particles occur and leading to the surface area loss under the conditions of SUSD cycling.
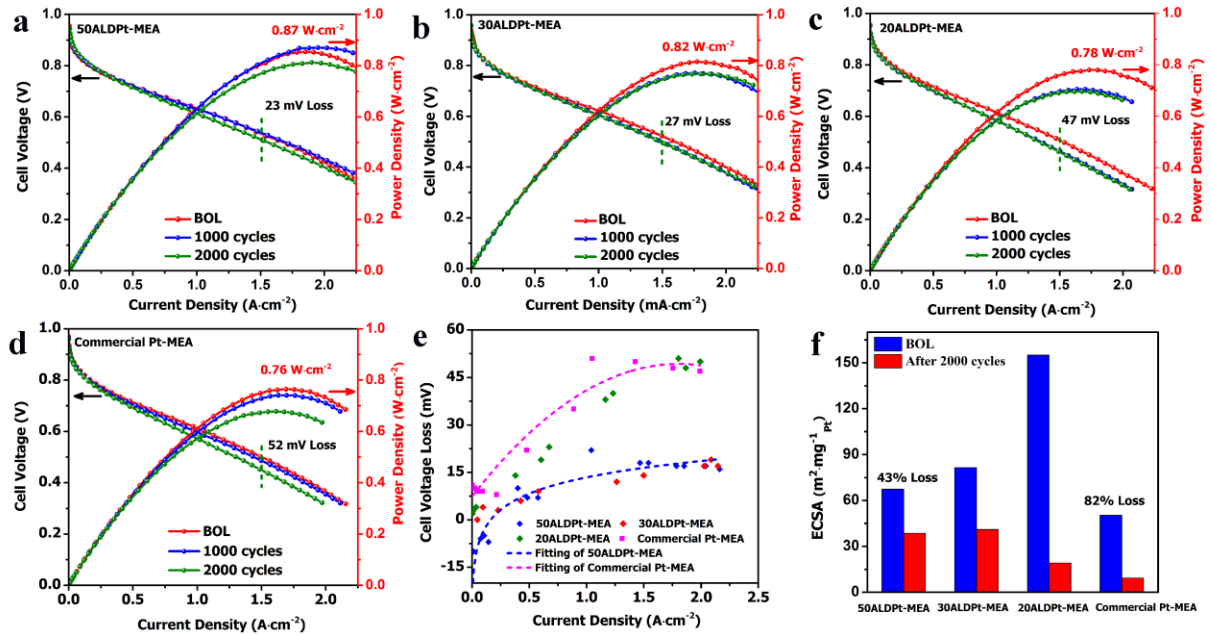
Figure 6.4. H₂-air PEMFC polarization and power density curves for MEAs with cathode of 0.4 mg·cm⁻² commercial Pt/C and anode of (a) 0.035 mg·cm⁻² 50ALDPt, (b) 0.02 mg·cm⁻² 30ALDPt, (c) 0.01 mg·cm⁻² 20ALDPt, (d) 0.035 mg·cm⁻² commercial Pt/C catalyst. (e) The relationship between voltage loss and current density for MEAs after 2000 SUSD cycling. (f) the ECSA of ALDPt-MEAs and commercial Pt-MEA before and after SUSD cycling (BOL: beginning-of-life, EOL: end-of-life after 2000 cycles).

By analysis the anode catalyst ECSA of ALDPt-MEAs and commercial Pt-MEA before and after 2000 SUSD cycling as indicated in Figure 6.4f, it was found that, the 50ALDPt-MEA shows BOL ECSA of 67.4 m²·g⁻¹$_{Pt}$ much higher than that of 50.3 m²·g⁻¹$_{Pt}$ for commercial Pt-MEA. After 2000 SUSD cycling, 38.6 m²·g⁻¹$_{Pt}$ of anode ECSA with 43% loss was revealed on 50ALDPt-MEA, which is 4.2 times higher than that of 9.3 m²·g⁻¹$_{Pt}$ (82% loss) for commercial Pt-MEA, implying the much-enhanced durability and activity of Pt catalyst achieved by ALD techniques. Furthermore, the ultra-low ALDPt of 0.02 and 0.01 mg·cm⁻² Pt loading exhibit the much-enhanced beginning ECSA of 81.5 m²·g⁻¹$_{Pt}$ and 155.0 m²·g⁻¹$_{Pt}$, respectively. With continuous SUSD cycling, the ECSA decreased to 41.0 m²·g⁻¹$_{Pt}$ (49% loss) and 19.1 m²·g⁻¹$_{Pt}$ (87% loss) for 30ALDPt-MEA and 20ALDPt-MEA, respectively,

which are still higher than the ECSA of 9.3 $m^2 \cdot g^{-1}_{Pt}$ for commercial Pt-MEA. The ECSA loss of anode catalyst indicate the anode Pt surface degradation during the SUSD operation, which is also confirmed through the anode HOR current measurement before and after ADT (shown in Figure S6.2). Evidently, the high ECSA and power density suggest that ALDPt-MEAs can enhance Pt utilization using a small amount of Pt in PEMFC anode layer. The improved performance can be attributed to the well-dispersed Pt particles on the outer surface of the MEA anode layer; in contrast, most of the Pt particles in the commercial Pt-MEA are dispersed on the interior surface of the electrode, resulting in low Pt utilization. The SUSD cycling test confirms that the ALD-MEAs even under the extremely low Pt loading provide excellent durability in comparison with the commercial Pt-MEA. Based on these results, it could be concluded that the ALD technique provides electrode catalysts that not only with ultra-low Pt loading, but also exhibit high catalytic activity, high performance and excellent durability for PEMFC applications.

Cross-section analysis of cycled-MEAs

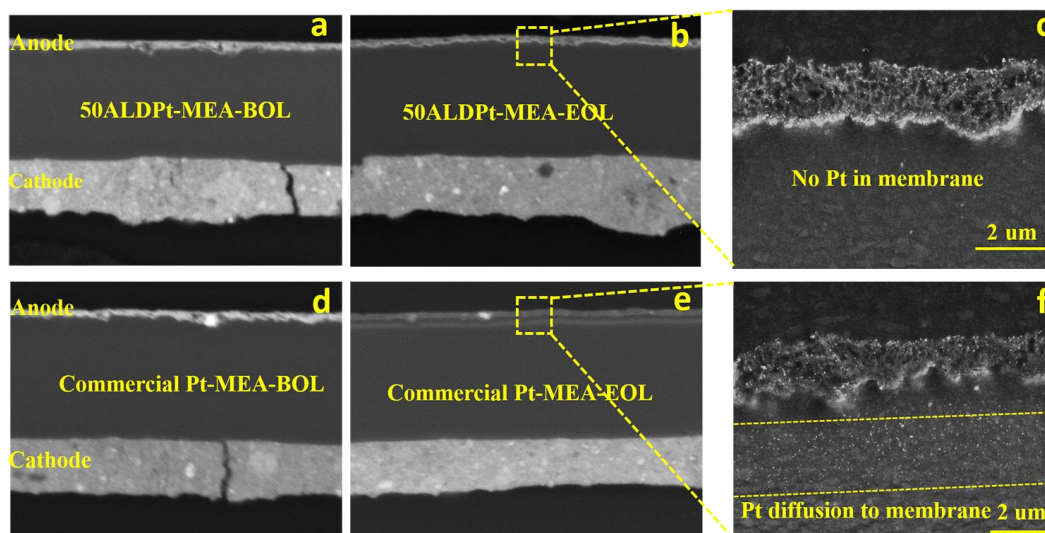**Figure 6.5. FESEM images of MEA cross-sections for (a) 50ALDPt-MEA-BOL before SUSD cycling and (b-c) 50ALDPt-MEA-EOL after SUSD cycling, (d) commercial Pt-MEA-BOL before SUSD cycling and (e-f) commercial Pt-MEA-EOL after SUSD cycling.**

Figure 6.5 shows cross-sectional SEM images of the anode/membrane interface for the ALDPt-MEAs and commercial Pt-MEA before and after 2000 SUSD cycling. As shown in the SEM images, three distinct layers can be identified: the cathode catalyst layer, the electrolyte membrane layer, and the anode catalyst layer. The thicknesses of the cathode catalyst layer and electrolyte membrane layer show little variation before and after SUSD cycling, indicating no excessive carbon corrosion of the cathode catalyst layer and no severe thinning of the electrolyte layer during anode SUSD cycling. However, there is a significant difference of anode/membrane boundary for ALDPt-MEAs and commercial Pt-MEA after cycling. From Figure 6.5a-b, it is obviously to know that the anode thickness and anode/membrane boundary have no change of 50ADLPt-MEA after cycling. By zoom in the anode/membrane boundary of 50ALDPt-MEA end-of-life after cycling (50ALDPt-MEA-EOL, Figure 6.5c), no dissolved and redeposited Pt particles were detected in the anode/membrane interface region. Moreover, no observation of the Pt particles in a cycled ALDPt-MEA even under ultra-low Pt loadings (Figure S6.3) of 0.02 mg·cm^{-2} and 0.01 mg·cm^{-2}, which suggests the ALDPt exhibit excellent durability due to the highly dispersion and strong Pt-carbon interactions. However, for the commercial Pt-MEA as shown in Figure 6.5 d-f, it is indicated that an obvious Pt band present in the membrane of commercial Pt-MEA-EOL after cycling, which provides a direct evidence for the commercial Pt dissolution and redeposition into the membrane during the SUSD cycling. The Pt particles in the membrane are formed by the chemical reduction of the diffused Pt ions (such as Pt^{2+}) with hydrogen gas that has crossed over from the anode through the membrane toward the cathode, e.g., Pt^{2+} + H$_2$ → Pt + 2H$^+$. Such Pt ion species can be generated by the dissolution of anode Pt NPs, which migrate into the membrane in the ionomer phase and reprecipitate there in form of Pt particles. Therefore, the Pt dissolution and subsequent migration into the membrane leads to a substantial loss of Pt surface area and lower Pt utilization for catalyzing the HOR at PEMFCs anode. In contrast, Pt deposition in the membrane was almost undetectable in cycled ALDPt-MEAs at anode, which indicated the significantly enhanced stability of Pt prepared by ALD.
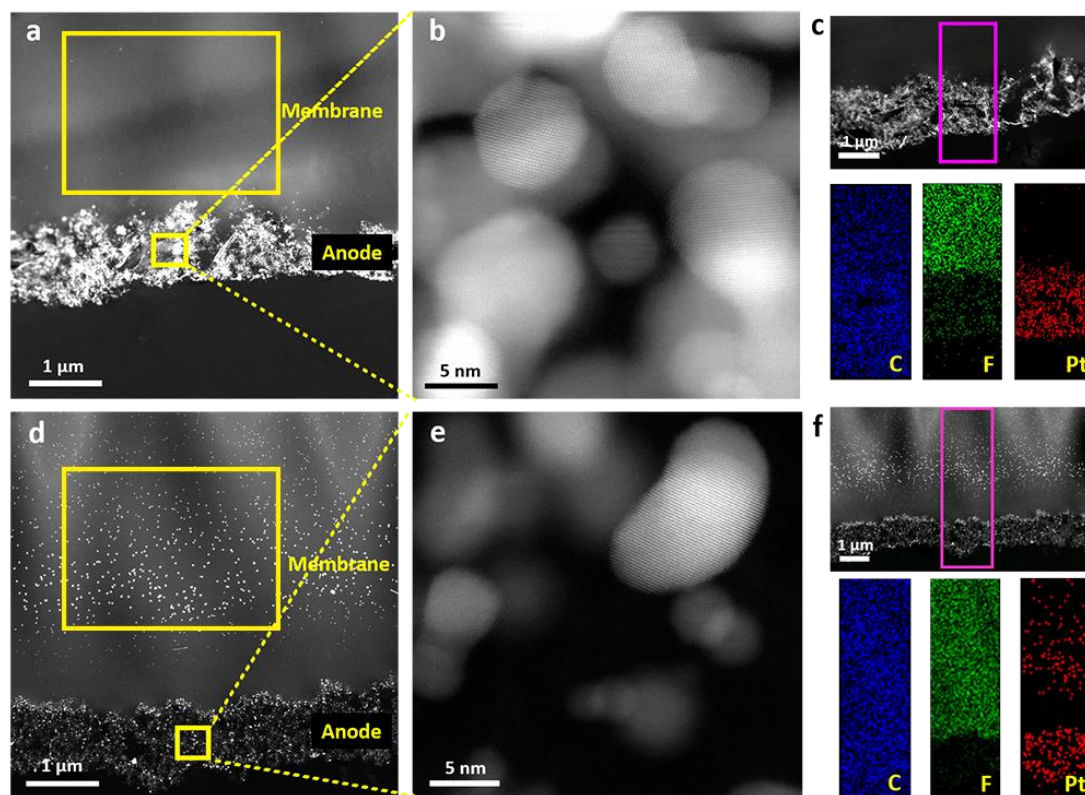
Figure 6.6. Characterization of cycled MEA cross-sections: (a) cross-sectional HAADF-STEM image of the 50ALDPt-MEA-EOL, (b) high-resolution HAADF-STEM image of the Pt catalyst from 50ALDPt-MEA-EOL anode layer, (c) EDX maps of the 50ALDPt-MEA-EOL cross-section, (d) cross-sectional HAADF-STEM image of commercial Pt-MEA-EOL, (e) high-resolution HAADF-STEM image of the Pt catalyst from commercial Pt-MEA-EOL anode layer, (f) EDX maps of the commercial Pt-MEA-EOL cross-section.

To further understand the Pt particles distribution and size change after SUSD cycling, the STEM images coupled with EDX maps were carried out on the 50ALDPt-MEA and commercial Pt-MEA. Figure 6.6a shows the HAADF-STEM image of the cycled 50 ALDPt-MEA-EOL cross-section, the anode and membrane are clearly visible from the image. The HAADF-STEM image is known as a Z-contrast image, where the contrast of the image is proportional to the Z number of the elements present in the material. The heavier Pt particles are brighter in the image, while the lighter elements, carbon and fluorine, are shown in darker contrast. Clear differences are observed between the 50ALDPt-MEA-EOL sample and

commercial Pt-MEA-EOL sample from the cross-sectional STEM images shown in Figure 6.6a and d. The cross-section of 50ALDPt-MEA-EOL after cycling shows only minor changes compared to that before cycling, as shown in Figure S6.4. The anode layer of cycled 50ALDPt-MEA-EOL sample exhibits similar bright contrast compared to the 50ALDPt-MEA-BOL sample, suggesting there is no significant loss of Pt in the anode layer during cycling. Meanwhile, no obvious Pt diffusion is observed in the membrane of the cycled sample, indicating the lab-designed ALDPt-MEA underwent minor Pt diffusion. In contrast, significant amount of Pt is diffused from the commercial Pt-MEA anode into the membrane, evident by the bright Pt-based particles observed from the membrane of the commercial Pt-MEA-EOL, as shown in Figure 6.6d. The dramatic Pt diffusion is also clearly revealed from the low-magnification image in Figure S6.5, with a diffusion depth of ~5 μm into the membrane. Figure 6.5b and 6.5e show the high-resolution STEM images of the Pt particles in the anode layer of the two MEA samples, revealing the existence of Pt catalyst in the anode after cycling for both the 50ALDPt-MEA-EOL and commercial Pt-MEA-EOL, although the retained amount could be quite different. For the commercial Pt-MEA-EOL, a large amount of Pt has dissolved into the membrane and only small part of Pt NPs are remained in the anode layer (Figure 6.6 d and f). Additionally, the Pt particle size has a wide distribution from 1.5-7.0 nm (Figure 6.6 e) in commercial Pt-MEA-EOL anode layer, which is due to the Pt degradation mechanism of migration/aggregation and dissolution/redeposition occur for the commercial Pt catalyst. The elemental distribution across the anode/membrane interface is further studied by EDX mapping. Figure 6.6c shows the elemental maps of cycled 50ALDPt-MEA-EOL. As can be seen, C is detected throughout the anode and membrane, Pt is mostly concentrated in the anode, a significant amount of F is detected in the membrane, while almost no Pt is observed in the membrane, which is consistent with the STEM results discussed above. The elemental maps obtained from the cycled commercial Pt-MEA-EOL sample shows clear difference, the Pt is not only concentrated in the anode layer, but also detected in the membrane, as displayed in the Pt map, which further confirms the Pt diffusion into the membrane that observed from the STEM images shown in Figure 6.6d and Figure S6.4.

Regarding the excellent performance and excellent stability of the ALDPt-MEAs with extremely low Pt loading, it is believed that the enhanced performance of ALDPt is caused

by following factors: (1) The high dispersion of ALD Pt NPs. It is confirmed that the high dispersion of active components will result in high active surface and high mass activity of Pt catalyst. (2) The high accessibility of the ALD Pt catalyst. In the ALDPt-MEAs, almost all Pt NPs are accessible for the hydrogen fuel because of the deposition pattern of the Pt atoms on the ionomer-carbon-membrane (three-phase boundary), which is not covered by the binder or blocked by the support surface. (3) The high chemical and physical stability of ALD Pt NPs. The strong chemical interaction between the Pt NPs and carbon support achieved by ALD promotes the durability performance of the ALD Pt catalyst than that of commercial Pt.

6.4　Conclusion

The deposition of Pt NPs on PEMFC anode carbon layers by ALD has been studied. ALD enables the Pt NPs uniform dispersion on the carbon surface. Importantly, the Pt particle size and loading can be precisely controlled by the number of ALD cycles. An ALDPt-MEA with extremely low anode Pt loading of 0.01 mg$\cdot$cm^{-2} is achieved by 20 ALD cycles, which shows better H$_2$-air PEMFC performance to that of commercial Pt-MEA with higher Pt loading of 0.035 mg$\cdot$cm^{-2}. Moreover, the anode potential cycling accelerated stress test indicate that the ALDPt anode shows much improved durability compared to that of commercial Pt/C anode. The cycling potential range is between 0.1V and 1.0V in order to mimic the anode potential alternation in fuel cell air/air start-up/shutdown processes. After 2000 anode potential cycles, the 50ALDPt-MEA exhibit excellent durability with only 8.0% power density loss. Even under the ultra-low Pt loading of 0.01 mg$\cdot$cm^{-2}, the 20ALDPt anode shows the extremely high beginning ECSA of 155 m$^2\cdot$g$^{-1}_{Pt}$ and power density of 0.78 W$\cdot$cm^{-2}, with only 10.2% power loss after cycling, which is the lowest anode Pt loading and best durability among the reported PEMFC using Pt catalyst. This research work reveals that the application of ALD for Pt deposition directly on the electrode carbon layers can effectively reduce the Pt loading while enhancing the Pt dispersion, utilization, and high durability, even with ultralow anode Pt loading. Our work suggests that ALD process has a great potential for fabrication of next-generation Pt catalyst with high activity and durability.

Acknowledgment

Reference

[1].   Debe, M.K., Nature, 2012. **486**: p. 43.

[2].   Eberle, U., B. Muller, and R. von Helmolt, Energy & Environmental Science, 2012. **5**(10): p. 8780-8798.

[3].   Yoshida, T. and K. Kojima, The Electrochemical Society Interface, 2015. **24**(2): p. 45-49.

[4].   Banham, D. and S. Ye, ACS Energy Letters, 2017. **2**(3): p. 629-638.

[5].   Banham, D., T. Kishimoto, Y. Zhou, T. Sato, K. Bai, J.-i. Ozaki, Y. Imashiro, and S. Ye, Science advances, 2018. **4**(3): p. eaar7180.

[6].   Anderson, R.M., D.F. Yancey, L. Zhang, S.T. Chill, G. Henkelman, and R.M. Crooks, Accounts of Chemical Research, 2015. **48**(5): p. 1351-1357.

[7].   Su, L., W. Jia, C.-M. Li, and Y. Lei, ChemSusChem, 2014. **7**(2): p. 361-378.

[8].   Fuel Cell Technologies Office. Multi-Year Research, D., and Demonstration Plan. http://energy.gov/sites/prod/files/2016/10/f33/fcto_myrdd_fuel_cells.pdf.

[9].   Durst, J., C. Simon, F. Hasché, and H.A. Gasteiger, Journal of The Electrochemical Society, 2015. **162**(1): p. F190-F203.

[10]. Scofield, M.E., Y. Zhou, S. Yue, L. Wang, D. Su, X. Tong, M.B. Vukmirovic, R.R. Adzic, and S.S. Wong, ACS Catalysis, 2016. **6**(6): p. 3895-3908.

[11]. Neyerlin, K., W. Gu, J. Jorne, and H.A. Gasteiger, Journal of The Electrochemical Society, 2007. **154**(7): p. B631-B635.

[12]. Wang, J.X., T.E. Springer, and R.R. Adzic, Journal of the Electrochemical Society, 2006. **153**(9): p. A1732-A1740.

[13]. Karan, K., Electrochemistry Communications, 2007. **9**(4): p. 747-753.

[14]. Sheng, W., H.A. Gasteiger, and Y. Shao-Horn, Journal of The Electrochemical Society, 2010. **157**(11): p. B1529-B1536.

[15]. Durst, J., A. Siebel, C. Simon, F. Hasche, J. Herranz, and H.A. Gasteiger, Energy & Environmental Science, 2014. **7**(7): p. 2255-2260.

[16]. Yun, S.W., S. Park, T.J. Kim, J.H. Kim, G.W. Pak, and Y.T. Kim, ChemSusChem, 2017. **10**(3): p. 489-493.

[17]. Eom, K., G. Kim, E. Cho, J.H. Jang, H.-J. Kim, S.J. Yoo, S.-K. Kim, and B.K. Hong, International Journal of Hydrogen Energy, 2012. **37**(23): p. 18455-18462.

[18]. Durst, J., A. Orfanidi, P.J. Rheinländer, F. Hasché, C. Eickes, P. Suchsland, M. Binder, and H.A. Gasteiger, ECS Transactions, 2015. **69**(17): p. 67-76.

[19]. Zhang, T., P. Wang, H. Chen, and P. Pei, Applied Energy, 2018. **223**: p. 249-262.

[20]. Qin, C., J. Wang, D. Yang, B. Li, and C. Zhang, Catalysts, 2016. **6**(12): p. 197.

[21]. He, P., T. Cheng, R. Bashyam, A.P. Young, and S. Knights, ECS Transactions, 2010. **33**(1): p. 1273-1279.

[22]. Ettingshausen, F., J. Kleemann, A. Marcu, G. Toth, H. Fuess, and C. Roth, Fuel Cells, 2011. **11**(2): p. 238-245.

[23]. Dang, D., H. Zou, Z.a. Xiong, S. Hou, T. Shu, H. Nan, X. Zeng, J. Zeng, and S. Liao, ACS Catalysis, 2015. **5**(7): p. 4318-4324.

[24]. Qayyum, H., C.-J. Tseng, T.-W. Huang, and S.-y. Chen, Catalysts, 2016. **6**(11): p. 180.

[25]. Su, H.-N., Q. Zeng, S.-J. Liao, and Y.-N. Wu, International journal of hydrogen energy, 2010. **35**(19): p. 10430-10436.

[26]. Su, H.-N., S.-J. Liao, T. Shu, and H.-L. Gao, Journal of Power Sources, 2010. **195**(3): p. 756-761.

[27]. Dang, D., S. Liao, F. Luo, S. Hou, H. Song, and P. Huang, Journal of Power Sources, 2014. **260**: p. 27-33.

[28]. Martin, S., B. Martinez-Vazquez, P. Garcia-Ybarra, and J. Castillo, Journal of Power Sources, 2013. **229**: p. 179-184.

[29]. Mougenot, M., A. Caillard, P. Brault, S. Baranton, and C. Coutanceau, international journal of hydrogen energy, 2011. **36**(14): p. 8429-8434.

[30]. Cheng, N., Y. Shao, J. Liu, and X. Sun, Nano Energy, 2016. **29**: p. 220-242.

[31]. Cheng, N., M.N. Banis, J. Liu, A. Riese, X. Li, R. Li, S. Ye, S. Knights, and X. Sun, Advanced Materials, 2015. **27**(2): p. 277-281.

[32]. Cheng, N., S. Stambula, D. Wang, M.N. Banis, J. Liu, A. Riese, B. Xiao, R. Li, T.-K. Sham, and L.-M. Liu, Nature communications, 2016. **7**: p. 13638.

[33]. Sun, S., G. Zhang, N. Gauquelin, N. Chen, J. Zhou, S. Yang, W. Chen, X. Meng, D. Geng, M.N. Banis, R. Li, S. Ye, S. Knights, G.A. Botton, T.-K. Sham, and X. Sun, Scientific Reports, 2013. **3**: p. 1775.

[34]. Cheng, N., J. Liu, M.N. Banis, D. Geng, R. Li, S. Ye, S. Knights, and X. Sun, International Journal of Hydrogen Energy, 2014. **39**(28): p. 15967-15974.

Supporting information
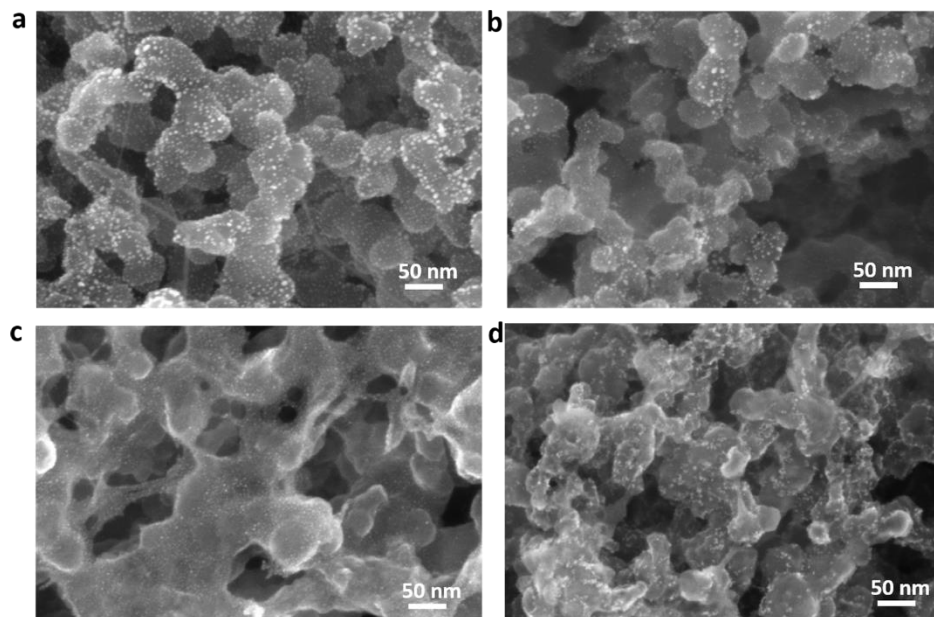
Figure S6.1 FESEM images of anode catalyst layer with Pt NPs made by (a) 50ALD, (b)30ALD, (c)20ALD and (d)commercial Pt/C.
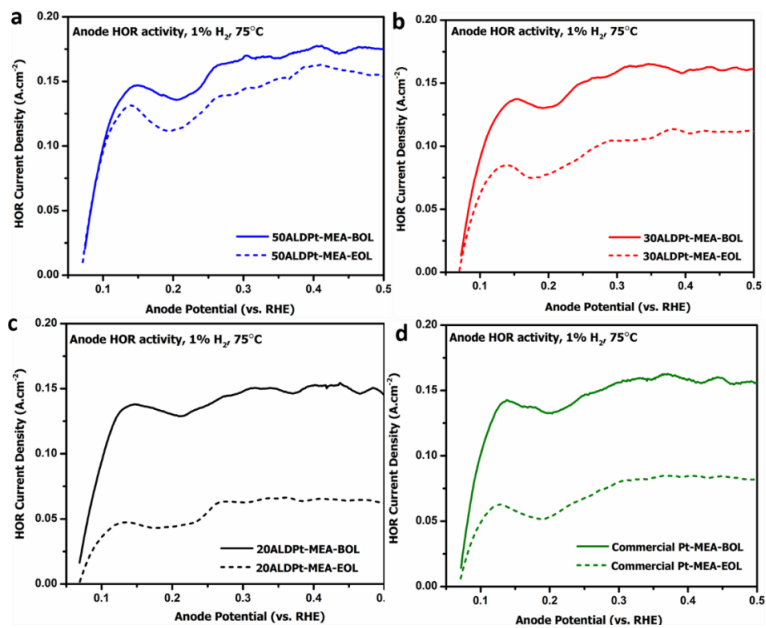
Figure S6.2. The HOR polarization curves for ALDPt-MEAs and commercial Pt-MEA before and after 2000 SUSD cycling. (a) 50ALDPt-MEA, (b) 30ALDPt-MEA, (c) 20ALDPt-MEA, (d) commercial Pt-MEA.
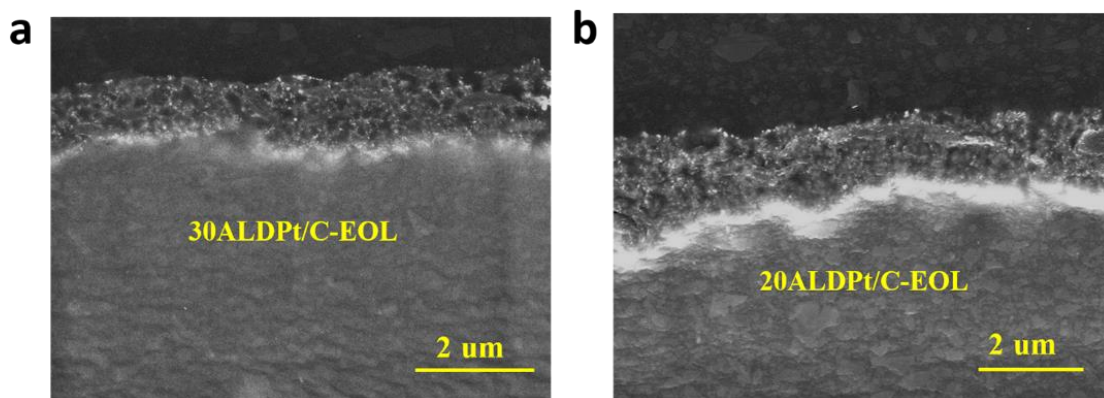
Figure S6.3. The cross-section SEM images of 30ALDPt-MEA (a) and 20ALDPt-MEA (b) after 2000 SUSD cycling.
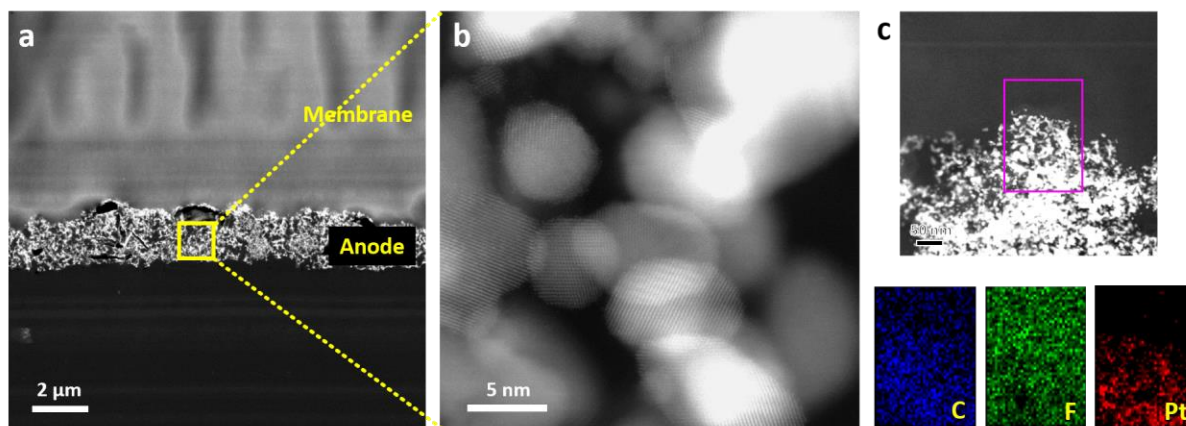
Figure S6.4. Characterization of 50ALDPt-MEA-BOL cross-section sample: (a) Cross-sectional HAADF-STEM image of 50ALDPt-MEA-BOL, (b) high-resolution HAADF-STEM image of the Pt catalyst in the 50ALDPt anode, (c) EDX maps of the 50ALDPt-MEA-BOL cross-section.
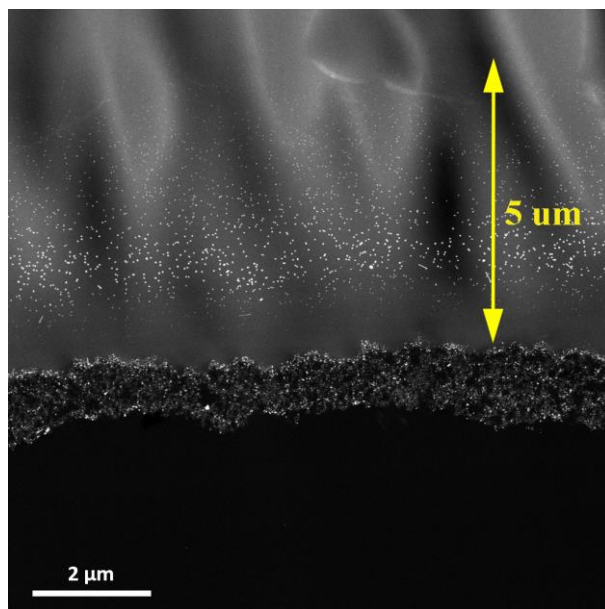
Figure S6.5. HAADF-STEM image of commercial Pt-MEA cross-section sample.

Chapter 7

7 Platinum single-atom and subnano-cluster on MOFs-carbon as superior oxygen reduction reaction catalysts

*This chapter is to be submitted for peer-reviewed publication.

Single-atom catalysts (SACs), in which metal atoms are dispersed on the support without forming nanoparticles (NPs), have been used for various electrochemical reactions. SACs have the utmost atom utilization efficiency of metal atoms. Here we report on a practical synthesis method to produce the supported Pt single atoms and subnano-clusters catalysts using the atomic layer deposition technique (ALD). To investigate the impact of atom utilization on the electrocatalysis for oxygen reduction reaction (ORR), Pt single atoms, subnano-clusters as well as NPs with different size and density on MOFs-derived carbon support were designed. The characteristics of scanning transmission microscopy (STEM) and X-ray absorption fine structure were used to determine the Pt single atoms/subnano-clusters size distribution and electronic structure. Electrochemical analysis on these ALDPt catalysts indicated that the Pt single atoms/subnano-cluster synthesized with 1 and 2 min Pt precursor exposure during ALD synthesis exhibit better ORR catalytic activity and excellent long-term stability than that of the Pt NPs catalyst.

7.1 Introduction

Polymer electrolyte membrane fuel cells (PEMFCs) are promising alternative power sources for transportation and portable applications due to their high efficiency, room temperature operation, and zero emissions.[1-5] Noble metals, especially platinum (Pt), are usually regarded as the most effective catalysts to facilitate both hydrogen oxidation (HOR) and oxygen reduction (ORR) in PEMFCs.[6-11] However, Pt utilization in these bulk electrocatalysts is extremely low, as the active sites are only located on the surface of the catalyst particles.[12] Thus, downsizing metal NPs to clusters in sub-nanometer scale or even single atoms provides an effective way to maximize the atom utilization while reduce the cost of the electrocatalysts.[13, 14] Furthermore, at microscopic level, some characteristics of single atom catalyst (SACs) are significantly different from those of NPs, including (i)

unsaturated coordination configuration of catalytic centers, which produces active sites that are accessible to reactant; (ii)strong metal–support interactions, which guarantee charge transfer between metal and associated interface, and promote the good durability of metal atom species; (iii) foreign atom effect, which would produce asymmetrical spin and charge density, thereby rendering SACs to possess extraordinary catalytic selectivity, activity, and stability. To date, many efforts have been focused on developing the supported SACs, which can greatly boost the specific activity of the electrocatalyst.[15-20] Our previous study showed that the nitrogen-doped graphene supported Pt SACs exhibit higher catalytic activity for hydrogen evolution reaction compared with the Pt NPs.[21] Additionally, the Pt SACs also exhibited a significantly improved catalytic activity towards methanol oxidation, up to 10 times greater than the commercial Pt catalyst.[22] However, with decreasing Pt particle size, the atom surface free energy increases and the atoms tend to aggregate into clusters or particles. Therefore, selection of an appropriate supports that interact strongly with the isolated Pt atoms is necessary, for creating the stable and finely dispersed atomic active sites.

As a new type of crystalline porous materials, metal-organic frameworks (MOFs) and their derived materials have been widely employed for energy conversion reactions due to their unique characteristics including the organic-inorganic hybrid nature, high surface area, well-defined porosity, tunable chemical composition. It has been shown that the atomically dispersed metal sites in pristine MOFs and MOF-derived materials played very important roles on electrocatalysis of the energy conversion reactions. For electrocatalytic energy conversion applications, the atomically active sites should not only possess the high activity, the comparable electrochemical stability and durability is also important. To achieve the high stable atomically dispersed active sites, atomic layer deposition (ALD) is a promising technique for precisely controlling the metal-support interface. ALD proceeds by forming chemical bonds between the initial layer of atoms of a reactive precursor and the surface of the support, ensuring a strong interaction between the deposited metal atoms and support.

In this work, a MOFs-derived nanocarbon (ZIF-C) material was prepared and provided as the support for Pt SAC. Based on the advantages of high surface area, high porosity and rich of nitrogen doped species, [23-28] ZIF-C was anticipated to be a promising support for SACs. In this strategy, the supported Pt SACs were prepared by ALD via chemical incorporation Pt

atoms into the nitrogen or oxygen species from ZIF-C, which is considered to enable the sinter-resistant isolated Pt atoms with high dispersion on the ZIF-C support. The catalyst of ALDPt-ZIF-C with Pt single atoms shows high activity and 4e- pathway for ORR, which demonstrates 4.8 times higher mass activity than that of the Pt NPs catalysts on ZIF-C support. Moreover, the resulting catalyst of Pt-ZIF-C with Pt single atoms/subnano-clusters shows excellent long-term stability with negligible activity loss even after 10,000 cycles of durability test. This is for the first time using ALD technique to achieve the Pt single atoms catalyst on MOFs-carbon support as advanced electrocatalyst toward ORR. It is expected that the Pt single atoms and subnano-clusters could be one of the promising highly active next generation catalysts. Moreover, the MOFs-derived nanocarbon could offer a new type of catalyst support for stabilizing Pt SACs.

7.2   Experiment

7.2.1   Synthesis of MOFs-derived nanocarbon

A typical MOFs of zinc-based zeolitic imidazolate framework-8 (ZIF-8) was choose as a template and precursor to develop the MOFs-derived nanocarbon (ZIF-C). Then this ZIF-C was used as a substrate for Pt deposition via an ALD approach. Synthesis of ZIF-8 crystals was conducted following the procedure outlined by J. Cravillon. [29] In a typical experiment, two solutions are initially prepared by dissolving a known quantity of 2-methylimidazole (6.78 g, 82.0 mmol) in 250 ml of methanol and $Zn(NO_3)_2 \cdot 6 H_2O$ (6.15 g, 20.5 mmol) in 250 ml of methanol. The solution of $Zn(NO_3)_2 \cdot 6 H_2O$ was then dropwise added into 2-methylimidazole solution, combining with the white precipitate appears. The resulting mixture was stirred for 1h and aged for another 24h at room temperature. Subsequently, the ZIF-8 crystals were collected by centrifugation and washed several times with methanol to remove the excess reactants. The as-prepared ZIF-8 powder was carbonized at 1000°C for 8 h in Ar atmosphere to achieve the nitrogen-doped nanocarbon of ZIF-C. the morphology and microstructure of ZIF-8 and ZIF-C before and after high temperature carbonizations were determined by SEM and XRD techniques, and the corresponding characterization results are shown in Figure S7.1 and Figure S7.2.

7.2.2   ALD process and loading analysis for Pt deposition on ZIF-C

Pt was deposited on ZIF-C substrate by ALD (Savannah 100, Cambridge nanotechnology Inc., USA) using trimethyl(methylcyclopentadienyl)-platinum (IV) (MeCpPtMe$_3$) as a precursor. High purity N$_2$ (99.999%) was used as both a purging and carrier gas. MeCpPtMe$_3$ was held in an external reservoir kept at 65°C to provide a steady exposure of Pt precursor. Gas lines were held at 100°C to avoid precursor condensation. [30, 31] Since ALD valves can only be opened for 30 seconds (s) at a time, 1-minute (min) exposure of Pt precursor consisted of two 30 s pulses separated by a 10 s purge. The same routine was applied for 2 min and 5 min exposure of MeCpPtMe$_3$ to achieve the samples of Pt2min-ZIF-C and Pt5min-ZIF-C, respectively. Pt loading was analyzed using an inductively coupled plasma optical emission spectrometer (ICP-OES) with samples dissolved in hot fresh aqua regia overnight and filtered.

7.2.3   Physical characterization

The morphology and microstructure of as-prepared ZIF-C was obtained from a scanning electron microscope (SEM, Hitachi S-4800). High resolution transmission electron (HRTEM) and scanning transmission electron (STEM) images of ALDPt particles were acquired using an equipment of JEOL2010FEG operated at 200 KV. X-ray diffraction (XRD) patterns were collected on a Bruker D8 Advance diffractometer using Cu Ka radiation at 40 kV and 40 mA. The Pt content for Pt-ZIF-C prepared with different ALD exposure time were determined by ICP-OES. From ICP analysis, the Pt loading in Pt1min-ZIF-C, Pt2min-ZIF-C, Pt5min-ZIF-C were determined of 0.7wt%, 1.5wt%, and 15wt%, respectively.

7.2.4   X-ray Absorption Spectroscopy

X-ray absorption near edge structure (XANES) and extended X-ray adsorption fine structure (EXAFS) measurement at the Pt L3-edge (11564 eV) and L2-edge (13273 eV) were performed on the 061D superconducting wiggler at the hard X-ray microanalysis (HXMA) beamline at the Canadian Light Source. The spectra were collected in fluorescence yield mode using a 32 Ge solid-state detector, and the spectra of high purity metal Pt foil were collected in transmission mode for comparison and mono energy calibration. The acquired

XANES data were processed according to the standard procedures using the Athena module. The XANES oscillation functions were obtained by subtracting the pre-edge, post-edge background from the overall absorption spectra and then normalized with respect to the edge-jump step to unity. The background R_{bkg} value of 1.0 was used for all samples. Subsequently, k_3-weighted $\chi(k)$ functions were Fourier transformed to the R space to analysis the Pt chemical bonding distance.

7.2.5   Electrochemical characterization

The electrochemical characterizations were performed in a three-electrode system using a rotating-disk electrode (RDE) setup with an Autolab electrochemistry station and rotation control (Pine Instruments). The catalyst ink was prepared by mixing 3.0 mg of catalyst in 3.0 ml of aqueous solution containing 0.6 mL of isopropyl alcohol and 30 µL of Nafion (5.0 wt%). Then 30 min sonication was conducted to ensure good dispersion and wetting of the catalyst. 20 µL of the catalyst ink was pipetted onto a polished glassy carbon electrode (Pine, 5.0 mm dia., 0.196 cm^2) and allowed to dry at room temperature. All electrochemical measurements were carried out in 0.1M $HClO_4$ electrolyte using a Pt wire as a counter electrode and reversible hydrogen electrode (RHE) as a reference electrode. All potentials reported henceforth are vs. RHE. Each electrode was activated by scanning from 0.05 to 1.1 V at 50 mV·s^{-1} in N_2-saturated 0.1 M $HClO_4$ until no changes were observed in the cyclic voltammetry (CV) curves. O_2 was then bubbled into $HClO_4$ for 30 min to achieve O_2-saturated electrolyte. Then ORR linear sweep voltammetry (LSV, 10 mV·s^{-1}) was conducted in O_2-saturated 0.1M $HClO_4$ on the RDE system with a rotation speed of 1600 rpm. The LSV curves obtained under N_2 were subtracted from the LSV curves obtained under O_2 to remove the non-Faradaic current. The electrochemically active surface area (ECSA) was calculated by integrating the area of the CV curves in the hydrogen underpotential deposition (HUPD) region and using the charge value of 210 µC·cm^{-2} corresponding to a monolayer adsorption of hydrogen atoms on a polycrystalline Pt catalyst. [32] To evaluate the catalysts durability, an accelerated durability test (ADT) of potential cycling from 0.6 to 1.0 V vs. RHE protocol was conducted on the as-prepared electrocatalysts. A total of 10,000 cycles in O_2-saturated 0.1 M $HClO_4$ at 50 mV·s^{-1} were performed to evaluate the catalysts durability.

7.3 Result and discussion
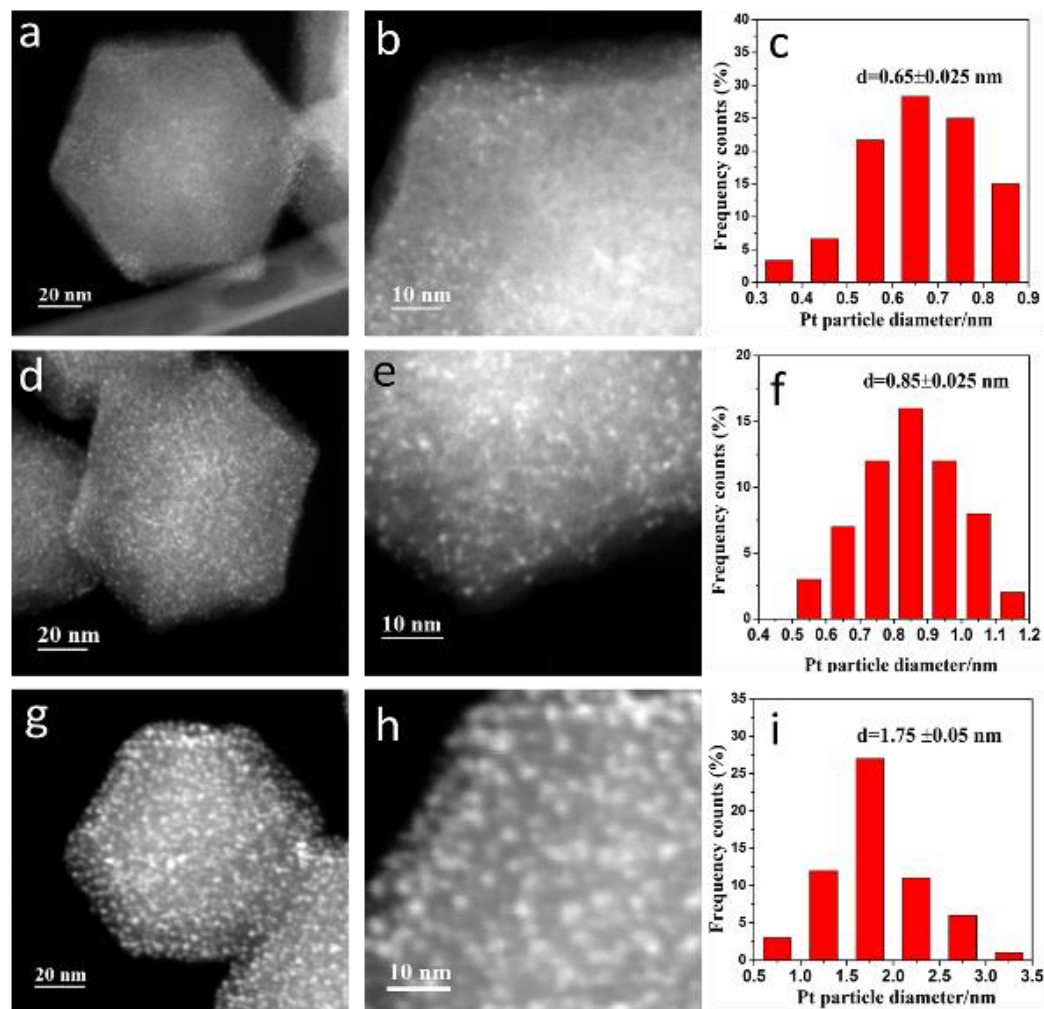
Figure 7.1. STEM images and Pt size distribution for samples of (a-c) Pt1min-ZIF-C, (d-f) Pt2min-ZIF-C, and (g-i) Pt5min-ZIF-C prepared by ALD.

Figure 7.1 illustrates the STEM images of ALDPt-ZIF-C catalysts prepared by varying ALD MeCpPtMe$_3$ exposure time to the ZIF-C substrate for 1 min, 2 min and 5 min at 250°C. A distribution of bright spots, corresponding to Pt single atoms and subnano-clusters can be found on the surface of Pt1min-ZIF-C catalyst (Figure 7.1a-b). The particle size distribution histograms for Pt atoms in Pt1min-ZIF-C is shown in Figure 7.1c. As can be seen from Figure 1a-c, the Pt species with an average size of 0.65±0.025 nm could be obtained with 1 min precursor exposure for ALD synthesis, which suggests that Pt particles are present in the form of single isolated atoms and clusters with a few atoms. Furthermore, with increasing the

precursor exposure time to 2 min and 5 min, more Pt atoms could be deposited on the ZIF-C support, resulting in the growth of Pt single atoms to subnano-clusters or even crystalline NPs. Specifically, for the 2 min exposure of MeCpPtMe$_3$ precursor, the Pt subnano-clusters with an average size of 0.85±0.025 nm larger than that of 0.65±0.025 nm for Pt1min-ZIF-C could be achieved. The STEM images in Figure 7.1d-e demonstrate that Pt2min-ZIF-C shows much higher Pt density than that of Pt1min-ZIF-C, which implies a saturation of Pt surface sites can be reached by prolonging the precursor pulse time. After the saturated ALD reaction, the decomposition of MeCpPtMe$_3$ precursor may occur on an active surface that contains coordinatively unsaturated Pt atoms, thus result the Pt atoms further deposition on the growing surface and lead to the formation of larger Pt clusters. [33] With further supplying of Pt precursor to 5min, the Pt subnano-clusters continuously grow up and form the Pt NPs with the average size of 1.75±0.05 nm in Pt5min-ZIF-C. Meanwhile, the Pt loading amount is increased to 15wt% on the ZIF-C support much higher than those of 1.5wt% and 0.7wt% achieved for Pt2min-ZIF-C and Pt1min-ZIF-C, respectively. The small subnano-cluster size and narrow size distribution observed in the Pt1min-ZIF-C suggests that the Pt precursor is initially anchored to an active site of ZIF-C support. Prolonged pulse time result in larger clusters or particles size, implying the removal of precursor organic ligands and particle further growth. Considering the Pt density, loading, and proportion of larger subnano-clusters with increasing pulse time, it could be concluded that after surface sites saturated atomic adsorption, the growth up of Pt particles occurs through autocatalysis effect of unsaturated Pt atoms, which generates the removal of precursor organic ligands and promotes the Pt atoms further deposition on the growing surface.[33-35] Therefore, by controlling the precursor exposure time during ALD synthesis, the obtained Pt in the forms of single atoms, subnano-clusters and crystalline NPs can be achieved on the ZIF-C support.
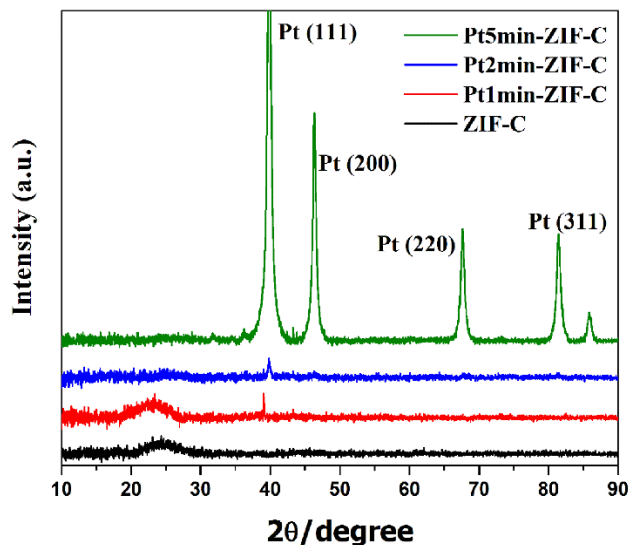
Figure 7.2. The X-ray diffraction patterns for Pt5min-ZIF-C, Pt2min-ZIF-C, Pt1min-ZIF-C and ZIF-C.

The X-ray diffraction patterns of the pure ZIF-C, and ALDPt-ZIF-C catalysts produced with 1 min, 2min and 5min ALD exposure of Pt precursor are shown in Figure 7.2. For the pure ZIF-C support, two diffraction peaks at around 26° and 43° are assigned to the characteristic (002) and (100) crystal planes of the graphite carbon, respectively. [36] After 1min ALD of Pt on ZIF-C, the XRD pattern of Pt1min-ZIF-C is almost the same with that of ZIF-C. There is no observable Pt crystal peak can be tracked in the Pt1min-ZIF-C sample, which is probably due to the low loading amount of Pt and very tiny Pt single atoms. With 2min ALD of Pt on ZIF-C, a very small diffraction peak at 39.8° is appeared, and which can be denoted as the (111) crystal plane of face-centered-cubic (fcc) metallic Pt. The relative low intensity of Pt crystalline peak suggests the small amount of Pt crystals in Pt2min-ZIF-C, which is probably due to the formation of some Pt clusters. This agrees well with the results revealed by STEM images. Furthermore, with continuously increase ALD pulse time to 5min, obvious Pt diffraction peaks at 39.8°, 46.2°, 67.6°, 81.4° associated to the (111), (200), (220), (311) crystal planes of the Pt NPs could be detected, respectively. [37] These diffraction patterns for the samples of ALDPt-ZIF-C imply that the crystalline Pt NPs can be formed with 5min exposure of ALD Pt precursor. With further shortening the precursor pulse time, the Pt with tiny particle size could be highly dispersed on the ZIF-C support surface, which is consistent with the TEM results.
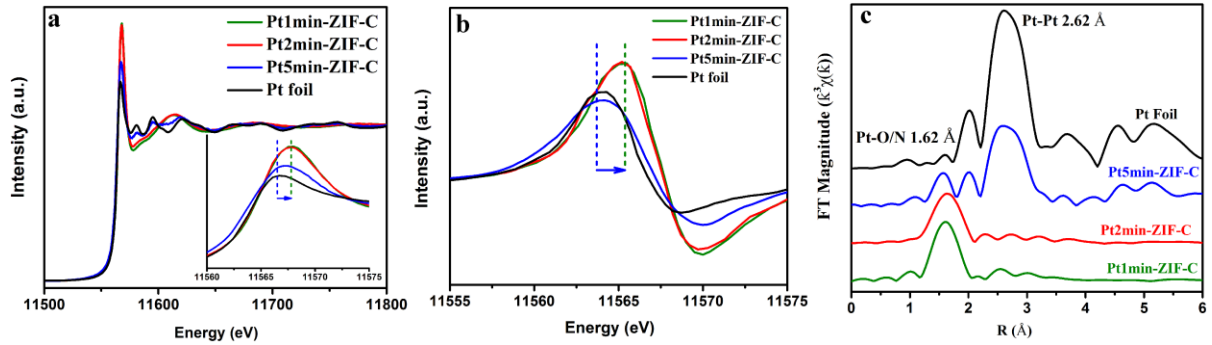
Figure 7.3. The XAFS structural characterization. (a) the normalized XANES, (b) the derivative spectra and (c) the K$_3$-weighted Fourier transform spectra of Pt1min-ZIF-C, Pt2min-ZIF-C, Pt5min-ZIF-C and Pt foil at the Pt L$_3$-edge.

To elucidate the local coordination electronic structure and chemical environment of Pt single atoms, subnano-clusters and particles on ZIF-C support, the XANES and EXAFS spectra at Pt L$_3$- edge were studied. Figure 7.3 a present the L$_3$ edge X-ray absorption spectra for samples of Pt1min-ZIF-C, Pt2min-ZIF-C, Pt5min-ZIF-C, alongside standard metallic Pt sample. It should be noted that the white line peak in the XANES for the Pt L$_3$ edge correspond to an electronic transition from 2p2/3 to unoccupied 5d states. [38] A lower white line intensity indicates that the Pt has a more reduced electronic structure. The white line intensity was much higher for Pt1min-ZIF-C and Pt2min-ZIF-C than that of metallic Pt foil, indicating the oxidized electronic structure of the Pt single atoms and subnano-clusters in Pt1min-ZIF-C and Pt2min-ZIF-C. By contrast, the white line intensity was much lower for Pt NPs in Pt5min-ZIF-C, which indicated that a more reduced state and metallic Pt structure was presented in Pt5min-ZIF-C. Moreover, the derivative spectra for Pt L$_3$-edge in Pt1min-ZIF-C and Pt2min-ZIF-C demonstrated an obvious positively shifted peak energy compared with Pt5min-ZIF-C and Pt foil, which further confirms the oxidized state of Pt single atoms and subnano-clusters in Pt1min-ZIF-C and Pt2min-ZIF-C instead of metallic Pt in Pt5min-ZIF-C. However, this oxidized electronic structure of Pt single atoms/subnano-clusters is an alternate stoichiometry from bulk PtO$_2$, which means the Pt atoms are probably connect to an element with higher electronegativity than Pt, such as O, N, or C species from ZIF-C support. The Pt-support interaction generates an electron transfer from Pt atoms to the neighboring element and result Pt with high depletion of 5d states, showing as a relatively high white line intensity and positively shifted threshold energy.

Furthermore, to study the local atomic structure of Pt using X-ray absorption spectra, the Fourier transformed curve in the real-space (R-space) of the EXAFS region are plotted in Figure 7.3c. The Pt foil reference sample exhibits a well-resolved peak at ~2.62 Å, which is assigned to the Pt-Pt coordination peak. However, for Pt1min-ZIF-C and Pt2min-ZIF-C, no available Pt-Pt coordination peak can be detected, which suggest most of the Pt species are presented as single atoms or tiny clusters in the Pt1min-ZIF-C and Pt2min-ZIF-C, almost no Pt nanocrystals. Interestingly, the Pt1min-ZIF-C and Pt2min-ZIF-C have a very strong peak at 1.62 Å, which is associated with Pt bonded to low Z elements (C, N or O though not distinguishable due to similar backscattering phase and amplitude as well as bond length). [19, 39] This observation indicates that only small-sized Pt subnano-clusters and single atoms dominate in the samples of Pt1min-ZIF-C and Pt2min-ZIF-C, absence of Pt NPs. In Pt1min-ZIF-C and Pt2min-ZIF-C, single Pt atoms interacts with ZIF-C support through Pt-O or Pt-N bonding while small Pt subnano-cluster has more surface atoms for more extensive Pt-ZIF-C interaction. For the Pt5min-ZIF-C sample, there present two kinds of Pt local atomic structure of Pt-N/O coordination bonding at 1.62 Å and Pt-Pt coordination at 2.62 Å, which suggest both Pt single atoms and nanoparticles are prepared in the Pt5min-ZIF-C sample. This EXAFS observation confirms the Pt single atoms and small-sized Pt subnano-clusters in the Pt1min-ZIF-C and Pt2min-ZIF-C, while Pt atoms and nanoparticles in Pt5min-ZIF-C, which agrees well with the XANES and HRTEM results.
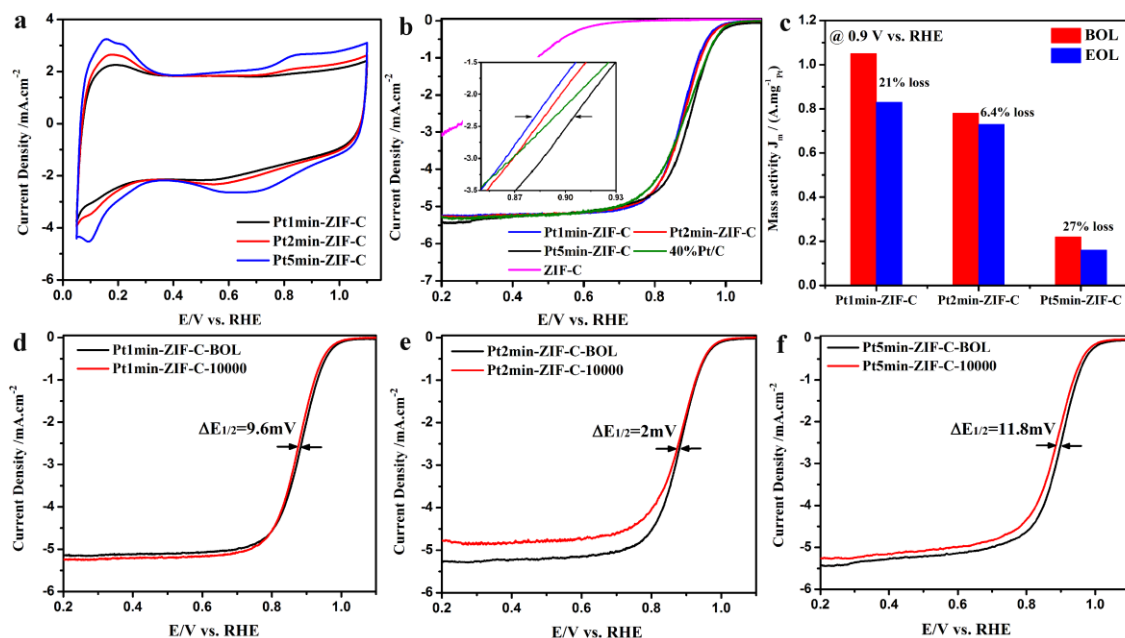
Figure 7.4. Electrocatalytic performance. (a) the CV curves, (b) the ORR curves and (c) the mass activity of the catalysts Pt1min-ZIF-C, Pt2min-ZIF-C, Pt5min-ZIF-C before and after cycling. The ORR performance of the catalysts (d) Pt1min-ZIF-C, (e) Pt2min-ZIF-C, (f) Pt5min-ZIF-C before and after 10,000 cycles durability test.

The electrochemical performance of the as-prepared ALDPt-ZIF-C with Pt single atoms, subnano-clusters and NPs are evaluated as catalysts toward ORR, respectively. From the CV curves of Pt1min-ZIF-C, Pt2min-ZIF-C and Pt5min-ZIF-C catalysts (Figure 7.4 a), it could be found that the current density generated from the hydrogen adsorption and desorption on Pt surface shows a close relationship with ALD exposure time and Pt loading on ZIF-C support. For 5min exposure of ALD Pt, there presents distinct hydrogen adsorption peaks on Pt nanocrystals, which suggest the Pt are presented as crystalline NPs in Pt5min-ZIF-C. With shorten ALD Pt precursor exposure time to 2min and 1min while Pt loading down to 1.5wt% and 0.75wt%, respectively. The small current and non-crystal hydrogen adsorption peak imply the Pt single atoms and subnano-clusters dominate in Pt2min-ZIF-C and Pt1min-ZIF-C catalysts. Figure 7.4 b shows the oxygen reduction currents measured on the RDE, the high onset-potential (~1.0 V vs. RHE) and limiting current density (~5.5 mA·cm^{-2}) suggest that oxygen is reduced following a 4e- pathway for both Pt1min-ZIF-C, Pt2min-ZIF-C and Pt5min-ZIF-C catalysts. The ORR can follow either of a 4e- or 2e- pathway. [16, 19, 40, 41]

Both oxygen atoms of the oxygen molecule need to be adsorbed on surface active sites to dissociate the strong O=O double bond. At least two adjacent active sites are necessary for the 4e- pathway. The isolated single-atom sites would not be able to break O=O bonds, following the 2e- pathway. In our case, the 4e- oxygen reduction pathway occurs on Pt single atoms and subnano-clusters active sites from Pt1min-ZIF-C and Pt2min-ZIF-C catalysts. There are two main reasons contribute to the 4e- oxygen reduction on Pt1min-ZIF-C and Pt2min-ZIF-C: (1) Pt single atom-nitrogen doped-support interaction, it is known that the catalytic activity of Pt single atoms for ORR could be triggered tremendously by the N-dopant atoms to a high level and 4e- reduction pathway due to a synergetic effect between doped-N and Pt single atoms. (2) high density of Pt single atoms on ZIF-C support, two adjacent Pt atoms combing with the ZIF-C support may cleave O=O bond and promote the O=O double bond dissociation/reduction.

By comparing the ORR performance and mass activity of ALDPt-ZIF-C catalysts (Figure 7.4 b), it can be concluded that the Pt1min-ZIF-C with both Pt single atoms and subnano-clusters exhibit the best beginning ORR activity than that of Pt2min-ZIF-C and Pt5min-ZIF-C. Normalized to the Pt loading, the mass activity at 0.9 V (vs. RHE) for each catalyst is calculated using the Koutecky-Levich equation. Remarkably, the mass activity of 1.05 $A \cdot mg^{-1}_{Pt}$ for the Pt1min-ZIF-C is 4.8 times greater than that of 0.22 $A \cdot mg^{-1}_{Pt}$ the Pt NPs catalyst for Pt5min-ZIF-C (Figure 7.4c). This finding suggests that the Pt single atoms and sub-clusters can significantly enhance the Pt utilization efficiency in comparison to their NPs counterparts. Because smaller Pt sub-clusters can offer more available catalytic positions per unit mass of Pt for electrochemical reaction from under-coordinated surface atom than that of Pt NPs.

Another challenge for the ultra-small metal catalyst is their long-term stability for PEMFC application. The surface free energy of metal atoms increases significantly with decreasing particle size, promoting the migration and aggregation between the adjacent atoms. Using an appropriate support material that strongly interacts with the Pt species prevents this aggregation, creating stable, finely dispersed Pt clusters with high catalytic activity and stability. In this case, the long-term operation stability of ALDPt-ZIF-C catalysts was evaluated by CV cycling the catalyst between 0.6-1.0 V (vs. RHE) at $50 mV \cdot s^{-1}$ in an O_2-

saturated 0.1M HClO$_4$. As for the Pt1min-ZIF-C (Figure 7.4d), 9.6 mV negative shift of E$_{1/2}$ and 21% mass activity loss after 10,000 ADT cycling indicates the deterioration of Pt single atoms occurred on Pt1min-ZIF-C. By contrast, the Pt2min-ZIF-C with both single atoms and subnano-clusters showed a much better long-term durability, as shown in Figure 7.4e, no detectable E$_{1/2}$ negatively shift after 10,000 continuous ADT cycles and only 6.4 % mass activity loss. The high stability of Pt2min-ZIF-C could be attributed to the well-known anchoring effect of N-dopants to the Pt atoms, which has been confirmed by the EXAFS results. On the other hand, the extra enhanced stability of Pt sub-clusters in Pt2min-ZIF-C compared than that of Pt1min-ZIF-C is contributed from the stabilization effect arising from the Pt atoms to the Pt atoms. The high activity and excellent long-term stability indicate that the ZIF-C supported Pt single-atom/subnano-cluster electrocatalyst obtained by ALD is indeed one of the most promising alternatives to the Pt NPs for ORR in PEMFCs.

7.4 Conclusion

In summary, a class of novel Pt catalysts supported by MOFs-derived nanocarbon are proposed by the ALD technique. It is showed that the morphology, size, density and loading of Pt ranging from single atoms, subnano-clusters, to NPs on MOFs-carbon support can be precisely controlled by adjusting the exposure of Pt precursor to the substrate. The Pt1min-ZIF-C catalyst with Pt single atoms demonstrated exceptionally high activity as ORR catalyst compared with the Pt NPs catalysts. The remarkable performance of the single Pt atoms arises from their small size and the unique electronic structure originating from of the adsorption of the single Pt atoms on the N-doped nanocarbon support, as confirmed by XANES and EXAFS. It should be noted that, besides its high ORR performance, the Pt2min-Pt-ZIF-C catalyst with both Pt single atoms and subnanocluster offers the excellent long-term stability due to the supporting anchoring and Pt atoms self-stabilization effect metal-support interactions. This work provides a promising approach for designing of highly active and stable next generation catalysts based on single Pt atoms and subnano-clusters, which has a great potential to reduce the Pt loading and contributes to reduce the high cost of noble metal catalysts for PEMFCs application.

Acknowledgment

References

[1].   Debe, M.K., Nature, 2012. **486**(7401): p. 43-51.

[2].   Banham, D. and S. Ye, ACS Energy Letters, 2017. **2**(3): p. 629-638.

[3].   Banham, D., T. Kishimoto, Y. Zhou, T. Sato, K. Bai, J.-i. Ozaki, Y. Imashiro, and S. Ye, Science advances, 2018. **4**(3): p. eaar7180.

[4].   Eberle, U., B. Muller, and R. von Helmolt, Energy & Environmental Science, 2012. **5**(10): p. 8780-8798.

[5].   Yoshida, T. and K. Kojima, The Electrochemical Society Interface, 2015. **24**(2): p. 45-49.

[6].   Chung, D.Y., J.M. Yoo, and Y.-E. Sung, Advanced Materials, 2018: p. 1704123.

[7].   Service, R.F., Science, 2007. **315**(5809): p. 172-172.

[8].   Su, L., W. Jia, C.-M. Li, and Y. Lei, ChemSusChem, 2014. **7**(2): p. 361-378.

[9].   Sui, S., X. Wang, X. Zhou, Y. Su, S. Riffat, and C.-j. Liu, Journal of Materials Chemistry A, 2017. **5**(5): p. 1808-1825.

[10].   Cheng, X., Y. Li, L. Zheng, Y. Yan, Y. Zhang, G. Chen, S. Sun, and J. Zhang, Energy & Environmental Science, 2017. **10**(11): p. 2450-2458.

[11]. Bostjan, G., S. Ram, S. Dusan, T. Dusan, S.V. R., and M.N. M., Angewandte Chemie International Edition, 2011. **50**(24): p. 5468-5472.

[12]. Wang, Y.-J., N. Zhao, B. Fang, H. Li, X.T. Bi, and H. Wang, Chemical Reviews, 2015. **115**(9): p. 3433-3467.

[13]. Kim, J., H.-E. Kim, and H. Lee, ChemSusChem, 2018. **11**(1): p. 104-113.

[14]. Yang, X.-F., A. Wang, B. Qiao, J. Li, J. Liu, and T. Zhang, Accounts of Chemical Research, 2013. **46**(8): p. 1740-1748.

[15]. Zhang, H., G. Liu, L. Shi, and J. Ye, Advanced Energy Materials, 2018. **8**(1): p. 1701343.

[16]. Liu, J., M. Jiao, L. Lu, H.M. Barkholtz, Y. Li, Y. Wang, L. Jiang, Z. Wu, D.-j. Liu, L. Zhuang, C. Ma, J. Zeng, B. Zhang, D. Su, P. Song, W. Xing, W. Xu, Y. Wang, Z. Jiang, and G. Sun, Nature Communications, 2017. **8**: p. 15938.

[17]. Qiao, B., A. Wang, X. Yang, L.F. Allard, Z. Jiang, Y. Cui, J. Liu, J. Li, and T. Zhang, Nature Chemistry, 2011. **3**: p. 634.

[18]. Wang, X.X., D.A. Cullen, Y.-T. Pan, S. Hwang, M. Wang, Z. Feng, J. Wang, M.H. Engelhard, H. Zhang, Y. He, Y. Shao, D. Su, K.L. More, J.S. Spendelow, and G. Wu, Advanced Materials, 2018. **30** (11): p. 1706758.

[19]. Yang, S., J. Kim, Y.J. Tak, A. Soon, and H. Lee, Angewandte Chemie International Edition, 2016. **55**(6): p. 2058-2062.

[20]. Zhang, H., S. Hwang, M. Wang, Z. Feng, S. Karakalos, L. Luo, Z. Qiao, X. Xie, C. Wang, D. Su, Y. Shao, and G. Wu, Journal of the American Chemical Society, 2017. **139**(40): p. 14143-14149.

[21]. Cheng, N., S. Stambula, D. Wang, M.N. Banis, J. Liu, A. Riese, B. Xiao, R. Li, T.-K. Sham, and L.-M. Liu, Nature communications, 2016. **7**: p. 13638.

[22]. Sun, S., G. Zhang, N. Gauquelin, N. Chen, J. Zhou, S. Yang, W. Chen, X. Meng, D. Geng, and M.N. Banis, Scientific reports, 2013. **3**: p. 1775.

[23]. Xia, W., A. Mahmood, R. Zou, and Q. Xu, Energy & Environmental Science, 2015. **8**(7): p. 1837-1866.

[24]. Yang, Q., Q. Xu, and H.-L. Jiang, Chemical Society Reviews, 2017. **46**(15): p.4774-4808.

[25]. Wang, W., X. Xu, W. Zhou, and Z. Shao, Advanced Science, 2017. **4**(4): p. 1600371.

[26]. Song, Z., N. Cheng, A. Lushington, and X. Sun, Catalysts, 2016. **6**(8): p. 116.

[27]. Shen, K., X. Chen, J. Chen, and Y. Li, ACS Catalysis, 2016. **6**(9): p. 5887-5903.

[28]. Mahmood, A., W. Guo, H. Tabassum, and R. Zou, Advanced Energy Materials, 2016. **6**(17): p. 1600423.

[29]. Cravillon, J., R. Nayuk, S. Springer, A. Feldhoff, K. Huber, and M. Wiebcke, Chemistry of Materials, 2011. **23**(8): p. 2130-2141.

[30]. Adriaan, J.M.M., J.W. Matthieu, F.W.T. Nick, G.-A. Diana, H.J.V. René, A. Simone, A.B. Ageeth, A.V. Marcel, and M.M.K. Wilhelmus, Nanotechnology, 2016. **27**(3): p. 034001.

[31]. Grillo, F., H. Van Bui, J.A. Moulijn, M.T. Kreutzer, and J.R. van Ommen, The Journal of Physical Chemistry Letters, 2017. **8**(5): p. 975-983.

[32]. Trasatti, S. and O. Petrii, Pure and applied chemistry, 1991. **63**(5): p. 711-734.

[33]. Takakusagi, S., K.-i. Fukui, R. Tero, F. Nariyuki, and Y. Iwasawa, Physical Review Letters, 2003. **91**(6): p. 066102.

[34]. Hiratani, M., T. Nabatame, Y. Matsui, K. Imagawa, and S. Kimura, Journal of The Electrochemical Society, 2001. **148**(8): p. C524-C527.

[35]. Mackus, A.J.M., N. Leick, L. Baker, and W.M.M. Kessels, Chemistry of Materials, 2012. **24**(10): p. 1752-1761.

[36]. Song, Z., W. Liu, N. Cheng, M.N. Banis, X. Li, Q. Sun, B. Xiao, Y. Liu, A. Lushington, and R. Li, Materials Horizons, 2017. **4**(5): p. 900-907.

[37]. Li, Y., W. Gao, L. Ci, C. Wang, and P.M. Ajayan, Carbon, 2010. **48**(4): p. 1124-1130.

[38]. Weihan, L., L. Minsi, H. Yongfeng, L. Jun, L. Andrew, L. Ruying, W. Tianpin, S. Tsun-Kong, and S. Xueliang, Small Methods. **0**(0): p. 1700341.

[39]. Yan, H., Y. Lin, H. Wu, W. Zhang, Z. Sun, H. Cheng, W. Liu, C. Wang, J. Li, and X. Huang, Nature communications, 2017. **8**(1): p. 1070.

[40]. Yang, S., Y.J. Tak, J. Kim, A. Soon, and H. Lee, ACS Catalysis, 2017. **7**(2): p. 1301-1307.

[41]. Kamiya, K., R. Kamai, K. Hashimoto, and S. Nakanishi, Nature Communications, 2014. **5**: p. 5040.
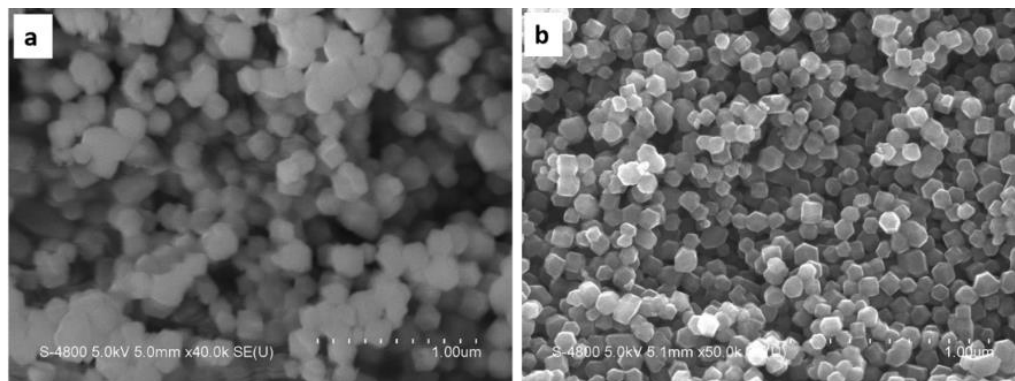
Supporting information

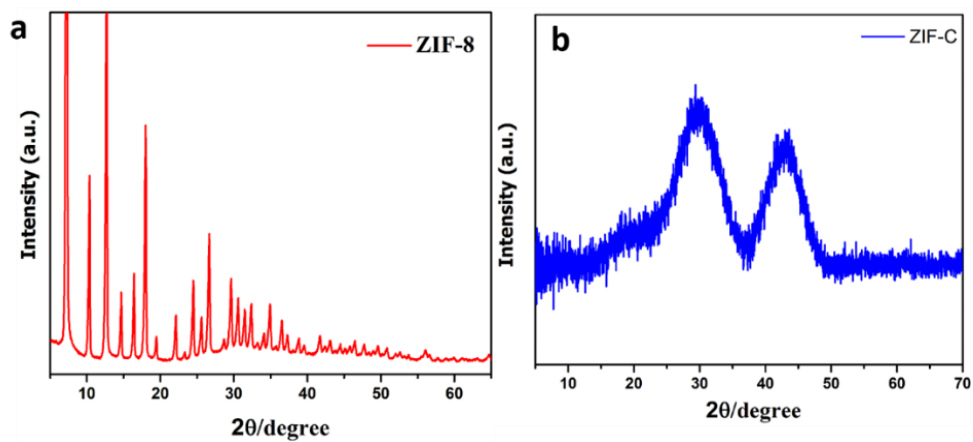**Figure S7.1. The SEM images of (a) ZIF-8 and (b) ZIF-C.**

Figure S7.2. The X-ray diffraction patterns of (a) ZIF-8 and (b) ZIF-C.
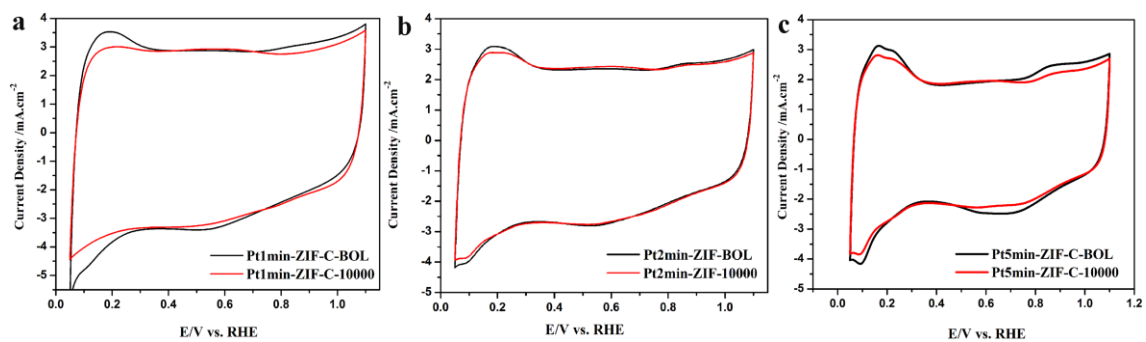
Figure S7.3. The CV curves of (a) Pt1min-ZIF-C, (b) Pt2min-ZIF-C and (c) Pt5min-ZIF-C before and after 10000 ADT cycles.

Chapter 8

8   Origin of the high oxygen reduction reaction of nitrogen and sulfur co-doped MOFs-derived nanocarbon electrocatalysts

Developing an economical, highly active and durable material to replace the conventional, expensive noble metal electrocatalyst is an important milestone in the development of fuel cell technology. Nanocarbon materials are considered as promising catalysts toward the oxygen reduction reaction (ORR) in fuel cells, due to their reasonable balance between low-cost, long-life durability and high catalytic activity in alkaline media. In this work, we present the fabrication of N,S-co-doped nanocarbon derived from a metal-organic frameworks (MOFs) precursor for use as an electrocatalyst towards ORR. High resolution transmission electron microscopy (HRTEM) mapping demonstrates the uniform distribution of N and S atoms into the nanocarbon skeleton. The nitrogen absorption– desorption isotherms indicate that the MOFs-derived N,S-co-doped nanocarbon has a high specific surface area (2439.9 $m^2 \cdot g^{-1}$) and a porous structure. Importantly, the N,S-co-doped nanocarbon exhibits higher catalytic activity toward ORR, better long-term stability and methanol tolerance than commercial Pt/C catalyst. First-principles calculations demonstrate that the remarkable electrochemical properties of N,S-co-doped nanocarbon are mainly attributed to the synergistic effect from the N and S dopants. Moreover, for the first time, it is revealed that the N,S-coupled dopants in nanocarbon can create active sites with higher catalytic activity for ORR than the isolated N and S-dopants. This finding on the structure–performance relationship of the co-doped nanocarbon provides guidelines for the design of high performance electrocatalysts.

8.1   Introduction

With remarkable efficiency, high energy density and negligible emission of harmful gases, the polymer electrolyte membrane fuel cell (PEMFC) is considered to be a green technology

that meets the energy requirement for future electrical vehicles and portable electronics.[1] Unfortunately, a major limitation for the low-temperature PEMFCs is the kinetically-sluggish oxygen reduction reaction (ORR) at the cathode, which requires a large amount of catalysts to reach the adequate energy output.[2–4] The state-of-the-art high-performance catalysts for ORR are the noble metal Pt-based catalysts.[5–10] However, Pt catalysts suffer from several issues including high cost, poor stability, the crossover effect and CO poisoning.[1] These bottlenecks hamper the widespread commercialization of PEMFCs. Therefore, it is highly desirable to replace the conventional, expensive catalysts with non-noble metal electrocatalysts that have all the characteristics of high activity, low cost and long-term stability. Recently, the nanocarbon has attracted much attention as an alternative catalyst due to its reasonably low cost, high activity, as well as its unique physical and chemical characteristics. Conventional nanocarbons like carbon black and carbon nanotubes generally exhibit an insufficient catalytic activity toward ORR in fuel cell applications. Several approaches have been investigated to modify nanocarbons in a way that enhances their catalytic activity. The chemical modification of nanocarbons is especially found to be an effective way of improving their intrinsic activity. [11–14] In particular, heteroatom-doping, such as doping nanocarbons with nitrogen (N), [15–17] boron (B), [18] sulfur (S), [19] and/or phosphorus (P), [20–22] has been reported as an excellent strategy for adjusting the surface polarity and the electronic properties of nanocarbons. The electronegative-N-doped nanocarbon induces the atomic charge density and the spin density redistribution, which consequently promotes the oxygen adsorption and reduction. [23] Moreover, recent pioneering work revealed that binary or ternary-co-doped nanocarbons possess a superior catalytic activity compared to single doped-nanocarbons due to the synergistic effect. The synergistic effect, arising from atomic charge and spin-density change, is favorable for O_2 reduction and electron transfer; this contributes to the enhanced ORR activity. [24–28]

The metal-organic framework (MOFs) is an extensive class of crystalline materials with ultrahigh porosity and enormous surface area, and it has attracted great interest in the field of catalysis.[29,30] Apart from its direct use, MOFs has also been found to be useful as a sacrificial precursor and a template to fabricate various functional nanomaterials.[30–34] By delicately designing the MOFs precursor and with careful post treatment, the benefits of high porosity and catalytic activity of a MOFs can be fully transferred into a MOFs-derived

nanomaterial. For example, a high surface area N-doped nanocarbon derived from the ZIF-8 precursor was shown to have abundant N-doping sites and excellent catalytic activity. [35,36] Although some newly developed N-doped-nanocarbons have shown performance, the improvement in the ORR catalytic activity has still been very limited due to the low amounts of the active sites. Thus, it is imperative to design a nanocarbon electrocatalyst with high loading of active sites. Before that, to gain an insight into the active sites that lead to the ORR performance is a significant challenge to be overcome.

Here, we report a novel strategy to fabricate N,S-co-doped nanocarbons as catalysts for ORR through adjusting the pore structure and active sites of the MOFs-derived nanocarbon. The N,S-co-doped nanocarbon is synthesized using MOFs as a solid precursor, followed by carbonization and pore size design, then further co-doping sulfur to generate more active sites. In our design, the typical Zn-based zeolitic imidazolate framework of ZIF-8 is selected as a template/precursor due to its high content of N-containing organic ligands, and its easy removal of the Zn species at a high temperature. The resulting N,S-co-doped nanocarbon demonstrates a high catalytic activity toward ORR, remarkable long-term stability and strong methanol tolerance in alkaline media. First-principles calculations prove that N,S-co-doped nanocarbons possess enhanced ORR activity compared to N-doped carbon. More importantly, this work for the first time reveals that the N,S-coupled dopants can create active sites with higher activity than the isolated N and S dopants.

8.2 Experimental

8.2.1 Synthesis of N, S-co-doped nanocarbon

Synthesis of ZIF-8 crystals was conducted by a chemical solvent method. In a typical experiment, two solutions are initially prepared by dissolving a known quantity of 2-methylimidazole (6.78 g, 82.0 mmol) in 250 ml of methanol and $Zn(NO_3)\cdot6H_2O$ (6.15 g, 20.5 mmol) in 250 ml of methanol. The solution of $Zn(NO_3)\cdot6H_2O$ was then added to 2-methylimidazole in a dropwise manner. The resulting mixture was stirred for 1h and aged for 24h at room temperature. Subsequently, white powder (ZIF-8 crystals) were collected by centrifugation and washed several times with methanol to remove the excess reactants. After dried in a vacuum at 60°C, the as-prepared ZIF-8 powder was carbonized at 1000°C for 8 h

in Ar to produce N-doped nanocarbon (ZIF-C). Then, the as-prepared ZIF-C was treated with ammonia for different time at 1000°C to control pore size, such as 3 min, 5 min, 7 min. The corresponding products were denoted as NH_3-C-3, NH_3-C-5, NH_3-C-7. To synthesis N, S co-doped nanocarbon, 20 mg of NH_3-C-7 was mixed with 300 mg of thiourea (w/w=1:15) in 5 ml of ethanol/water (v/v=4:1) to generate a suspension under sonication. The mixture was continuously stirred for 3h to facilitate a thiourea/NH_3-C-7 solid composite after drying. Thiourea/NH_3-C-7 was heated at 900°C for 1 h under an Ar atmosphere to generate the N, S-co-doped nanocarbon denoted as N, S-NH_3-C-7. For comparison, the N, S-ZIF-C of N, S-co-doped ZIF-C but no NH_3 treatment was prepared using a same procedure.

8.2.2   Physical characterization

The morphology and microstructure of as-prepared samples were obtained from a scanning electron microscope (SEM, Hitachi S-4800) and high-resolution transmission electron microscope (HRTEM, JEOL2010FEG) equipped with an electron energy loss spectrometer (EELS). X-ray diffraction (XRD) patterns were recorded using a Bruker D8-Advance diffractometer equipped with a Cu $K_{\acute{a}}$ radiation source. The background was subtracted from the patterns to remove the impact of detector. Raman spectra were performed on a HORIBA Scientific LabRAM HR Raman spectrometer using a laser excitation wavelength of 532.0 nm. Chemical compositions of as-synthesized samples were investigated by X-ray photoelectron spectroscopy (XPS, Kratos Axis Ultra spectrometer). The nitrogen absorption-desorption isotherms were measured using the equipment of Micromeritics Tristar II. The total specific surface area is calculated from the Brunauer-Emmett-Teller (BET) equation. The mesopore size distribution is determined by the Barrett–Joyner–Halenda (BJH) method from the adsorption isotherms. The micropore area and volume are obtained from a t-plot method.

8.2.3   Electrochemical measurements

Electrochemical measurements were performed on an Autolab electrochemical workstation in a conventional three-electrode cell, with Ag/AgCl electrode and Pt wire as the reference and counter electrodes. A catalyst-modified glassy carbon electrode was used as the working electrode. Catalyst ink was prepared by ultrasonically dispersing 3.0 mg of each catalyst powder in 3.0 ml ethanol containing 30 uL of Nafion (5wt%) for 0.5 h. Subsequently, 20 uL

of prepared catalyst ink was pipetted onto a polished glassy carbon electrode surface (0.196 cm^2) and dried at room temperature. The loading amount of catalyst was determined to be 0.1 mg·cm^{-2}. For comparison, commercial 20% Pt/C was prepared on the electrode using a similar procedure as described above with a Pt loading of 10 ug·cm^{-2}. Cyclic voltammetry (CV) experiments were conducted in N_2-saturated 0.1 M KOH solution with a scan rate of 50 mV·s^{-1} within a potential range of -0.9 V to 0.3 V (vs. Ag/AgCl). ORR linear sweep voltammetry (LSV) measurements were performed on a rotating disc electrode (RDE) in O_2-saturated 0.1 M KOH solution with background subtraction, at a scan rate of 10 mV·s^{-1} and rotating speed of 1600 rpm.

Simulation method and computation modeling

Spin polarized density functional theory (DFT) computations were performed at the generalized gradient approximation (GGA) level within the projector augmented-wave-Perdew-Burke-Ernzerhof (PAW-PBE) formalism using the plane wave basis set Vienna a/b initio simulation package (VASP) code. The models were built in a 6×6 orthorhombic graphene supercell with lattice parameters of a = 14.81 Å, b=14.81 Å, which contains a defect of 6-carbon atoms missing and with periodic boundary conditions in 3-dimensions. A large vacuum layer of 15 Å is maintained along the z-axis to avoid artificial interactions between graphene layers. A Monkhorst-Pack grid of 3×3×1 was used for geometric optimization. The simulation was run with a setup using 520 eV cut off energy. All atoms are allowed completely relax during optimization to gain an optimized cell shape with minimum energy while convergence criterion was set to 1×10^{-5} eV. The structural optimization process for all atoms were finished until the final force on each atom was less than 0.01 eV/Å.
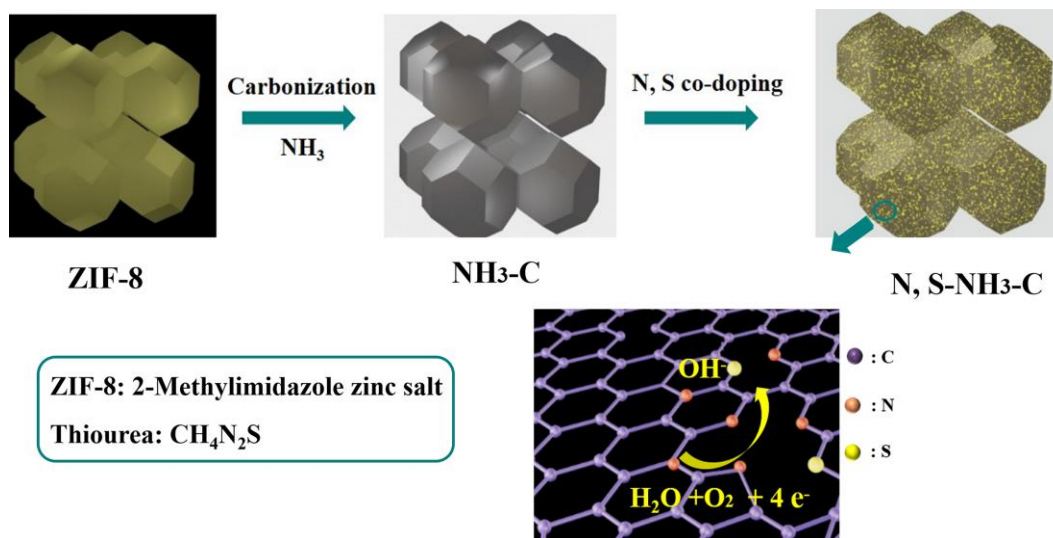
8.3 Results and discussion

Figure 8.1. Schematic illustration of the fabrication of the N,S-co-doped nanocarbon as the electrocatalyst toward ORR.

The fabrication of the integrated N,S-co-doped nanocarbon based on the MOFs concept is illustrated in Fig. 8.1. First, the ZIF-8 precursor, with an ordered rhombic dodecahedral morphology, is synthesized at the average particle size of 80 nm (Fig. SI8.1, ESI†). After carbonization at 1000 °C, the ZIF-8 crystals are converted into porous N-doped nanocarbon (ZIF-C). Subsequently, under thermal treatment with ammonia gas (NH_3), a much rougher surface is formed on the derived NH_3-C-x particles compared to ZIF-C. The SEM images indicate that ZIF-C (Fig. SI8.2, ESI†) and NH_3-C-7 nanocarbons (Fig. 8.2(a)) fully inherit the morphology and particle size of the ZIF-8 precursor, without framework collapse during the carbonization and NH_3 treatment. A rough surface of NH_3-C-7 after NH_3 treatment suggests that NH_3 may act as a surface modifier, similar to traditional activating agents such as KOH [37] and CO_2, [38] to etch carbon or oxygen atoms from the nanocarbon framework and tune the porous structure. [39,40] Finally, the as-proposed N,S-co-doped nanocarbon (N,S-NH_3-C-7) is developed by doping S into the NH_3-C-7 carbon skeleton. As indicated from the SEM images, there is a minimal change in the particle size between nanocarbons of NH_3-C-7 (Fig. 8.2(a)) and N,S-NH_3-C-7 (Fig. 8.2(b)). The local structure and composition of the as-prepared N,S-NH_3-C-7 is further confirmed by HRTEM. As shown in Fig. 8.2(c), it can be

clearly noted that the N,S-NH$_3$-C-7 nanocarbon has a polyhedral morphology with a rough surface, which is consistent with the observations noted by SEM analysis. In addition, the electron energy loss spectroscopy (EELS) elemental chemical mapping (Fig. 8.2(d)) reveals the uniform distribution of elemental carbon, nitrogen, and sulfur in N,S-NH$_3$-C-7 matrix. This confirms that heteroatoms of nitrogen and sulfur are successfully doped into the carbon skeleton.
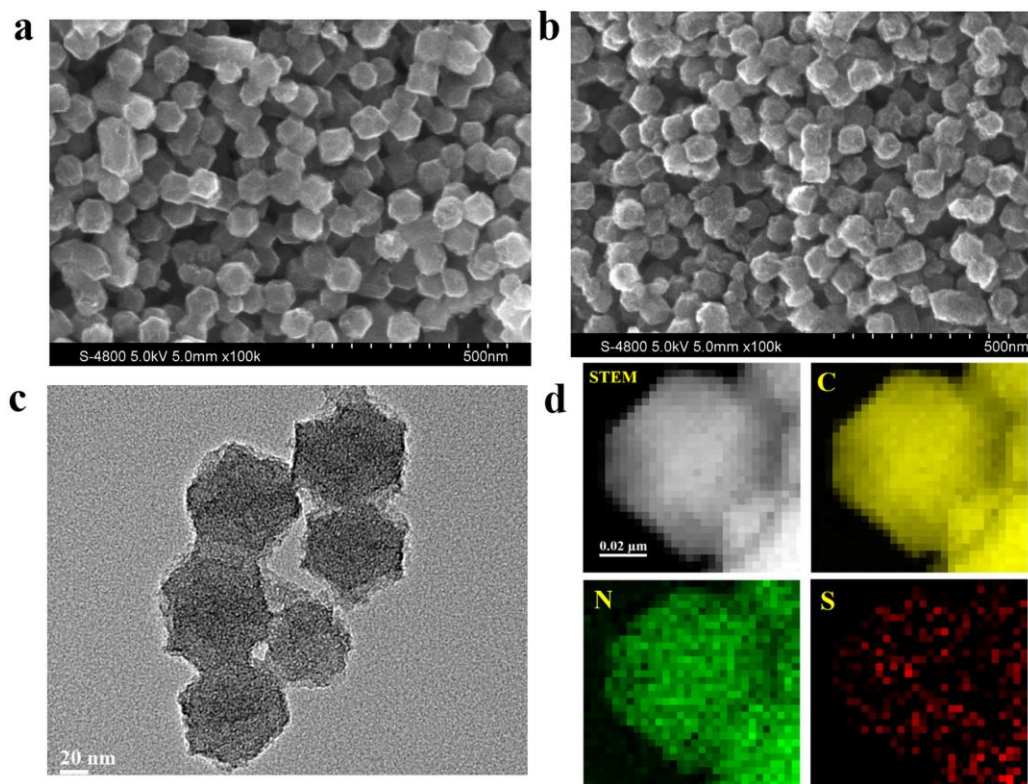

Figure 8.2. SEM images of (a) NH$_3$-C-7 and (b) N,S-NH$_3$-C-7; (c) TEM image of N,S-NH$_3$-C-7; (d) STEM images of N,S-NH$_3$-C-7 and EELS mapping of C, N, S.

The physical properties of the as-prepared nanocarbons are further investigated by XRD and Raman spectroscopy. The XRD patterns of ZIF-C, NH$_3$-C-7 and N,S-NH$_3$-C-7 are shown in Fig. 8.3(a). These patterns display two broad peaks at around 26° and 43°, corresponding to the characteristic carbon (002) and (100)/(101) diffractions, respectively. Additionally, no diffraction peaks of Zn/ZnO impurities could be observed, which means most of the Zn species have been removed during high temperature carbonization. Fig. 8.3(b) presents the Raman spectra obtained for the nanocarbons. A typical D band (1350 cm^{-1}) resulting from in-

plane imperfections of disordered carbon, and a G band (1580 cm^{-1}) resulting from the stretching mode of highly ordered graphitic carbon, is observed for all the samples. Raman spectra are sensitive to subtle structural variations in nanocarbons and the band intensity ratio (I_D/I_G) can reflect the defect generation or defect disappearance on the carbon matrix. A lower I_D/I_G ratio suggests less defects and therefore a higher structural quality. [41] Interestingly, the I_D/I_G ratio for ZIF-C (I_D/I_G = 0.9) is lower than that found for NH$_3$-C-7 (I_D/I_G = 1.13), indicating that the modification of graphitic carbon occurs during the NH$_3$ treatment process. In particular, when the exposure time of NH$_3$ is extended from 3min to 7min, there is a gradual increase in the I_D/I_G ratio, from 1.03 to 1.13 (Fig. SI8.3, ESI†). This further confirms that the increased duration of NH$_3$ gas exposure results in the generation of additional defective sites. Therefore, the N-doped nanocarbon of NH$_3$-C-7 with high defects is optimized for further S-doping to produce the co-doped nanocarbon of N,S-NH$_3$-C-7. A higher I_D/I_G ratio (1.17) found for N,S-NH$_3$-C-7 implies that an increased number of heteroatom doping sites (N-doped-C, S-doped-C, NS-coupled-C) can be created on the N,S-NH$_3$-C-7 nanocarbon. The large numbers of active doping sites are anticipated to accelerate the ORR process.
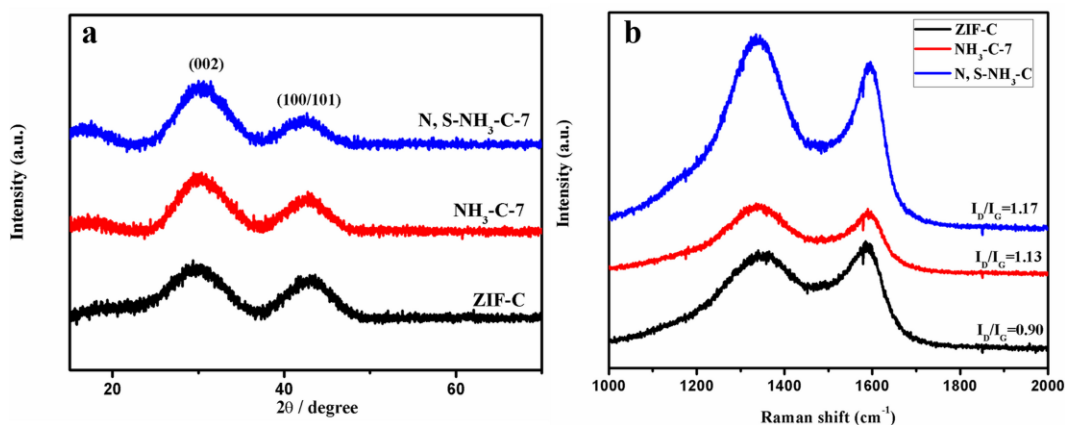
Figure 8.3. (a) XRD patterns and (b) Raman spectra of the nanocarbons of ZIF-C, NH$_3$-C-7 and N,S-NH$_3$-C-7.

The pore structure of catalyst materials plays a significant role in promoting the ORR activity as an appropriate pore size is essential for the diffusion of smooth reactants (O$_2$, –OH) and rapid mass transport. [42] Thus, the impact of NH$_3$ etching on the textural properties of the MOFs-derived nanocarbon is studied by nitrogen absorption/desorption isotherms. The

specific surface area and pore size distribution of all synthesized nanocarbons as well as textural properties are shown in Fig. 8.4 and Table 8.1, respectively. Generally, at low partial pressures ($P/P_0 < 0.1$), a significant uptake in the isotherms indicates that the MOFs-derived nanocarbons exist in the microporous structure (pore size <2 nm). The hysteresis of desorption between the partial pressures P/P_0 of 0.5–1.0 suggests the presence of mesopores (pore size of 2–50 nm) in NH_3-C-x nanocarbons. [43] As illustrated in Fig. 8.4(a), the specific surface area of ZIF-C is only 852.5 $m^2 \cdot g^{-1}$. After NH_3 treatment, it increases to 1926.8 $m^2 \cdot g^{-1}$, 2276.8 $m^2 \cdot g^{-1}$ and 2439.9 $m^2 \cdot g^{-1}$, for NH_3-C-3, NH_3-C-5 and NH_3-C-7, respectively. The isotherms are further analyzed using the Barrett–Joyner–Halenda (BJH) and the t-plot method to fit the pore size distribution and micropore volume, respectively. In Fig. 8.4(b), the samples of ZIF-8 and ZIF-C exhibit a narrow micropore size distribution, centered at ~1.8 nm, suggesting that the major pores in ZIF-8 and ZIF-C are micropores; they have a pore volume of 0.80 $cm^3 \cdot g^{-1}$ and 0.52 $cm^3 \cdot g^{-1}$ (Table 8.1), respectively. It is interesting to note that there is an increase in pore volume from 1.23 $cm^3 \cdot g^{-1}$ to 1.69 $cm^3 \cdot g^{-1}$ observed for NH_3-C-3 and NH_3-C-7 after NH_3 treatment. Meanwhile, NH_3 treatment of the nanocarbon develops the micropores into mesopores, with an increase in the mesopore volume of up to 88.6% for NH_3-C-7. Given the results presented by SEM, HRTEM and N_2 absorption/desorption isotherms, NH_3 treatment certainly plays a significant role in tuning the textural properties of MOFs-derived nanocarbons.
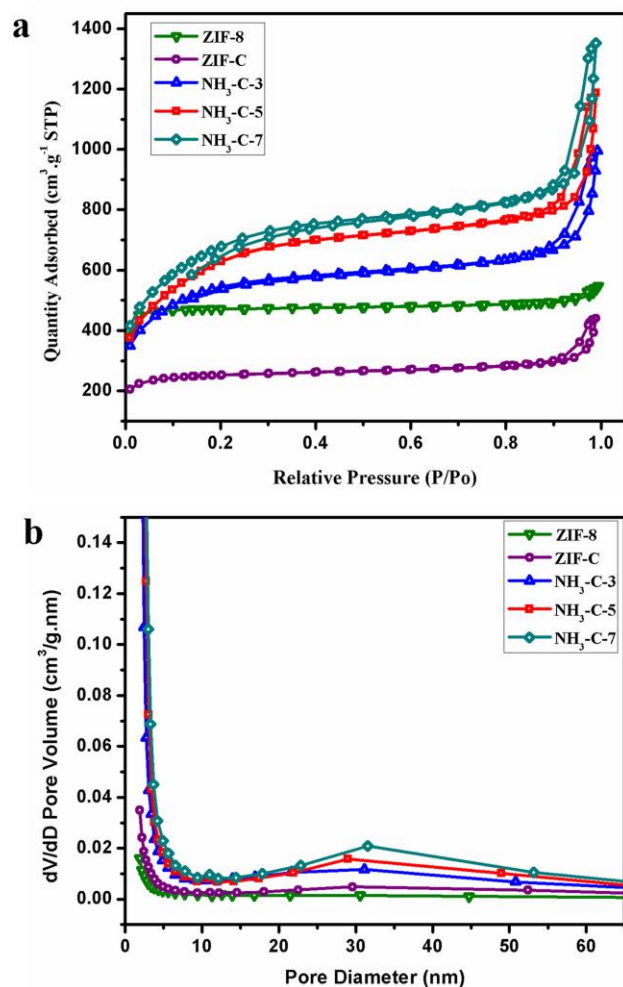
Figure 8.4. (a) N₂ adsorption–desorption isotherms and (b) pore size distribution data obtained by the Barrett–Joyner–Halenda (BJH) method of ZIF-8, ZIF-C and NH₃-C-x.

Table 8-1. Surface area and pore volume characteristics of ZIF-8, ZIF-C and NH₃-C-x.

Catalyst	Surface area ($m^2 \cdot g^{-1}$)	Total pore volume ($m^3 \cdot g^{-1}$)	Micropore volume ($m^3 \cdot g^{-1}$)	V_{meso}/V_{total} (%)
ZIF-8	1568.8	0.80	0.70	12.5
ZIF-C	852.5	0.52	0.31	40.7
NH₃-C-3	1926.8	1.23	0.35	72.0

NH$_3$-C-5	2276.8	1.43	0.12	80.6
NH$_3$-C-7	2439.9	1.69	0.19	88.6

To analyze the chemical bonding states of the doped nanocarbon, XPS measurements are carried out on N,S-NH$_3$-C-7, NH$_3$-C-7 and ZIF-C. In Fig. S8.4 (ESI†), the XPS survey spectra of N,S-NH$_3$-C-7 show that both N (~5.4 at%) and S (~0.3 at%) atoms are successfully incorporated into the nanocarbon framework. The N concentration in N,S-NH$_3$-C-7 (~5.4 at%) is almost the same with the N content found in NH$_3$-C-7 (~5.1 at%) and ZIF-C (~5.0 at%). This means that NH$_3$ treatment does not dope more N elements on MOFs-derived nanocarbons. The high resolution N1s spectra of N,S-NH$_3$-C-7, NH$_3$-C-7 and ZIF-C in Fig. 8.5(a) display the presence of four nitrogen species: pyridinic-N (~398.3 eV), pyrrolic-N (~399.5 eV), graphitic-N (~401.0 eV) and oxidized-N (~404.1 eV). Notably, NH$_3$ treatment plays a role in adjusting the relative quantities of pyridinic-N and graphitic-N. In Fig. 8.5(b), the proportions of pyridinic-N increased while those of graphitic-N decreased in NH$_3$-C-7 and N,S-NH$_3$-C-7 compared to those of ZIF-C which were not treated with NH$_3$. Based on the XPS analysis, it is found that the NH$_3$ heating process helps in the conversion of graphitic-N to pyridinic-N. Previous research has established that pyridinic-N with planar configurations is active toward ORR.[44] In contrast, graphitic-N atoms, which possess a 3D structure, are inactive toward ORR. Therefore, the N,S-NH$_3$-C-7 and NH$_3$-C-7 nanocarbons which contain more planar pyridinic-N atoms than ZIF-C, are considered to have higher ORR activity. High resolution S2p spectra of N,S-NH$_3$-C-7 are shown in Fig. 8.5(c). Due to spin–orbit coupling, signals originating from sulfur atoms are represented as a doublet. The S2p spectra of N,S-NH$_3$-C-7 reveal two major chemical bonding structures: one from C–S–C chemical bonding located at a low binding energy (165.8–167.1 eV), and another one at a slightly higher binding energy (166.8–168.0 eV) ascribed as –S–C–N–. Since N is more electronegative than S, it is going to hog the electrons in a covalent bond with S, which lead to a more electropositive configuration for S. Therefore, the electronic insufficient S atoms in the –S–C–N– chemical environment display a signal that is red shifted to a higher binding energy. These two different S chemical environments of C–S–C and –S–C–N– should exhibit different catalytic activities toward ORR. The –S–C–N– bonding structure, in which N and S are close to each other and doped on the same C atom, is expected to be the more active

doping site for ORR. To prove this speculation, further catalytic activity toward ORR of the nanocarbon electrocatalyst and the first-principles calculations are provided below.
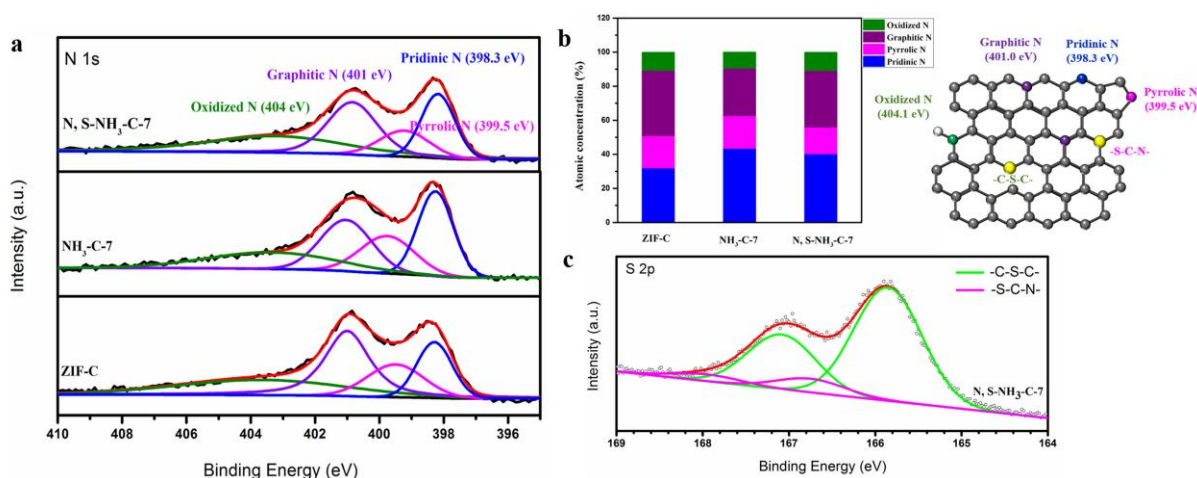

Figure 8.5. Chemical binding state of the nanocarbons. (a) N1s XPS spectra of N,S-NH₃-C-7, NH₃-C-7 and ZIF-C. (b) Bar diagrams representing the atomic concentration of four kinds of nitrogen species (left); atomic structure of the N,S-doped nanocarbon with chemical bonding configurations of nitrogen and sulfur dopants (right). (c) S2p XPS spectra of N,S-NH₃-C-7.

The electrochemical performance of the as-prepared nanocarbons toward ORR is analyzed and compared with their counterparts (NH₃-C-x, ZIF-C, and the commercial catalyst Pt/C). CV measurements of N,S-NH₃-C-7 in N₂-saturated and O₂-saturated 0.1 M KOH electrolytes are presented, respectively, in Fig. 8.6(a). Compared to the featureless CV curves obtained in the N₂-saturated electrolyte, a distinct oxygen reduction peak is observed at ~0.18 V (vs. Ag/AgCl) in O₂-saturated KOH solution, indicating the ORR catalytic activity for the N,S-NH₃-C-7 nanocarbon. Fig. 8.6(b) presents the LSV curves of the nanocarbon catalysts obtained in an O₂-saturated 0.1 M KOH electrolyte at a rotating speed of 1600 rpm. According to the analysis of the electrochemical performance, NH₃-C-7 displays a higher ORR half-wave potential ($E_{1/2}$ = -0.194 V) and an increased limiting current density (I_{lim} = 3.59 mA·cm^{-2}) compared to ZIF-C ($E_{1/2}$ = -0.286 V, I_{lim} = 2.80 mA·cm^{-2}). This indicates that the catalytic activity of the nanocarbons can be enhanced via NH₃ treatment. In addition, extension of the NH₃ treatment time of ZIF-C increases the catalytic activity of the nanocarbons. As shown in Fig. SI8.5 (ESI†), NH₃-C-7 shows a better catalytic activity

compared to NH_3-C-3 and NH_3-C-5. The good performance is embodied in the elevated limiting current density of NH_3-C-7 and a 90 mV positively shifted half-wave potential compared to NH_3-C-3. The excellent electrochemical performance of NH_3-C-7 compared to ZIF-C confirms the significance of tuning the mesoporous structure of the nanocarbon in promoting the ORR performance. After co-doping S atoms into the NH_3-C-7 nanocarbon, the nanocarbon of N,S-NH_3-C-7 shows the most positive-shifted half-wave potential of $E_{1/2}$ = -0.13 V. A halfwave potential is much higher than that of ZIF-C and NH_3-C-7 and comparable to that of the Pt/C catalyst ($E_{1/2}$ = -0.12 V). Moreover, the N,S-NH_3-C-7 nanocarbon has an enhanced limiting current density of 3.99 mA·cm^{-2}, a current density which is higher than that for NH_3-C-7 (3.59 mA·cm^{-2}) and Pt/C (3.75 mA·cm^{-2}). These results confirm that the enhanced ORR activity can be realized in the N,S-co-doped nanocarbon system. To prove the combination of NH_3 treatment and N,S-co-doping is necessary for the catalyst design, the nanocarbon of N,S-ZIF-C with only N,S-co-doping of ZIF-C but no NH_3 treatment is prepared. By analysis of the electrochemical performance of N,S-ZIF-C toward ORR, it shows that the N,S-ZIF-C nanocarbon exhibits improved activity compared to ZIF-C. However, the half-wave potential ($E_{1/2}$ = -0.192 V) and the limiting current (3.20 mA·cm^{-2}) are much lower than those of the N,S-NH_3-C-7 catalyst. It is supposed that the poor performance is due to the microporous structure of N,S-ZIF-C. The small size of the micropore is difficult for the reactants diffusion, which will increase the mass transport resistance and impact the ORR activity. To further investigate the ORR kinetics of the N,S-NH_3-C-7 catalyst, LSV polarization curves are generated using a rotating disc electrode. The tests are conducted at a variety of rotating speeds ranging from 400 to 2025 rpm, and the kinetic parameters are analyzed using the Koutecky–Levich (K–L) equation. In Fig. 8.6(c, d), the K–L plots of the N,S-NH_3-C-7 nanocarbon at -0.25 V, -0.4 V and -0.6 V exhibit good linearity and parallelism, indicating the presence of the first-order reaction kinetics in regard to the oxygen concentration, and a similar electron transfer number (n) toward ORR at various potentials. The values of n for N,S-NH_3-C-7, calculated from the slope of K–L plots, vary from 3.49 to 3.81 in the potential range of -0.6 V to -0.25 V. This means that the ORR process takes place in a four-electron pathway.
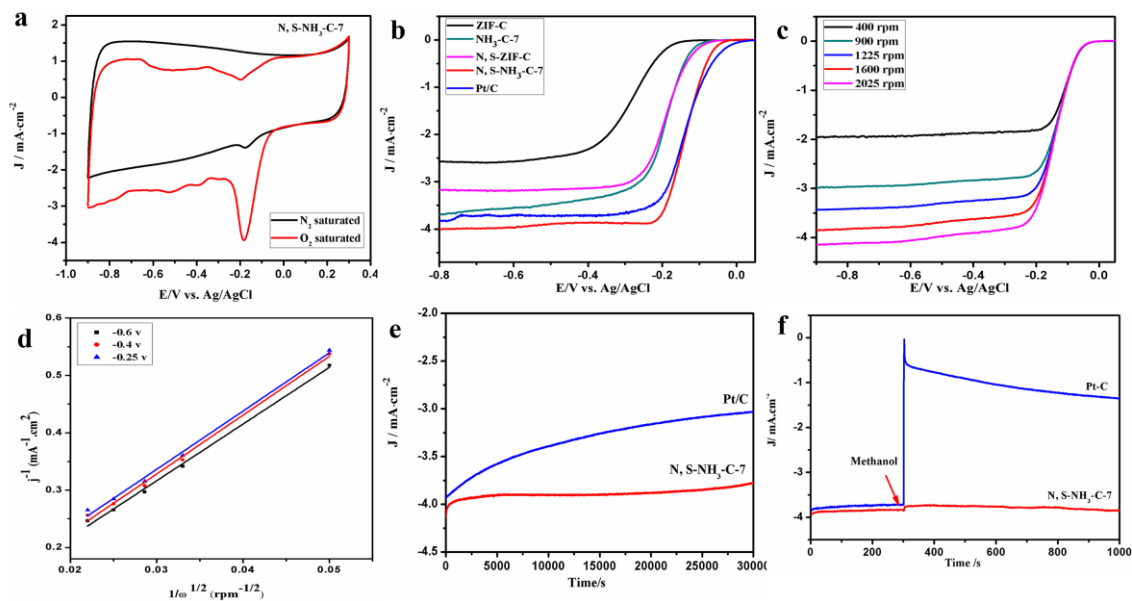
Figure 8.6. (a) Cyclic voltammograms of N,S-NH₃-C-7 with a scan rate of 10 mV·s⁻¹ in O₂-(red) and N₂-saturated (black) 0.1 M KOH solution. (b) Linear sweep voltammograms (LSVs) of ZIF-C (black), NH₃-C-7 (blue), N,S-NH₃-C-7 (red), and 20% Pt/C (cyan) in O₂-saturated 0.1 M KOH solution at 1600 rpm. The LSV curves for NH₃-C-X are shown in Figure SI8.5. (c) LSV curves of N,S-NH₃-C-7 in O₂-saturated 0.1 M KOH with various rotation speeds. The corresponding K-L plots at various voltages are shown in (d). Stability (e) and methanol tolerance (f) curves for N,S-NH₃-C-7 and Pt/C catalysts in O₂-saturated 0.1 M KOH.

The long-term durability is crucial for evaluating the performance of a new electrocatalyst. The durability of the N,S-NH₃-C-7 nanocarbon and the commercial Pt/C catalyst is analyzed at -0.4 V (vs. Ag/AgCl) in O₂-saturated 0.1 M KOH at 1600 rpm over 30 000 s of continuous operation. It is observed that the N,S-NH₃-C-7 catalyst is more stable than the commercial Pt/C catalyst (Fig. 8.6(e)). The current density of N,S-NH₃-C-7 changed from 4.03 mA·cm⁻² to 3.70 mA·cm⁻² with only 8.2% loss after the long-time durability testing, while a higher current density loss of 22.6% is observed for the Pt/C catalyst. Besides the excellent durability, the N,S-NH₃-C-7 catalyst also displays an excellent immunity towards methanol crossover reactions, which overcomes another disadvantage faced by the Pt/C catalyst. 1.0 M of methanol is added into a 0.1 M KOH electrolyte solution to investigate methanol tolerance for the N,S-NH₃-C-7 nanocarbon and the Pt/C catalyst (Fig. 8.6(f)). It was found that

methanol injection causes a sharp current decrease for the Pt/C catalyst, while it has almost no influence on the N,S-NH₃-C-7 nanocarbon, proving an excellent ORR selectivity and a good performance for methanol tolerance.
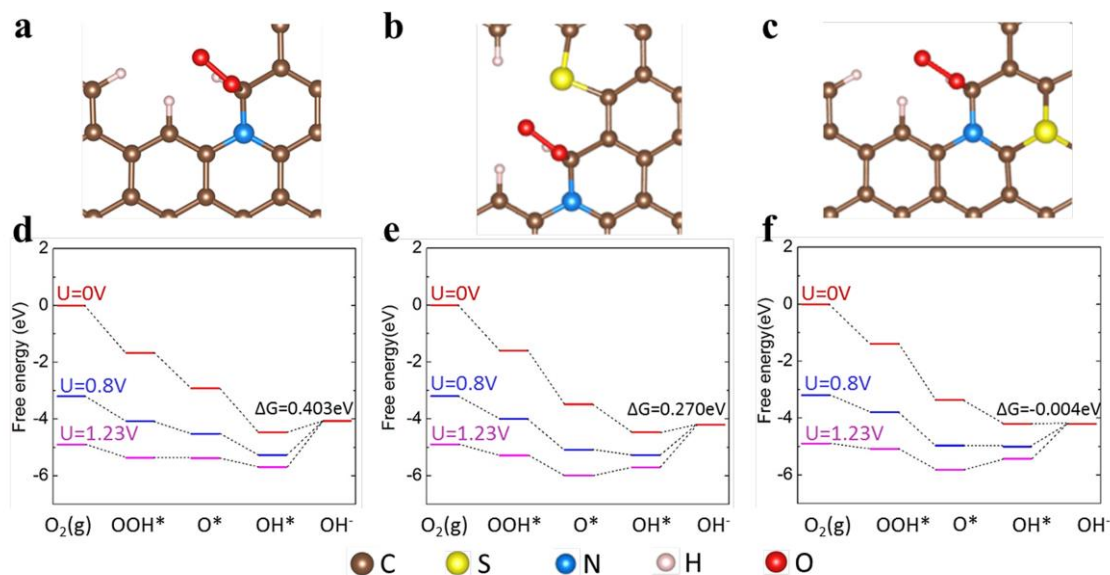

Figure 8.7. Optimized structures for the stable adsorbed O₂ on the N-doped nanocarbon (a), the N,S-isolated nanocarbon (b) and the N,S-coupled nanocarbon (c). Free-energy diagram of the ORR on the N-doped nanocarbon (d), the N,S-isolated nanocarbon (e) and the N,S-coupled nanocarbon (f) in alkaline media.

To understand the intrinsic ORR catalytic mechanism of the N,S-doping effect, first-principles calculations are carried out to determine the electronic structure and the catalytic reaction for the N-doped nanocarbon (Fig. 8.7(a)) and the N,S-co-doped nanocarbon. In the co-doped structure, N and S may exist within a framework in a variety of configurations, including N,S-isolated dopants (Fig. 8.7(b)), and N,S-coupled dopants (in which N and S are close to each other and doped on the same C atom) (Fig. 8.7(c)). The calculated free energy profiles, on these three structures are shown in Fig. 8.7(d–f), respectively. The corresponding intermediate configurations are shown in Fig. SI8.6(a–l) (ESI†). In Fig. 8.7(d–f), the free energy of each reaction (ΔG) is downhill for the first several steps, except for OH* + e⁻ → OH⁻ + *, which is thermodynamically uphill (endothermic). This result suggests that the reduction of OH* into OH⁻ is the rate determining step for the ORR process. As the

overpotential of the ORR is an important measure of the activity of a catalyst, we calculated the overpotential for each active site and determined the minimum overpotential for ORR on the doped structures. Thermodynamically, a lower overpotential means better catalytic activity. The N-doped, isolated N,S-doped, and N,S-coupled carbon structures are identified to have minimum ORR overpotentials of 0.403 V, 0.270 V, and -0.004 V at the electrode potential of 0 V, respectively. Obviously, the N,S-co-doped nanocarbon with N,S-coupled dopants has the lowest overpotential and exhibits the best catalytic activity toward ORR. As we know, the ORR reaction process has a close relationship with the charge transfer reaction between the adsorbates and the substrate. Taking O_2 adsorption as an example, the Bader charge [45] of the O_2 adsorbed on the corresponding doping structures has been studied. As shown in Table SI8.1 (ESI†), the Bader charges of O_2 adsorption on the N-doped nanocarbon, the N,S-isolated nanocarbon and the N,S-coupled nanocarbon, are 12.58, 13.19, and 13.30, respectively. The N,S-coupled nanocarbon, in which N and S atoms are close to each other, could provide a greater electron density to the adsorbed O_2 as opposed to the other two structures, making O_2 and its related species more active. This is the synergistic effect arising from N and S dopants. The synergistic effect of N,S-coupled dopants leads to more active sites of carbon and therefore enhances the ORR activity of the nanocarbon. Thus first-principles calculations prove that N,S-coupled dopants create active sites with a higher activity than the isolated N and S dopants. It is, for the first time, to pinpoint the doping-active sites, with solid evidences, which is a key factor to determine the performance of the nanocarbon catalyst. The discovery on the doping structure–performance relationship of the nanocarbon provides guidelines for the design of novel electrocatalysts with a high activity.

8.4 Conclusions

A novel N,S-co-doped nanocarbon electrocatalyst derived from a MOFs of ZIF-8 has been developed. It is found that compared to the noble-metal Pt/C catalyst, the N,S-co-doped nanocarbon exhibits excellent catalytic activity and long-term stability toward ORR in alkaline media. The high specific surface area and appropriate porosity built in the N,S-co-doped nanocarbon are beneficial for the mass transportation and facilitate the ORR process. More importantly, first-principles calculations reveal that the N,S-coupled dopants promote the carbon sites with a higher activity compared to the isolated N and S dopants. The N,S-

coupled nanocarbon provides a great electron density to the adsorbed O_2, thus making O_2 and its species to be reduced. The highly active co-doping sites resulting from the synergistic effect well explain the origin of the enhanced ORR activity for the N,S-co-doped nanocarbon. The approach and analysis adopted in this work offer a strategic consideration for designing the high performance nanocarbon electrocatalyst.

Acknowledgment

References

[1]. M. K. Debe, Nature, 2012, 486, 43–51.

[2]. G. Wu and P. Zelenay, Acc. Chem. Res., 2013, 46, 1878–1889.

[3]. B. C. H. Steele and A. Heinzel, Nature, 2001, 414, 345–352.

[4]. P. Chen, T.-Y. Xiao, Y.-H. Qian, S.-S. Li and S.-H. Yu, Adv. Mater., 2013, 25, 3192–3196.

[5]. N. Cheng, M. Norouzi Banis, J. Liu, A. Riese, S. Mu, R. Li, T.-K. Sham and X. Sun, Energy Environ. Sci., 2015, 8, 1450–1455.

[6]. N. Cheng, M. N. Banis, J. Liu, A. Riese, X. Li, R. Li, S. Ye, S. Knights and X. Sun, Adv. Mater., 2015, 27, 277–281.

[7]. B. Lim, M. Jiang, P. H. Camargo, E. C. Cho, J. Tao, X. Lu, Y. Zhu and Y. Xia, Science, 2009, 324, 1302–1305.

[8]. V. Mazumder, M. Chi, K. L. More and S. Sun, J. Am. Chem. Soc., 2010, 132, 7848–7849.

[9]. L. Yang, M. B. Vukmirovic, D. Su, K. Sasaki, J. A. Herron, M. Mavrikakis, S. Liao and R. R. Adzic, J. Phys. Chem. C, 2013, 117, 1748–1753.

[10]. N. Cheng, S. Stambula, D. Wang, M. N. Banis, J. Liu, A. Riese, B. Xiao, R. Li, T.-K. Sham, L.-M. Liu, G. A. Botton and X. Sun, Nat. Commun., 2016, 7, 13638.

[11]. W. Ding, L. Li, K. Xiong, Y. Wang, W. Li, Y. Nie, S. Chen, X. Qi and Z. Wei, J. Am. Chem. Soc., 2015, 137, 5414–5420.

[12]. W. Niu, L. Li, X. Liu, N. Wang, J. Liu, W. Zhou, Z. Tang and S. Chen, J. Am. Chem. Soc., 2015, 137, 5555–5562.

[13]. D. Geng, Y. Chen, Y. Chen, Y. Li, R. Li, X. Sun, S. Ye and S. Knights, Energy Environ. Sci., 2011, 4, 760–764.

[14]. X. Liu, L. Li, W. Zhou, Y. Zhou, W. Niu and S. Chen, ChemElectroChem, 2015, 2, 803–810.

[15]. K. Gong, F. Du, Z. Xia, M. Durstock and L. Dai, Science, 2009, 323, 760–764.

[16]. R. Liu, D. Wu, X. Feng and K. Mu¨llen, Angew. Chem., 2010, 122, 2619–2623.

17 G. Wu, K. L. More, C. M. Johnston and P. Zelenay, Science, 2011, 332, 443–447.

[18]. L. Yang, S. Jiang, Y. Zhao, L. Zhu, S. Chen, X. Wang, Q. Wu, J. Ma, Y. Ma and Z. Hu, Angew. Chem., 2011, 123, 7270–7273.

[19]. S. Inamdar, H.-S. Choi, P. Wang, M. Y. Song and J.-S. Yu, Electrochem. Commun., 2013, 30, 9–12.

[20]. Z. W. Liu, F. Peng, H. J. Wang, H. Yu, W. X. Zheng and J. Yang, Angew. Chem., 2011, 123, 3315–3319.

[21]. D.-S. Yang, D. Bhattacharjya, S. Inamdar, J. Park and J.-S. Yu, J. Am. Chem. Soc., 2012, 134, 16127–16130.

[22]. J. Zhang, Z. Zhao, Z. Xia and L. Dai, Nat. Nanotechnol., 2015, 10, 444–452.

[23]. W. Yang, T.-P. Fellinger and M. Antonietti, J. Am. Chem. Soc., 2010, 133, 206–209.

[24]. N. Ranjbar Sahraie, J. P. Paraknowitsch, C. Go¨bel, A. Thomas and P. Strasser, J. Am. Chem. Soc., 2014, 136, 14486–14497.

[25]. X. Gong, S. Liu, C. Ouyang, P. Strasser and R. Yang, ACS Catal., 2015, 5, 920–927.

[26]. M. Zhang and L. Dai, Nano Energy, 2012, 1, 514–517.

[27]. W. Yang, X. Yue, X. Liu, J. Zhai and J. Jia, Nanoscale, 2015, 7, 11956–11961.

[28]. W. Kicin´ski, M. Szala and M. Bystrzejewski, Carbon, 2014, 68, 1–32.

[29]. M. Fujita, Y. J. Kwon, S. Washizu and K. Ogura, J. Am. Chem. Soc., 1994, 116, 1151–1152.

[30]. Y. Zhao, Z. Song, X. Li, Q. Sun, N. Cheng, S. Lawes and X. Sun, Energy Storage Mater., 2016, 2, 35–62.

[31]. W. Chaikittisilp, K. Ariga and Y. Yamauchi, J. Mater. Chem. A, 2013, 1, 14–19.

[32]. Z. Song, N. Cheng, A. Lushington and X. Sun, Catalysts, 2016, 6, 116.

[33]. Q. L. Zhu, W. Xia, T. Akita, R. Zou and Q. Xu, Adv. Mater., 2016, 28, 6391–6398.

[34]. A. Mahmood, W. Guo, H. Tabassum and R. Zou, Adv. Energy Mater., 2016, 6, DOI: 10.1002/aenm.201600423.

[35]. L. Zhang, Z. Su, F. Jiang, L. Yang, J. Qian, Y. Zhou, W. Li and M. Hong, Nanoscale, 2014, 6, 6590–6602.

[36]. F. Zheng, Y. Yang and Q. Chen, Nat. Commun., 2014, 5, 5261.

[37]. Y. Lv, F. Zhang, Y. Dou, Y. Zhai, J. Wang, H. Liu, Y. Xia, B. Tu and D. Zhao, J. Mater. Chem., 2012, 22, 93–99.

[38]. L. Sun, C.-l. Wang, Y. Zhou, X. Zhang and J.-s. Qiu, Carbon, 2014, 71, 344–345.

[39]. X. Yang, G. Zhang, M. Zhong, D. Wu and R. Fu, Langmuir, 2014, 30, 9183–9189.

[40]. X. Li, Q. Sun, J. Liu, B. Xiao, R. Li and X. Sun, J. Power Sources, 2016, 302, 174–179.

[41]. M. V. Ivanova, C. Lamprecht, M. J. Loureiro, J. T. Huzil and M. Foldvari, Int. J. Nanomed., 2012, 7, 403–415.

[42]. N. Cheng, Y. Shao, J. Liu and X. Sun, Nano Energy, 2016, 29, 220–242.

[43]. Q. Wang, W. Xia, W. Guo, L. An, D. Xia and R. Zou, Chem. Asian J., 2013, 8, 1879–1885.

[44]. D. Guo, R. Shibuya, C. Akiba, S. Saji, T. Kondo and J. Nakamura, Science, 2016, 351, 361–365.

[45]. E. Sanville, S. D. Kenny, R. Smith and G. Henkelman, J. Comput. Chem., 2007, 28, 899–908.
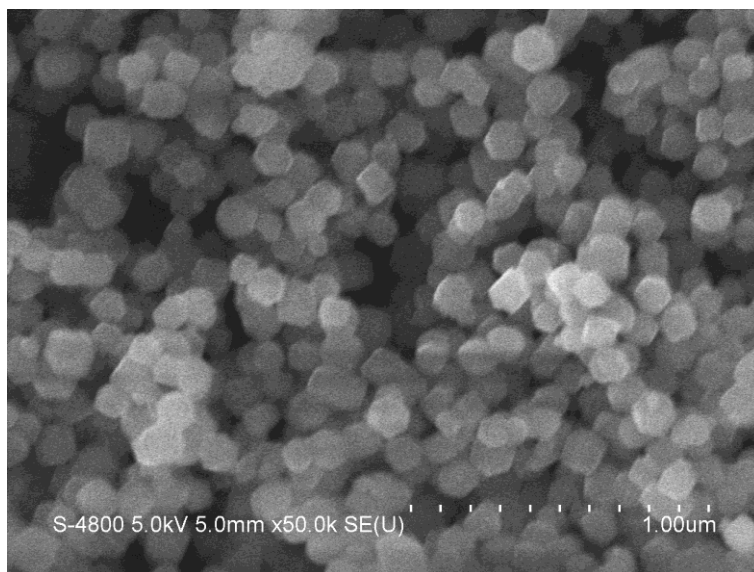
Supporting information

Figure SI 8.1. SEM image of ZIF-8.
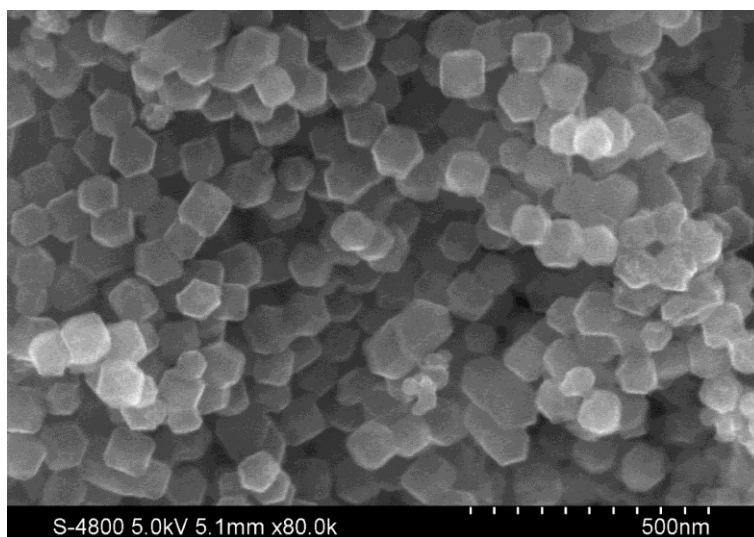

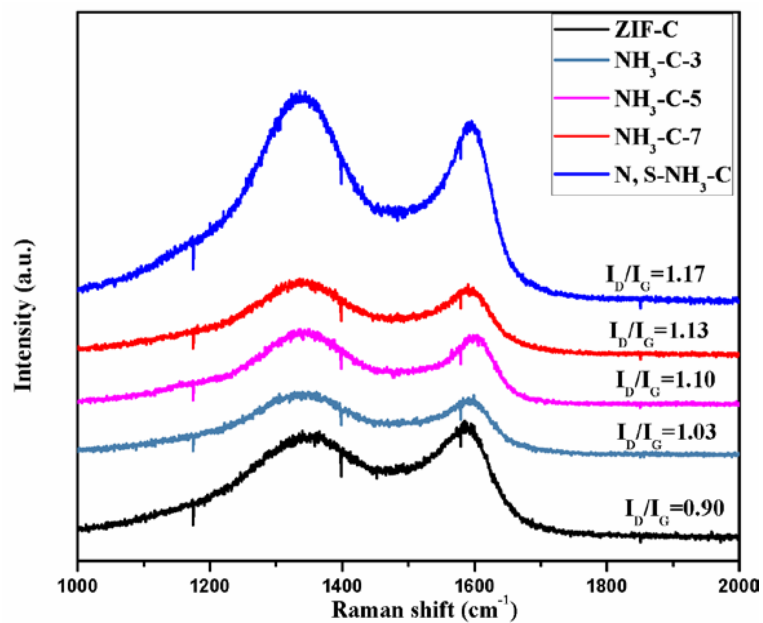**Figure SI 8.2. SEM image of ZIF-C nanocarbon.**

Figure SI 8.3. Raman spectra of the as-synthesized samples of ZIF-C, NH₃-C-x and N, S-NH₃-C-7.
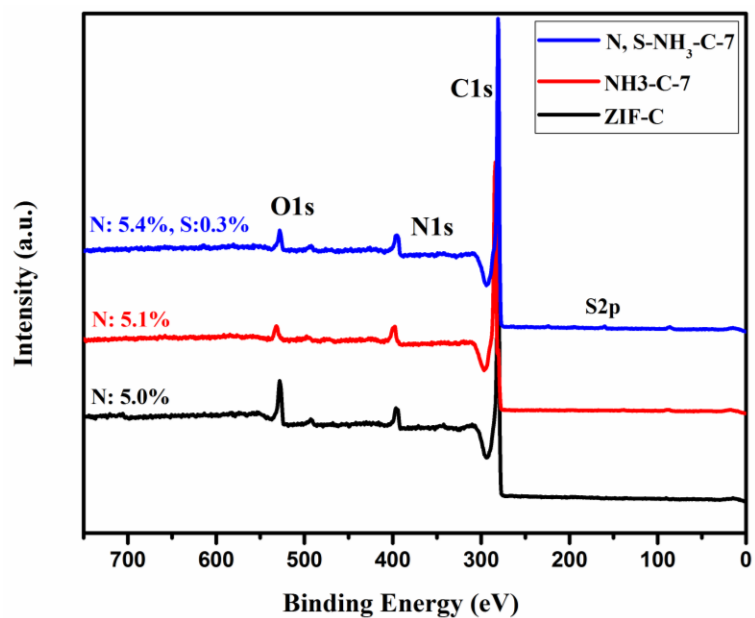
Figure SI 8.4. XPS spectra of samples of ZIF-C, NH₃-C-7 and N, S-NH₃-C-7.
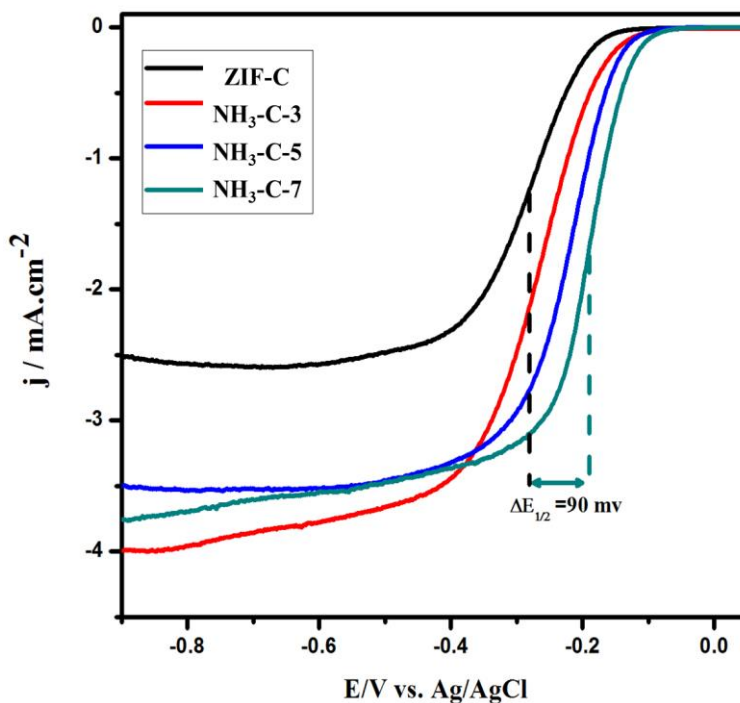
Figure SI 8.5. Linear sweep voltammograms (LSVs) of ZIF-C (black), NH₃-C-3 (red), NH₃-C-5 (blue) and NH₃-C-7 (cyan) in O₂-saturated 0.1 M KOH solution at 1600 rpm with a scan rate of 10 mV·s⁻¹.
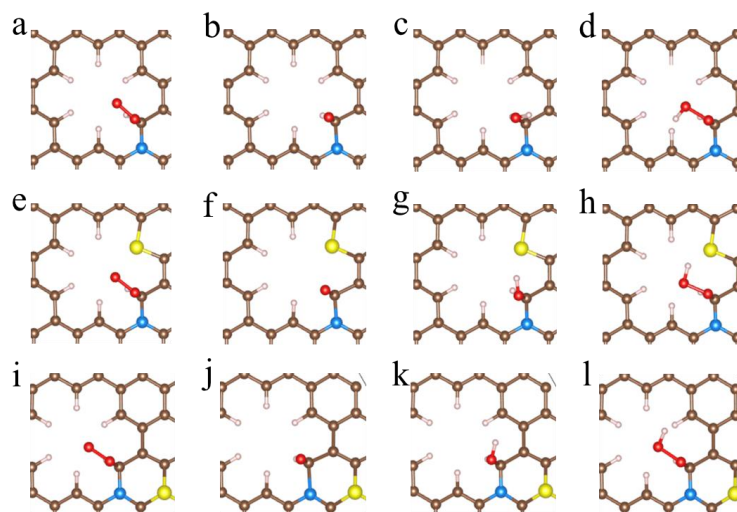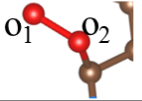
Figure SI 8.6. Optimized structures for the stable adsorbed O₂, O, OH, OOH on N-doped nanocarbon (a-d), N, S-isolated nanocarbon, (e-h), and N, S-coupled nanocarbon, (i-l), respectively.

Table SI 8.1. Bader charge of the stable adsorbed O_2 on the structures of N-doped nanocarbon, N, S-isolated nanocarbon and N, S-coupled nanocarbon.

structure	N-doped	N, S-isolated	N, S-coupled
Bader charge	6.2539 (o_1) 6.3281 (o_2)	6.4038 (o_1) 6.7855 (o_2)	6.3985 (o_1) 6.9002 (o_2)

Chapter 9

9   Conclusion and future perspectives

This chapter will summarize the work presented in this thesis. The highlights of each experimental chapter will be examined and discussed. A focus of this chapter is to analyze the work conducted and presented herein and the ALD technique contributions to the field of PEMFC electrocatalysts.

9.1   Conclusion

Polymer electrolyte membrane fuel cells (PEMFCs) as an innovative clean energy conversion device is considered as the technology of the future. PEMFCs use the chemical energy of hydrogen to cleanly and efficiently produce electricity, with water and heat as the only byproducts. PEMFCs have several benefits over conventional combustion-based technologies currently used in many power plants and passenger vehicles, such as the high efficiency, low emissions and the quiet operations etc. However, PEMFCs are still facing barriers for the widespread application, especially, high-cost, poor performance and durability are the key challenges in PEMFCs commercialization.

Atomic layer deposition (ALD) is an attractive approach for deposition of noble metal catalysts and metal oxides. Its ability to deposit uniformly distributed particles ranging from single atoms, sub-nanometer clusters, to nanoparticles (NPs), in a uniform manner on the available substrate surface, give it a competitive advantage over other deposition techniques. The primary advantages of ALD are derived from the sequential, self-saturating, gas-surface reactions that take place during the deposition process. Uniform deposition on three dimensionally-structured materials is made possible by self-terminating characteristics, which restricts the reaction at the surface to no more than one layer of precursor. With sufficient precursor pulse time, organometallic precursors can be uniformly exposed into deep trenches, allowing for complete reaction with the entire surface.

This thesis work is mainly focused on the highly stable and active nanostructured electrocatalyst design by the techniques of ALD for PEMFCs application. A series of

experimental programs were carried out in this study to fabricate various nanomaterials by ALD approach, such as transition metal/metal oxides, Pt catalysts from nanoparticles to single atoms, to construct anode and cathode electrocatalysts with excellent performance for PEMFCs. Different physical and electrochemical characterizations were conducted to determine the relationships between the physical properties of as-prepared materials and the electrochemical performance. Furthermore, the underlying mechanisms of nanomaterials and electrochemical performance were explored, such as the interactions between metal-catalysts and the support; The accessible active sites density, loading as well as the active particles size effect. In summary, this thesis focused on promising electrocatalysts design in PEMFCs and mainly on three parts: nano-electrocatalysts preparation by ALD, physical and electrochemical characterization, and understanding the underlying mechanisms from the nanostructures to the electrochemical PEMFCs performance. The work paves a path for the future use of ALD in promising field of fuel cells and it is believed that the studies and analysis have great potential to reduce the high cost of commercial PEMFCs.

Tantalum oxide (TaOx) NPs are deposited on a commercial Pt/C catalyst by an area-selective ALD approach to improve the electrocatalyst stability in PEMFCs operation. The TaOx loading on the Pt/C surface could be controlled precisely by varying the number of ALD cycles. When deposited on the Pt/C surface with 35 ALD cycles, the TaOx-anchored Pt NPs formed an excellent triple-junction structure of TaOx–Pt–carbon. The electrochemical durability tests indicated that the TaOx-anchored Pt/C catalyst showed superior long-term stability to Pt/C while maintaining the high electrocatalytic activity. The significantly enhanced catalyst stability is due to the anchoring effect of TaOx via strong metal oxide–support interactions. This strategy shows great potential of ALD in developing highly stable catalysts for PEMFCs.

Following the above work, nitrogen-doped tantalum oxide (N-Ta_2O_5) NPs were fabricated by ALD which were used as the bridge layer between Pt NPs and carbon support to construct the strong metal-support interaction. Herein an extremely stable electrocatalyst of Pt NPs dispersed on the N-Ta_2O_5-modified carbon support was demonstrated. The N-Ta_2O_5 nano-bridge layer synthesized by ALD not only provide the good conductivity for promoting the high activity, but also can effectively prevent Pt NPs from migration and aggregation during

PEMFCs operation, which enables the enhanced activity and long-term PEMFCs stability. X-ray absorption spectroscopy revealed the altered electronic structure of Pt NPs and strong interactions between Pt NPs and N-Ta_2O_5-carbon support, which contribute to the excellent activity and durability of Pt/N-ALDTa$_2O_5$/C catalyst. This strategy, by using ALD of N-doped metal oxide to tune the metal-support interface, results in strong interactions and will benefit the future design of a new electrocatalyst with an even better activity and long-term durability for PEMFCs application.

To achieve the extremely low Pt loading in the anode catalyst layer while maintain the high PEMFCs performance and long-life time, a series of high-performance membrane electrode assemblies (MEAs) with low Pt loading in anode layer are successfully prepared using an ALD technique. By controlling the ALD cycle number, the Pt NPs with different size and loading amount were directly deposited on the carbon coating layers to form the anode catalyst layers. The electron microscopy characterization indicated that ALDPt NPs with uniform particle size were highly dispersed on all the available carbon surface. The MEA using ALDPt/C as anode containing with extremely low Pt loading of 0.01 mg·cm^{-2} has even comparable PEMFCs performance to that of commercial Pt/C catalyst with much higher loading of 0.035 mg·cm^{-2}. Moreover, the startup/shutdown cycling test indicated that the ALDPt-MEA shows much improved durability than that of commercial Pt-MEA under the same Pt loading in anode layer, which has 4.2 times higher active surface area than that of commercial Pt catalyst after cycling.

Furthermore, single atom catalysts have the utmost atom utilization and thus maximize the usage efficiency of metal atoms. We reported on a practical synthesis method to produce the supported Pt single atoms and subnano-clusters catalysts using ALD technique. To investigate the impact of atom utilization on the electrocatalysis for oxygen reduction reaction (ORR), Pt single atoms, subnano-clusters as well as NPs with different size and density on MOFs-derived carbon support were designed. The characteristics of scanning transmission microscopy (STEM) and X-ray absorption fine structure were used to determine the Pt single atoms/subnano-clusters size distribution and electronic structure. Electrochemical analysis on these ALDPt catalysts indicated that the Pt single atoms/subnano-cluster synthesized with 1min and 2min Pt precursor exposure during ALD

synthesis exhibit the best ORR catalytic activity and excellent long-term stability than that of the Pt NPs catalyst. The X-ray absorption revealed that the unsaturated coordinated atom environment and unique Pt single atom-support interaction determined the superior ORR activity and durability performance.

At last, a noble-metal free electrocatalyst of nitrogen and sulfur-co-doped nanocarbon derived from metal-organic frameworks (MOFs) was developed as an electrocatalysts for ORR. It is found that compared to the noble-metal Pt/C catalyst, the N,S-co-doped nanocarbon exhibits excellent catalytic activity and long-term stability toward ORR in alkaline media. Importantly, first-principles calculations reveal that the N,S-coupled dopants promote the carbon sites with a higher activity compared to the isolated N and S dopants. The N,S-coupled nanocarbon provides a great electron density to the adsorbed O_2, thus making O_2 and its species to be reduced. The highly active co-doping sites resulting from the synergistic effect well explain the origin of the enhanced ORR activity for the N,S-co-doped nanocarbon. The approach and analysis adopted in this work offer a strategic consideration for designing the high performance nanocarbon electrocatalyst.

9.2 Perspectives

As discussed above, the fabrication of strong catalyst-support interactions is inevitable for enhancing the long-time stability of Pt catalysts. On the other hand, maximum the Pt atom utilization by develop the Pt single atom catalyst is in highly demand to decrease the cost while enhance the high catalytic activity. Recent candidates have been shown to be very promising; however, delicate analysis, mechanism understanding, and approaches are required for the application of novel catalysts to industrial electrochemical systems. Finally, we will provide some suggestions for future work:

(1) Nanoparticle-support interaction and development of durable support

Nanoparticle (NP) electrocatalysts, are generally deposited on support materials with high surface area to prevent agglomeration. However, the interaction between the NPs and the supports has not been sufficiently clarified. Because the support is not simply an inert conductive material and can affect the activity and durability via electron-transfer

interactions, more detailed analysis on the interface between the NPs and the support should be addressed. Furthermore, the development of durable support materials to replace the current carbon-based materials is very important. Because of the harsh and corrosive environment at high potentials, carbon materials themselves cannot fully protect NPs from coalescence and detachment during long-term operation. In the future, new concepts or supports that fulfill criteria such as high surface area, high electrical conductivity, and high corrosion resistance need to be developed.

(2) Single atom catalysts (SACs) of precious metal for electrochemical reactions

The correlation between the single atom properties and the electrocatalytic performance needs to be understood. Previous research has shown that the coordination number of Pt affects the bond strength of the intermediate and the ORR activity. Other conditions can modulate the catalytic activity, such as the number of coordinated ions, adsorbed vacancy sites, electron transfer from the support to the catalytic active site, and so on. This topic should be studied carefully in the future and could provide new insight into SACs. Moreover, the durability of SACs should be carefully determined. Electrochemical applications often undergo high voltages, especially in a full cell system. SACs might be easily agglomerated into NPs upon repeated reactions, and such changes should be suppressed.

(3) Systematic study on the origin of the discrepancy between liquid half-cell and full-cell tests

ORR electrocatalyst research has been intensively explored with the strong motivation to obtain valuable solutions for economic and technological challenges faced by the fuel-cell industry. Nevertheless, while hundreds of Pt-based electrocatalysts have been reported to outperform commercial Pt/C under the liquid half-cell condition, only limited cases of the electrocatalysts have been shown to be active or durable in the membrane electrode assembly (MEA) of fuel-cell devices, which indicates a critical limitation in the current research field. Another big issue of a large discrepancy in electrocatalytic activity occurs when electrocatalysts are applied to the MEA scale, especially in the case of intrinsically active electrocatalysts. This discrepancy might originate from the difference in the operating environment; unlike in a liquid half-cell test, a large amount of electrocatalyst is deposited

with an ionomer on the polymer electrolyte membrane in MEA. Due to the polymer electrolyte membrane and thick electrode configuration, electrocatalysts in MEA usually suffer from limited transport of protons and oxygen, as well as waterflooding within the cathodic electrode, which are usually neglected under the liquid half-cell condition. However, there have been only a few efforts to correlate these different operating conditions with activity discrepancy. Therefore, more systematic studies need to be organized to clarify the correlation between changes in operating conditions and electrocatalytic properties, which will set a milestone for bridging a large gap between liquid half-cell studies and MEA-based full-cell device application.

Appendices

Appendix A: Permission from Royal Society of Chemistry (RSC) For Published Article

Published article:

1. Atomic layer deposited tantalum oxide to anchor Pt/C for a highly stable catalyst in PEMFCs. **J. Mater. Chem. A**, 2017,**5**, 9760-9767.

2. Origin of the high oxygen reduction reaction of nitrogen and sulfur co-doped MOF-derived nanocarbon electrocatalysts. **Mater. Horiz.**, 2017,**4**, 900-907.

Re-use permission requests

Material published by the Royal Society of Chemistry and other publishers is subject to all applicable copyright, database protection, and other rights. Therefore, for any publication, whether printed or electronic, permission must be obtained to use material for which the author(s) does not already own the copyright. This material may be, for example, a figure, diagram, table, photo or some other image.

Author reusing their own work published by the Royal Society of Chemistry

You do not need to request permission to reuse your own figures, diagrams, etc, that were originally published in a Royal Society of Chemistry publication. However, permission should be requested for use of the whole article or chapter except if reusing it in a thesis. If you are including an article or book chapter published by us in your thesis please ensure that your co-authors are aware of this.

Reuse of material that was published originally by the Royal Society of Chemistry must be accompanied by the appropriate acknowledgement of the publication. The form of the acknowledgement is dependent on the journal in which it was published originally, as detailed in 'Acknowledgements'.

Appendix B: Permission from Elsevier for Published Article

Published article:

1. Metal organic frameworks for energy storage and conversion. **Energy Storage Materials**, 2 (2016) 35–62.

Curriculum Vitae

Name: Zhongxin Song

Post-secondary Education and Degrees: The University of Western Ontario
London, Ontario, Canada
2014-2018 Ph.D.

Qingdao University of Science and Technology
Qingdao, Shandong, China
2011-2014 M.Eng.

Qingdao University of Science and Technology
Qingdao, Shandong, China
2007-2011 B.Eng.

Honours and Awards: China Scholarship Council (CSC) Scholarship
2014-2018

Related Work Experience Co-op research assistant
Ballard Power Systems
May 2016-Aug. 2016; Mar. 2017-Sep. 2017

Publications:

(A) *First author*

1. Z. Song, W. Liu, N. Cheng, M. Banis, X. Li, Q. Sun, B. Xiao, Y. Liu, A. Lushington, R. Li, L. Liu, X. Sun. Origin of the high oxygen reduction reaction of nitrogen and sulfur co-doped MOF-derived nanocarbon electrocatalysts. **Mater. Horiz.**, 2017, 4, 900.

2. Z. Song, B. Wang, N. Cheng, L. Yang, D. Banham, R. Li, S. Ye, X. Sun, Atomic layer deposited tantalum oxide to anchor Pt/C for a highly stable catalyst in PEMFCs, **J. Mater. Chem. A**, 2017, 5, 9760.

3. Z. Song, M. Banis, L. Zhang, B. Wang, L. Yang, D. Banham, Y. Zhao, J. Liang, M. Zheng, R. Li, S. Ye, X. Sun. Origin of achieving the enhanced activity and stability of Pt

electrocatalysts with strong metal-support interactions via atomic layer deposition. **Nano Energy,** 2018.

4. Z. Song, L. Zhang, M. Zheng, X. Sun, MOFs-derived Materials for Extremely Efficient Electrocatalysis, 2018 RSC book of **Layered Materials for Energy Storage and Utilization**.

5. Z. Song, N. Cheng, A. Lushington, X. Sun, Recent Progress on MOF-Derived Nanomaterials as Advanced Electrocatalysts in Fuel Cells, **Catalysts** 2016, 6, 116.

6. Y. Zhao[1], **Z. Song[1]**, ([1] equal contribution), X, Li, Q, Sun, N, Cheng, S. Lawes, X, Sun, Metal organic frameworks for energy storage and conversion, **Energy Storage Materials**, 2016, 2, 35.

7. J. Cui[a], **Z. Song[a],** ([a] equal contribution), L. Xin, S. Zhao, Y. Yan, G. Liu , Exfoliation of graphite to few-layer graphene in aqueous media with vinylimidazole-based polymer as high-performance stabilizer. **Carbon**, 2016, 99, 249.

8. Z. Song, J. Dai, S. Zhao, Y. Zhou, F. Su, J. Cui, Y. Yan, Aqueous dispersion of pristine single-walled carbon nanotubes prepared by using a vinylimidazole-based polymer dispersant. **RSC Adv.,** 2014, 4, 2327.

9. Z. Song, M. Banis, H. Liu, L. Zhang, Y. Zhao, J. Li, M. Zheng, R. Li, P. He, S. Knights, X. Sun, Ultra-low loading and high-performing Pt catalyst for PEMFC anode achived by atomic layer deposition, 2018, ready to submit.

10. Z. Song, L. Zhang, H. Liu, M. Banis, J. Li, M. Zheng, R. Li, X. Sun. Platinum single-atom and subnano-cluster on MOF-carbon as superior oxygen reduction reaction catalysts, 2018, ready to submit.

 (B) *co-author*

11. A. MacIntosh, G. Jiang, P. Zamani, **Z. Song**, A. Riese, K. Harris, Xi. Fu, Z. Chen, X. Sun, G. Goward, Phosphorus and Nitrogen Centers in Doped Graphene and Carbon Nanotubes Analyzed through Solid-State NMR, **J. Phys. Chem. C**, 2018, 122, 6593.

12. C. Zhao, C. Yu, M. Banis, Q. Sun, M. Zhang, X. Li, Y. Liu, Y. Zhao, H. Huang, S. Li, X. Han, B. Xiao, **Z. Song**, R. Li, J. Qiu, X. Sun, Decoupling atomic-layer-deposition ultrafine RuO2 for high-efficiency and ultralong-life Li-O2 batteries, **Nano Energy**, 2017, 34, 399.

13. J. Liang, Y. Sun, Q. Sun, **Z. Song**, Y. Zhao, A. Koo, Q. Li, Y. Liu, X. Li, C. Wang, K. Adair, W. Li, M. Li, Y. Hu, R. Li, X. Sun, Stabilize PEO-based solid polymer electrolyte in LiCoO$_2$ solid-state batteries by atomic layer deposition interface engineering, ready to submit.

14. S. Zhao, **Z. Song**, J. Cui, C. Li, Y. Yan, Improving dispersion and integration of single-walled carbon nanotubes in epoxy composites by using a reactive noncovalent dispersant. **Journal of Polymer Science Part A: Polymer Chemistry**, 2012, 50, 4548.

15. C. Zhao, C. Yu, S. Li, W. Guo, Y. Zhao, Q. Dong, X. Lin, **Z. Song,** X. Tan, C. Wang, M. Zheng, X. Sun, J. Qiu, Ultrahigh-Capacity and Long-Life Lithium Metal Batteries Enabled by Engineering Carbon Nanofibers-Stabilized Graphene Aerogel Film Host, **Small,** 2018.

Conference oral presentations:

1. **Z. Song**, X. Sun, "Electrocatalysts for Fuel Cells: From Nanocatalysts to Single-Atom Catalysts", 2018 MRS Spring Meeting &Exhibit, Phoenix, Arizona, U.S.A.

2. **Z. Song**, M. Banis, X. Sun, "Atomically controlled Pt-based electrocatalysts with high stability and ultra-low loading for PEM fuel cells", CaRPE-FC Annual Technical Review Meeting, 2017, Vancouver, BC, Canada.

3. **Z. Song**, M. Banis, X. Sun, "Catalysis Research for Polymer Electrolyte Fuel Cells", 5th Annual CaRPE-FC Technical Review Meeting, 2016, Vancouver, BC, Canada.

Conference posters:

1. **Z. Song**, N. Cheng, M. Banis, R. Li, S. Ye, P. He, S. Knights, X. Sun, "Designing Highly Active and Durable Pt-based Electrocatalysts by Atomic Layer Deposition", CaRPE-FC Annual Technical Review Meeting, 2017, Vancouver, BC, Canada.

2. **Z. Song**, N. Cheng, M. Banis, R. Li, X. Sun, "N, S-co-doped MOFs-Carbon as Electrocatalysts for Enhanced Oxygen Reduction Reaction", 5th Annual CaRPE-FC Technical Review Meeting, 2016, Vancouver, BC, Canada.